HIGHLY-CONFIGURABLE MULTI-OBJECTIVE OPTIMIZATION FOR PHYSICAL PARAMETER EXTRACTION USING TERAHERTZ TIME-DOMAIN SPECTROSCOPY

A dissertation submitted in partial fulfillment of the
requirements for the degree of
Doctor of Philosophy

By

ANDREW JOHN NIKLAS
M.S., Wright State University, 2012
B.S., University of Cincinnati, 2007

2018
Wright State University

WRIGHT STATE UNIVERSITY

GRADUATE SCHOOL

April 19, 2018

I HEREBY RECOMMEND THAT THE DISSERTATION PREPARED UNDER MY SUPERVISION BY **Andrew John Niklas** ENTITLED **Highly-Configurable Multi-Objective Optimization for Physical Parameter Extraction using Terahertz Time-Domain Spectroscopy** BE ACCEPTED IN PARTIAL FULFILLMENT OF THE REQUIREMENTS FOR THE DEGREE OF **Doctor of Philosophy.**

_____

Jason A. Deibel, Ph.D.
Dissertation Director

_____

K.T. Arasu, Ph.D.
Director, Interdisciplinary Applied Science and Mathematics PhD Program

_____

Barry Milligan, Ph.D.
Interim Dean of the Graduate School

Committee on Final Examination:

_____

Elliott R. Brown, Ph.D.

_____

Sara Pollock, Ph.D.

_____

Michael A. Saville, Ph.D., P.E.

ABSTRACT

Niklas, Andrew John. Ph.D. Interdisciplinary Applied Science and Mathematics Graduate Program, Wright State University, 2018. Highly-Configurable Multi-Objective Optimization for Physical Parameter Extraction using Terahertz Time-Domain Spectroscopy.

The use of terahertz time-domain spectroscopy provides one of the most versatile and promising techniques for the robust determination of optical parameters, which is needed to enable identification of materials for quality control, materials science advancement, tamper prevention, drug enforcement, and hidden explosives detection. Previously, the state-of-the-art relied on legacy error measures for minimization of simulation error and the standard practice was to use a single unique measurement for each unknown material in a sample. Successful optical parameter extraction for uniformly varying optical property materials is correlated with low variation in extracted optical properties. This work advances the state-of-the-art in optimization-based physical parameter extraction using terahertz time-domain spectroscopy. This is achieved by standardizing the signal processing methodology, clearly defining the best optimization formulation to yield low simulation error and optical property variation, and leveraging multiple measurements to reduce the impact of system-dependent artifacts on extracted

optical properties. A thorough analysis of alternative error measures across numerous objective function formulations demonstrates that a 28% reduction in the Fabry-Perot etalon effect in the optical property of materials is achievable, compared with legacy approaches. The research conclusively demonstrates that time-domain objective function formulations yields simulation error that is 83% less than frequency-domain objective function formulations. Furthermore, the research shows that multi-measurement optimizations reduce oscillations in optical properties caused by the Fabry-Perot etalon effect by as much as 92%, compared with single-measurement optimizations. The research validates the numerical solutions to less than 6% error compared with analytical solutions, for uniform and non-uniform optical property materials. Importantly, the research extends the state-of-the-art by demonstrating the ability to simultaneously determine the effective sample thickness and orientation for high absorption samples comprised of solid and granular materials with uniform and non-uniformly varying optical properties. The outcomes of the research include a novel and comprehensive suite of methodologies that address fundamental complexities associated with exploitation of time-domain terahertz spectroscopic data.

TABLE OF CONTENTS

LIST OF FIGURES

LIST OF TABLES

1. INTRODUCTION

The terahertz (THz) region of the electromagnetic spectrum is typically defined as frequencies of radiation ranging between 0.1–10 THz [1]. Low to moderate power THz radiation is nondestructive to all dielectric materials [2]. The optimization of a physical model in combination with Nondestructive Evaluation (NDE) characterization of materials with Terahertz Time-Domain Spectroscopy (THz-TDS) facilitates a determination of physical parameters such as thickness and the frequency-dependent complex index of refraction [3]. The physical parameters can then be used to characterize and identify the materials for integration into sophisticated exploitation processes such as manufacturing quality control, material identification, and device tampering detection [4].

The NDE measurements of materials consists of irradiating a sample in open-air with THz frequency radiation. The graphic in Figure 1.1 shows the frequency range of THz radiation on the electromagnetic spectrum. The samples are irradiated and time-domain measurements are conducted using a commercial-off-the-shelf (COTS) broadband ultrafast laser-pumped THz-

TDS pulsed spectroscopy system manufactured by Teraview [5]. The data acquired with the time-domain system can be Fourier transformed to obtain magnitude and phase information in the frequency-domain [3]. Although the measurement apparatus facilitates reflection and transmission measurements, only transmission measurements are evaluated in this work. The samples investigated in this research consist of High Resistivity Silicon (HRSi), High-Density Polyethylene (HDPE), α-Lactose monohydrate, pharmaceutical-grade Oxycodone, and Hydrocodone with a configurable stacking of layers. All references to Lactose in this research imply α-Lactose monohydrate, and all references to Oxycodone imply pharmaceutical-grade Oxycodone. Acknowledgement is given to Dr. Elliott Brown, Ph.D., and Dr. Weidong Zhang, Ph.D., for providing the α-lactose monohydrate, pharmaceutical-grade Oxycodone, and Hydrocodone samples. The five dielectric materials examined in the research are assumed to be homogeneous and isotropic, with no magnetic response to the incident radiation in the THz regime. Each HRSi and HDPE material surface is assumed to be planar with all material interfaces coplanar. The HRSi and HDPE material surfaces used in the measurements are assumed to be smooth relative to the submillimeter wavelengths of the THz frequency radiation. The α-lactose monohydrate, pharmaceutical-grade Oxycodone, and Hydrocodone are measured in aggregate particulate form and

as such no assumptions are made about the uniformity of the particle density or the undulations of the casing surface.

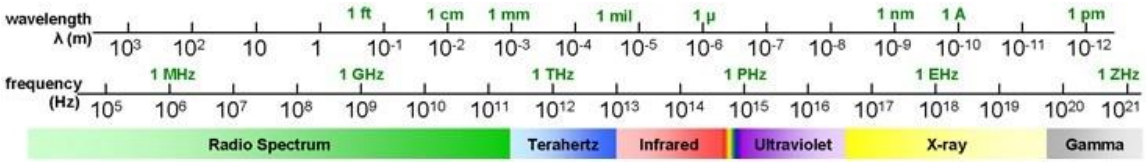

Figure 1.1) The location of the terahertz region (blue bar) on the electromagnetic spectrum [Credit: The Southeastern Universities Research Association (SURA)].

The time-domain measurement of terahertz frequency radiation scattered from materials, combined with physical parameter extraction algorithms, can enable the determination of material properties such as material thickness, index of refraction, and absorption coefficient. This research demonstrates the ability of computer-based mathematical optimization to solve the inverse problem using the Fresnel model of electromagnetic scattering. The physical measurements are obtained using a commercial-off-the-shelf broadband pulsed terahertz spectroscopy system. The physical model utilizes the transfer matrix method to generate the reflection and transmission transfer functions representing the effective interaction of electromagnetic radiation with multi-layered materials. The optimization utilizes the differential evolution and Nelder-Mead algorithms to facilitate parameter extraction in the frequency-domain and time-domain. The feasibility and accuracy of the approach is verified by the presentation of

quantitative results which demonstrate the performance and rigor of the technique.

The thickness and density of the samples are assumed to be constant across the dimensions of the sample, however it is acknowledged that the thickness of the samples are unlikely to be constant and perfectly uniform. In particular, the thickness and density of the particulate samples is unlikely to be constant and uniform. Therefore, the locality of the illumination spot of the THz light on the sample is important when comparing measurements. Additionally, the material surfaces used in the measurements are assumed to be smooth relative to the submillimeter wavelengths of the THz frequency radiation.

The method developed for determining the material physical parameters leverages the techniques published in the discipline of parameter extraction using NDE by THz-TDS [6]. The published techniques and the motivation for the research are presented in Section 2. The theoretical formulation of the proposed method, measurements recorded to facilitate the process, and the computational optimization process are presented in Section 3, Section 4, and Section 5, respectively. The results of the physical parameter extractions and computational runtimes using the methods developed in the research are presented in Section 6 and Section 7, respectively.

In summary, the research provides a versatile and promising solution for robust optimization-based extraction of physical parameters. The solution is achieved by standardizing the signal processing methodology, clearly defining the best optimization formulation to yield low simulation error, and leveraging multi-measurement optimization to reduce the impact of system-dependent artifacts on extracted optical properties. A thorough analysis of alternative error measures across numerous objective function formulations demonstrates that a 28% reduction in the Fabry-Perot etalon effect in the optical property of materials is achievable, compared with legacy approaches. The research demonstrates that a time-domain objective function formulation yields simulation error that is 83% less than frequency-domain objective function formulations. Furthermore, the research shows that multi-measurement optimizations reduce oscillations in optical properties caused the Fabry-Perot etalon effect by as much as 92%, compared with single-measurement optimizations. The research validates the numerical solutions to less than 6% error compared with analytical solutions, for uniform and non-uniform optical property materials. The outcomes of the research include a novel and comprehensive suite of methodologies that have far-reaching and long-lasting fundamental impact associated with exploitation of THz-TDS data.

2. BACKGROUND

The process of physical parameter extraction, for the purposes of this research, begins with the recording of the electric field of THz pulses after they propagate through the material being evaluated. Physical parameter extraction is facilitated by two fundamental components of THz-TDS data. The two components are the THz field amplitude and the time delay at which the amplitude occurs. The result of assembling a sequence of amplitude and time delay pairs in a single measurement is constitutes the time-domain signal. The time-domain signal is represented in the plot shown in Figure 2.1. In Figure 2.1, the time-domain signal of air is shown in blue. The time-domain signal resulting from placing a 1.6 millimeter sheet of plastic, in air, between the transmitter and receiver is shown as the red signal in Figure 2.1.

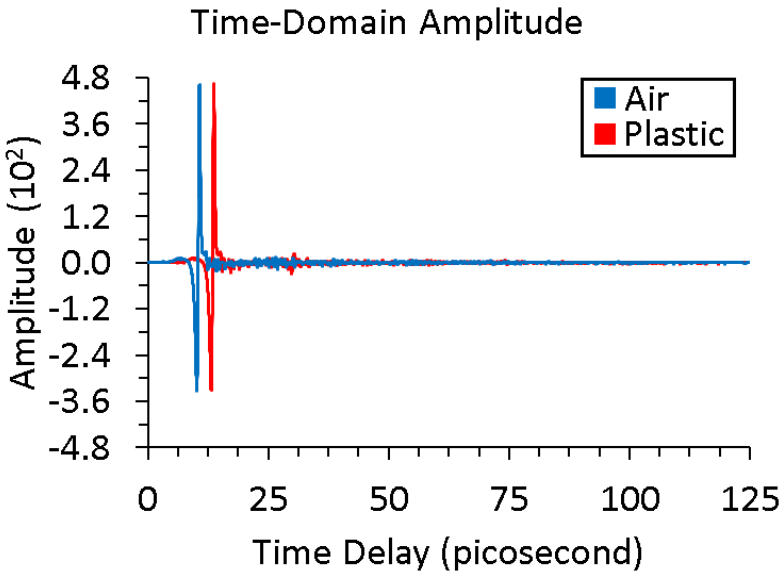

Figure 2.1) The time-domain signal resulting from THz pulse transmission through air (blue) and plastic (red).

The physical parameters are grouped into frequency-dependent and frequency-independent properties. The frequency-independent properties are material thickness, and orientation with respect to the incident THz pulse propagation direction. The frequency-dependent properties are material refractive index and absorption coefficient. There are several rudimentary pieces of information that can be gathered about optical properties based on the comparison of two time-domain signals. The first piece of information is the difference in arrival time of the THz pulses between the two time-domain signals. The second piece of information is the difference in recorded energy level of the THz pulses between the two time-domain signals. Figure 2.2 demonstrates these two rudimentary pieces of information with an instructional graphic, and two simplistic equations. In the graphic, the green

arrows indicate the incident and transmitted THz light pulses. The blue medium labelled with n_1 and α_1 is air, for example. The red medium labelled with n_2 and α_2 is plastic, for example. The variables n_1 and n_2 represent the unitless refractive index of the materials. The variables α_1 and α_2 represent the absorption of the materials, in units of inverse distance. As indicated in Figure 2.2, the distance travelled in each medium is the same.

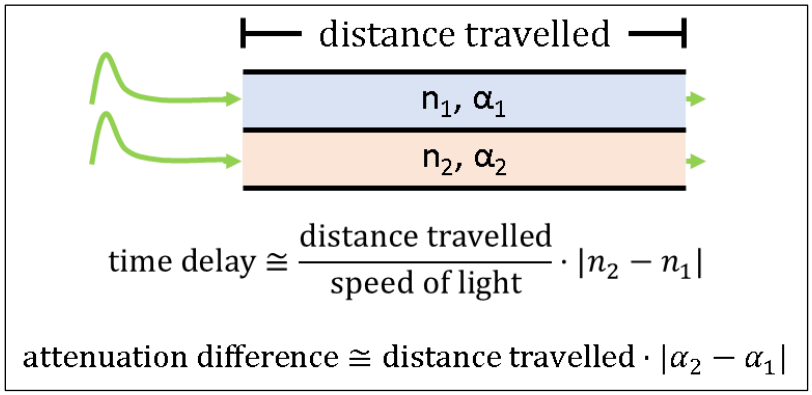

Figure 2.2) The time delay and attenuation difference caused by the propagation of THz pulses through two different media.

The information provided in Figure 2.2, the preceding explanation, and the two time-domain signals are used to make an initial inference about the optical properties of the two materials. First, in Figure 2.1, the peak amplitude of the plastic time-domain signal occurs later than the peak amplitude of the air time-domain signal. This observation indicates that $n_2 > n_1$ and furthermore if n_1 is known then n_2 can be estimated. Secondly, in Figure 2.1, the minimum and maximum amplitude of the air and plastic time-domain signal appear approximately the same. This observation indicates that $\alpha_2 \approx$

α_1, which indicates that at THz frequencies the average optical absorption property of plastic is not much different than the average absorption property of air. Here it is instructive to define physical parameters

A more rigorous approach to assessing the physical parameters of a material requires Fourier transforming the real-valued time-domain signal into a complex-valued frequency-domain signal. The frequency-domain signal is in-turn transformed into spectral magnitude and phase profiles. The spectral magnitude of air (red) and plastic (blue) is shown in the left plot of Figure 2.3. The spectral phase of (air) and plastic (blue) is shown in the right plot of Figure 2.3. The rudimentary time-domain analysis facilitates frequency-averaged assessment of the optical properties of materials, whereas a rigorous frequency-domain analysis facilitates frequency-dependent assessment of the optical properties.

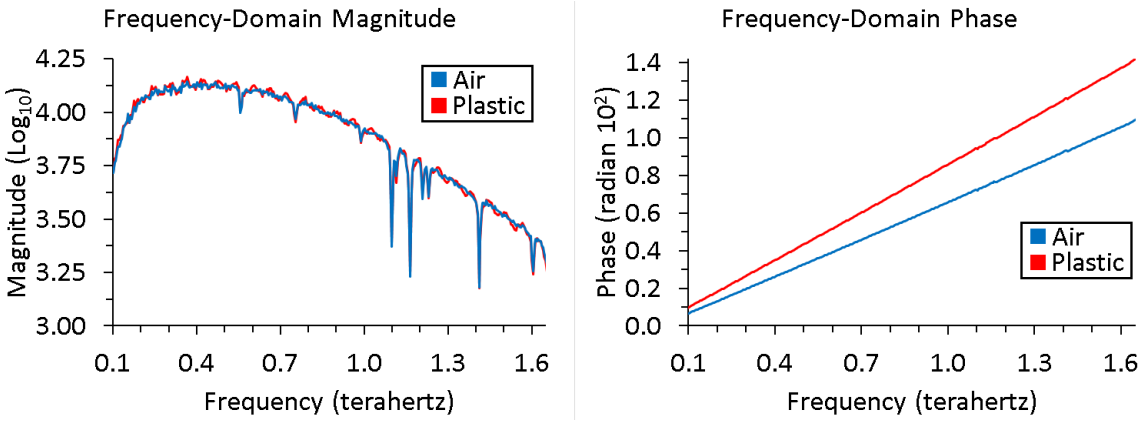

Figure 2.3) The frequency-domain magnitude and phase resulting from THz pulse transmission through air (blue) and plastic (red).

As with the rudimentary time-domain analysis, there are two pieces of information determined by analyzing the spectral magnitude and phase profiles shown in Figure 2.3. The first observation is that the spectral magnitude profile of air is directly overlays the spectral magnitude profile of plastic. This observation indicates that either the absorption of the plastic is sufficiently small, or the thickness of the plastic sheet is sufficiently thin, or both, that the amount of THz energy absorbed by the plastic sheet is nearly indifferentiable compared with the absorption through air. Also, evident in the spectral magnitude profile are steeply depressed magnitude features which are caused by non-negligible water vapor absorption at specific frequencies. The oscillations observed in the spectral magnitude profile are the result of multiple internal reflections prior to transmission out of the plastic sample, and will be discussed in detail throughout the research. The second observation is that spectral phase profile of plastic has a steeper slope compared with that of air. This observation indicates that either the plastic has a measurably larger refractive index than air, or that the thickness of the plastic sample is sufficiently large to exaggerate a small difference in refractive index between plastic and air. Because the plastic has a larger phase than air, the THz energy evolves through more sinusoidal revolutions as compared with air. The increased phase evolution in plastic is ultimately caused by the THz

pulses taking more time to transmit through the plastic compared with less time in air.

The combination of time-domain amplitude and spectral magnitude and phase multi-signal comparative analysis is a powerful tool when determining frequency-dependent and frequency-independent material properties. The tools are used by a numerical framework, based on mathematical and computer science principles, that leverages a physics model to accurately describe the observed phenomenology. The numerical framework is concisely called an optimization algorithm. The type of optimization algorithm developed in this research is a nested optimization approach, which is shown in Figure 2.4. The nested optimization approach facilitates the simultaneous solution of unknown frequency-independent and frequency-dependent physical parameters. At the core of the optimization algorithm is a comparison of the physics model estimate to the measurement data. The physics model estimate is called the simulation data. The core of the nested optimization algorithm uses the comparison to decide if the physical parameters that populate the physics model improve on previous parameter estimates. Generally, if the current physical parameter estimates improve the similarity between measurement and simulation, then the better physical parameter estimates are retained and additional sets of parameter estimates are sought by

the algorithm to further improve the similarity between measurement and simulation.

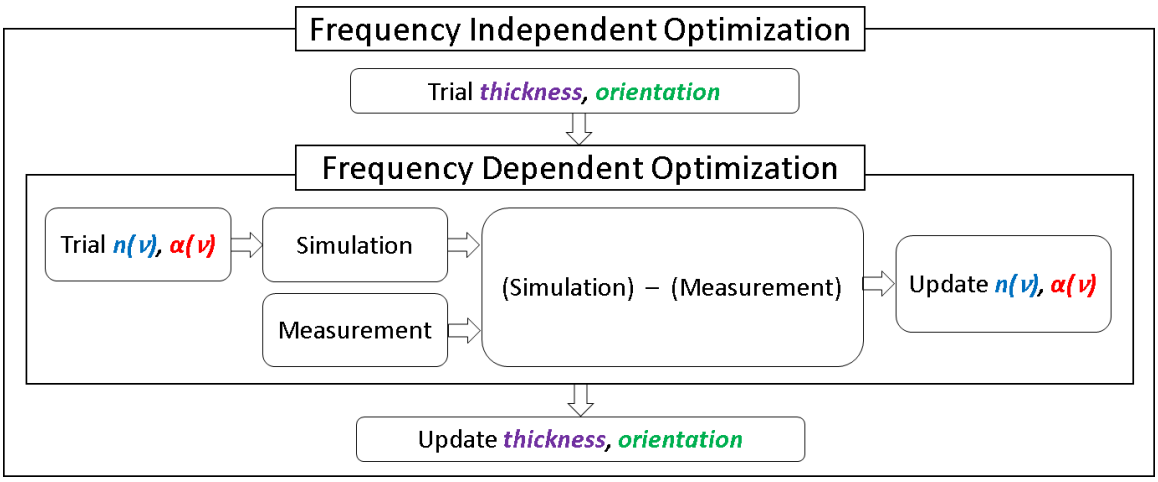

Figure 2.4) Generalized workflow of a nested physical parameter extraction procedure.

The extraction of physical parameters THz-TDS NDE measurements of dielectric materials has been actively researched for over twenty years [7]. The fundamental approach involves minimization of an error function defined as the total difference between theoretical simulations and physical measurements. The minimization can occur in either the frequency-domain or time-domain. In the time-domain, the minimizations act on the difference in real-valued amplitudes [8, 9]. In the frequency-domain, the minimizations can act on the complex transfer functions, complex signal, or phase and magnitude [10, 11, 12, 13, 14].

One of the first steps in the optimization process is the initialization of the physical parameters, such as sample layer thicknesses, sample orientation,

and optical properties of the materials being evaluated. Typically, two approaches for initialization are used in the published literature either separately or in combination: frequency-averaged values derived from the measured data using a Time of Flight (TOF) model, and a priori knowledge of the materials under investigation [8, 9, 10, 11, 12, 13, 14]. Once initialization is complete, the optimization uses the model parameters to update the physical parameters [7].

The model used for estimating the theoretical signal representation originates with the Fresnel model combined with propagation coefficients for the reference and medium and sample materials to obtain transfer functions, known as the sample response. The sample response describes the effective interaction of radiation with the sample. In addition to the model accounting for initial interaction with the sample, it is necessary to sufficiently account for the Fabry-Perot (FP) etalon effect [15]. The FP etalon effect is described by echo pulses, arising from the transmission after internal reflections within the sample at the layer interfaces. In some of the reported research literature, the model for the FP etalon effect is presented as a series expansion of pulse detections [7, 9, 10, 11, 12, 13, 14], and in others, the model is presented in the context of the transfer matrix method [8, 16, 17].

There are two scenarios discussed in the research literature to account for the FP etalon effect in single-layer samples: optically thick and optically thin samples. The first case defines an optically thick sample such that the spacing between time-domain echo pulses caused by the FP etalon effect is sufficiently large that the echo pulses are distinguishable. The second case defines an optically thin sample such that the time-domain echo pulses caused by the FP etalon effect are not well separated. The published research identifies the scenario that is applicable, and typically implements a method that is unique to the optically thick or optically thin scenario.

The categorization of a material as optically thick or optically thin is terminology used in the discipline of THz-TDS to define whether two separate time-domain pulses overlap within a time-domain signal, but does not translate into an explanation of the optical depth of a material [9]. Whether a sample of material is optically thick or thin depends on the frequency-dependent index of refraction, n, and physical thickness, d, of the sample. As an example, consider two emitters Tx_1 and Tx_2 with a separation of $\Delta x = x_1 - x_2 = 2d$ that emit identical pulses of energy at the exact same time, and a detector to detect the two simultaneous emissions. The hypothetical setup is shown in Figure 2.5. Next, define the time-domain width of a pulse as the width for which all the transmitted energy arriving at the detector is contained.

If the pulse width is 5 picoseconds (ps), the question then remains how small the physical thickness *d* can be and still avoid mixing energy from Tx_1 and Tx_2. If the index of refraction is hypothetically constant n = 1.0, 1.5, and 3.5 then d = 250, 167, and 72 micrometer (μm), respectively. If the pulse width is instead 3.3 ps, then d = 375, 250, and 107 μm, respectively.

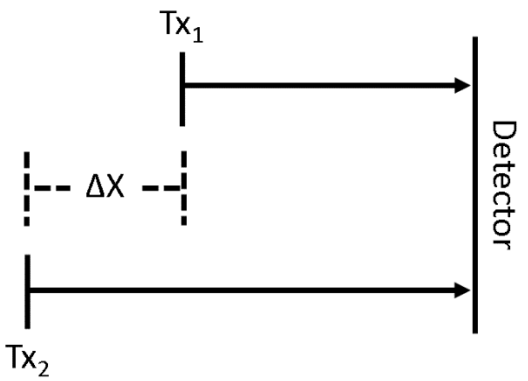

Figure 2.5) Hypothetical setup of two detectors Tx_1 and Tx_2 with spatial separation Δx which each simultaneously emit a single pulse of identical energy to a detector.

The sample response in the optically thick case is modeled to include a series summation of the FP etalon effect and the time-domain data after a certain number of echo pulses is truncated, with regions in between echoes set to a bias value [7, 10, 11, 12, 13]. The truncation can be extensive; all the FP echo pulses are truncated and the model does not include the FP etalon effect, as observed by Fastampa et al. [17]. Alternatively, the measured sample signal has been used to suppress the echo pulses and use a sample response model which does not include the FP etalon effect [18]. In contrast to optically thick samples, the sample response in the optically thin case is modeled with the

complete FP etalon effect and there is no manipulation of the measured sample signal [9, 11]. In either case, it is necessary to accurately model the sample response with the signal representation used in the objective function to obtain a meaningful minimization.

The minimization of the objective function is achieved by changing the model's optical parameters, such as thickness, index of refraction, and absorption. The optimization of the objective function is achieved using a variety of methods including: brute force grid sampling [11], Nelder-Mead [9, 12], Differential Evolution [8], Gradient Descent [7, 11], and Newton Methods [9]. The published research articles indicate that the objective function should include at least as many non-redundant measured equations of the same sample as there are unknown parameters in the problem [10, 18]. The case of many unknown parameters for each layer of a sample will necessitate many measurements. The non-redundant measurements are obtained by rotating the sample relative to the incident radiation so that the sample is uniquely irradiated at multiple angles of incidence [19].

The optimization of the sample thickness has been achieved for unknown index of refraction and absorption using an assumption of minimal variation in the index of refraction as a function of frequency, which has been demonstrated with measurements of HRSi and HDPE [8, 9, 10, 11, 12, 13].

The minimal variation approach essentially states that the variation of the true index of refraction should be small at THz frequencies. The technique states that variation in the algorithmically extracted index of refraction is primarily due to an incorrect sample thickness used in the optimization process. In the simple case of constant optical property as a function of frequency, the optimal sample thickness is the thickness for which the extracted index of refraction is constant and has zero variation. However, the minimal variation method is challenged when investigating materials with index of refraction that have absorption induced dispersion or non-uniform index of refraction spectral features. The research performed by Palka et al. [8] has shown that, for a known index of refraction, the thickness of the layers of a sample can be extracted without holding the index of refraction constant. Other research has incorporated the thickness determination into the index of refraction optimization algorithm [18]. In these cases, the result is a frequency-dependent sample thickness and the reported thickness is a scalar statistical value that is computed from the frequency-dependent thicknesses.

2.1. MOTIVATION

The previous state-of-the-art relies on legacy error measures for minimization of simulation error and the standard practice is to use a single unique measurement for each unknown material in a sample. This research is

motivated to standardize the signal processing methodology, clearly define the best optimization formulation to yield low simulation error and optical property variation, and leverage multiple measurements to reduce the impact of system-dependent artifacts on extracted optical properties. The previous state-of-the-art also relies on separate treatments depending on the effective optical thickness of the sample and no clearly defined consolidated solution exists for simultaneous thickness and orientation determination. Therefore, the research is motivated to achieve simultaneous thickness and orientation determination for low absorption and high absorption samples comprised of solid and granular materials with uniform and non-uniformly varying optical properties. The goal of the research is production of a comprehensive and proven suite of methodologies that address fundamental complexities associated with exploitation of time-domain terahertz spectroscopic data.

1. Bypass signal truncation, suppression, or replacement to process Fabry-Perot echo pulses.
    - This would avoid the need for a series-based-solution of FP etalon effect in the sample response transfer function and manipulation of the signal data.

2. Integrated frequency determination for thickness and orientation optimization.

    - This would avoid ambiguity in the extracted thickness caused by statistical representations of frequency-dependent thicknesses.

3. Nontrivial index of refraction and absorption of air as used in optimization process [20, 21].

    - This would reduce the error induced by transmission and reflection at exterior interfaces, and propagation losses in the sample region.

4. Account for uncertainty in sample mounting as reported by Duvillaret et al. [10] and Dorney et al. [11].

    - This would invoke a three-dimensional determination of the plane of incidence, angle of incidence, and coefficients for a linear superposition of perpendicular polarization states.

5. Achieve simultaneous determination of layer thickness and sample orientation.

    - This would implement an approach to yield optimal values of thickness and orientation.

These five directions provide a basis for the motivation of this research and pose significant development efforts requiring a substantial level of coordination between physics, the phenomenology of electro-optical measurement, mathematical and computational methods, and computer engineering. The expectation is that completion of each of the five items presents an advancement in the state-of-the-art in THz-TDS physical parameter extraction. The successful integration across the five items will simultaneously increase the robustness and improve the accuracy of the physical parameter extraction capability thus extending the effectiveness of THz-TDS measurements.

3. THEORETICAL PHYSICS MODEL

The physical model that is used to define the objective function within the optimization is built on a physical and geometric theoretical foundation. The theoretical physics model is implemented for plane waves. The geometric theory facilitates quantification of the sample orientation with respect to the incident radiation. The sample orientation is used within the physical model to determine the angle of incidence and polarization state resulting from the measurement configuration. There are four primary components that constitute the theoretical foundation: sample orientation uncertainty, Fresnel model, Transfer Matrix Method (TMM), and the objective function. Each of the four components are described in this section.

3.1. FRESNEL MODEL

The physical model computes the Fresnel coefficients for reflection and transmission at each interface for both perpendicular and parallel polarization states. The Fresnel equations are plane-wave solutions to Maxwell's equations. The notation for the Fresnel reflection coefficient in parallel and

perpendicular polarization is $r_{\ell,\ell+1_{||}}$ and $r_{\ell,\ell+1_{\perp}}$, respectively. The notation for the Fresnel transmission coefficient in parallel and perpendicular polarization is $t_{\ell,\ell+1_{||}}$ and $t_{\ell,\ell+1_{\perp}}$, respectively. The Fresnel coefficients use the optimization values of each sample layer ℓ for complex index of refraction $\tilde{n}_{\ell}$, complex magnetic permeability $\tilde{\mu}_{\ell}$, angle of incidence $\theta_{i_{\ell+1}}$, and critical angle $\theta_{c_{\ell}}$. These quantities are defined in Equations 3.1–3.6. The textual references for the Fresnel equations is obtained from multiple sources [22, 23, 24, 25, 26].

$$s_{\ell,\ell+1} = \begin{cases} \sqrt{\tilde{n}_{\ell+1}^{\,2} - \tilde{n}_{\ell}^{\,2}\sin^2(\theta_{i_{\ell}})} & \theta_{i_{\ell}} < \theta_{c_{\ell}} \\ i\tilde{n}_{\ell+1}\sqrt{\dfrac{\sin(\theta_{i_{\ell}})}{\sin(\theta_{c_{\ell}})}} & \theta_{i_{\ell}} > \theta_{c_{\ell}} \end{cases} \tag{3.1}$$

$$\theta_{c_{\ell}} = \sin^{-1}\left(\frac{\Re\mathrm{e}(\tilde{n}_{\ell+1})}{\Re\mathrm{e}(\tilde{n}_{\ell})}\right) \tag{3.2}$$

$$r_{\ell,\ell+1_{||}} = \frac{\tilde{n}_{\ell}\cos(\theta_{i_{\ell}}) - \dfrac{\tilde{\mu}_{\ell}}{\tilde{\mu}_{\ell+1}}s_{\ell,\ell+1}}{\tilde{n}_{\ell}\cos(\theta_{i_{\ell}}) + \dfrac{\tilde{\mu}_{\ell}}{\tilde{\mu}_{\ell+1}}s_{\ell,\ell+1}} \tag{3.3}$$

$$r_{\ell,\ell+1_{\perp}} = \frac{\tilde{n}_{\ell}s_{\ell,\ell+1} - \dfrac{\tilde{\mu}_{\ell}}{\tilde{\mu}_{\ell+1}}\tilde{n}_{\ell+1}^{\,2}\cos(\theta_{i_{\ell}})}{\tilde{n}_{\ell}s_{\ell,\ell+1} + \dfrac{\tilde{\mu}_{\ell}}{\tilde{\mu}_{\ell+1}}\tilde{n}_{\ell+1}^{\,2}\cos(\theta_{i_{\ell}})} \tag{3.4}$$

$$t_{\ell,\ell+1_{||}} = \frac{2\tilde{n}_{\ell}\cos(\theta_{i_{\ell}})}{\tilde{n}_{\ell}\cos(\theta_{i_{\ell}}) + \dfrac{\tilde{\mu}_{\ell}}{\tilde{\mu}_{\ell+1}}s_{\ell,\ell+1}} \tag{3.5}$$

$$t_{\ell,\ell+1_{\perp}} = \frac{2\tilde{n}_{\ell}\tilde{n}_{\ell+1}\cos(\theta_{i_{\ell}})}{\tilde{n}_{\ell}s_{\ell,\ell+1} + \frac{\tilde{\mu}_{\ell}}{\tilde{\mu}_{\ell+1}}\tilde{n}_{\ell+1}{}^{2}\cos(\theta_{i_{\ell}})} \quad 3.6$$

The complex-valued index of refraction and magnetic permeability of each layer of a sample are denoted $\tilde{n}_{\ell}$ and $\tilde{\mu}_{\ell}$ respectively, as a function of frequency ν, and are defined in Equations 3.7–3.8. The sample layer dependent index of refraction n_{ℓ} and extinction coefficient κ_{ℓ} are the real and imaginary components of the complex index of refraction, respectively. The sample layer dependent magnetic permeability components μ'_{ℓ} and μ''_{ℓ} are the real and imaginary components of the complex magnetic permeability, respectively.

$$\tilde{n}_{\ell}(\nu) = n_{\ell}(\nu) - i\kappa_{\ell}(\nu) \quad 3.7$$

$$\tilde{\mu}_{\ell}(\nu) = \mu'_{\ell}(\nu) - i\mu''_{\ell}(\nu) \quad 3.8$$

The magnetic permeability currently implemented in the algorithm uses a constant real value of one, and imaginary value of zero for all materials. The assumption of the research to-date is that all the investigated materials have been non-magnetic materials meaning that they do not have a magnetic response to incident THz radiation. This is true for many materials in the THz frequency range. One item of interest for the research is to obtain a magnetic material that does not strongly absorb, perform NDE measurements on the

material, and subsequently extract the physical parameters including an optimal magnetic permeability.

3.2. SUPERPOSITION OF POLARIZATION STATES

The Cartesian coordinate system, defined in Equations 3.9–3.11, is used as the basis vectors that define the three dimensional space in which the radiation propagates and the sample is rotated. All simulations in the research have the cartesian unit vectors $\hat{x}$ and $\hat{y}$ lying in the plane of the sample directed surface of the focusing lens. The transmitter and receiver focusing lenses are assumed to be exactly coplanar for all measurements. The Cartesian unit vector $\hat{z}$ is always perpendicular to the surface of the focusing lens. The orientation of the $\hat{z}$ unit vector within the geometry is such that it is always directed from the center of the receiver lens and pointing towards the center of the transmitter lens.

$$\hat{x} = \begin{bmatrix} 1 \\ 0 \\ 0 \end{bmatrix} \tag{3.9}$$

$$\hat{y} = \begin{bmatrix} 0 \\ 1 \\ 0 \end{bmatrix} \tag{3.10}$$

$$\hat{z} = \begin{bmatrix} 0 \\ 0 \\ 1 \end{bmatrix} \tag{3.11}$$

The physical model first computes the sample surface normal vector from the ZXY intrinsic Tait-Bryan rotation matrix A_{ZXY} defined in Equation 3.12 with supporting formula defined in Equations 3.13–3.21. The Tait-Bryan rotations, also called Cardan angles, are a class of intrinsic and not strictly proper Euler angle rotations [27]. The rotation matrix A_{ZXY} is used to theoretically rotate the sample. The yaw, pitch, and roll angles of the sample are defined by ψ, θ, and ϕ, respectively. A rotation about the Z, X, and Y Cartesian axes corresponds to yaw, pitch, and roll, respectively. The angular information for the Tait-Bryan rotation comes from the YPR optimization values provided to NM by the DE optimization. The yaw, pitch, and roll angles are constrained by ninety degrees according to Equations 3.22–3.24.

$$A_{\mathrm{ZXY}} = \begin{bmatrix} A_{1,1} & A_{1,2} & A_{1,3} \\ A_{2,1} & A_{2,2} & A_{2,3} \\ A_{3,1} & A_{3,2} & A_{3,3} \end{bmatrix} \tag{3.12}$$

$$A_{1,1} = \mathrm{Cos}(\phi)\mathrm{Cos}(\psi) - \mathrm{Sin}(\phi)\mathrm{Sin}(\theta)\mathrm{Sin}(\psi) \tag{3.13}$$

$$A_{2,1} = \mathrm{Cos}(\psi)\mathrm{Sin}(\phi) + \mathrm{Cos}(\phi)\mathrm{Sin}(\theta)\mathrm{Sin}(\psi) \tag{3.14}$$

$$A_{3,1} = -\mathrm{Cos}(\theta)\mathrm{Sin}(\psi) \tag{3.15}$$

$$A_{1,2} = -\mathrm{Cos}(\theta)\mathrm{Sin}(\phi) \tag{3.16}$$

$$A_{2,2} = \mathrm{Cos}(\phi)\mathrm{Cos}(\theta) \tag{3.17}$$

$$A_{3,2} = \mathrm{Sin}(\theta) \tag{3.18}$$

$$A_{1,3} = \mathrm{Sin}(\phi)\mathrm{Cos}(\psi) + \mathrm{Cos}(\phi)\mathrm{Sin}(\theta)\mathrm{Sin}(\psi) \tag{3.19}$$

$$A_{2,3} = \mathrm{Sin}(\phi)\mathrm{Sin}(\psi) - \mathrm{Cos}(\phi)\mathrm{Cos}(\psi)\mathrm{Sin}(\theta) \tag{3.20}$$

$$A_{3,3} = \mathrm{Cos}(\theta)\mathrm{Cos}(\psi) \tag{3.21}$$

$$0 \leq \psi \prec \frac{\pi}{2} \tag{3.22}$$

$$0 \leq \theta \prec \frac{\pi}{2} \tag{3.23}$$

$$0 \leq \phi \prec \frac{\pi}{2} \tag{3.24}$$

The radiation field vectors are always defined such that Equations 3.25–3.27 always hold true. The wave vector defining the direction of propagation of the incident radiation, given by $\vec{k}_{\ell=0}$, is always opposite to $\hat{z}$. Therefore, the incident wave vector is antiparallel to $\hat{z}$ such that it travels in the direction from the transmitter to the receiver. The electric and magnetic field of the incident radiation $\vec{E}_{\ell=0}$ and $\vec{B}_{\ell=0}$ are defined to be always parallel to the unit vector $\hat{y}$ and $\hat{x}$, respectively. The radiation field vectors defined in Equations 3.25–3.27 are only valid in the initial state of the incident radiation. As the radiation propagates through the sample, the radiation field vectors change direction based on electromagnetic interactions with adjacent materials at each interface of the sample.

$$\vec{k}_{\ell=0} = -\hat{z} \tag{3.25}$$

$$\vec{E}_{\ell=0} = \hat{y} \tag{3.26}$$

$$\vec{B}_{\ell=0} = \hat{x} \tag{3.27}$$

The initial incident angle $\theta_{i_{\ell=0}}$ defined in Equation 3.28 is dependent on the initial incident wave vector $\vec{k}_{\ell=0}$ and the sample surface normal vector $\vec{s}_{\perp}$. There are three vectors that define the surface orientation of the sample. Two vectors are parallel to the surface of the sample and are labelled $\vec{s}_{||_1}$ and

$\vec{s}_{||_2}$, and one vector is normal to the sample surface and labelled $\vec{s}_{\perp}$. The sample surface normal vector and the incident radiation propagation vector enable the computation of the initial angle of incidence.

The three sample orientation vectors are defined by Equations 3.29–3.31. As defined by Equations 3.29–3.31, the sample orientation vectors $\vec{s}_{||_1}$, $\vec{s}_{||_2}$, and $\vec{s}_{\perp}$ are dependent on the yaw, pitch, and roll angles in the A_{ZXY} Tait-Bryan rotation matrix. Because the $\hat{x}$ unit vector relates to $\vec{s}_{||_1}$ and $\vec{B}_{\ell=0}$, a rotation of the sample about $\hat{x}$ constitutes a pitch of the sample. Therefore, the pitch angle θ alone controls the parallel polarization state when the yaw ψ and roll ϕ angles are both zero. Because the $\hat{y}$ unit vector relates to $\vec{s}_{||_2}$ and $\vec{E}_{\ell=0}$, a rotation of the sample about $\hat{y}$ constitutes a roll of the sample. Therefore, the roll angle alone controls the perpendicular polarization state when the yaw and pitch angles are both zero.

$$\theta_{i_{\ell=0}} = \mathrm{Cos}^{-1}\left(\frac{\vec{k}_{\ell=0} \cdot \vec{s}_{\perp}}{\left\|\vec{k}_{\ell=0}\right\|_2 \cdot \left\|\vec{s}_{\perp}\right\|_2}\right) \tag{3.28}$$

$$\vec{s}_{||_1} = A_{\mathrm{ZXY}}\hat{x} \tag{3.29}$$

$$\vec{s}_{||_2} = A_{\mathrm{ZXY}}\hat{y} \tag{3.30}$$

$$\vec{s}_{\perp} = A_{\mathrm{ZXY}}\hat{z} \tag{3.31}$$

Once the initial angle of incidence is determined, all subsequent radiation propagation is contained within the plane of incidence. The plane of incidence is defined by the three vectors given in Equations 3.32–3.34. The vector given in Equation 3.32 is the first vector parallel to the plane of incidence $\vec{p}_{||_1}$ and is equal to the sample surface normal vector. The vector given in Equation 3.33 is the vector perpendicular to the plane of incidence, $\vec{p}_{\perp}$. The vector given in Equation 3.34 is the second vector parallel to the plane of incidence, $\vec{p}_{||_2}$. The angle between the sample surface normal vector and the plane of incidence surface normal vector is given in Equation 3.35.

$$\vec{p}_{||_1} = \vec{s}_{\perp} \tag{3.32}$$

$$\vec{p}_{\perp} = \frac{\vec{k}_{\ell=0} \times \vec{p}_{||_1}}{\left\|\vec{k}_{\ell=0}\right\|_2 \cdot \left\|\vec{p}_{||_1}\right\|_2 \cdot \mathrm{Sin}(\theta_{i_{\ell=0}})} \tag{3.33}$$

$$\vec{p}_{||_2} = \frac{\vec{p}_{\perp} \times \vec{p}_{||_1}}{\left\|\vec{p}_{\perp}\right\|_2 \cdot \left\|\vec{p}_{||_1}\right\|_2 \cdot \mathrm{Sin}(\theta_p)} \tag{3.34}$$

$$\theta_p = \mathrm{Cos}^{-1}\left(\frac{\vec{p}_{||_1} \cdot \vec{p}_{\perp}}{\left\|\vec{p}_{||_1}\right\|_2 \cdot \left\|\vec{p}_{\perp}\right\|_2}\right) = \frac{\pi}{2} \tag{3.35}$$

Due to Snell's law, the angle of incidence is dependent on the layer of the sample that the radiation is propagating through. Once the radiation enters the sample, all radiation propagation occurs in the plane of incidence, with the angles of incidence within the plane of incidence defined according to

Equation 3.36. The change in the angle of incidence between two layers of a sample is defined by Equation 3.37.

$$\theta_{i_{\ell+1}} = \sin^{-1}\left(\frac{\mathfrak{Re}(\tilde{n}_{\ell+1})}{\mathfrak{Re}(\tilde{n}_{\ell})}\sin(\theta_{i_{\ell}})\right) \quad 3.36$$

$$\theta_{\Delta_{\ell,\ell+1}} = \theta_{i_{\ell}} - \theta_{i_{\ell+1}} \quad 3.37$$

The radiation field vectors are also dependent on the layer of the sample that the radiation is propagation through. The radiation field vectors are rotated in the plane of incidence about the plane of incidence surface normal vector $\vec{p}_{\perp}$ by the amount of change in the angle of incidence defined by Equation 3.37. The wave vector, electric field vector, and magnetic field vector in each layer of the sample are labelled as $\vec{k}_{\ell+1}$, $\vec{E}_{\ell+1}$, and $\vec{B}_{\ell+1}$, defined in Equations 3.38–3.40. The function $\mathcal{R}$ in Equations 3.38–3.40 performs a rotation of one vector about the axis of a second vector by an angle. The rotation performed by the function $\mathcal{R}$ is clockwise, from the perspective of the tail-to-head of the vector about which axis the rotation is occurring. The subscript on $\mathcal{R}_{p_{\perp}}$ indicates that the vector about which axis the rotation takes place, in this research, is always that of the plane of incidence surface normal vector.

$$\vec{k}_{\ell+1} = \mathcal{R}_{p_{\perp}}(\vec{k}_{\ell}, \vec{p}_{\perp}, \theta_{\Delta_{\ell,\ell+1}}) \quad 3.38$$

$$\vec{E}_{\ell+1} = \mathcal{R}_{p_{\perp}}(\vec{E}_{\ell}, \vec{p}_{\perp}, \theta_{\Delta_{\ell,\ell+1}}) \quad 3.39$$

$$\vec{B}_{\ell+1} = \mathcal{R}_{p_\perp}(\vec{B}_\ell, \vec{p}_\perp, \theta_{\Delta_{\ell,\ell+1}}) \quad 3.40$$

The rotation function $\mathcal{R}$ in Equations 3.38–3.40 outputs a three-element vector. Specifically, the function $\vec{a}_3 = \mathcal{R}(\vec{a}_1, \vec{a}_2, \Delta)$ is a function which rotates an arbitrarily oriented vector $\vec{a}_1$ about the axis of an arbitrarily oriented vector $\vec{a}_2$ by an amount Δ, resulting in a vector $\vec{a}_3$. The vectors $\vec{a}_1$ and $\vec{a}_2$ do not need to be orthogonal, and neither of the two vectors need to lie entirely along one of the three Cartesian unit vectors $\hat{x}$, $\hat{y}$, or $\hat{z}$. The rotation function uses a Gramm-Schmidt process to orthogonalize the set of linearly independent vectors $\vec{a}_1$ and $\vec{a}_2$ to obtain orthogonal vectors $\vec{a}_2$ and $\vec{c}_2$ with the same span. The cross product of the vectors $\vec{a}_2$ and $\vec{c}_2$ yield a third orthogonal vector $\vec{c}_3$. The process is defined in several steps using Equations 3.41–3.48. The labeling notation for vectors and scalars used in Equations 3.41–3.48 are used to improve the readability of the steps to compute $\mathcal{R}$ and do not apply to any quantities outside of Equations 3.41–3.48.

$$b_1 = \frac{\vec{a}_1 \cdot \vec{a}_2}{\vec{a}_2 \cdot \vec{a}_2} \quad 3.41$$

$$\vec{c}_1 = \vec{a}_2 \cdot b_1 \quad 3.42$$

$$\vec{c}_2 = \vec{a}_1 - (\vec{a}_2 \cdot b_1) \quad 3.43$$

$$\vec{c}_3 = \vec{a}_2 \times \vec{c}_2 \quad 3.44$$

$$b_2 = \frac{\mathrm{Cos}(\Delta)}{\left\|\vec{c}_2\right\|_2} \quad 3.45$$

$$b_3 = \frac{\mathrm{Sin}(\Delta)}{\left\|\vec{c}_3\right\|_2} \tag{3.46}$$

$$\vec{c}_4 = \left\|\vec{c}_2\right\|_2 \cdot (b_2 \cdot \vec{c}_2 + b_3 \cdot \vec{c}_3) \tag{3.47}$$

$$\mathcal{R}_b(\vec{a}_1, \vec{a}_2, \Delta) = \vec{a}_3 = \vec{c}_4 + \vec{c}_1 \tag{3.48}$$

The set of three of radiation field vectors in all layers of the sample and outside of the sample are mutually orthogonal vectors. The orthogonality relationships are expressed in Equation 3.49.

$$\vec{E}_\ell \cdot \vec{B}_\ell = 0, \vec{E}_\ell \cdot \vec{k}_\ell = 0, \vec{k}_\ell \cdot \vec{B}_\ell = 0 \tag{3.49}$$

The angle of incidence changes at each layer interface due to the mismatch in index of refraction at the boundary as defined by Snell's law. The change in angle of incidence as the radiation propagates through the sample layers causes corresponding changes in the electric field vector. Because of the changing direction of the electric field vector, the coefficients for the linear superposition of orthogonal polarization states therefore also change at each layer interface.

The layer dependent transmission and reflection coefficients, $t_{\ell,\ell+1}$ and $r_{\ell,\ell+1}$ respectively, are a function of the weighted parallel and perpendicular polarization transmission and reflection coefficients as defined in Equations 3.50–3.51. The $\ell, \ell + 1$ notation is used to indicate the interface boundary. The parallel and perpendicular polarization weighting coefficients are labelled

as $h_{\ell,\ell+1_{||}}$ and $h_{\ell,\ell+1_{\perp}}$, respectively. The plane of incidence surface normal vector $\vec{p}_{\perp}$ and layer dependent electric field vector $\vec{E}_{\ell}$ enable the computation of the parallel and perpendicular polarization coefficients $h_{\ell,\ell+1_{||}}$ and $h_{\ell,\ell+1_{\perp}}$ respectively, for each layer interface. Referring to Equations 3.50–3.51, the parallel polarization transmission and reflection coefficients are labelled $t_{\ell,\ell+1_{||}}$ and $r_{\ell,\ell+1_{||}}$, respectively. The perpendicular polarization transmission and reflection coefficients are labelled $t_{\ell,\ell+1_{\perp}}$ and $r_{\ell,\ell+1_{\perp}}$, respectively. The transmission and reflection coefficients are defined in Equations 3.3–3.6.

$$t_{\ell,\ell+1} = h_{\ell,\ell+1_{||}} \cdot t_{\ell,\ell+1_{||}} + h_{\ell,\ell+1_{\perp}} \cdot t_{\ell,\ell+1_{\perp}} \quad 3.50$$

$$r_{\ell,\ell+1} = h_{\ell,\ell+1_{||}} \cdot r_{\ell,\ell+1_{||}} + h_{\ell,\ell+1_{\perp}} \cdot r_{\ell,\ell+1_{\perp}} \quad 3.51$$

The layer dependent parallel polarization weighting coefficient $h_{\ell,\ell+1_{||}}$ is defined by Equation 3.52, where the angle $\theta_{p_{\perp},E_{\ell}}$ between the plane of incidence surface normal vector $\vec{p}_{\perp}$ and the electric field vector $\vec{E}_{\ell}$ is defined in Equation 3.53. The angle $\theta_{p_{\perp},E_{\ell}}$ is constrained between 0°–90°, as given in Equation 3.54. The layer dependent perpendicular polarization weighting coefficient $h_{\ell,\ell+1_{\perp}}$ is defined by the conservation property in Equation 3.55.

$$h_{\ell,\ell+1_{||}} = \frac{\theta_{p_{\perp},E_{\ell}}}{\frac{\pi}{2}} \quad 3.52$$

$$\theta_{p_\perp,E_\ell} = \mathrm{Cos}^{-1}\left(\frac{\vec{p}_\perp \cdot \vec{E}_\ell}{\left\|\vec{p}_\perp\right\|_2 \cdot \left\|\vec{E}_\ell\right\|_2}\right) \quad 3.53$$

$$0 \leq \theta_{p_\perp,E_\ell} \leq \frac{\pi}{2} \quad 3.54$$

$$h_{\ell,\ell+1_\perp} = 1 - h_{\ell,\ell+1_{||}} \quad 3.55$$

The linear superposition of the two orthogonal polarization states is a weighted summation of the parallel and perpendicular polarization coefficients for transmission or reflection. In the case of purely perpendicular polarization, $\psi = 0$ and $\theta = 0$, therefore $h_{\ell,\ell+1_{||}} = 0$, $h_{\ell,\ell+1_\perp} = 1$, which causes $t_{\ell,\ell+1} = t_{\ell,\ell+1_\perp}$ and $r_{\ell,\ell+1} = r_{\ell,\ell+1_\perp}$. In the case of purely parallel polarization, $\psi = 0$ and $\phi = 0$, therefore $h_{\ell,\ell+1_{||}} = 0$, $h_{\ell,\ell+1_\perp} = 1$, which causes $t_{\ell,\ell+1} = t_{\ell,\ell+1_{||}}$ and $r_{\ell,\ell+1} = r_{\ell,\ell+1_{||}}$. If $\theta = 0$ and $\phi = 0$, then the radiation is normally incident on the sample with $t_{\ell,\ell+1_\perp} = t_{\ell,\ell+1_{||}}$ and $r_{\ell,\ell+1_\perp} = r_{\ell,\ell+1_{||}}$ regardless of the yaw angle ψ.

3.3. TRANSFER MATRIX METHOD

The Transfer Matrix Method (TMM) is used to generate the theoretical transmission and reflection transfer functions at the frequency of the solution [23, 24, 25]. The TMM is comprised of a propagation matrix P_ℓ, dynamical matrix $D_{\ell,\ell+1}$, and a total scattering matrix M_{Total}, all three of which are defined in Equations 3.56–3.59. The propagation matrix, P_ℓ, models the

propagation effects relating to phase evolution and absorption through the propagation media. The dynamical matrix, $D_{\ell,\ell+1}$, models the reflection and scattering at the interfaces of different media. The total scattering matrix, M_{Total}, models the combined propagation and scattering effect for all the media being modelled. The transmission and reflection components of the transfer function are defined in Equations 3.60–3.61, respectively.

$$P_\ell = \begin{bmatrix} e^{\frac{i\omega\tilde{n}_\ell d_\ell}{c}} & 0 \\ 0 & e^{-\frac{i\omega\tilde{n}_\ell d_\ell}{c}} \end{bmatrix} \quad 3.56$$

$$d_\ell = \frac{d_{\text{sample}_\ell}}{\cos(\theta_{i_\ell+1})} \quad 3.57$$

$$D_{\ell,\ell+1} = \frac{1}{t_{\ell,\ell+1}} \begin{bmatrix} 1 & r_{\ell,\ell+1} \\ r_{\ell,\ell+1} & 1 \end{bmatrix} \quad 3.58$$

$$M_{\text{Total}} = \prod_{\ell=0}^{N} P_\ell D_{\ell,\ell+1} = \begin{bmatrix} M_{11} & M_{12} \\ M_{21} & M_{22} \end{bmatrix} \quad 3.59$$

$$T = \frac{1}{M_{11}} \quad 3.60$$

$$R = \frac{M_{21}}{M_{11}} \quad 3.61$$

The angular frequency of the radiation is ω and the propagation distance in the sample layer is d_ℓ as defined in Equation 3.57. The case of $\ell = 0$ or $\ell = N$ then $d_\ell = 0$ because $\ell = 0, N$ is the ambient air background layer. Inside the sample θ_{i_ℓ} is the refracted angle in layer ℓ or equivalently the incident angle at layer $\ell + 1$. Similarly, $\theta_{i_{\ell+1}}$ is the refracted angle in layer $\ell + 1$ or equivalently the incident angle at layer $\ell + 2$.

3.4. PROPAGATION CORRECTION

The NDE of a sample using THz-TDS requires a reference measurement and a sample measurement to compute the transfer function of the sample. The radiation of a reference measurement only passes through the reference medium, typically air for the research, and does not pass through the sample being investigated. Generally, the propagation effect is the difference in propagation of the reference measurement radiation relative to the sample measurement radiation. The difference in propagation is corrected within the measured reference signal using a theoretical adjustment to the propagation coefficient. Therefore, the adjustment of the propagation effect is called the propagation correction and the propagation effect is removed from the reference measurement. The propagation correction is proportional to the length of the projected path through each layer of the sample in the direction of the reference radiation. The propagation correction used in the research is leveraged from Dorney et al. [11]. Equations 3.62–3.63 define the propagation correction.

$$m_\ell = d_\ell \cos(\theta_{i_\ell} - \theta_{i_{\ell+1}}) \tag{3.62}$$

$$C = e^{\frac{\mathrm{i}\omega\tilde{n}_0 \sum_{\ell=1}^{N-1} m_\ell}{c}} \tag{3.63}$$

The projected path length difference m_ℓ is proportional to the physical thickness d_ℓ of the ℓth sample layer. The research labels a general angle of

incidence as θ_{i_ℓ}. The angle the radiation is incident on the ℓth sample layer, including the reference medium as a layer, is θ_{i_ℓ}. The angle the radiation is refracted into the $\ell + 1$ sample layer, including the reference medium as a layer, is $\theta_{i_{\ell+1}}$. Regarding Equation 3.63, ω is the angular frequency of the radiation, c is the speed of light in vacuum, $\tilde{n}_0$ is the complex refractive index of the reference medium, and the m_ℓ of each layer is summed over the N sample layers. The i in the exponent if Equation 3.63 is the imaginary number $\mathrm{i} = \sqrt{-1}$, not to be confused with the labelling syntax i used to identify the angle of incidence. The propagation correction term C defined in Equation 3.63 is used in the next section to more accurately relate the measured reference signal to the measured sample signal.

3.5. SIGNAL CONFLATION

A frequency-domain complex-valued signal $\tilde{Y}(\nu)$ is computed from the Discrete Fourier Transform (DFT) of a time-domain real-valued signal $Y(t)$ defined in Equation 3.64, where the DFT is labelled as $\mathcal{F}$ and the tilde indicates that the variable is complex-valued. A variable without a tilde represents a real-valued quantity. Next, a conflation of the measured sample signal $\tilde{Y}_{\text{measured}}$, reference signal $\tilde{Y}_{\text{reference}}$, and theoretical transfer functions is generated in the frequency-domain using either Equation 3.65 or Equation

3.66. Both Equation 3.65 and 3.66 for the conflated complex-valued signal $\tilde{Y}_{\text{conflated}}$ and transfer function $\tilde{H}_{\text{conflated}}$ are conditional. If the measurement is a transmission or reflection measurement then the theoretical transfer function is the transmission $\tilde{T}$ or $\tilde{R}$, respectively. In Equations 3.65–3.66, the frequency being optimized is labelled as ν_k and all other frequencies are labelled as ν such that $\nu \neq \nu_k$. The frequency-domain complex-valued signals and transfer functions are related by Equations 3.67–3.68. The inverse DFT defined in Equation 3.69 is used to transform a complex-valued frequency-domain signal to a real-valued time-domain signal, where the inverse DFT is labelled $\mathcal{F}^{-1}$.

$$\tilde{Y}(\nu) = \mathcal{F}(Y(t)) \tag{3.64}$$

$$\tilde{Y}_{\text{conflated}}(\nu) = \begin{cases} \tilde{Y}_{\text{measured}}(\nu) & \nu \neq \nu_k \\ \tilde{Y}_{\text{reference}}(\nu_k) \cdot \tilde{R}(\nu_k) & \nu = \nu_k \end{cases} \quad \text{Reflection}$$
$$\begin{cases} \tilde{Y}_{\text{measured}}(\nu) & \nu \neq \nu_k \\ \tilde{Y}_{\text{reference}}(\nu_k) \cdot \tilde{T}(\nu_k) & \nu = \nu_k \end{cases} \quad \text{Transmission} \tag{3.65}$$

$$\tilde{H}_{\text{conflated}}(\nu) = \begin{cases} \dfrac{\tilde{Y}_{\text{measured}}(\nu)}{\tilde{Y}_{\text{reference}}(\nu)} & \nu \neq \nu_k \\ \tilde{R}(\nu_k) & \nu = \nu_k \end{cases} \quad \text{Reflection}$$
$$\begin{cases} \dfrac{\tilde{Y}_{\text{measured}}(\nu)}{\tilde{Y}_{\text{reference}}(\nu)} & \nu \neq \nu_k \\ \tilde{T}(\nu_k) & \nu = \nu_k \end{cases} \quad \text{Transmission} \tag{3.66}$$

$$\tilde{Y}(\nu) = \frac{\tilde{Y}_{\text{reference}}(\nu) \cdot \tilde{H}(\nu)}{C} \tag{3.67}$$

$$\tilde{H}(\nu) = \frac{\tilde{Y}(\nu)}{\tilde{Y}_{\text{reference}}(\nu)} \cdot C \tag{3.68}$$

$$Y(t) = \mathcal{F}^{-1}(\tilde{Y}(\nu)) \tag{3.69}$$

Quantities with physical meaning are calculated from complex-valued variables using Equations 3.70–3.72. The frequency-domain magnitude is defined in Equation 3.70 and the phase is defined in Equation 3.71, where the asterisk in Equation 3.70 indicates the complex conjugate. In Equation 3.71, the $\mathcal{T}an_2{}^{-1}$ function is the four quadrant inverse tangent and the $\mathcal{U}nwrap$ function corrects the radian phase angles in a discrete vector of wrapped phase by adding multiples of ±2π when absolute jumps between consecutive elements of the wrapped phase are greater than or equal to the default jump tolerance of π radians.

$$|\tilde{X}| = \sqrt{\tilde{X} \cdot \tilde{X}^*} \tag{3.70}$$

$$\angle\tilde{X} = \mathcal{U}nwrap(\mathcal{T}an_2{}^{-1}(\Im\mathfrak{m}\left(\tilde{X}\right), \Re\mathfrak{e}(\tilde{X}))) \tag{3.71}$$

$$\tilde{X} = |\tilde{X}| \cdot e^{(-i\cdot(\angle\tilde{X}))} \tag{3.72}$$

The complex-valued discrete variable $\tilde{X}$ in Equations 3.70–3.72 is general notation to represent either the complex-valued frequency-domain signal $\tilde{Y}$ or transfer function $\tilde{H}$. Physically, the magnitude $|\tilde{X}|$ and phase $\angle\tilde{X}$ are used to represent the complex-valued frequency-domain signal or transfer function as a phasor, which is defined in Equation 3.72.

3.6. KRAMERS-KRONIG TRANSFORMATION

The Kramers-Kronig relationship is an analytical physics relationship which connects the imaginary component of the complex-valued optical property of a material to the real component [24]. The research uses the complex-valued refractive index to describe the optical properties of materials. The Kramers-Kronig Transformation (KKT), shown on the right-hand side of Equation 3.73, enables an analytical calculation of refractive index n using the extinction coefficient κ of the material [28, 29].

$$n(\nu) = n_{\infty} + \frac{2}{\pi}\int_{0}^{\infty} \frac{\nu' \cdot \kappa(\nu')}{\nu'^{2} - \nu^{2}} d\nu' \qquad 3.73$$

The KKT is defined analytically as a continuous integral of the extinction coefficient over all frequencies. The refractive index offset n_{∞} is a constant that calibrates the spectral profile generated by the Kramers-Kronig transformation. It is reported in literature that as $\nu \to \infty$, the integral goes to zero and thus $n(\nu) \to n_{\infty}$ [30, 31]. The frequency difference $\nu'^{2} - \nu^{2}$ at constant ν is essentially a weighting factor that scales the extinction coefficient at integration frequencies $d\nu'$ such that $\nu'^{2} \gg \nu^{2}$. As the absolute frequency separation $|\nu'^{2} - \nu^{2}|$ increases, the extinction coefficients are scaled to be less impactful in the transformation at the frequency ν.

4. EXPERIMENTAL PHYSICS MEASUREMENTS

The research employs the use of experimental measurement data, in addition to a theoretical physics model, to facilitate physical parameter extraction by optimization techniques. The experimental physics measurements are conducted using a THz-TDS system. The measurements are transmission measurements. The process used to generate and detect terahertz pulses of light is first explained. Next, the software settings used to configure the THZ-TDS measurement instrumentation is detailed. The THz-TDS measurements are performed using two instruments, each located at different institutions. The two THz-TDS instruments are Terview products located at Wright State University (WSU) and The Ohio State University (OSU). The samples measured and the system configurations employed to collect the measurements are provided for each instrument, at each institution. Lastly, four impacts of physical measurements on the accuracy and validity of the theoretical physics model are provided.

4.1. GENERATION OF TERAHERTZ RADIATION

The content of this section describes how the Teraview system generates and detects THz frequency radiation. The generation of THz pulses is a multi-step process that begins with visible wavelength light and concludes with THz frequency pulse emissions from a fabricated photolithographic transmitter. First, a continuous wave visible light laser with a wavelength of 532 nanometers (nm) pumps a titanium:sapphire laser. Mode locking, or locking of the phase of the laser frequencies, of a titanium:sapphire laser establishes phase coherency which is essential to obtain the short pulse widths to get an ultrafast laser [32, 33, 34, 35]. The laser uses Kerr-lens mode locking due to the nonlinear photorefractive nature of titanium sapphire. The result of this process is an 800 nm wavelength ultrafast laser with 100 femtosecond (fs) pulse widths. The pulse repetition rate is 76 megahertz (MHz) and the photon energy corresponding to 800 nm of the center of the pulse is 1.55 electron-volt (eV) [36]. The process that converts the 800 nm wavelength radiation to THz radiation is shown in Figure 4.1.

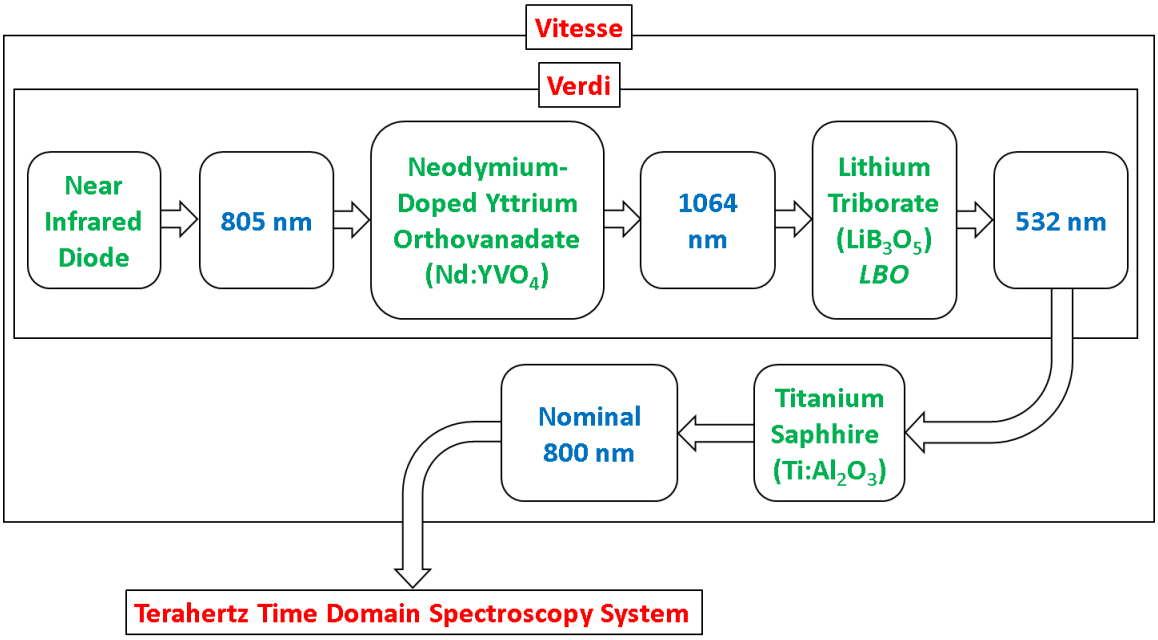

Figure 4.1) The coherent terahertz radiation is generated within the terahertz time-domain spectroscopy system using mode locked 800 nm center-wavelength pulses of light produced by a Vitesse laser system

The generation of pulsed THz radiation occurs when the ultrafast laser pulse is incident on a photo-conductive dipole antenna, shown in Figure 4.2, which has been fabricated with photolithography on one side of a semiconducting gallium arsenide (GaAs) substrate [37, 38]. The ultrafast pulses from the laser excite electrons from the valence band of the GaAs to the conduction band. The band gap of the GaAs is 1.42 eV, which is lower than the photon energy of the laser pulse and therefore enabling the GaAs to behave as a conductor allowing electrons to move freely.

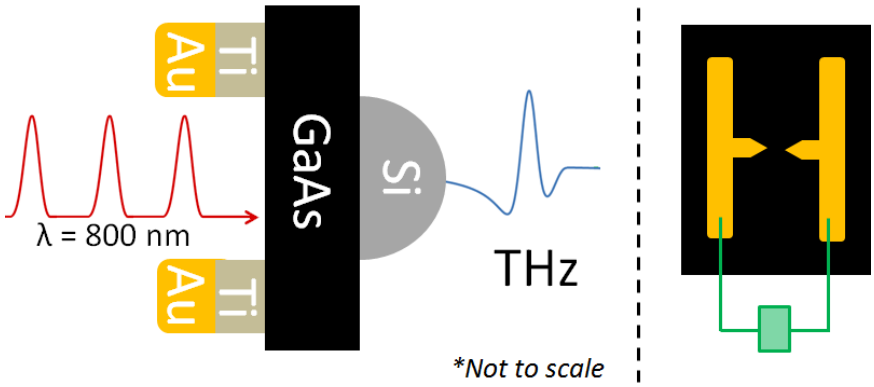

Figure 4.2) From left to right are diagrams of the side-view and top-view, respectively, of the transmitter-receiver assembly. The diagram components are not to scale.

The dipole antenna is an electrode structure with an electrode channel width of 10 μm and a gap at the center. The gap size can range from 1–100 μm, depending on the desired bandwidth and THz signal strength desired. The antenna electrodes are a dual layer of Gold (Au) on top of Titanium (Ti), with the Ti contacting the GaAs semiconductor. The electrodes are biased with a direct current (DC) voltage which allows the acceleration of the free charge carriers from the GaAs. The maximum voltage bias is proportional to both the electrode gap size and applied electric field strength with a typical DC bias in the range of 15–30 volts (V).

The density of the free charge carriers varies with a temporal periodicity that is proportional to the rise time of the ultrafast laser pulse. The result of a temporally dependent flux of free electrons through the DC bias is a time varying current. This time varying current, which is proportional to the optical pump power, and the DC bias, produces emission of THz pulses from the

antenna. At low currents, the power of the THz radiation increases linearly with pump power and voltage bias. The optical pump power typically is in the range of 10–50 milliwatt (mW), and the emitted THz power is hundreds of nanowatts with a ceiling of 1–2 microwatt (μW). As with all semiconductors, too large of a current will result in saturation and begin to induce nonlinear responses and eventual dielectric breakdown of the material. After creating THz radiation from the antenna laser interaction, the THz pulses are coupled from the GaAs to a convex hyper-hemispherical Silicon (Si) lens on the opposite side of the 500 μm thick GaAs substrate. The entirety of the GaAs substrate, antenna, and hemispherical lens is called the transmitter.

The purpose of the Si lens is to enable the THz radiation, created in the GaAs, to exit the transmitter assembly and enter free space. Without the Si lens, the significant mismatch of refractive index of GaAs to air would cause the radiation to perpetually reflect inside the semiconductor. The Si lens has a refractive index less than that of GaAs but greater than that of air and acts as a bridge from GaAs to free space. Thus, the Si lens facilitates the refraction of THz radiation out of the GaAs and into the Si, and then refraction out of the Si and into air. Lastly, the convex shape of the Si lens provides the geometric mechanism by which the THz radiation is approximately collimated upon entering free space.

The detection of THz radiation is essentially the THz generation process in reverse with several additional steps occurring before THz detection. In a THz-TDS system as used in this work, the 800 nm ultrafast laser is split into two beams, the pump and probe beams, with a beam splitter. The pump beam delivers 90% of the laser power to the transmitter, while the other 10% in the probe beam is sent to the detection system.

The probe beam passes through a mechanically scanning optical delay line that variably increases and decreases the time it takes the ultrafast probe pulses to travel to the receiver. The delay line accomplishes this by proportionally changing the distance travelled by the probe beam by sliding a system of retro-reflecting mirrors either closer to or further away from the THz receiver. The purpose of the delay line is to ensure that the ultrafast probe pulses arrive at the THz receiver at the same time as the THz pulse from the transmitter. The delay line is continuously sliding to allow the femtosecond pulse to scan the THz pulse to obtain peak amplitude information. As an example, after the delay line is initialized and begins operation, it will sample a portion of the pulse based on the desired time resolution. Next, the delay line moves one step and the ultrafast probe pulse interacts with a different part of the THz pulse. The delay line moves in this manner until the delay line scans the probe pulse through the THz pulse at each time resolution interval

to construct the entire THz signal. The optical delay line, along with the other basic components of the laser-pumped THz-TDS pulsed spectroscopy system, are shown in Figure 4.3.

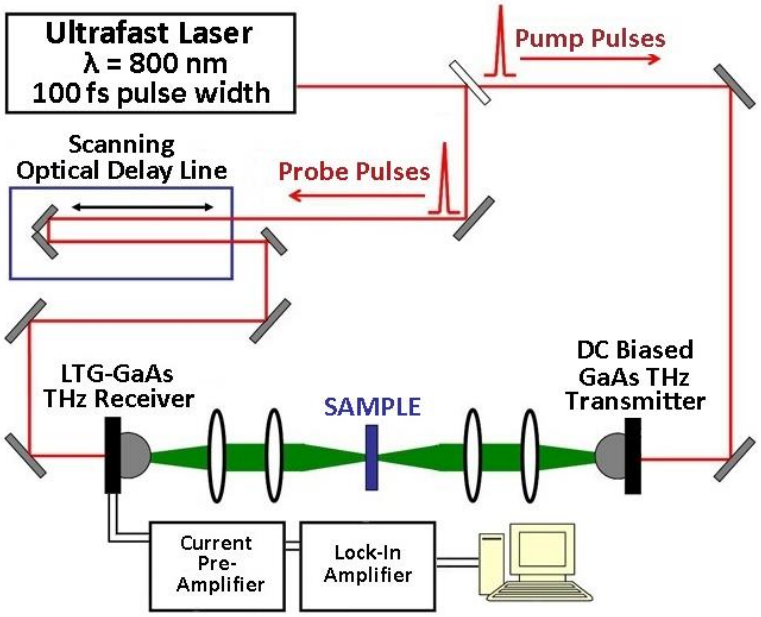

Figure 4.3) The ultrafast laser driven THz-TDS pulsed spectroscopy system. The green graphical elements represent the THz frequency radiation.

Referring to Figure 4.3, after travelling through the scanning optical delay line the probe beam is incident on a receiver antenna. The receiver antenna is identical to the transmitter antenna, which has been photolithographically defined on a GaAs semiconductor substrate. The GaAs substrate has a silicon convex lens on the opposite side of the antenna, which is used to focus the incoming THz radiation from the transmitter onto the electrode gap. The GaAs substrate used in detection differs from the transmitter substrate because it is dual layered on the electrode side with an

epitaxial layer of low temperature grown (LTG) GaAs, which has sub-picosecond electron relaxation times [39]. The low temperature growth creates arsenic anti-sites that trap the electrons faster than the valence band and this mechanism is necessary for femtosecond time resolution. The LTG-GaAs semiconductor is not necessary in the emitter assembly, and since it is more expensive financially to manufacture than standard GaAs, LTG-GaAs is found only in the detector assembly. The assembly of detection antenna and LTG GaAs comprises the THz receiver. In contrast to the transmitter antenna, the THz receiver antenna does not require a DC voltage bias on the Ti/Au electrodes.

The electric field from the THz pulses arriving at the receiver antenna from the transmitter creating a high frequency time varying voltage bias across the receiver electrode gap. Because the ultrafast laser pulses are synchronous in time with the transmitted THz radiation, the probe pulses strike the electrode gap at the same time a voltage bias is established by the THz radiation. The ultrafast pulses then generate free charges in the LTG-GaAs to produce a small pico-amp current. The current is then amplified using analog methods and digitally recorded to recreate the THz signal. In this manner, the ultrafast probe pulses are used to sample the transmitted THz radiation to recreate the signal. If there is no transmitted THz radiation, a

voltage bias is not established to enable the probe pulses to accelerate charge carriers out of the valence band of the LTG-GaAs substrate. Varying magnitudes of THz radiation can be recorded because the stronger the incident THz electric field is, the stronger the induced voltage bias response, and therefore the stronger the induced current. The induced current is composed of the free charge carriers that are already present in the conduction band due to the probe beam.

4.2. LABORATORY MEASUREMENTS

The laboratory measurements have been obtained using two different Teraview TPS Spectra 3000 instruments, each at two facilities. One of the instruments is operated by the Wright State University (WSU) Terahertz and Ultrafast Photonics Research Group, and the other instrument is operated by the Ohio State University (OSU) Hyperspectral Engine Lab for Integrated Optical Systems (HELIOS). The WSU data collection is described first, followed by the OSU data collection. All of the data that has been collected as of the writing of this document is transmission mode data. On average, the OSU and WSU internal transmission data exhibits better confidence in the transmitter-detector alignment and sample orientation with respect to the incident radiation compared with the WSU external transmission data. The internal transmission modality of the Teraview system uses a transmitter and

receiver permanently installed inside the housing of the Teraview unit with the base of the housing unit used to install the sample mounts. In contrast, the external transmission modality uses a transmitter and receiver that are installed by the researchers to mounting gantries outside of the Teraview housing unit with the base of the sample mount constructed by the researches on top of an optical workbench. However, the WSU data has higher time-domain peak signal amplitudes compared with the OSU data. Neither of these two observations are meant to indicate a preference of the OSU or the WSU measurements with respect to data quality. The details of the WSU and OSU data are described in Section 4.3 and Section 4.4, respectively.

4.3. WRIGHT STATE UNIVERSITY DATA

The data collected at WSU is from two operating configurations of the Teraview instrument. The first operating configuration is an internal configuration of the instrument with the THz emitter and detector located inside the housing of the Teraview TPS Spectra floor unit, whereas the second is an external configuration with the emitter and detector located outside of the floor unit but connected to the instrument with slightly flexible fiber optic cables. The internal data is collected in 2012 by Mr. Justin Wheatcroft for use in his Master of Science dissertation from WSU [40]. There are two features which differ between the Teraview internal and external systems. The first

feature is signal clutter and the second feature is bandwidth. Generally, the signal clutter of the internal system is qualitatively better than the external system for identical TPS Spectra software settings. Additionally, the external system experiences reduced bandwidth which is due to dispersion induced pulse broadening in the fiber-optic cables connecting the transmitter and receiver modules to the Teraview unit. There is some pre-compensation performed by the Teraview system to mitigate the dispersion induced pulse broadening, but the compensation does not completely compensate for the dispersion effects.

The data collected by Mr. Wheatcroft are two time-domain measurements at normal incidence of 500 μm thick High Resistivity Silicon (HRSi) and 3070 μm thick High Density Polyethylene (HDPE). The two measurements collected in 2012 are single-layer measurements. These two samples are the same samples used in measurements collected at later dates by Mr. Jordan Lewis and the author at WSU and OSU laboratories. The WSU internal data from 2012 has the largest peak time-domain signal amplitude of all the data collected for the research. The WSU measurement data from 2012 also has the smallest Num Scans value of all the data, for optimization purposes, in the research. This is because the internal configuration lacks the complications associated with the additional optical path components required

by the external configuration, and because the instrument State of Health (SOH) in 2012 is nearly nominal compared to the instrument SOH in 2017. Reference signals representative of each of the operating configurations are shown in Figure 4.4.

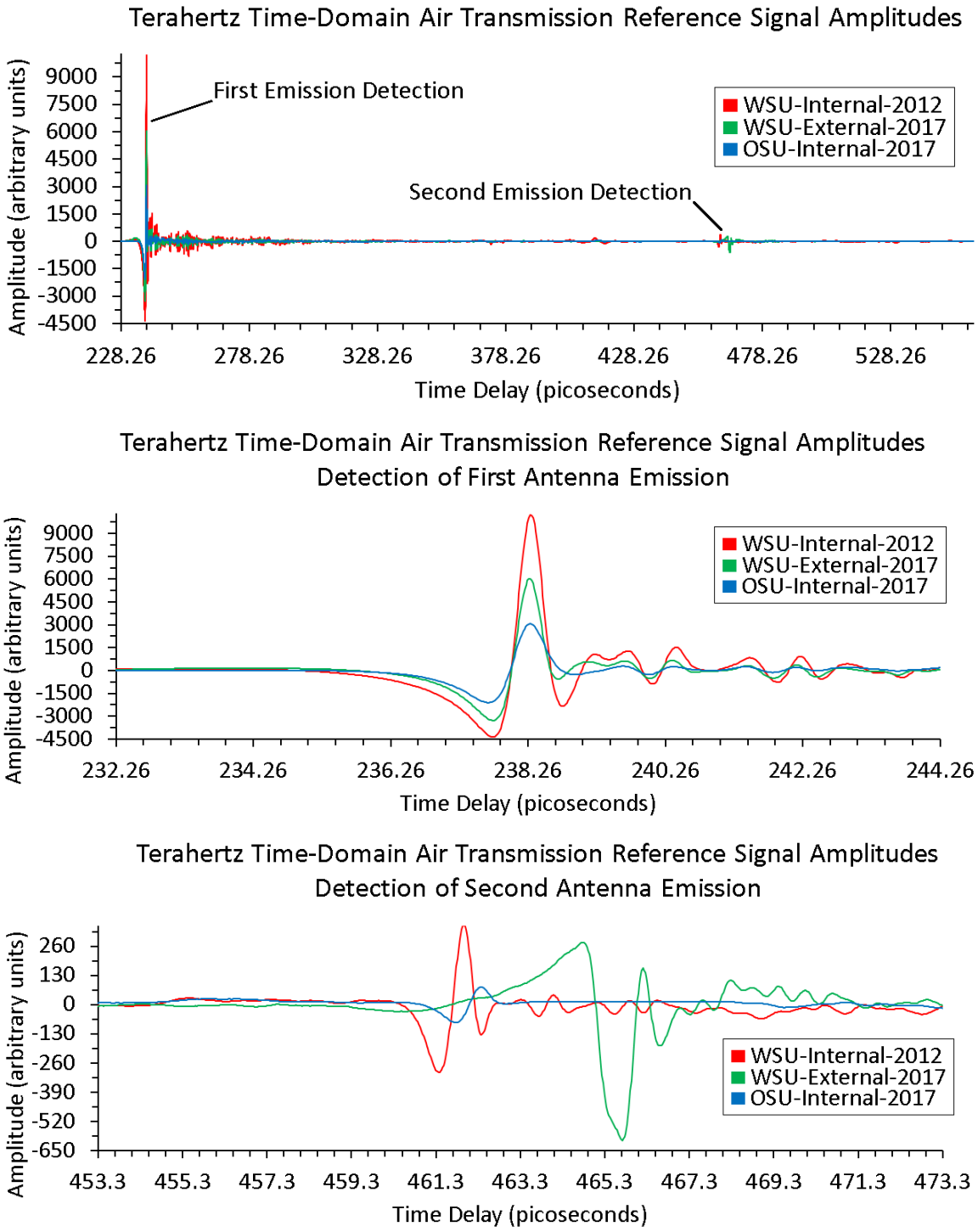

Figure 4.4) Graphic of terahertz time-domain reference signals in air. Top plot is the entire time window of the measurement. Center plot is the detected transmission from the first antenna emission. Bottom plot is the transmission detection of the second antenna emission.

Transmission measurement data is collected by the author using the WSU instrument internal and external configuration from April–September 2017, and data is collected on the same system by Mr. Jordan Lewis from October–December 2017. The data collected with the external configuration qualitatively has higher clutter and lower signal strength compared with the internal configuration data collected during 2012, for the same Num Scans value. The higher clutter and lower signal strength is also in part due to the use of the fiber-optic cable connecting the external modules to the Teraview unit. The signal measured by the external system is lower because it is not possible to pump the internal and external transmitter antennas at the same optical powers. This limitation is due to the optical fiber becuase pulse broadening increases with increasing power. The Num Scans value of the WSU 2012 measurement data is 30. The software settings, excluding the Num Scans value, for the Teraview instrument are constant for all measurements performed by the author in 2017.

There is uncertainty in the alignment of the sample with respect to the emitter detector modules. The uncertainty is caused by slightly different orientation angles of the laser modules and focusing lenses relative to the sample surface. The orientation angles of the laser modules and focusing lenses are different from the sample orientation because of the independent

installation of the modules and sample on the optical workbench. The lowest uncertainty in sample orientation is at normal incidence at which angle the orientation minimally contributes and in which case the live feed of the signal data from the Teraview system is used to fine tune the initial orientation. The external configuration for parallel and perpendicular polarization measurements is shown in Figure 4.5 and Figure 4.6, respectively.

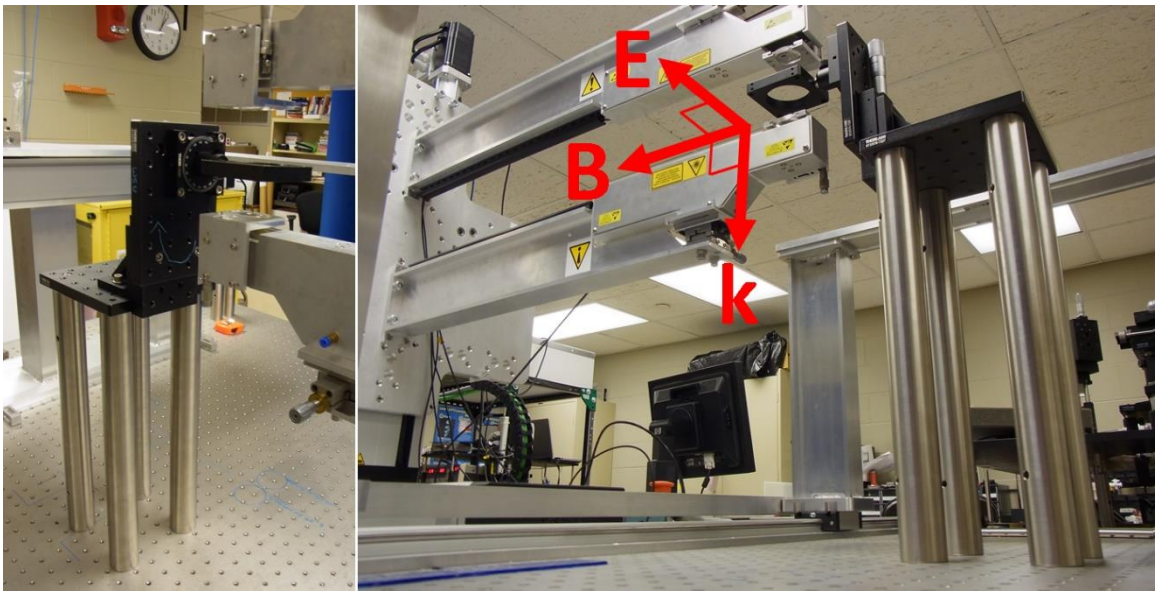

Figure 4.5) The graphic is the external transmission experimental setup to conduct measurements in parallel polarization configurations. The left image is the external measurement apparatus with incident angles as white demarcations on the base of the mounting apparatus. The right image shows another view of the measurement apparatus with incident radiation vectors in red.

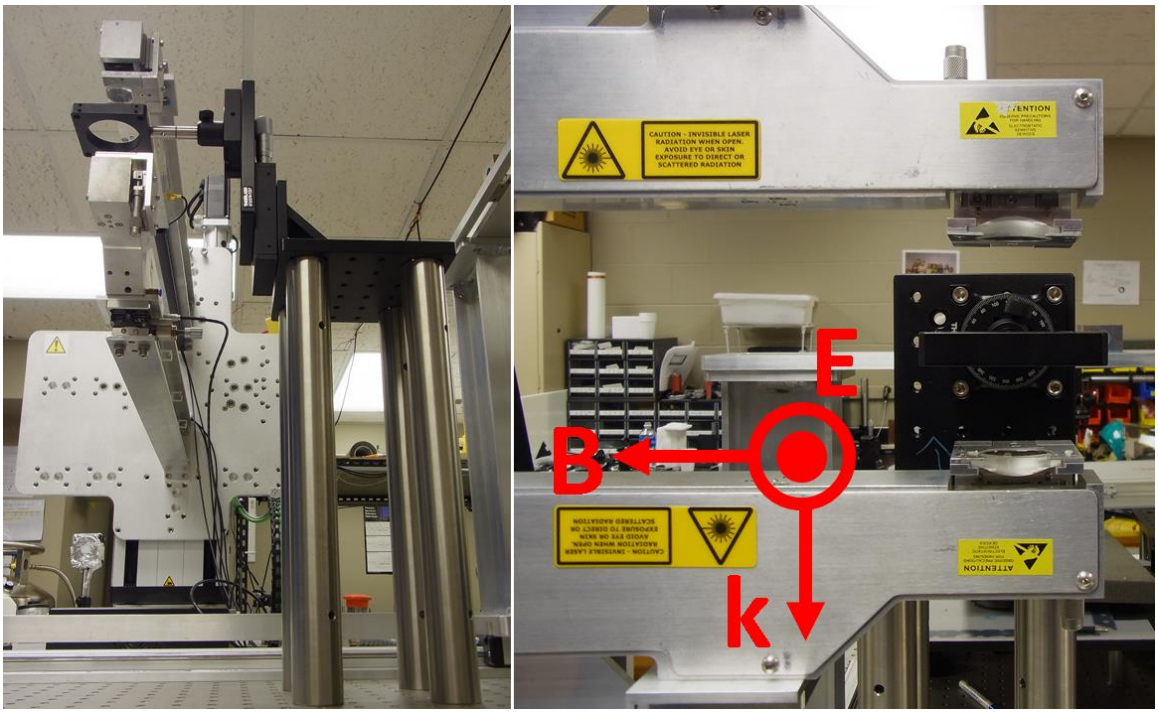

Figure 4.6) The graphic is the external transmission experimental setup to conduct measurements in perpendicular polarization configurations. The left image is the external measurement apparatus with incident angles as white demarcations on the base of the mounting apparatus. The right image shows another view of the measurement apparatus with incident radiation vectors in red.

Seven samples are used for the data collection with the WSU instrument. Four of the samples are solid material: HRSi, and three thicknesses of HDPE. The remaining three samples are compressed particulates: α-lactose monohydrate, pharmaceutical-grade Oxycodone, and Hydrocodone. In addition to measuring each of the four solid materials in single-layer arrangements, the solid materials are stacked one on another in combination with a known thickness air gap in between the layers. The particulate samples are only measured in single-layer arrangements. The arrangement of measurements and angles of incidence recorded at WSU are

presented in Table 4.1. The HRSi sample came with a resistivity characterization from the manufacturer. The resistivity of the HRSi is 5.0×10^{3} $\Omega \cdot cm^{-1}$, which can be inverted to obtain a conductivity of 0.2×10^{-3} $S \cdot cm^{-1}$, and assuming a sample thickness of 500 μm is equivalent to a sheet resistance of 1.0×10^{5} Ω. Due to the small conductivity, the HRSi is likely to exhibit low absorption at THz frequencies [41].

Table 4.1a) The different arrangement of materials and measurement configurations for experiments at WSU.

Sample Arrangement	Angle of Incidence (degrees)	Number of Measurements at Each Angle	Polarization	Configuration	Num Scans
HRSi	0	1	Perpendicular	Internal	30
HDPE-A	0	1	Perpendicular	Internal	30
HRSi	0, 5, 10, 15, 20, 25, 30, 35, 40, 45, 50, 55, 60	10	Perpendicular	Internal	100
HDPE-A	0, 5, 10, 15, 20, 25, 30, 35, 40, 45, 50, 55, 60	10	Perpendicular	Internal	100
HDPE-B	0, 5, 10, 15, 20, 25, 30, 35, 40, 45, 50, 55, 60	10	Perpendicular	Internal	100
HRSi	0.0, 25.0, 40.0	1	Parallel	External	100
HDPE-A	0.0, 27.0, 45.5	1	Parallel	External	100
HDPE-B	0.0, 22.0, 43.0	1	Parallel	External	100
HRSi | Air | HDPE-A	0.0, 8.5, 12.5, 19.0, 23.0, 33.5, 37.0, 41.5, 47.0	1	Parallel	External	100

Table 4.1b) The different arrangement of materials and measurement configurations for experiments at WSU.

Sample Arrangement	Angle of Incidence (degrees)	Number of Measurements at Each Angle	Polarization	Configuration	Num Scans
HDPE-A | Air | HRSi	0.0, 8.0, 12.5, 23.0, 27.0, 31.0, 35.0, 40.0, 42.0	1	Parallel	External	100
HDPE-A | Air | HDPE-B	0.0, 4.0, 7.5, 11.0, 15.0, 19.0, 23.0, 26.0, 30.0, 34.0, 37.5, 41.0, 45.0	1	Parallel	External	100
HDPE-A | Air | HDPE-A	0.0, 6.0, 11.0, 15.5, 20.5, 23.0, 26.5, 30.0, 34.0, 37.5, 40.5, 43.5, 46.5	1	Parallel	External	100
HDPE-B | Air | HDPE-B	0.0, 9.0, 15.0, 21.0, 31.0, 35.0, 37.0, 42.5, 44.0	1	Parallel	External	100
HRSi	0, 5, 10, 15, 20, 25, 30, 35, 40, 45	1	Parallel	External	1000
HDPE-A	0, 5, 10, 15, 20, 25, 30, 35	1	Parallel	External	1000
HDPE-B	0, 5, 10, 15, 20, 25, 30	1	Parallel	External	1000
HDPE-A | Air | HRSi	0, 5, 10, 15, 20, 25, 30, 35, 40	1	Parallel	External	1000
HDPE-B | Air | HDPE-A	0, 5, 10, 15, 20, 25	1	Parallel	External	1000
HDPE-A | Air | HDPE-A	0, 5, 10, 15, 20, 25	1	Parallel	External	1000

Table 4.1c) The different arrangement of materials and measurement configurations for experiments at WSU.

Sample Arrangement	Angle of Incidence (degrees)	Number of Measurements at Each Angle	Polarization	Configuration	Num Scans
HRSi	0, 5, 10, 15, 20, 25, 30, 35, 40, 45, 50, 55, 60	1	Perpendicular	External	1000
HDPE-A	0, 5, 10, 15, 20, 25, 30, 35, 40, 45, 50, 55, 60	1	Perpendicular	External	1000
HDPE-B	0, 5, 10, 15, 20, 25, 30, 35, 40, 45, 50	1	Perpendicular	External	1000
HDPE-C	0, 5, 10, 15, 20, 25, 30, 35, 40, 45	1	Perpendicular	External	1000
HDPE-A | Air | HRSi	0, 5, 10, 15, 20, 25, 30, 35, 40, 45	1	Perpendicular	External	1000
HDPE-B | Air | HDPE-A	0, 5, 10, 15, 20, 25, 30	1	Perpendicular	External	1000

In Table 4.1, the rows highlighted in blue are recorded by Mr. Justin Wheatcroft during the Summer of 2012, those in green are recorded by Mr. Jordan Lewis 10/2017-12/2017, and non-highlighted rows are recorded by the author 04/2017-05/2017. The multi-layer stacks labelled in the sample arrangement column of Table 4.1 are such that the incident radiation travels from left to right. For example, in the HRSi | Air | HDPE-A stack, HRSi is on the initial incidence side, and HDPE-A is on the exit side of the stack. Indicated in Table 4.1, The polarization of the measurements performed at WSU are in the perpendicular and parallel polarization state. In the case of

perpendicular polarization, the incident electric field is always parallel to the plane of incidence. To give a sense of scale with respect to the evolution of the peak time-domain air reference signal amplitude in Table 4.1, the range of amplitude in 2012 recorded with the WSU internal system corresponding to the HRSi air reference is 14,600 non-calibrated amplitude units, and with the WSU external system corresponding to the HDPE-C air reference is 800 non-calibrated amplitude units.

All the thicknesses have been measured with a Vernier style Mitutoyo branded micrometer. The caliper has an advertised accuracy of $\pm$ 25.4 μm, precision of 12.7μm, and range of 0–150 mm. The readout of the caliper is limited to 0.01 mm, which consequently limits the repeatability to 10 μm. The thickness of the HRSi layer is measured using the caliper to be 500 μm, HDPE-A is 3070 μm, HDPE-B is 6050 μm, and HDPE-C is 1640 μm. The air gap between the two external layers is created by a Thor-Labs optical cage plate which is used as the sample mount. The thickness reported by Thor-Labs is and confirmed with the Vernier micrometer is 12700 μm, equivalent to one-half inch. The α-lactose monohydrate, pharmaceutical-grade Oxycodone, and Hydrocodone particulate samples are compressed into the cavity of metal washers using one layer of extremely thin clear plastic wrap adhered to the top and bottom of the washer. The compression torque applied to secure the

Lactose sample is 25 ft-lb. The compression torque on the Oxycodone and Hydrocodone samples is unknown, but based on a visual inspection, the torque is hypothesized to be lower than that used for Lactose. The Lactose has 100% concentration, while the Oxycodone and Hydrocodone concentrations are not exactly known [42]. Furthermore, the Oxycodone sample is pharmaceutical-grade Oxycodone. Pharmaceutical-grade Oxycodone uses α-lactose monohydrate as an inert filler material. The thickness of the washers used to enclose the α-lactose monohydrate, pharmaceutical-grade Oxycodone and Hydrocodone is measured with the Vernier micrometer to be 2390 μm, 900 μm, and 1550 μm, respectively. The solid material samples are attached to the mounting apparatus using rubber bands along the perimeter, whereas mechanical spring clamps are used for the particulate samples.

The measurement process involves the time-domain sampling of the transmitted propagating electric field using a THz laser source. Because the NDE measurements are conducted in open air, the reference measurement measures the response of air to the THz radiation. A reference measurement is made without the sample present for each sample arrangement. Each measurement conducted in Table 4.1 has an associated reference measurement that is recorded immediately prior to the sample measurement and the reference measurement is assumed valid for all angles of incidence

for a single sample arrangement. In addition, an ambient measurement is obtained at the end of each day of measurements by blocking the instrument emitter antenna with a sheet of metal and recording the ambient environment.

A significant challenge associated with the WSU external data collected in 2017 is the inability of the optical delay rail to reset at a consistent location after each scan. The result of this issue is that each time-domain measurement has an initial time delay that is unique, and unique time-domain delay rail sampling positions. If left untreated, the non-synchronized measurements cannot be directly compared at the same delay rail positions and therefore prohibits time-domain multi-measurement optimization. Fortunately, the delay rail reset issue is not present in the OSU data as discussed in Section 4.3. The plots in Figure 4.7 demonstrate the WSU delay rail reset defect.

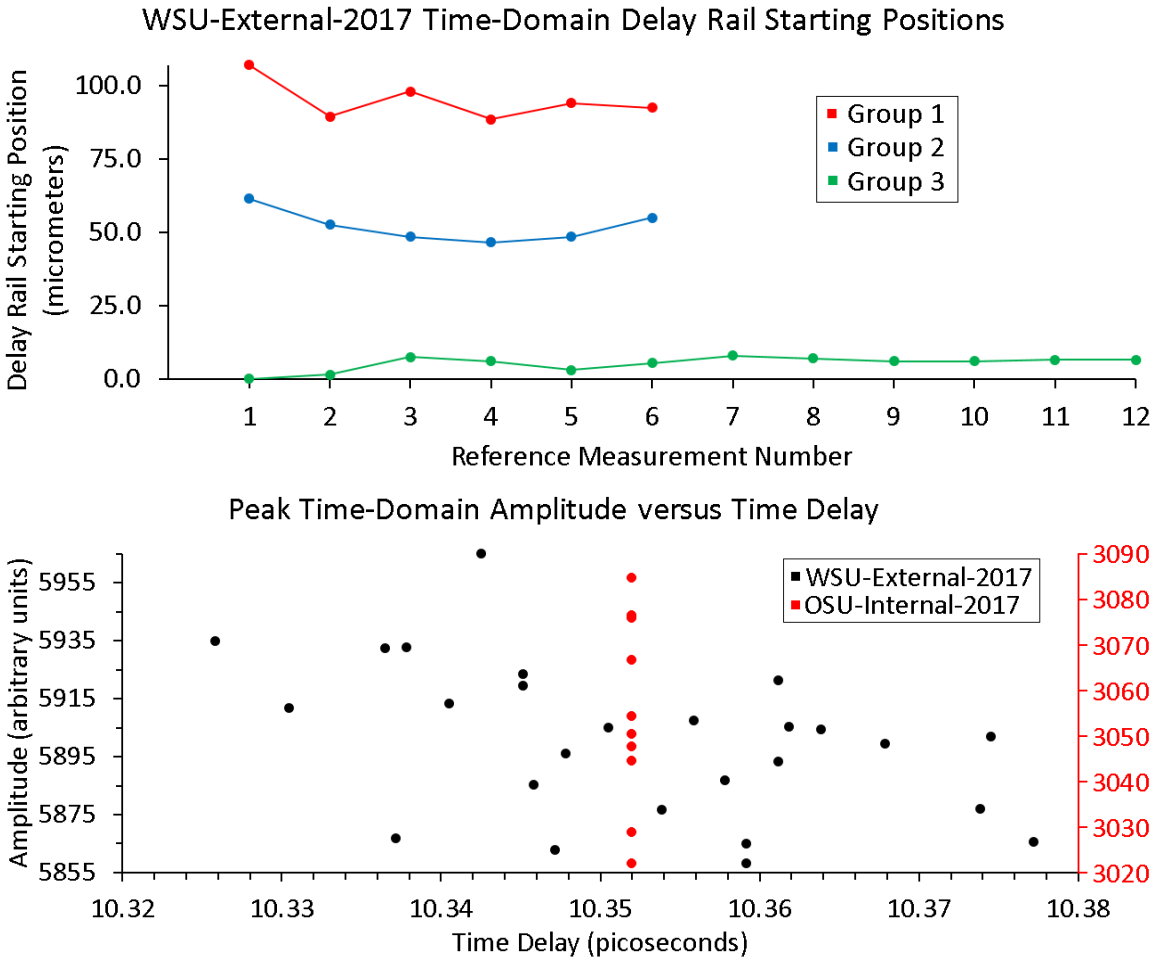

Figure 4.7) The data collected using the WSU external configuration in 2017 has a delay rail reset issue. Top plot is three separate groups with multiple measurements in each group showing that the delay rail does not correctly reset after a measurement. Bottom plot shows the time delay locations of twenty-six WSU external reference signal peaks and ten OSU internal peaks with the OSU delay rail resetting correctly after each measurement.

Measurements that are collected close in time to one another will have variation in the peak amplitude of the measured signal for a constant measurement configuration. Additionally, the WSU external data from 2017 has a delay rail initialization which wanders from subsequent measurements. Fortunately, the WSU instrument produces measurements that have approximately constant time-domain sampling intervals within the same

measurement and in subsequent measurements, for constant measurement configurations.

Time-domain measurements are recorded with the WSU external transmission system for which the line-of-sight (LOS) between the transmitter and receiver is obstructed by a large thick copper plate. The spectral magnitude of the signal from the non-obstructed and obstructed aperture measurement are used to compute the signal-to-noise ratio (SNR). The research hypothesizes that this approach for computing the SNR is more representative of the true SNR because it is clutter-exclusive. A clutter-exclusive SNR means that the SNR is not derived from variation in the reference signal and therefore excludes signal clutter in the SNR characterization, in contrast to other published clutter-inclusive approaches [43, 44, 45]. The measured sample signal or reference signal can be used for the non-obstructed signal measurement, depending on if the reference signal SNR or a sample-dependent SNR is desired. The measured spectral magnitude of the non-obstructed and obstructed signal measurement is labelled $|\tilde{Y}_{\text{signal}}|$ and $|\tilde{Y}_{\text{noise}}|$, respectively. The calculation of SNR is defined in Equation 4.1, where ν is the frequency.

$$\mathrm{SNR}(\nu) = \frac{|\tilde{Y}_{\mathrm{signal}}|}{|\tilde{Y}_{\mathrm{noise}}|} \qquad 4.1$$

The time-domain amplitude of representative air reference measurements at three Num Scans values are shown in the plots of the left column in Figure 4.8. The time-domain amplitude of representative occluded receiver measurements at the three Num Scans values are shown in the plots of the right column in Figure 4.8. The three Num Scans values are 50, 75, and 100. The top, middle, and bottom row in Figure 4.8 correspond to measurements recorded using Num Scans values of 50, 75, and 100, respectively. The set of air reference measurements and aperture obstructed measurements for a specific Num Scans value are recorded within ten minutes of one another. Notably, the delay rail translations are observed as eight apparent discontinuities in the time-domain noise measurement plots in the right column of Figure 4.8. Observed in the time-domain air reference plots in the left column of Figure 4.8, the length of the pre-pulse region is not constant between the three Num Scans settings. The straight lines connecting the data points in the plots of Figure 4.8 are for illustrative purposes. The length of the pre-pulse region, which is defined as the number of temporal sampling points preceding the arrival of the initial THz pulses at the detector, is not controlled by the Num Scans value.

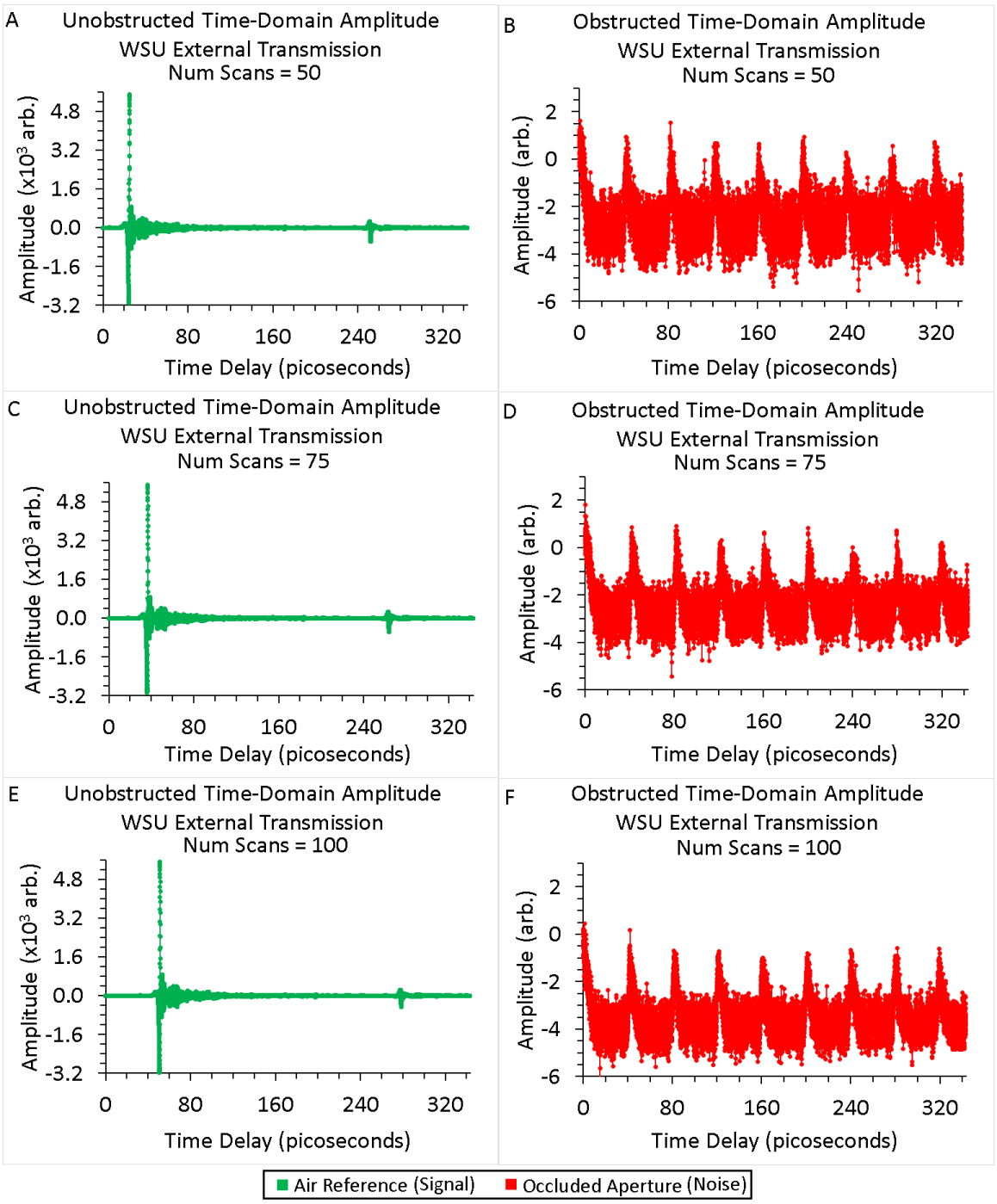

Figure 4.8) Plot A and plot B are the air reference and noise measurement for Num Scans value of 50. Plot C and plot D are the air reference and noise measurement for Num Scans value of 75. Plot E and plot F are the air reference and noise measurement for Num Scans value of 100.

The frequency-dependent SNR is obtained by dividing the air reference spectral magnitude by the noise spectral magnitude. The SNR for

representative air reference measurements using Num Scans values of 50, 75, and 100 are shown in Figure 4.9. The two plots in the top row of Figure 4.9 correspond to measurements using a Num Scans value of 50. The two plots in the middle row of Figure 4.9 correspond to measurements using a Num Scans value of 75. The two plots in the bottom row of Figure 4.9 correspond to measurements using a Num Scans value of 100. The green circle markers in plot A, plot C, and plot E of Figure 4.9 are the air reference measurements for Num Scans values of 50, 75, and 100, respectively. The red circle markers in plot A, plot C, and plot E of Figure 4.9 are the noise measurements for Num Scans values of 50, 75, and 100, respectively. The blue circle markers in plot B, plot D, and plot F of Figure 4.9 are the SNR obtained for the measurements using Num Scans values of 50, 75, and 100, respectively. The straight lines connecting the data points in the plots of Figure 4.9 are for illustrative purposes. Notably, the SNR is observed to decrease by an order of magnitude from 1 THz to 2 THz.

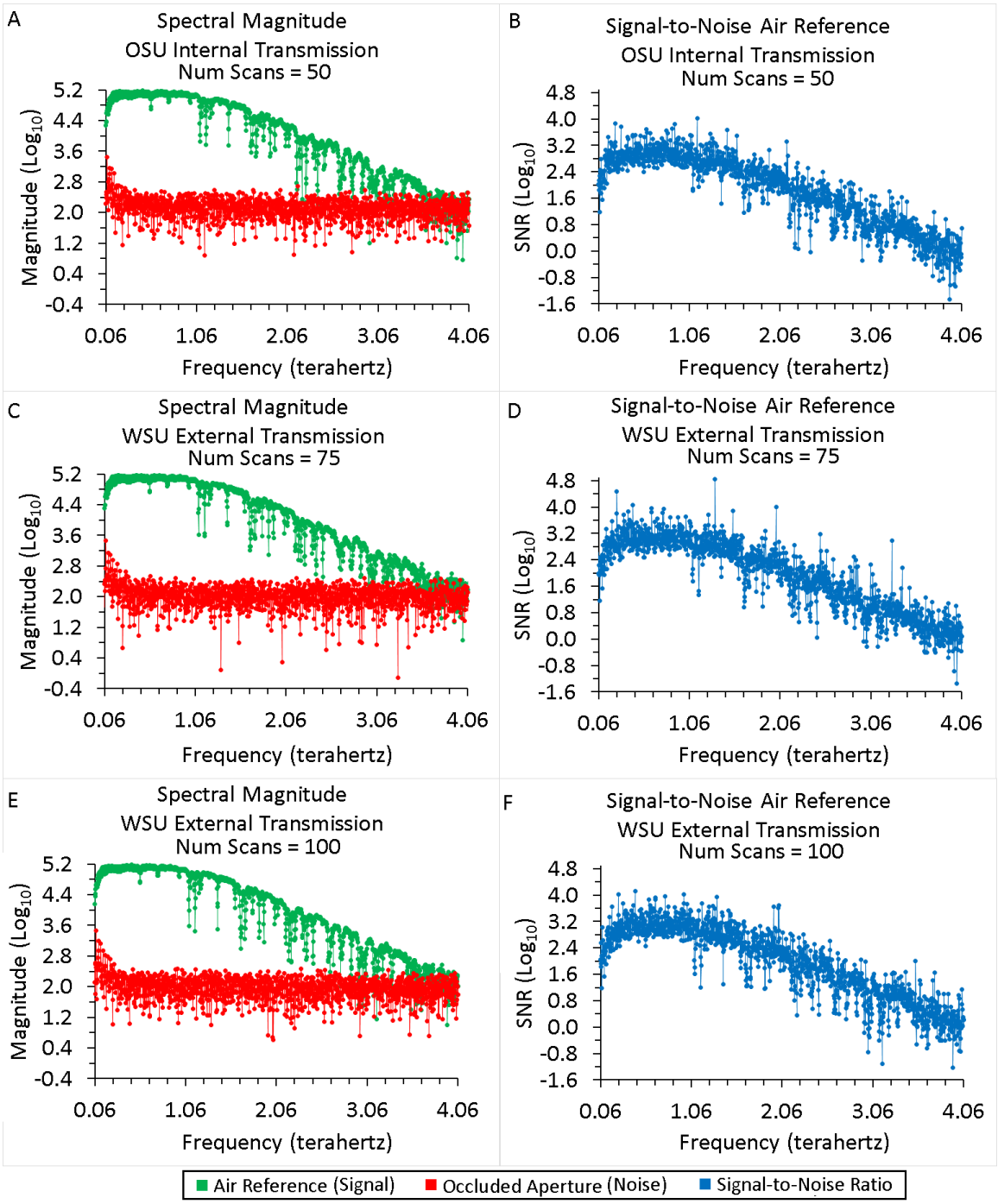

Figure 4.9) The spectral magnitude profiles for air reference (green) and noise (red) measurements for three Num Scans values. The frequency-dependent signal-to-noise ratio (blue) is calculated at each of the three Num Scans values.

The SNR analysis shows that the WSU external transmission measurement data is strongest in a 2 THz bandwidth up to a frequency of 2

THz. The linearity of the SNR in Figure 4.9 indicates a logarithmic decrease in SNR beginning at a frequency of 1 THz. The SNR computed is used to compute a decibel (dB) metric. The SNR in decibels (SNR_{dB}) is calculated symbolically as $\mathrm{SNR_{dB}} = 20 \cdot \mathrm{Log_{10}}(\mathrm{SNR})$. The $\mathrm{SNR_{dB}}$ inferred from the SNR plots in Figure 4.9 at 1 THz, 2 THz, and 3 THz is approximately 60 dB, 40 dB, and 20 dB, respectively.

4.4. THE OHIO STATE UNIVERSITY DATA

The data collected at OSU by the author is strictly from the internal operating configuration of the Teraview instrument. Data was collected by the author at OSU on June 14–15, 2017. Although the internal configuration at OSU lacks the dispersion associated with the fiber optic cables, the Teraview instrument at OSU suffers from a stitching artifact in the delay rail registration. The stitching artifact is shown in Figure 4.10, which unfortunately results in time-domain regions of corrupted data which can negatively impact the transmitted pulse recordings.

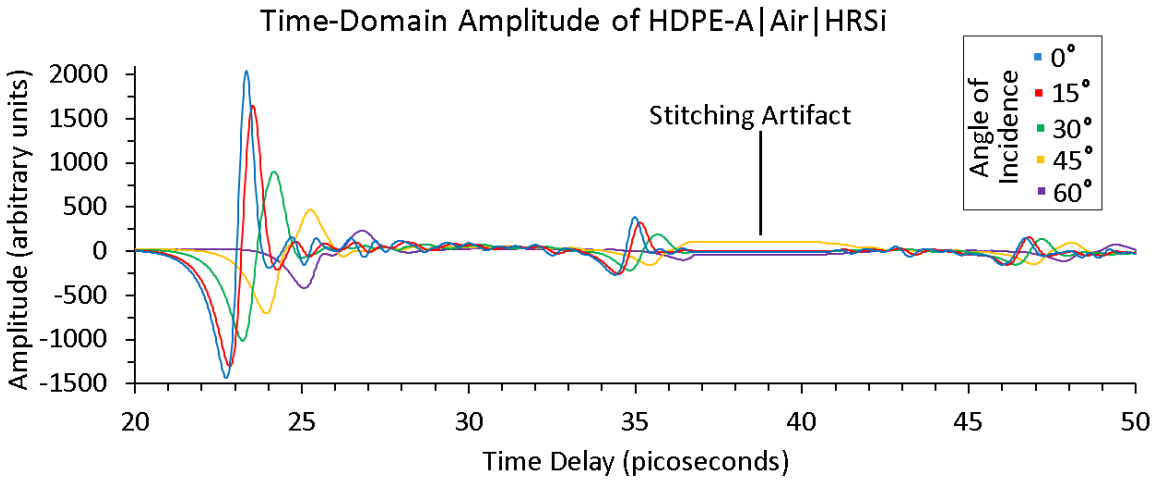

Figure 4.10) The stitching artifact in the OSU measurements result in corrupted information which can degrade important regions of time-domain data.

The stitching artifact results in partially corrupted data which unfortunately can render critical portions of the signal where time-domain peaks are located unusable. The software settings for the Teraview instrument are constant for all the OSU measurements and identical to those used in the WSU measurements, and the stitching artifact is located at the same time-domain positions for all the OSU data. Each region of the time-domain signal that contains the stitching artifact is observed as a region of constant amplitude. The time-domain indices are identified and the regions are changed from the typically non-zero constant amplitude to an amplitude of zero for all corrupted regions so that the regions, as shown in Figure 4.10, do not contribute energy to the signal. The same three materials from WSU are used for the OSU measurements and the measurement configurations are shown in Table 4.2.

Table 4.2) The different arrangement of materials and measurement configurations for experiments at OSU.

Sample Arrangement	Angle of Incidence (degrees)	Number of Measurements at Each Angle	Polarization	Config-uration	Num Scans
HRSi	0, 5, 10, 15, 20, 25, 30, 35, 40 ,45, 50, 55, 60	10	Perpendicular	Internal	100
HDPE-A	0, 5, 10, 15, 20, 25, 30, 35, 40 ,45, 50, 55, 60	10	Perpendicular	Internal	100
HDPE-B	0, 5, 10, 15, 20, 25, 30, 35, 40 ,45, 50, 55, 60	10	Perpendicular	Internal	100
HDPE-A | Air | HRSi	0, 5, 10, 15, 20, 25, 30, 35, 40 ,45, 50, 55, 60	10	Perpendicular	Internal	100
HDPE-B | Air | HRSi	0, 5, 10, 15, 20, 25, 30, 35, 40 ,45, 50, 55, 60	10	Perpendicular	Internal	100
HDPE-B | Air | HDPE-A	0, 5, 10, 15, 20, 25, 30, 35, 40 ,45, 50, 55, 60	10	Perpendicular	Internal	100
HDPE-A | Air | HDPE-A	0, 5, 10, 15, 20, 25, 30, 35, 40 ,45, 50, 55, 60	10	Perpendicular	Internal	100

As can be seen in Table 4.2, each angle of incidence for a given sample arrangement is duplicated ten times. The reason for this is as follows. The WSU measurements displayed a measurable variation in the peak reference signal time-domain amplitude over the span of several minutes. This observation was made after the WSU data collection dates. The discovery of the time dependency of repeated measurements while all controllable measurement variables within are held constant is taken into consideration when planning the OSU data collections. It is decided that each of the OSU measurements should be duplicated ten times to provide a better

understanding of the average measurement. Thus, not only are the sample measurements duplicated, but the reference measurements are duplicated ten times also. Again, the measurement is duplicated because the recorded signal varies with each measurement, even if the mounting apparatus has not been manipulated and the time between subsequent measurements is less than one minute.

The signal variation between two OSU internal transmission system air reference measurements is shown in Figure 4.11. The percentages in the top plot of Figure 4.11 represent the percent change between the two measurements relative to the largest amplitude range of the two time-domain signals. The amplitude range is defined as the difference of the maximum to minimum amplitude, or equivalently most positive to most negative peak, within a time-domain signal. The time separating the recording of the two measurements used in Figure 4.11 is approximately one minute, with the Num Scans value set to 100. Also shown in the top plot of Figure 4.11 in green are the periodic stitching artifacts present in the data.

The two air reference measurements used in Figure 4.11 are selected because the two measurements are sequentially recorded with the largest percent change in amplitude range of all the sequentially recorded OSU measurements. The amplitude range of the two measurements is 5105.17 and

5197.72 with a percent change in amplitude range between the two measurements of 1.78%. The two measurements are both recorded on 06/14/2017 at approximately 11:17am and 11:18am EST. Also shown in Figure 4.11 are the delay rail stitching artifacts indicated by the green lines.

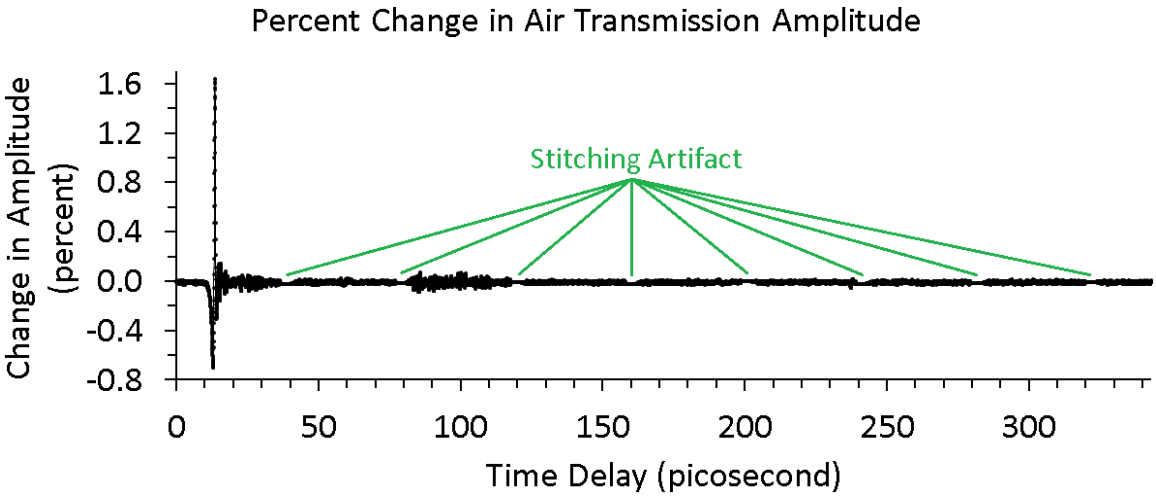

Figure 4.11) The percent difference between two OSU internal transmission system air reference measurements with the recording of each measurement separated in time by approximately one minute.

The percent change shown in Figure 4.11 is for two air reference signals recorded sequentially using the OSU internal transmission system. The signal variability is also analyzed for a group of ten sequentially recorded air reference signals. The minimum, maximum, and median signal values shown in Figure 4. 12 are for ten sequentially recorded air reference measurements at a Num Scans value of 100. The measurements are recorded on 06/14/2017 at approximately 15:30 EST. The set of ten measurements are selected because they have the largest average range of amplitude variation. The

recording of each of the ten measurements are separated in time by six minutes. The two plots in the top row of Figure 4.12 show the time-domain air reference signal variability as the minimum (blue markers), median (black markers) and maximum (red markers) of the set of ten measurements. As seen in the top row of Figure 4.12, the amplitude of the time-domain signals varies over tens of minutes. Additionally, the location of the peak amplitude as shown in plot B of Figure 4.12 also varies.

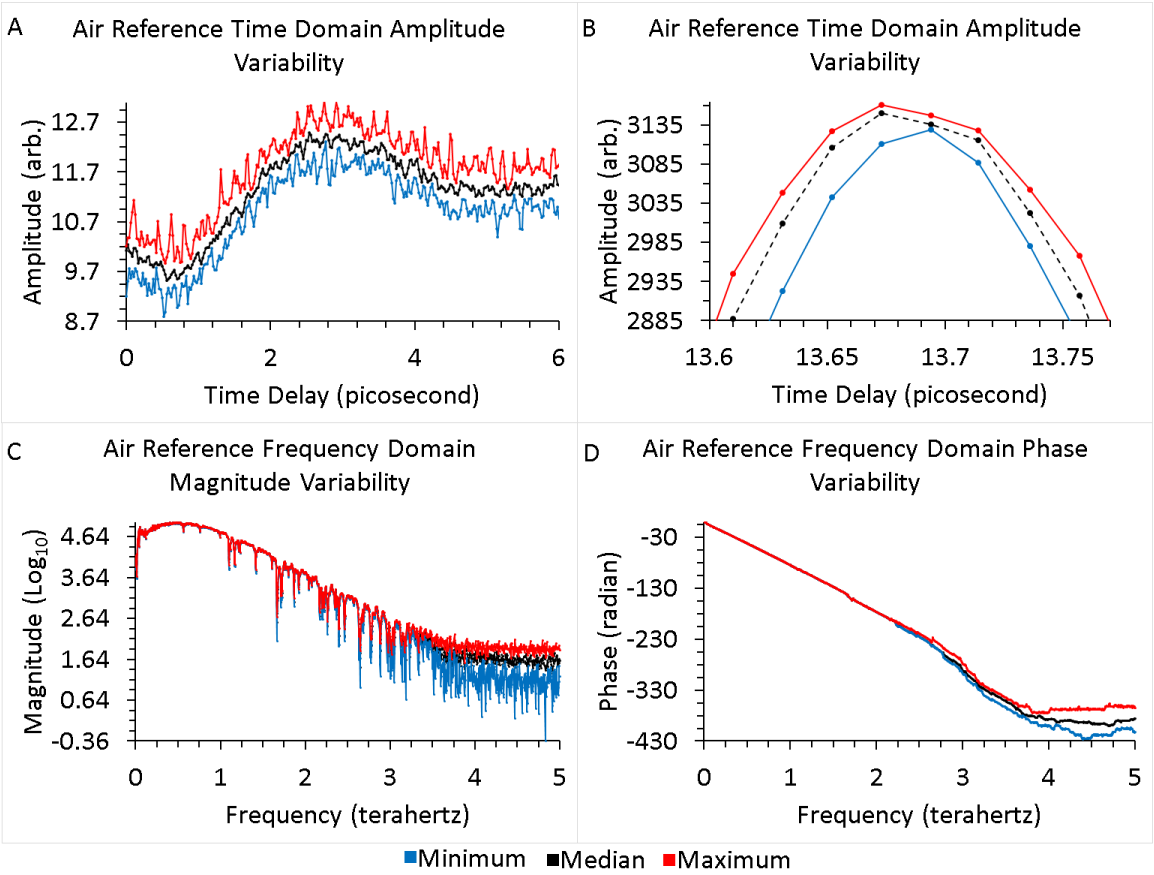

Figure 4.12) The minimum (blue), median (black), and maximum (red) air reference values from a set of ten sequentially recorded measurements separated by six minutes.

The bottom row of plots in Figure 4.12 shows the minimum, median, and maximum magnitude (plot C) and phase (plot D) of the frequency-domain air reference signals. The magnitude variation shown in plot C of Figure 4.12 indicates that the variation in the time-domain is manifest at frequencies for which the signal clutter is increasing and the signal strength is decreasing, with respect to the peak signal strength near 0.5 THz. The phase variation shown in plot D of Figure 4.12 also indicates that the time-domain signal variation is most significant at frequencies for which the signal clutter is increasing and signal strength is decreasing, particularly at frequencies greater than 2.25 THz.

Due to the added complexity of recording the OSU measurements, the process for mounting samples and recording data at OSU is explained to facilitate an understanding of the experimental procedure. First, the base of the mounting apparatus is fixed to the Teraview measurement chamber for each sample measurement campaign using double sided 3M brand tape rated at 30 pounds. Next, the target sample is installed on the mounting apparatus and the sample is measured at thirteen unique incidence angles in 5° increments which start at normal incidence and conclude at 60°. The angle of incidence is calibrated using the real-time feed of the signal data from the Teraview system. The starting angle on the mounting apparatus that

corresponds to normal incidence is the angle on the apparatus at which the measured signal peak has reached a minimum in time delay. Ideally, the sample orientation at which the time delay of the signal peak is minimum also corresponds to the maximum peak signal. The resolution of the angular demarcations on the sample mounting apparatus is 1°, and the uncertainty of the angular recording is estimated to be approximately 0.25°. The samples are installed on the mounting apparatus using rubber bands. The cage plate that the samples are mounted to has a thickness reported by Thor-Labs of 0.5 inches. The measurement chamber is shown in Figure 4.13.

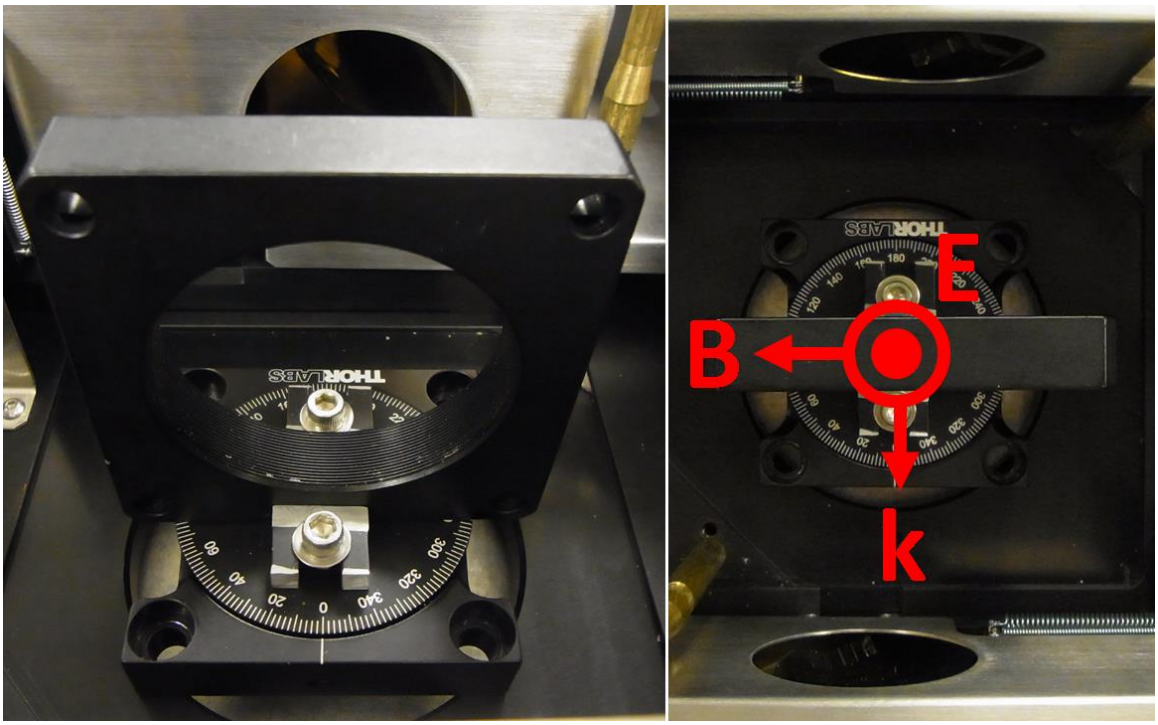

Figure 4.13) The graphic is the internal transmission experimental setup to conduct measurements in perpendicular polarization configurations. The left image is the internal measurement apparatus with incident angles as white demarcations on the base of the mounting apparatus. The right image shows a top-side view of the measurement apparatus with incident radiation vectors in red.

The electric field of the incident radiation for the OSU measurements are such that the electric field vector is nominally parallel to the sample surface at all angles of incidence. In addition, the sample measurements are repeated ten times at each angle of incidence such that at the end of a sweep across incident angles, 130 time-domain transmission measurements have been recorded. As with the reference measurements, the sample measurements are repeated because of the time-dependent variability in the recorded signal.

The 130 sample measurements requires up to two hours to record and it is conceivable that the atmospheric conditions in the laboratory may have changed sufficiently, such that the reference measurements which are accurate for the first part of the sample measurement campaign are not equally accurate for the latter part. Therefore, the reference measurement procedure is repeated after the sample measurements have been made to facilitate a linear interpolation of the reference signal to any of the sample measurements. The ten reference measurements made after the sample measurements is the final round of measurements for a given sample. The workflow of NDE measurements is shown in Figure 4.14.

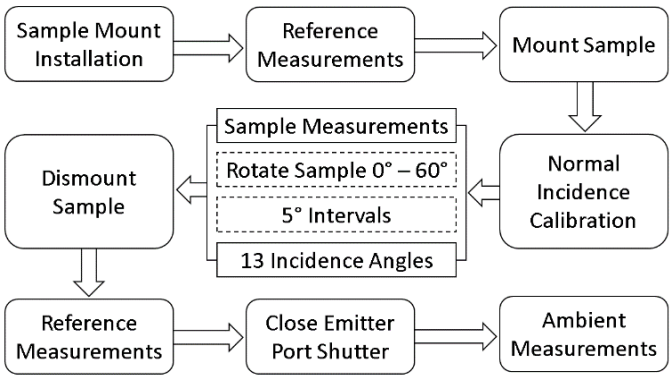

Figure 4.14) Workflow of NDE measurements for a sample. The ambient measurement only occurs for the last measurement of the day, but is approximately constant for all the measurements.

The result of performing the experimental procedure represented in Figure 4.14, combined with the sample arrangements in Table 4.2, results in 910 sample measurements. Associated with the sample measurements are 140 reference measurements to facilitate accurate interpolation through time to the instant that the sample measurement is recorded. The ambient measurements are obtained by blocking the instrument emitter antenna with a sheet of metal and recording the ambient environment. There are twenty ambient measurements, ten measurements made at the end of each day of measurements.

The emitter port shutter is closed by placing a large thick aluminum plate directly in front of the receiver aperture. Obstructing the LOS between the transmitter and receiver effectively occludes the detector relative to the emitter. The time-domain measurement resulting from the obstruction of the receiver aperture by the metal plate yields a measurement of the detector

noise. The time-domain measurements that result from the occlusion are shown in plot A of Figure 4.15. The frequency-domain spectral magnitude of the occlusion measurements are shown in plot B of Figure 4.15. The purple circle markers in the plots of Figure 4.15 is a representative measurement obtained on 06/14/2017 using a Num Scans value of 100. The red circle markers in the plots of Figure 4.15 is a representative measurement obtained on 06/14/2017 by averaging ten measurements using a Num Scans value of 100 to produce an effective Num Scans value of 1000. The time-domain noise amplitudes in plot A of Figure 4.15 shows that as the Num Scans value increases, the measurement noise variance decreases. The frequency-domain spectral magnitudes in plot B of Figure 4.15 shows that the average noise level decreases with increasing Num Scans value. The observation regarding the dependence of the noise on the Num Scans value indicates a correlation between the system noise and the number of scans that are averaged. Additionally, discontinuities caused by the delay rail stitching artifact at the locations of the delay rail translations are observed in the time-domain noise measurement in Figure 4.15.

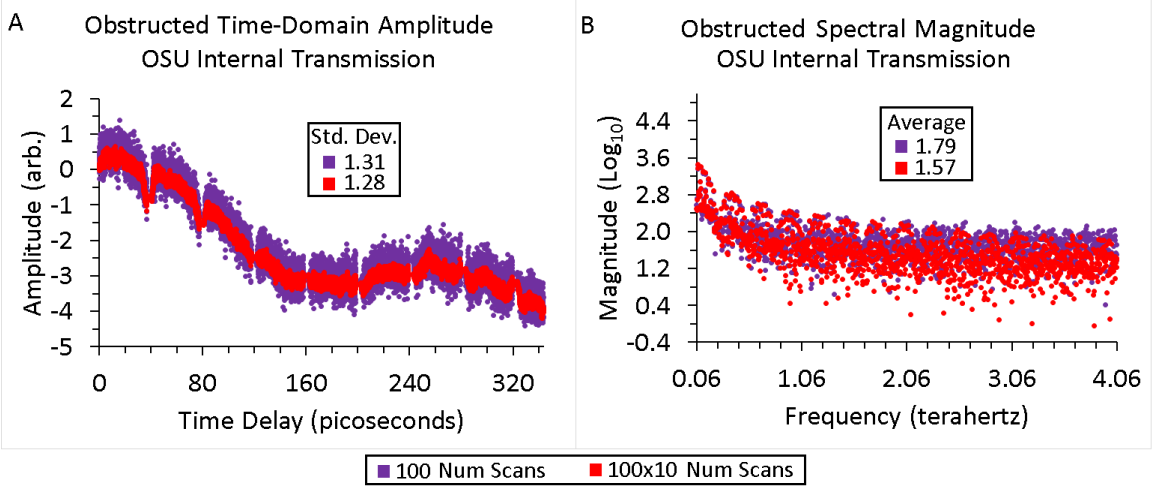

Figure 4.15) The time-domain noise measurement is shown in plot A on the left, and the frequency-domain spectral magnitude of the noise is shown in plot B on the right.

The obstructed aperture measurements are combined with non-obstructed air reference measurements to enable the calculation of a measurement-dependent, frequency-dependent, system signal-to-noise ratio (SNR) estimate. The time-domain amplitude of a representative air reference measurement and noise measurement obtained on 06/14/2017 and 06/15/2017 are shown in Figure 4.16. The top row in Figure 4.16 correspond to measurements recorded on 06/14/2017, and the bottom row corresponds to measurements recorded on 06/15/2017. The measurements used to generate the plots in Figure 4.16 are recorded at approximately 4:00pm EST. The air reference and noise measurements shown in Figure 4.16 are the result of averaging ten measurements recorded using a Num Scans value of 100, for an effective Num Scans value of 1000. The time-domain noise measurement, shown in plot B and plot D, is observed to vary between the two adjacent days.

On each day, the set of air reference measurements and aperture obstructed measurements are recorded within half an hour of one another. The apparent discontinuities observed in the time-domain noise measurements in the right column of Figure 4.16 are at the location of the delay rail translation and correspond to the delay rail stitching artifact.

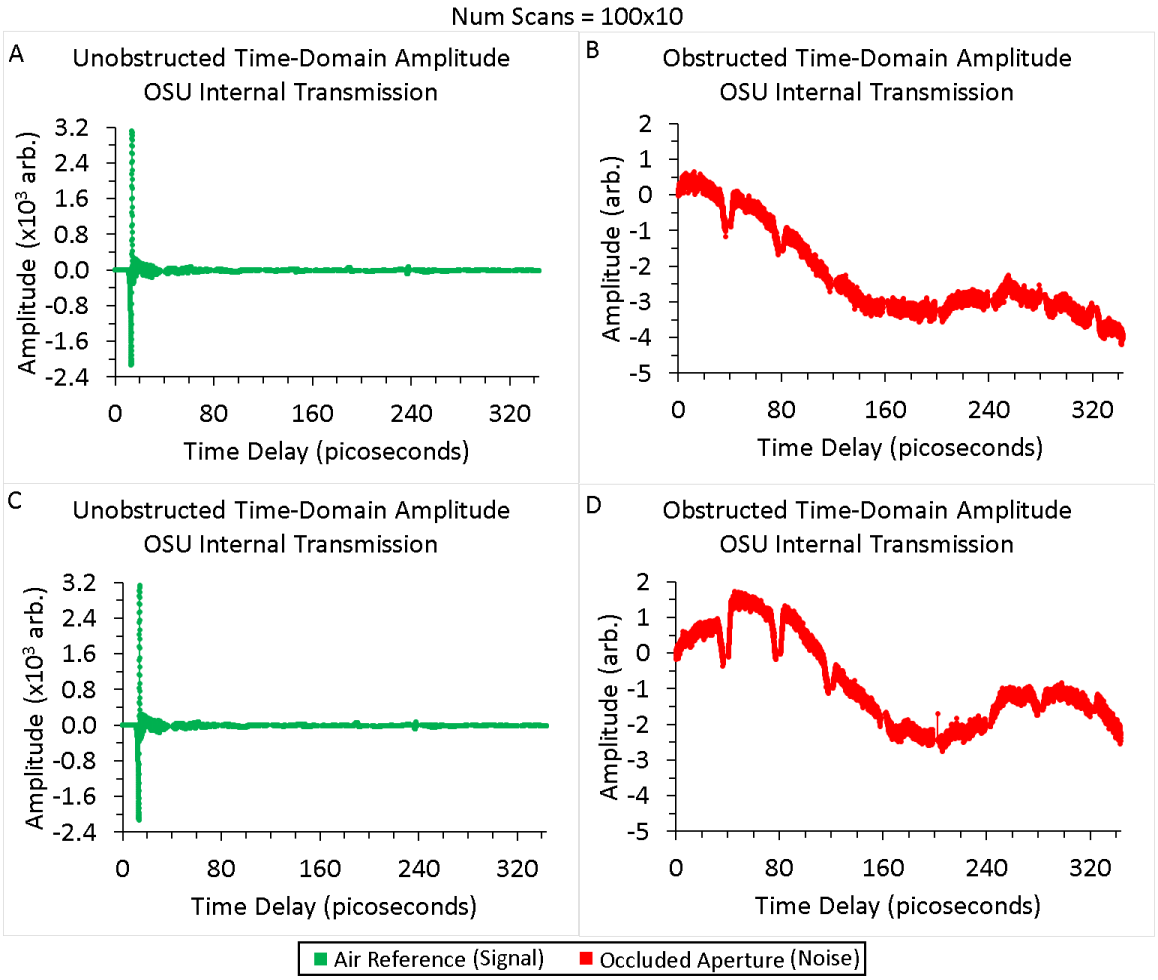

Figure 4.16) Plot A is the air reference measurement recorded on 06/14/2017. Plot B is the noise measurement recorded on 06/14/2017. Plot C is the air reference measurement recorded on 06/15/2017. Plot D is the noise measurement recorded on 06/15/2017.

The frequency-dependent SNR is obtained by dividing the air reference spectral magnitude by the noise spectral magnitude. The SNR for

representative air reference measurements on 06/14/2017 and 06/15/2017 are shown in Figure 4.17. The two plots in the top row of Figure 4.17 correspond to measurements on 06/14/2017, and the two plots in the bottom row correspond to measurements on 06/15/2017. The green circle markers in plot A and plot C of Figure 4.17 are the air reference measurement with an effective Num Scans value of 1000. The red circle markers in plot A and plot C of Figure 4.17 are the noise measurement with an effective Num Scans value of 1000. The blue circle markers in plot B and plot D of Figure 4.17 are the SNR obtained for the measurements on 06/14/2017 and 06/15/2017, respectively. The straight lines connecting the data points in the plots of Figure 4.17 are for illustrative purposes. Notably, the SNR is observed to decrease by an order of magnitude from 1 THz to 2 THz.

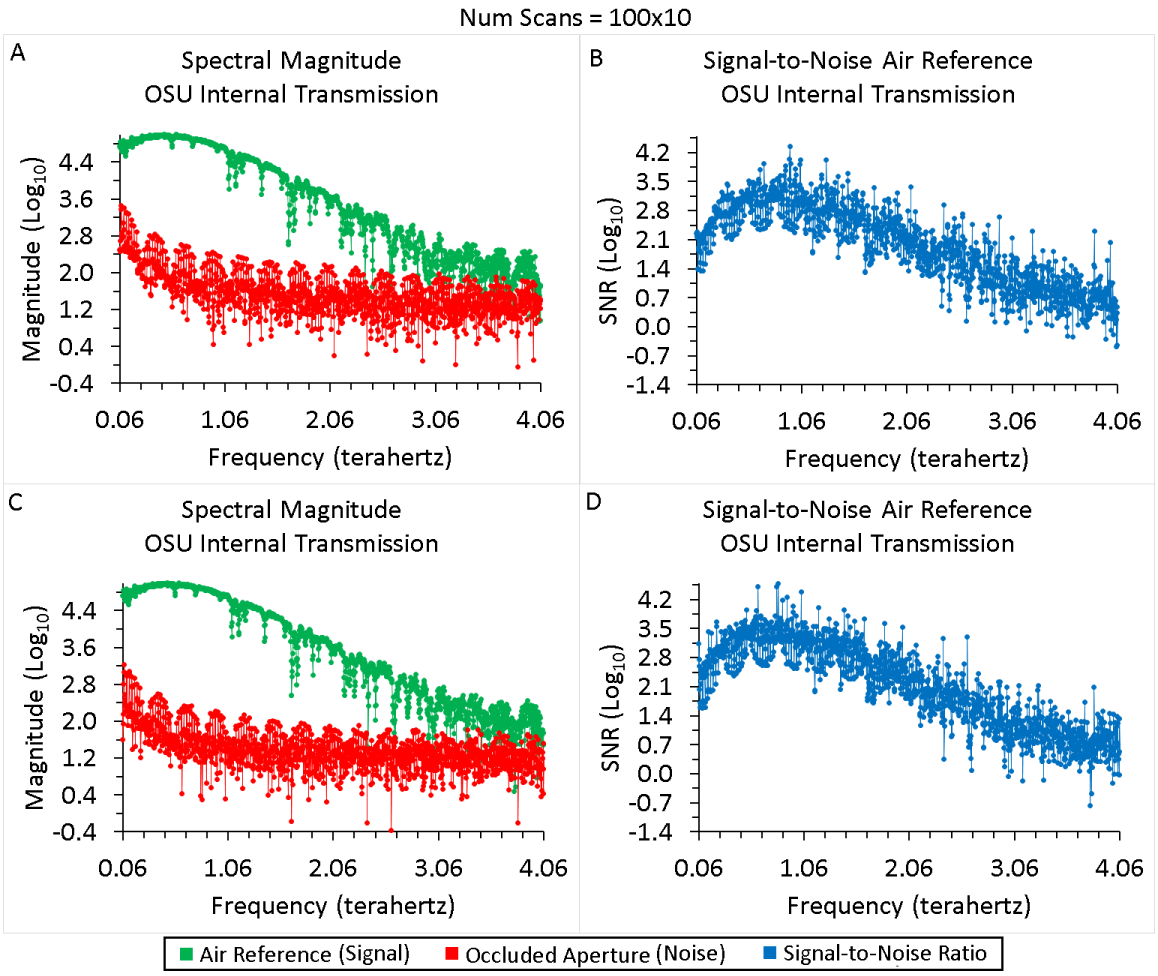

Figure 4.17) Plot A shows the air reference (green) and noise (red) spectral magnitude on 06/14/2017. Plot C shows the air reference (green) and noise (red) spectral magnitude on 06/15/2017. Plots B and D are the SNR on 06/14/2017 and 06/15/2017, respectively.

The SNR analysis shows that the SNR of the OSU internal transmission measurement data is strongest in a 2 THz bandwidth up to a frequency of 2 THz. The SNR analysis also indicates a dependence of the measurement noise on the number of scans that are averaged.

4.5. MEASUREMENT NUMERICAL PRECISION

The precision of the computations and extracted physical parameters is defined by the precision of the measured time-domain data. The time-domain

data is comprised of delay rail position and signal amplitude pairs. The delay rail positions and signal amplitudes represent the abscissa and ordinate of the measured data, respectively. The precision, or equivalently the number of significant digits, of the abscissa and ordinate are both determined by computing the statistical mode of the number of meaningful digits contained in the respective data. The measured abscissa and ordinate data is stored in an ASCII formatted text file. Because the measured data is stored as text, the numbers quantifying the data are initially loaded into computer memory as strings of characters for each pair of data. The statistical mode is computed to determine the number of significant digits because the number of characters, or string length, of each data entry is variable. The number of abscissa and ordinate pairs for a single time-domain measurement exceeds 16,000 entries for the TPS Spectra software settings used in the research.

As an example, two abscissa entries representative of the abscissa values are loaded as ’32.64’ and ‘32.6431’. The algorithm for determining the number of meaningful digits in the abscissa example removes the decimal character resulting in ‘3264’ and ’326431’ and the number of meaningful digits are four and six, respectively. Two representative ordinate values are loaded as ‘-0.0190367’ and ‘5629.4’. The algorithm for determining the number of meaningful digits in the ordinate example removes the decimal and

negative sign characters resulting in ‘190367’ and ‘56294’ and the number of meaningful digits are six and five, respectively. The number of meaningful digits for each abscissa and ordinate pair are computed and the statistical mode of the list of meaningful digits is defined as the number of significant digits. The number of occurrences of meaningful digits computed for representative WSU and OSU abscissa and ordinate pairs are shown in Table 4.3 as a demonstration of the distribution of precision in measured data.

Table 4.3) The number of meaningful digits for representative WSU and OSU data presented as the number of times that a value contains a given number of meaningful digits.

Number of Digits	**WSU**		**OSU**	
	Abscissa	**Ordinate**	**Abscissa**	**Ordinate**
1	0	0	0	0
2	2	2	0	2
3	14	20	16	15
4	162	161	162	136
5	1593	1582	1552	1582
6	15097	15103	14800	14795
7	0	0	0	0

Referring to Table 4.3, it is demonstrated that the most frequently occurring meaningful number of digits, or statistical mode, is six for both the abscissa and ordinate values for data recorded using the WSU and OSU Teraview system. The trailing significant digit has uncertainty. In this context, an evaluation of all the measured data indicates that the precision of all the data is six significant digits with uncertainty in the trailing digit. A number with six significant digits is not a machine precision number, however all

calculations in the parameter extraction algorithm are performed using single precision floating point arithmetic because the Python programming language requires the use of machine precision arithmetic. Therefore, all numbers are rounded to six significant digits after each calculation in the extraction algorithm. Enforcing the non-machine precision of data throughout the extraction algorithm eliminates accumulated error from machine precision digits beyond the precision of the measured data and ensures that all calculations and algorithm output is consistent with the precision of the measured data.

4.6. IMPACTS ON PHYSICAL PARAMETER EXTRACTION

The optimization-based physical parameter extraction is impacted by multiple factors. The impact on physical parameter extraction tends to degrade the confidence of the results. The confidence is degraded because of the presence of physical phenomenology that is not included in the theoretical physics model. There are four impacts that are considered by the research. The four impacts are not an exhaustive list. The first impact is a consequence of the conservation of energy. The second impact is due to the presence of system-dependent clutter in the measurement data. The third impact is the divergence of the THz beam as the beam propagates through a sample. The

fourth impact is the contribution of scattering in particulate samples such as α-lactose monohydrate, pharmaceutical-grade Oxycodone, and Hydrocodone.

4.6.1. CONSERVATION OF ENERGY

The measurements recorded during the research are transmission measurements. Direct measurement of the reflected energy is not performed. The fraction of energy that is transmitted, reflected, and absorbed is theoretically conserved using the power balance equation. The power balance equation is a statement requiring conservation of energy. The equation governing the conservation of energy is defined in Equation 4.2. In Equation 4.2, the frequency-dependent total incident radiation power is $E^2(\nu)$, the spectral total transmitted power is $T^2(\nu)$, the spectral total reflected power is $R^2(\nu)$, and the spectral total absorbed power is $A^2(\nu)$. The squared terms representing power in Equation 4.2 are defined, for example, as $E^2 = |\tilde{E}|^2 = \tilde{E} \cdot \tilde{E}^*$.

$$E^2(\nu) = T^2(\nu) + R^2(\nu) + A^2(\nu) \qquad 4.2$$

The two quantities in Equation 4.2 which are measured during the research are the total incident radiation power E^2 and the total transmitted power T^2. The total reflected power R^2 and total absorbed power A^2 are not measured. Rearranging Equation 4.2 to isolate known quantities from

unknown quantities results in a more suggestive form of the power balance equation defined by Equation 4.3.

$$(1 - \frac{T^2}{E^2}) = (\frac{R^2}{E^2} + \frac{A^2}{E^2}) \quad 4.3$$

The quantity on the left-hand side of Equation 4.3, specifically $(1 - \frac{T^2}{E^2})$, is a known measured quantity. The quantity on the right-hand side of Equation 4.3, specifically $(\frac{R^2}{E^2} + \frac{A^2}{E^2})$, is an unknown non-measured quantity. However, $(\frac{R^2}{E^2} + \frac{A^2}{E^2})$ contains the two unknowns $\frac{R^2}{E^2}$ and $\frac{A^2}{E^2}$. Without direct measurements of either the R^2 or the A^2 contribution, Equation 4.3 represents a theoretically underdetermined equation. The function of the optimization algorithm is to determine physical parameter values that produce a simulated signal from the theoretical physics model for which the simulation most agrees with measurement. Because of the underdetermined nature of the power balance equation, in the context of the research, there is unavoidable ambiguity in the assignment of energy to the reflection and absorption contribution.

4.6.2. SAMPLE-INVARIANT SYSTEM CLUTTER

The research hypothesizes that there is a limit on the ability to numerically extract absorption coefficients of low absorption and highly reflecting materials using the optimization algorithm. The limit is fundamentally caused by the presence of system-dependent signal clutter in the measurement data. In cases of low transmission out of a sample, the extracted coefficients have a high likelihood to be greater than zero. The research hypothesizes that the limit depends on the total attenuation through the material and the reflection off the sample interfaces. The research extends the definition of reflection to include any portion of incident energy that is not transmitted through the sample to the detector and is not absorbed in the sample. Therefore, reflection is any non-absorbed energy that does not reach the receiver.

The research characterizes the sample-invariant complex-valued system clutter $\tilde{H}_{\text{clutter}}$ for the Teraview instrument. The characterization of the system clutter provides valuable information regarding the confidence of the extracted optical properties of the samples. There are three transmission mode instrument systems for which the system clutter is characterized: OSU internal, WSU internal, and WSU external transmission. The sample-invariant

system clutter characterizations are observed to be dependent on the value of the Num Scans setting. The research presents a total of six clutter characterizations based on combinations of system instrument and Num Scans setting. The six system configurations are provided in Table 4.4. The system clutter is determined using adjacently recorded air reference measurements for each of the six configurations. The adjacent air reference measurements are collected such that there is approximately one minute separating each reference measurement. The number of adjacent air reference measurements used to generate the clutter characterization of each system configuration is provided in the last column of Table 4.4.

Table 4.4) The configurations used to characterize the sample-invariant system clutter.

Instrument	**Mode**	**Num Scans**	**Number of Measurements**
OSU	Internal	100	90
WSU	Internal	100	40
WSU	External	1	20
WSU	External	10	20
WSU	External	100	30
WSU	External	1000	20

The procedure for generating the complex-valued system clutter characterizations $\tilde{H}_{\text{clutter}}$ only divides air reference measurements that are adjacent in time. The division of air reference measurements is performed using the complex-valued frequency domain signals and results in air-to-air transfer functions, one for each measurement. The air-to-air transfer functions

are bootstrapped because adjacent transfer functions have one air reference measurement in common. In the absence of system clutter, the air-to-air transfer function is trivial with a relative magnitude of unity and relative phase of zero. However, system measurement clutter is present in collections by the open-air Teraview instruments. Consequently, the measured air-to-air transfer function is nontrivial with a relative magnitude that is not unity and a relative phase that is not zero.

The system clutter is determined using air reference measurements collected with each system at each of the Num Scans values provided in Table 4.4. The result is a characterization of the signal clutter as a function of system and Num Scans values. The sample-invariant clutter estimate for the transmission power in the OSU internal transmission system at a Num Scans value of 100 is shown in Figure 4.18, and the sample-invariant clutter estimate for the transmission power in the WSU internal transmission system at a Num Scans value of 100 is shown in Figure 4.19. In Figure 4.18 and Figure 4.19, the blue circle markers are the average clutter power estimate and the vertical bars represent the uncertainty of the clutter power estimate.

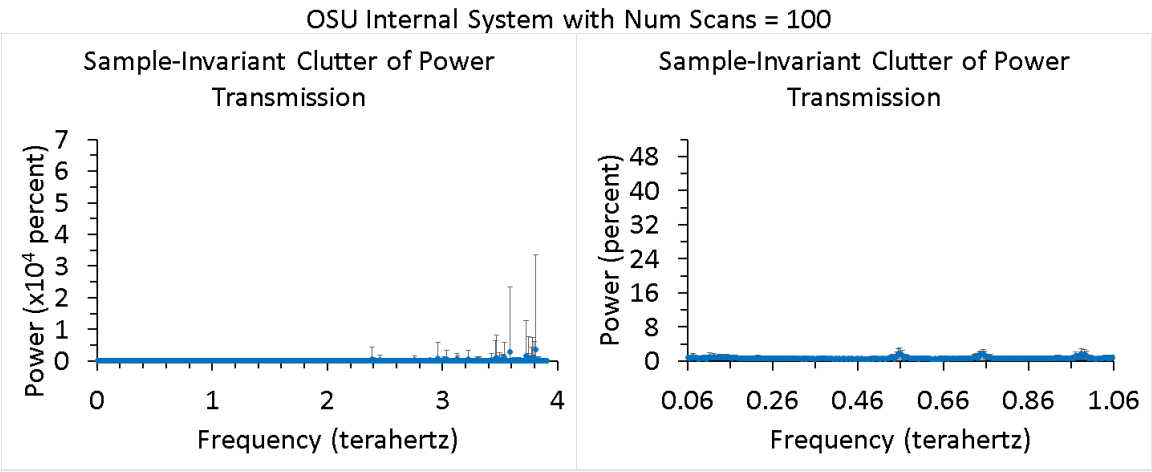

Figure 4.18) The sample-invariant measurement power clutter for the OSU internal transmission system using a Num Scans value of 100.

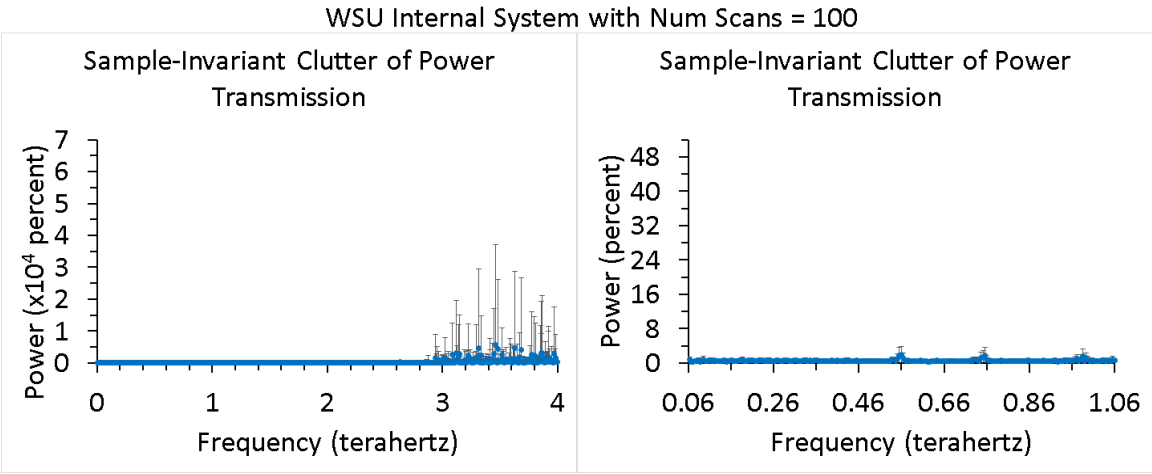

Figure 4.19) The sample-invariant measurement power clutter for the WSU internal transmission system using a Num Scans value of 100.

A comparison of Figure 4.18 and Figure 4.19 shows that the clutter power estimate uncertainty is more pronounced in the WSU internal system at frequencies greater than 3 THz compared with the OSU internal system. However, both the OSU and WSU internal system show qualitatively low clutter power estimates at frequencies less than 3 THz. The frequency range of 0–1 THz in Figure 4.18 and Figure 4.19 show that the average clutter power estimate is limited to a couple of percent in fractional power. There are three

features in the 0 – 1 THz frequency range with elevated clutter and these three regions coincide with water vapor absorption features. The elevated clutter at the three water vapor absorption features indicates that water vapor variation effects are a contribution to the clutter signal.

The sample-invariant clutter estimate for the transmission power in the WSU external transmission system at a Num Scans values of 1, 10, 100, and 1000 are shown in Figure 4.20, Figure 4.21, Figure 4.22, and Figure 4.23, respectively. In Figure 4.20, Figure 4.21, Figure 4.22, and Figure 4.23, the blue circle markers are the average clutter power estimate and the vertical bars represent the uncertainty of the clutter power estimate. The clearest observation in the WSU external system clutter power estimate is that the clutter decreases with increasing Num Scans values. The decrease in clutter corresponds to a sample-invariant increase in the measurement bandwidth. Therefore, larger Num Scans values will result in a larger effective system-dependent measurement bandwidth.

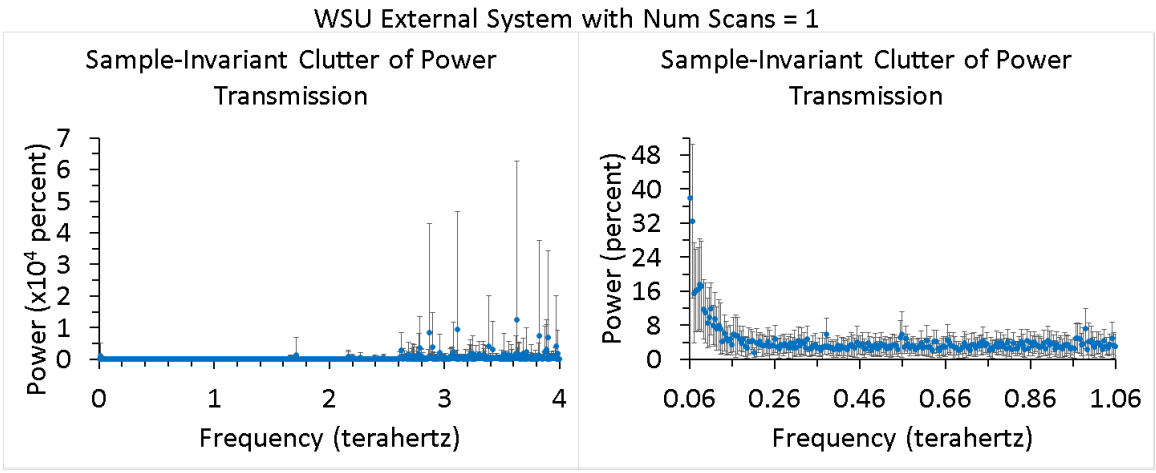

Figure 4.20) The sample-invariant measurement power clutter for the WSU external transmission system using a Num Scans value of 1.

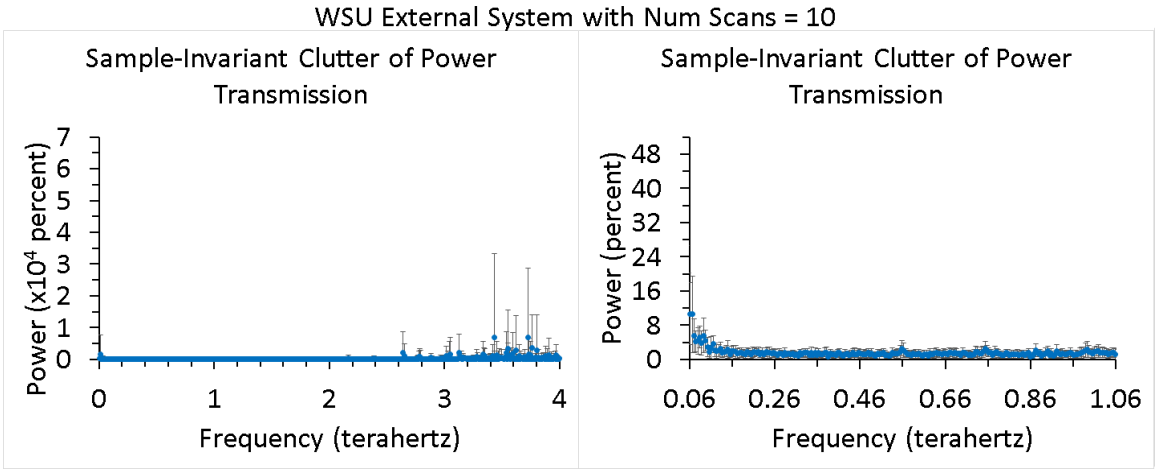

Figure 4.21) The sample-invariant measurement power clutter for the WSU external transmission system using a Num Scans value of 10.

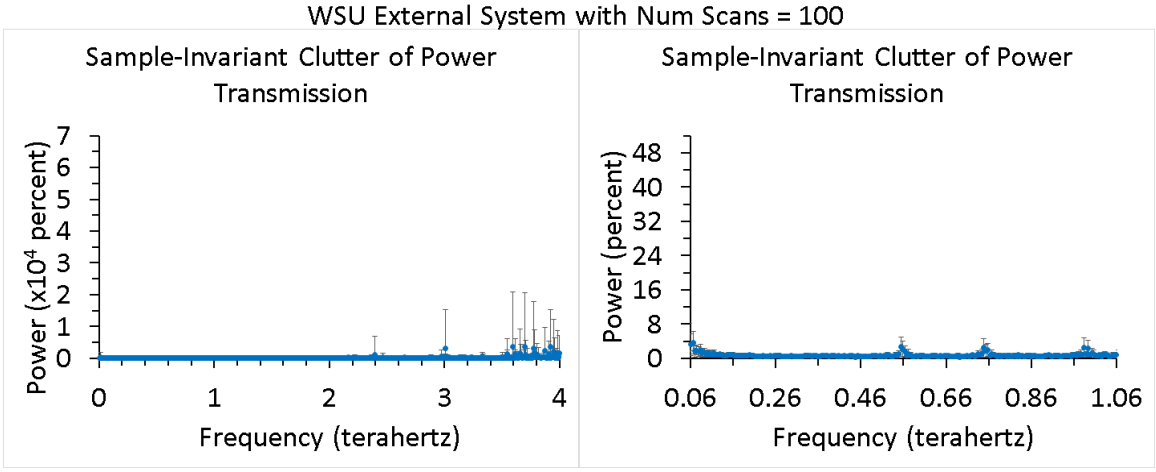

Figure 4.22) The sample-invariant measurement power clutter for the WSU external transmission system using a Num Scans value of 100.

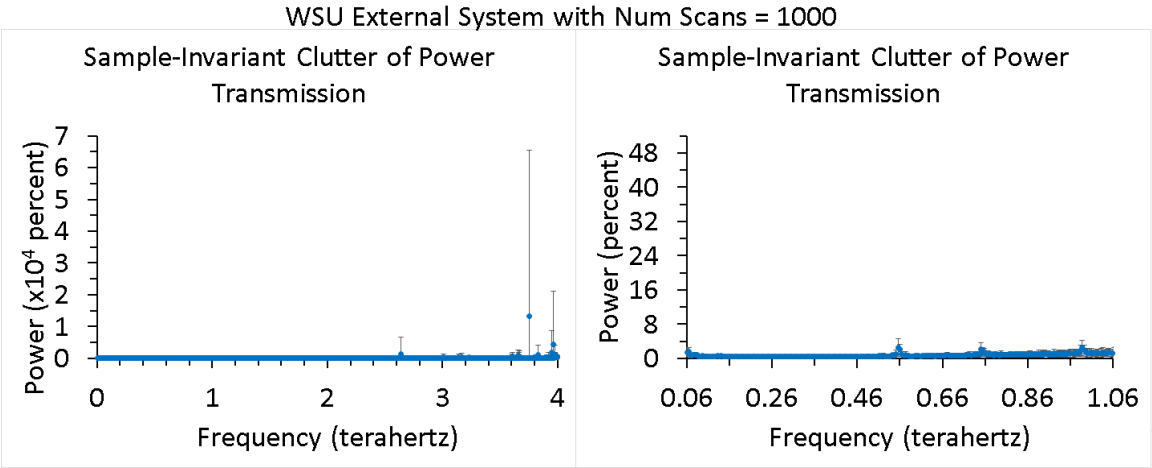

Figure 4.23) The sample-invariant measurement power clutter for the WSU external transmission system using a Num Scans value of 1000.

The power clutter estimated from the transmission through air results in a limit on the optimization algorithm to extract the optical properties of samples. The limit is a function of the thickness, optical absorption, and refractive index of the materials in the sample. The implication for samples with low attenuation and little reflection, most noticeably in the HDPE-C sample which has a small refractive index and low optical absorption, is that there are frequency regions in the transfer function magnitude transmission profile where the transmission is greater than unity which implies positive gain. However, HDPE is not a positive gain material. Although the HRSi sample is three-times less thick and six-times less optically absorptive than the HDPE-C sample, the HRSi is a high-index material which causes strong reflections at the interfaces. The high refractive index of HRSi sufficiently decreases the transmitted energy to the receiver that absorption coefficient extraction is not as problematic, compared to the HDPE-C absorption

coefficient extraction. The threshold limit required for unambiguous absorption coefficient extraction is defined in Equation 4.4. In Equation 6.3, $\frac{R^2(\nu)}{E^2(\nu)}$ and $\frac{A^2(\nu)}{E^2(\nu)}$ are the fractional percent total reflection and absorption, respectively. The term $(|\tilde{H}_{\text{clutter}}(\nu)|)^2$ in Equation 4.4 is the transmission measurement-derived, frequency-dependent and system-dependent, fractional percent system clutter.

$$(\frac{R^2(\nu)}{E^2(\nu)}+\frac{A^2(\nu)}{E^2(\nu)}) > (|\tilde{H}_{\text{clutter}}(\nu)|)^2 \qquad 4.4$$

The inequality defined in Equation 4.4 is used to theoretically determine if a sample is above or below the threshold limit based on the clutter power estimate as a function of frequency. The evaluation results are presented graphically in Figure 4.24 and Figure 4.25. Figure 4.24 corresponds to the evaluation at a frequency of 60 GHz, and Figure 4.25 corresponds to the evaluation at a frequency of 1.06 THz. The dark blue bars in Figure 4.24 and 4.25 represent the average clutter power estimate $(|\tilde{H}_{\text{clutter}}(\nu)|)^2$ at the evaluation frequency. The light blue bars in Figure 4.24 and Figure 4.25 represent the uncertainty of the clutter power estimate at the evaluation frequency. Five system configurations are examined. The systems are labelled in blue text in Figure 4.24 and Figure 4.25 as: OSU internal 100, WSU internal 100, WSU external 10, WSU external 100, and WSU external 1000. The

number trailing the system name designation is the Num Scans value. Four samples are included in the evaluation. The samples are labelled in black text in Figure 4.24 and 4.25 as: HDPE-C, HDPE-A, HDPE-B, and HRSi. The thicknesses used to generate the theoretical quantity $(\frac{R^2(\nu)}{E^2(\nu)} + \frac{A^2(\nu)}{E^2(\nu)})$ for HDPE-C, HDPE-A, HDPE-B, and HRSi are 1600 μm, 3000 μm, 6000 μm, and 500 μm, respectively. The complex refractive index used to generate the theoretical quantity $(\frac{R^2(\nu)}{E^2(\nu)} + \frac{A^2(\nu)}{E^2(\nu)})$ for HDPE and HRSi are $\tilde{n}_{\mathrm{HDPE}} = (1.6 - 0.00064)$ and $\tilde{n}_{\mathrm{HRSi}} = (3.5 - 0.00012)$, respectively. The red and green bars in Figure 4.24 and Figure 4.25 represent the non-transmitted fractional power quantity $(\frac{R^2(\nu)}{E^2(\nu)} + \frac{A^2(\nu)}{E^2(\nu)})$ for each of the four samples at the evaluation frequency. The red bars are used to indicate that the non-transmitted power from the sample is less than the clutter power estimate plus the uncertainty, and the green bars are used to indicate that the non-transmitted power from the sample is greater than the clutter power estimate plus uncertainty. The research hypothesizes that samples with non-transmitted power less than the clutter will have degraded confidence in the absorption coefficient extracted by the optimization at the evaluation frequency.

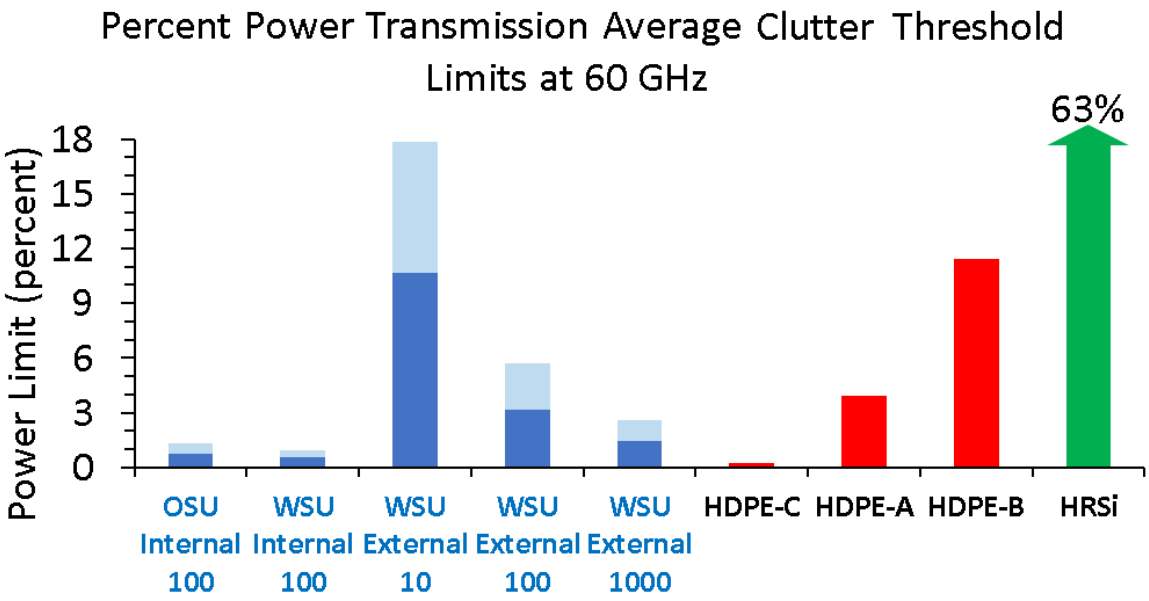

Figure 4.24) The transmission measurement power clutter threshold limit at a frequency of 60 GHz.

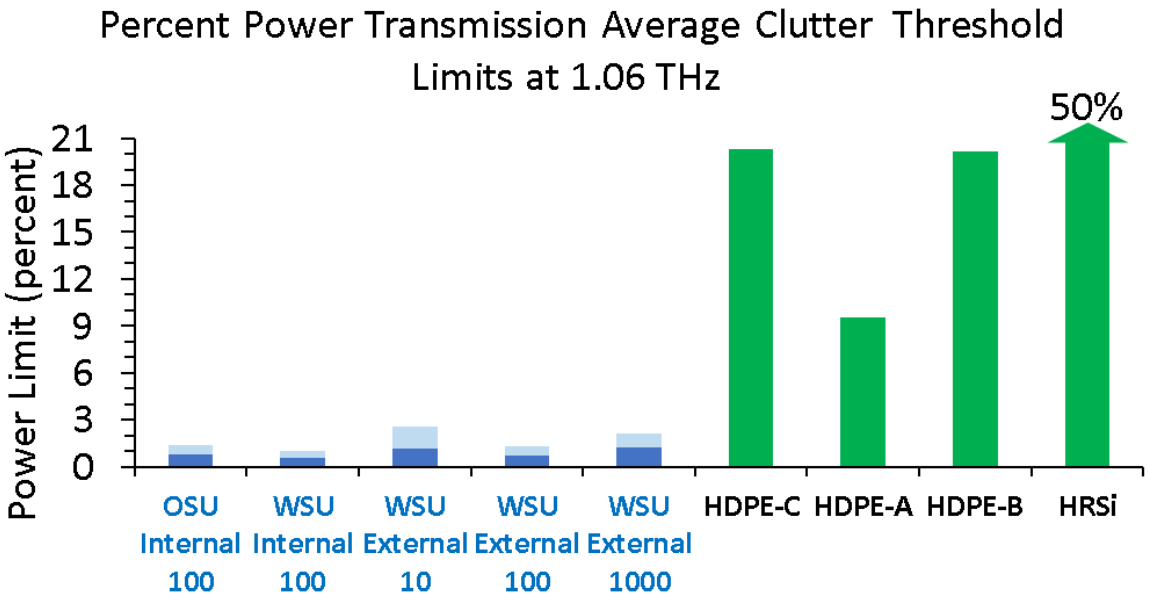

Figure 4.25) The transmission measurement power clutter threshold limit at a frequency of 1.06 THz.

There are two components to the frequency-domain phasor representation of the measured signal clutter. The first component is the clutter power which is derived from the spectral magnitude. The spectral magnitude of the sample-invariant clutter signal is used, in combination with

the sample and reference measurement spectral magnitude, to compute the signal-to-clutter ratio (SCR). The measured spectral magnitude of the sample and reference are labelled $|\tilde{Y}_{\text{sample}}|$ and $|\tilde{Y}_{\text{reference}}|$, respectively. The sample transmission transfer function is labelled $|\tilde{H}_{\text{sample}}(\nu)|$. The SCR as a function of frequency ν, defined in Equation 4.5, is essentially the measured transfer function spectral magnitude divided by the positive square root of the clutter power. Therefore, the SCR is inevitably a sample-dependent, system-dependent, quantity.

$$\text{SCR}(\nu) = \frac{\left(\frac{|\tilde{Y}_{\text{sample}}|}{|\tilde{Y}_{\text{reference}}|}\right)}{|\tilde{H}_{\text{clutter}}(\nu)|} = \frac{|\tilde{H}_{\text{sample}}(\nu)|}{|\tilde{H}_{\text{clutter}}(\nu)|} \tag{4.5}$$

The second component to system clutter is the phase clutter. The phase clutter is a characterization of the variation due to clutter in the phase of the measurement. Whereas the power clutter largely impacts the absorption coefficient extraction of a sample, the phase clutter largely impacts the refractive index extraction of a sample. The phase clutter is characterized for the following six systems: OSU internal using Num Scans of 100, WSU internal using Num Scans of 100, WSU external using Num Scans of 1, WSU external using Num Scans of 10, WSU external using Num Scans of 100, and WSU external using Num Scans of 1000.

The phase clutter $\angle\tilde{H}_{\text{clutter}}$ for a Num Scans value of 100 using the OSU internal and WSU internal systems are shown in Figure 4.26. The blue circle markers in Figure 4.26 are the average phase clutter estimates, and the vertical bars are the uncertainty of the estimate. The phase clutter plots shown in Figure 4.26 demonstrates that phase clutter limits the effective phase bandwidth to 2.5 THz for the internal transmission systems at Num Scans of 100. The side-by-side comparison in Figure 4.26 further demonstrates that the WSU internal transmission system has more phase clutter compared with the OSU internal transmission system for frequencies greater than 2.5 THz.

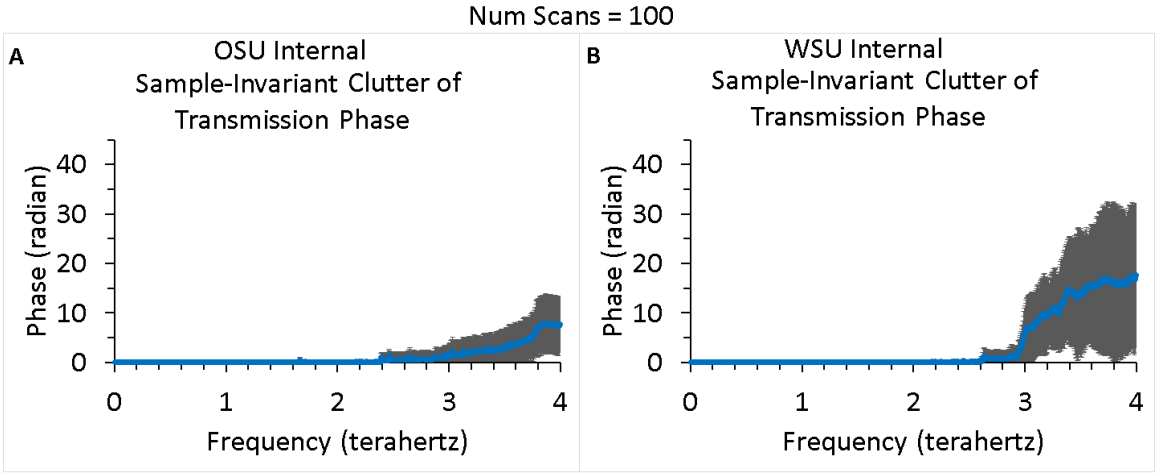

Figure 4.26) The system-dependent, sample-invariant, measurement phase clutter for the OSU (left) and WSU (right) internal transmission systems using a Num Scans value of 100.

The phase clutter for the WSU external transmission system is shown in Figure 4.27. Plots A, B, C, and D in Figure 4.27 correspond to Num Scans values of 1, 10, 100, and 1000, respectively. The blue circle markers in Figure 4.27 are the average phase clutter estimates, and the vertical bars are the

uncertainty of the estimate. The phase clutter plots shown in Figure 4.27 demonstrates the dependence of the phase clutter on the number of scans that are averaged. The smallest bandwidth of Figure 4.27 is approximately 1.5 THz and corresponds to plot A which is the WSU external system with a Num Scans value of 1. The largest bandwidth of Figure 4.27 is approximately 3.0 THz and corresponds to plot D which is the WSU external system with a Num Scans value of 1000. The analysis of Figure 4.27 demonstrates that the phase clutter decreases with increasing Num Scans value and that the clutter-limited bandwidth improves with increasing Num Scans value.

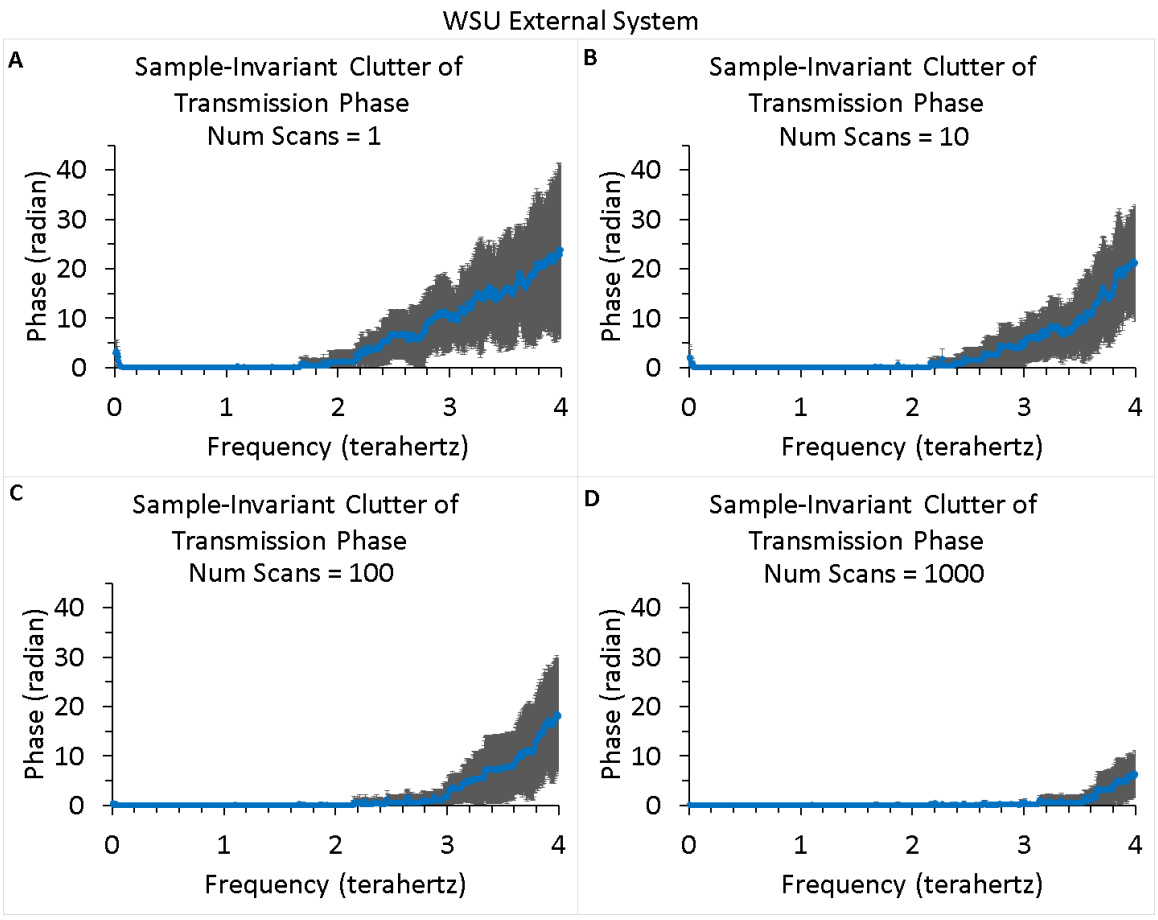

Figure 4.27) The sample-invariant, measurement phase clutter for the WSU external transmission system using a Num Scans value of 1 (plot A), 10 (plot B), 100 (plot C), and 1000 (plot D).

Both the power clutter and phase clutter is shown to decrease with increasing values of the Num Scans setting. The value of the Num Scans setting is essentially the number of measurement scans that are averaged together. The clutter analysis shows that decreasing the clutter extends the effective sample-invariant measurement bandwidth. The clutter analysis indicates that the clutter-limited sample-invariant phase bandwidth is not the same as the clutter-limited sample-invariant power bandwidth. A comparison of the clutter-limited sample-invariant power bandwidth to phase bandwidth

indicates that the phase bandwidth is typically less than the power bandwidth. The clutter analysis also quantifies a sample-dependent criterion, based on energy conservation, to predict the confidence of optical parameter extractions. The sample-dependent power analysis indicates that of the three HDPE and one HRSi samples measured in the research, the HDPE-C sample has the highest transmission. Consequently, the HDPE-C sample has a non-transmitted energy that is within the measurement clutter. Samples at frequencies for which the non-transmitted energy is within the measurement clutter have degraded confidence in the optical property extraction results.

4.6.3 TERAHERTZ BEAM CHARACTERIZATION

The beam profile of the THz light pulses is characterized theoretically. The beam profile is modelled as a Gaussian beam and the Gaussian beam equations employed are a result of the paraxial approximation [46]. The characterization of the beam profile along the optical axis of the instrument facilitates an understanding of the behavior of the plane wave theoretical physics model implemented in the research compared with Gaussian beam optics. The analysis contained in this section assumes that the focal point of the beam collocated with the surface of the sample closest to the transmitter and that the samples are oriented normal to the incident radiation. First, the

minimum beam radius r_0 is obtained at the focal point using the diffraction limited spot size for the first zero point of an Airy disk. The beam radius r_0 at the focal point is a function of radiation wavelength λ and f-number f_N of the lens. The transmitter and receiver focusing lenses of the external antenna functionality of the Teraview system are plano-convex in shape, have a focal length of 50 millimeters (mm), and f-number f_N equal to 2. The parameters that depend on the minimum beam radius are shown in Figure 4.28.

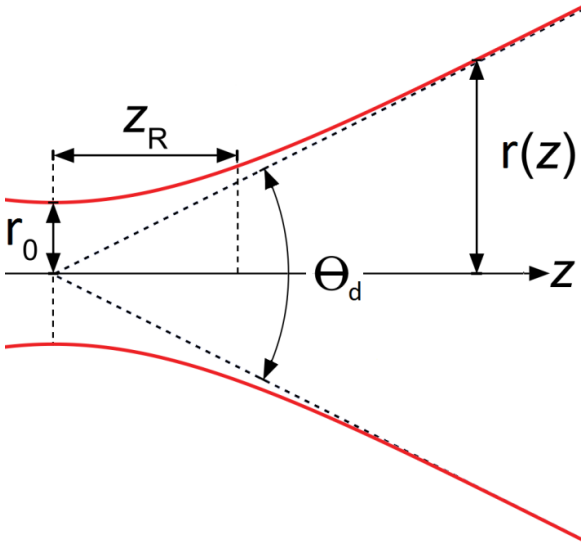

Figure 4.28) The Rayleigh length Z_R, angular beam divergence θ_d, and beam radius $r(z)$ are calculated from the minimum beam radius r_0.

The beam radius at the focal point r_0, Rayleigh length Z_R, confocal distance Z_c, beam radius as a function of distance along the focal point $r(z)$, beam divergence θ_d, radial beam divergence θ_r, Gaussian beam phase shift ϕ_z, radius of Gaussian beam curvature R_z, and radial phase variation ϕ_r relative to a plane for a fixed value of z as a function of $r(z)$, are calculated

using Equations 4.6–4.14 [47, 48]. The radial beam divergence is also called the asymptotic beam growth angle, and the Gaussian beam phase shift is also called the Gouy phase shift. The beam divergence and radial beam divergence equations are valid in the far-field limit defined as $z \gg Z_R$.

$$r_0 = 1.22 \cdot \lambda \cdot f_N \tag{4.6}$$

$$Z_R = \frac{\pi \cdot {r_0}^2}{\lambda} \tag{4.7}$$

$$Z_c = 2 \cdot Z_R \tag{4.8}$$

$$r(z) = r_0 \sqrt{1 + (\frac{z}{Z_R})^2} \tag{4.9}$$

$$\theta_d = 2\frac{r_0}{Z_R} \tag{4.10}$$

$$\theta_r = \frac{\theta_d}{2} \tag{4.11}$$

$$\phi_z = \tan^{-1}(\frac{z}{Z_R}) \tag{4.12}$$

$$R_z = z + \frac{{Z_R}^2}{z} \tag{4.13}$$

$$\phi_r \cong \frac{\pi \cdot r^2}{\lambda \cdot R_z} \tag{4.14}$$

The Rayleigh length is the distance, along direction of beam propagation, from the focal point to the position along the optical axis where the minimum spot size radius r_0 is doubled. The beam divergence is the angular increase in beam diameter with increasing distance from the focal point location. Figure 4.29 depicts the minimum beam radius and Rayleigh length as a function of wavelength and frequency for the external Teraview system with $f_N = 2$. The analysis of plot A and plot B in Figure 4.29 shows

that the beam radius at the focal point increases linearly with increasing radiation wavelength. The analysis of plot C and plot D in Figure 4.29 shows that the Rayleigh length also increases linearly with increasing wavelength.

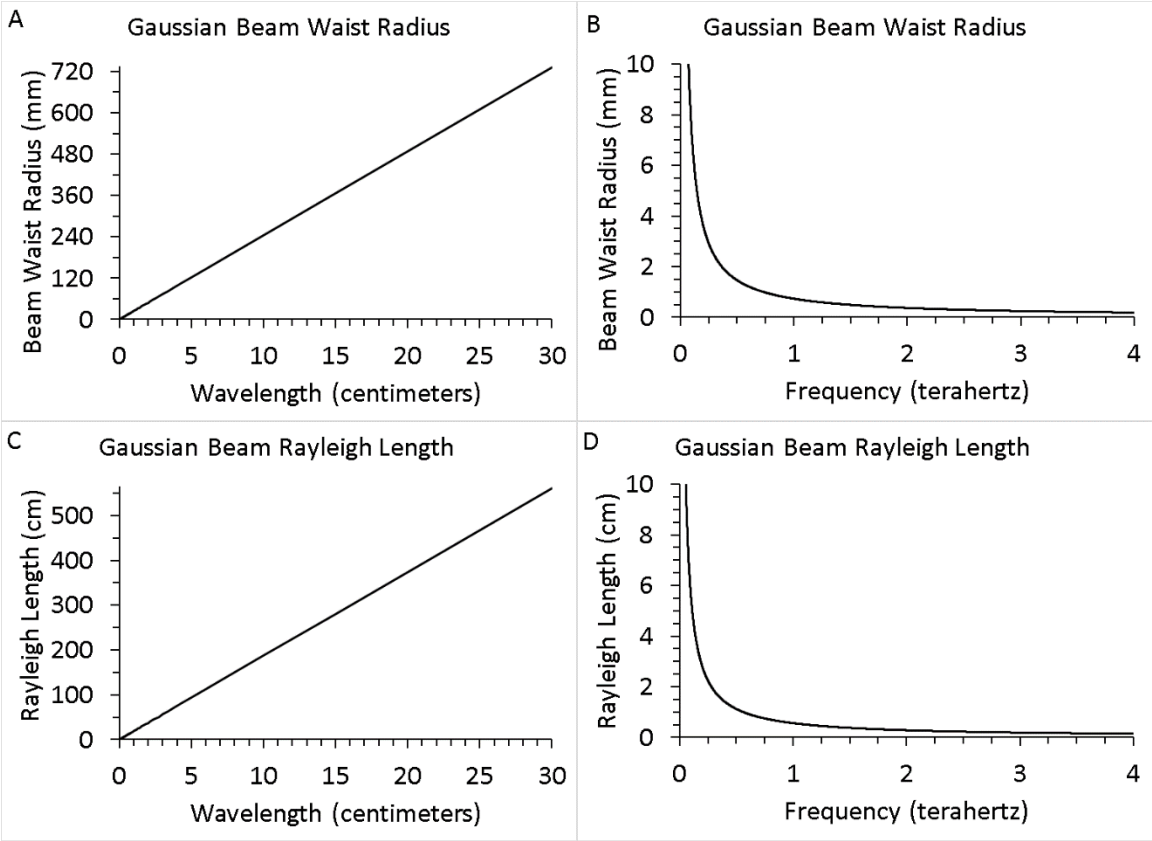

Figure 4.29) The top row is the beam radius at the focal point with the beam profile modeled as an Airy disk (plots A, B). The bottom row is the Rayleigh length (plots C, D).

An important observation in the Rayleigh length plots in Figure 4.29 are the locations along the y-axis of the sample thicknesses measured in the research. Specifically, the single-layer HDPE-C, HDPE-A, and HDPE-B samples have approximate thicknesses of 0.16 cm, 0.30 cm, and 0.60 cm. Therefore, the Rayleigh length is exceeded for the HDPE-C, HDPE-A, and HDPE-B samples at frequencies greater than 3.5 THz, 1.9 THz, and 0.9 THz,

respectively. The simple analysis assumes direct transmission through the sample at the surface of the sample closest to the receiver. In particular, the HDPE-B sample results in a beam spot size surface area at the transmission exit surface that is less than twice the area at the beam waist for only 1 THz of bandwidth. In contrast, the least thick sample is HRSi which for all intents and purposes does not exceed the Rayleigh length within the bandwidth of the system. A dramatic example is the HDPE-A|Air|HDPE-A sample stack which is approximately 3.14 cm thick. The HDPE-A|Air|HDPE-A sample exceeds the Rayleigh length at frequencies greater than 0.18 THz, which means the Rayleigh length is exceeded for nearly the entire bandwidth of the system. The result is that the plane wave theoretical physics model used in the research becomes less accurate for thicker samples.

The Gaussian beam radius $r(z)$, Gaussian beam Gouy phase shift ϕ_z, and radius of Gaussian beam curvature R_z, are shown in plots A, B, and C of Figure 4.30, respectively. The plot lines in Figure 4.30 are color coded, with each color denoting a specific frequency of radiation. The lines in plot A of Figure 4.30 show that the beam radius increases with decreasing frequency, but increases with increasing distance from the focal point. The beam radius plotted in Figure 4.30 approaches an asymptote in the far-field. In the far-field, the asymptote is characterized by the radial beam divergence which

simplifies to $\theta_r = \frac{1}{1.22 \cdot \pi \cdot f_N}$. Numerically, with $f_N = 2$, the radial beam divergence is $\theta_r \cong 7.5°$. The lines in plot B of Figure 4.30 show that the Gouy phase shift increases with increasing frequency, and also increases with increasing distance from the focal point. The frequency of 0.5 THz is located near the peak frequency-domain signal intensity of the measurement data. At a frequency of 0.5 THz, the Gouy phase shift at the direct transmission exit surface for the HRSi, HDPE-C, HDPE-A, and HDPE-B samples is approximately 2.6°, 8.1°, 15.0°, and 28.1°, respectively. In comparison, the phase shift for a plane wave is 0°. The plot lines in plot C of Figure 4.30 show that the Gaussian beam radius of curvature increases with decreasing frequency, but decreases with increasing distance from the focal point.

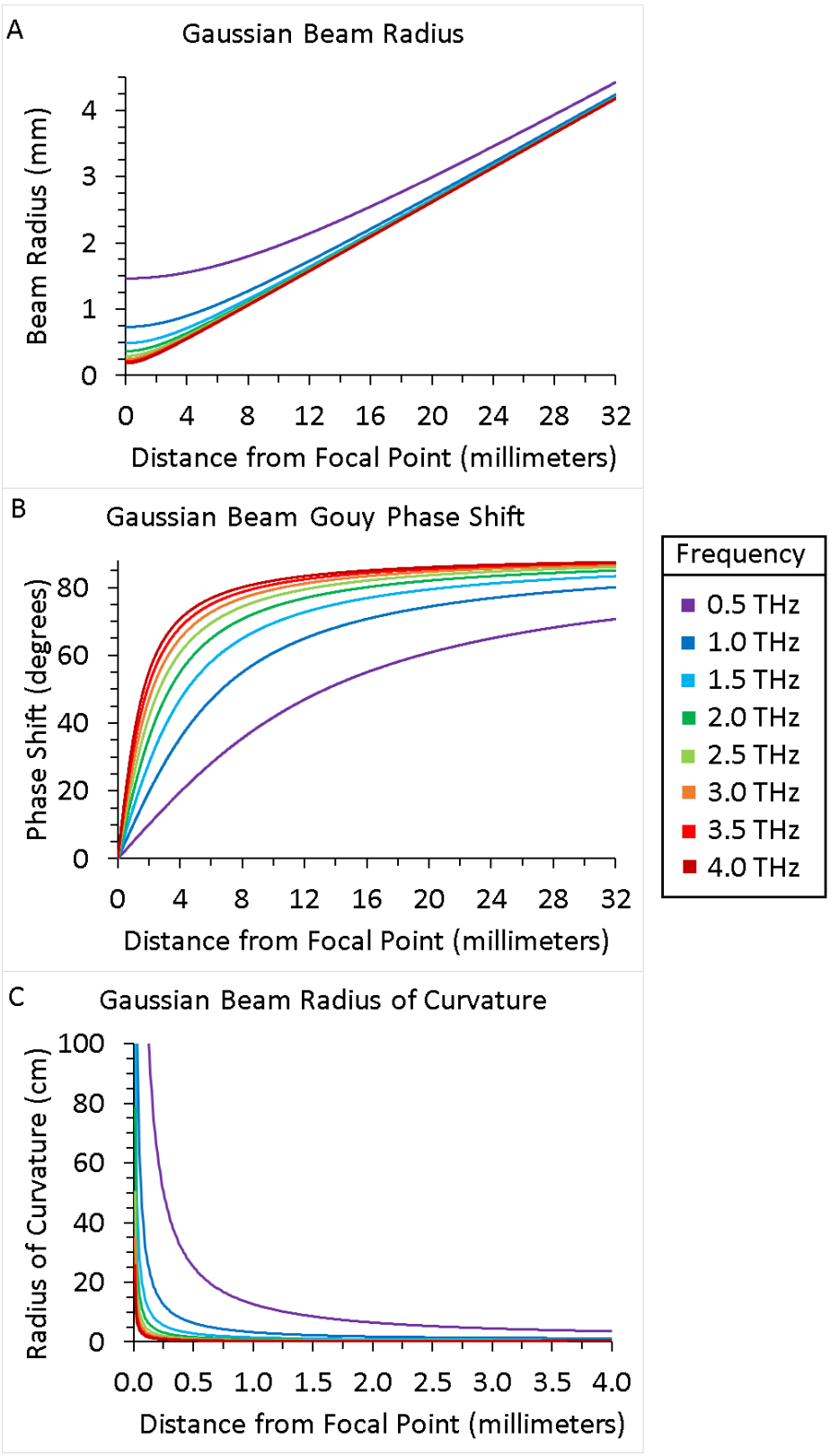

Figure 4.30) The THz beam radius (plot A), Gouy phase shift (plot B), and beam radius of curvature (plot C) as a function of distance from the focal point and frequency of radiation.

The radial phase variation ϕ_r is analyzed to determine the approximate radial phase variation at the minimum beam radius, and the maximum radial phase variation. The minimum beam radius is the radius of the beam at the focal point. The maximum radial phase variation occurs at the beam perimeter along the radial angular divergence angle. The phase variation at the minimum beam radius along the optical axis is shown in the left-most plot of Figure 4.31. The maximum phase variation at the beam perimeter along the optical axis is shown in the right-most plot of Figure 4.31. The colored lines in the plots of Figure 4.31 are the phase variation at different frequencies. The maximum phase variation increases with increasing distance from the focal point, and also increases with decreasing frequency.

The frequency of 0.5 THz is located near the peak frequency-domain signal intensity of the measurement data. At a frequency of 0.5 THz, the radial phase variation along the beam waist radius and the maximum phase variation are approximately the same. The phase variation for both radii at the direct transmission exit surface for the HRSi, HDPE-C, HDPE-A, and HDPE-B samples is approximately 0.26°, 0.82°, 1.53°, and 3.06°, respectively. However, at a frequency of 4.0 THz, the maximum radial phase variation at the direct transmission exit surface for the HRSi, HDPE-C, HDPE-A, and

HDPE-B samples is approximately 2.0°, 6.5°, 12.3°, and 24.5°, respectively. In comparison, the phase variation for a plane wave is 0°.

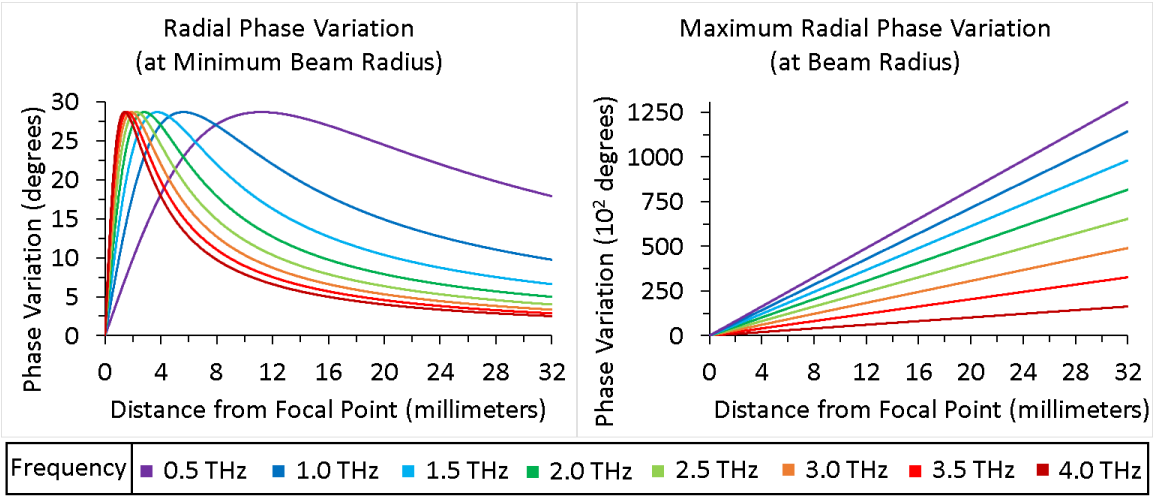

Figure 4.31) The THz beam radius changes with both frequency of radiation and distance from the focal point. The beam divergence causes the beam spot size to increase further from the focal point.

An important aspect of beam diffraction is that the radius at a fixed distance from the focal point changes with different frequencies. The external system lens aperture used in this thesis is a circular lens with a radius of 3.1 cm that is symmetrically cropped horizontally to 2.5 cm. The presence of the sample in the optical path changes the beam diameter along the optical path length compared with a reference measurement. As a result, the distribution of radiation energy that arrives at the hemispherical silicon dome on the receiver is different between the sample and reference measurement. The difference of the beam distribution at the receiver creates two effects between the sample and reference measurement. First, a path length difference is

created in air between the reference and sample radiation and the path length difference is frequency-dependent. Secondly, the difference in radiation distribution alters the proportion of energy that is reflected and transmitted along the curve of the silicon dome proportional to the fraction of energy at the incidence angle with the dome.

4.6.4. PARTICULATE SCATTERING

The Lactose, pharmaceutical-grade Oxycodone, and Hydrocodone powder samples are composed of particulate matter. The study of THz frequency radiation with powder samples is extensively studied [49, 50]. Particulates cause incident radiation to scatter depending on the size of the particulates and the wavelength of incident radiation. The scattering impacts the perceived absorption property of the powder samples results. The impact of scattering on the total sample absorption is defined in Equation 4.15, where α_{total} is the total attenuation coefficient of the sample [51]. The total attenuation coefficient of the sample is comprised of two components, the pure absorption $\alpha_{\text{absorption}}$ and scattered absorption α_{scatter}. Therefore, scattering must be considered for powder samples to correctly determine the pure absorption component of the total sample attenuation.

$$\alpha_{\text{total}} = \alpha_{\text{absorption}} + \alpha_{\text{scatter}} \quad 4.15$$

The Mie scattering theory is used to calculate the scattering [52]. A scattering regime factor defined in Equation 4.16 is used to determine the appropriate scattering regime, where x is the regime factor, r is the radius of the scatterer, and λ is the wavelength of light. The scattering regime considered for this research is when the particulates sizes are much smaller than the wavelength of the incident radiation, in which case $x \ll 1$ and the scattering regime is called Rayleigh scattering. The Rayleigh scattering approximation assumes elastic scattering by spheres. The Rayleigh regime enables use of the Rayleigh scattering cross-section defined in Equation 4.17, where σ_{rayleigh} is the scattering cross-section, n_{air} is the refractive index of air, and n is the refractive index of the powder sample [53]. The salient feature of the Rayleigh scattering cross-section is the dependence of the scattering cross-section on $\frac{r^6}{\lambda^4}$, which implies that shorter wavelengths, and therefore higher frequencies, are scattered more strongly for constant particulate size.

$$x = \frac{2 \cdot \pi \cdot r}{\lambda} \tag{4.16}$$

$$\sigma_{\text{rayleigh}} = \frac{8 \cdot \pi \cdot r^6}{3} \left(\frac{2 \cdot \pi \cdot n_{\text{air}}}{\lambda}\right)^4 \left(\frac{n^2 - {n_{\text{air}}}^2}{n^2 + 2 \cdot {n_{\text{air}}}^2}\right)^2 \tag{4.17}$$

The Rayleigh scattering is examined for Lactose to determine the strength of the scattering as a function of frequency and particulate size. Sizes of general purpose Lactose particulates can vary from 1–1000 μm, although

pharmaceutical-grade Lactose particulate sizes are typically $1\ \mu m < r < 10\ \mu m$ [54, 55, 56, 57]. The Rayleigh scattering cross-section σ_{rayleigh} is shown in plot A and plot B of Figure 4.32, and the scattering regime factor x is shown in plot C and plot D. Analysis of the scattering regime factor shows the Rayleigh scattering approximation is decreasingly valid for particulates with a radius greater than 6 μm, within the 4 THz operational bandwidth of the transmission system. Therefore, the research concludes that the scattering of THz radiation in the Lactose samples is best described by Mie scattering if the Lactose particulates are larger than 6 μm, and by Rayleigh scattering if the Lactose particulates are less than 6 μm. By extension, the research hypothesizes that the scattering occurring in the pharmaceutical-grade Oxycodone and Hydrocodone samples follows similar guidelines.

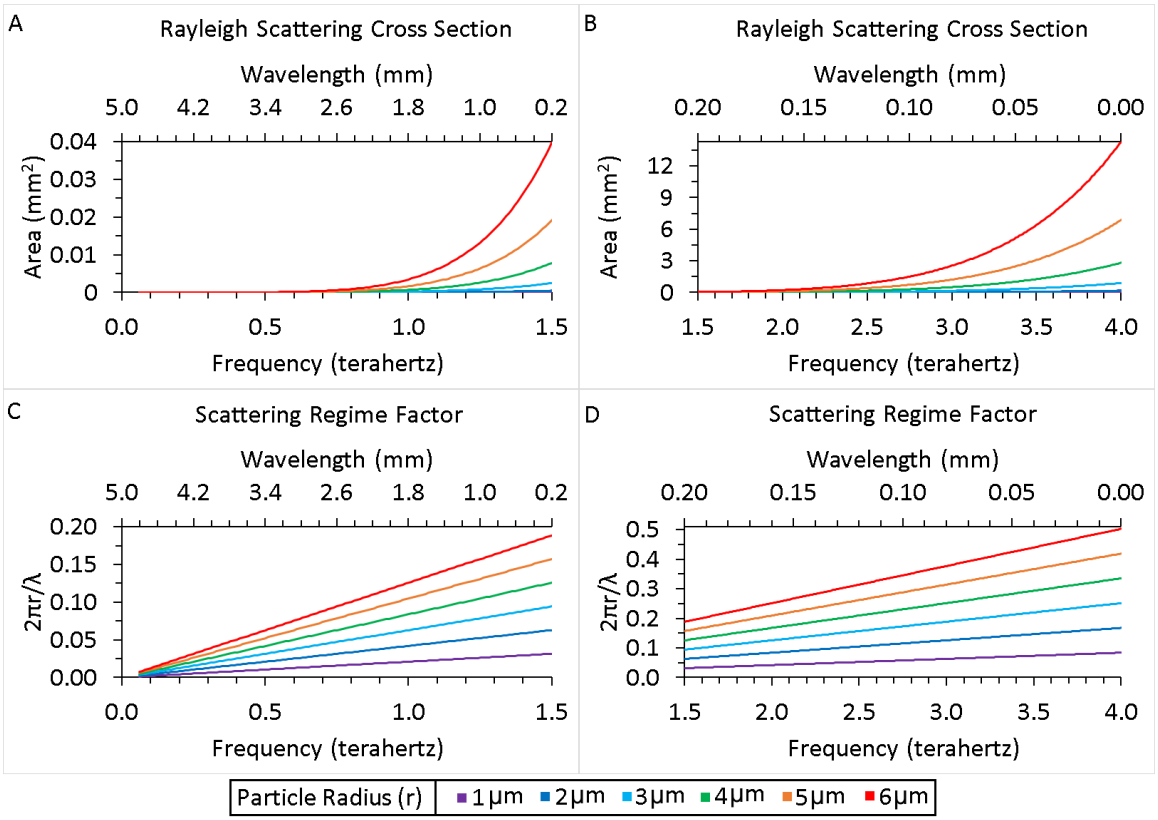

Figure 4.32) The Rayleigh scattering cross-section (plots A–B), and scattering regime factor (plots C–D) for six scattering particle radii.

The research developed a rudimentary approach to remove the scattered absorption α_{scatter} component from the total attenuation coefficient. The approach partially leverages a published concept which seeks to produce a minimum baseline slope in the profile of the pure absorption coefficient [58]. The approach implemented in this research computes a linear hull underneath each absorption feature for the Lactose, pharmaceutical-grade Oxycodone, and Hydrocodone samples. The linear hull is a local correction that is unique to each absorption feature. The linear hull is computed at the onset of each absorption feature and terminates at the end of each feature. The result of the

baseline hull correction is an absorption feature that has the local scattering contribution removed from the absorption. The correction enables more accurate reporting of peak absorption feature center frequency and absorption feature width.

4.6.5. KRAMERS-KRONIG TRANSFORMATION

The Kramers-Kronig Transformation (KKT) for continuous variables defined in Section 3.6 is an integration over an infinite frequency space. However, the THz-TDS measurement data are discrete variables with a finite range of frequencies. Therefore, the integration bounds for the KKT integral must be restricted to the operational bandwidth of the THz-TDS measurement data. The Kramers-Kronig relationship defined in Equation 3.73 of Section 3.6 is rewritten and rearranged in Equation 4.18 to emphasize the impact of the finite frequency range restriction, and how the extinction coefficient κ is treated at frequencies outside of the operational bandwidth. The lower and upper cutoff frequency of the operational bandwidth are labelled as ν_{lr} and ν_{ur}, respectively.

$$n(\nu) = n_{\infty} + \frac{2}{\pi}\int_{0}^{\nu_{\mathrm{lr}}} \frac{\nu' \cdot \kappa(\nu')}{\nu'^{2} - \nu^{2}} d\nu' + \frac{2}{\pi}\int_{\nu_{\mathrm{lr}}}^{\nu_{\mathrm{ur}}} \frac{\nu' \cdot \kappa(\nu')}{\nu'^{2} - \nu^{2}} d\nu' + \frac{2}{\pi}\int_{\nu_{\mathrm{ur}}}^{\infty} \frac{\nu' \cdot \kappa(\nu')}{\nu'^{2} - \nu^{2}} d\nu' \tag{4.18}$$

$$= n_\infty + \frac{2}{\pi}\int_0^{\nu_{\mathrm{lr}}} \frac{\nu' \cdot 0}{\nu'^2 - \nu^2}\, d\nu' + \frac{2}{\pi}\int_{\nu_{\mathrm{lr}}}^{\nu_{\mathrm{ur}}} \frac{\nu' \cdot \kappa(\nu')}{\nu'^2 - \nu^2}\, d\nu'$$
$$+ \frac{2}{\pi}\int_{\nu_{\mathrm{ur}}}^{\infty} \frac{\nu' \cdot 0}{\nu'^2 - \nu^2}\, d\nu'$$
$$= n_\infty + \frac{2}{\pi}\int_{\nu_{\mathrm{lr}}}^{\nu_{\mathrm{ur}}} \frac{\nu' \cdot \kappa(\nu')}{\nu'^2 - \nu^2}\, d\nu'$$

The discrete form of the KKT is computed using the discrete Hilbert transform. The discrete Hilbert transform is implemented using the scipy.signal.hilbert function in the SciPy library of Python [59]. The imaginary part of the complex conjugate of the discrete Hilbert transform is used to determine the integral terms of Equation 4.18. The refractive index offset n_∞ is a constant that calibrates the spectral profile generated by the Hilbert transform. The research computes the refractive index calibration offset n_∞ as the difference between the average optimized refractive index and non-calibrated Hilbert transform across all evaluation frequencies for the material being analyzed.

The impact on the refractive index by applying Equation 4.18 to the Kramers-Kronig relationship is determined using a water vapor absorption profile. The water vapor absorption profiles are shown in Figure 4.33 for two different percentages of water vapor content. The top-right plot in Figure 4.33, plot B, is the water vapor absorption coefficient profile for 1% water vapor

content. The bottom-right plot in Figure 4.33, plot D, is the water vapor absorption coefficient profile for 100% water vapor content. The evaluation of the Kramers-Kronig relationship is performed using two different bandwidths with the two different water content percentages. The first evaluation uses the 1% water vapor absorption in a 1 THz bandwidth from 0–1 THz, and a 4 THz bandwidth from 0–4 THz. The second evaluation uses the 100% water vapor absorption in a 1 THz bandwidth from 0–1 THz, and a 4 THz bandwidth from 0–4 THz. The water vapor residual refractive index obtained using 1 THz and 4 THz bandwidth are colored green and red, respectively, in Figure 4.33. The residual refractive index tends about the zero line of the y-axis because the residual refractive index is defined as $n(\nu) - n_{\infty}$ to isolate the Hilbert transform behavior.

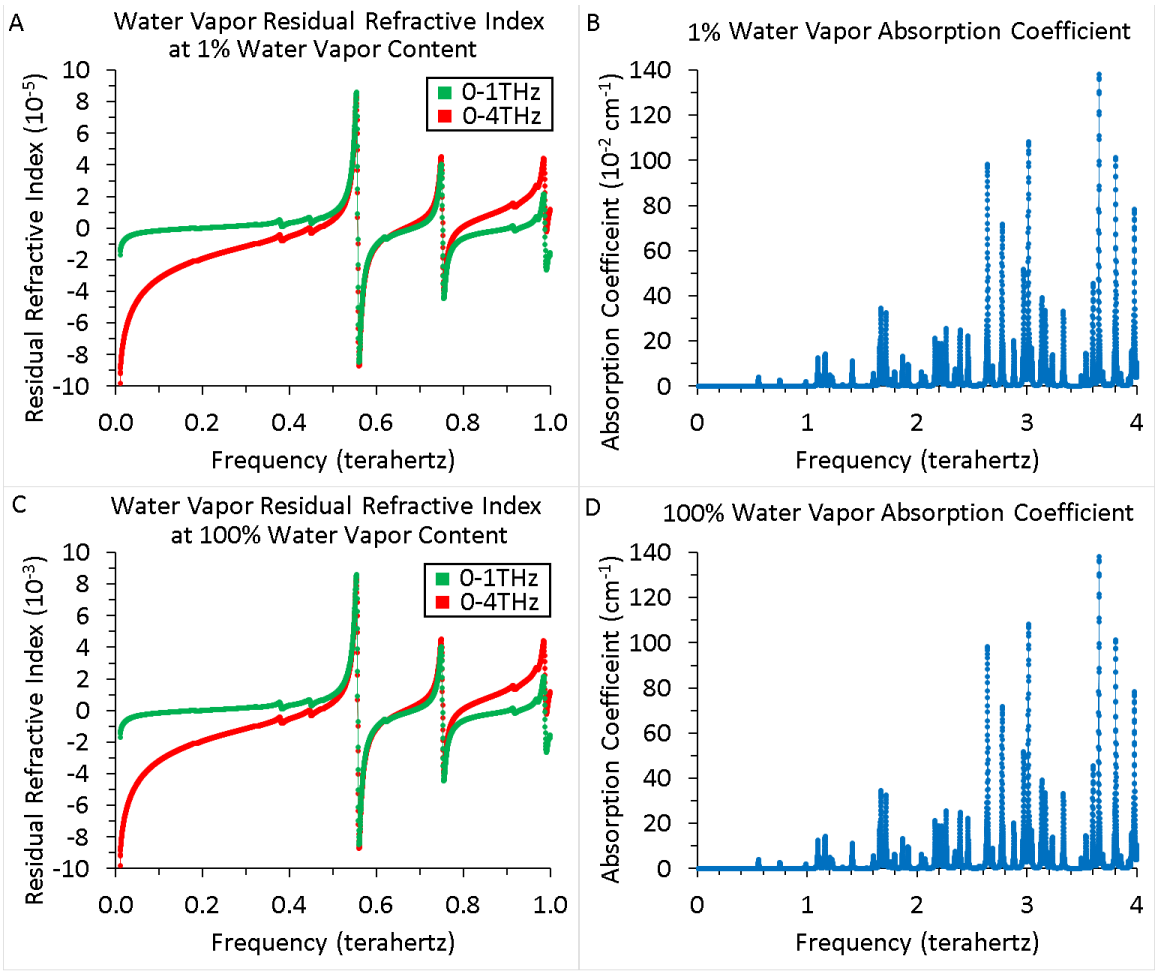

Figure 4.33) The refractive index of water vapor calculated from the Kramers-Kronig relationship using 1% water vapor content (top row, plots A and B), and 100% water vapor content (bottom row, plots C and D).

Analysis of the residual refractive index plots in Figure 4.33 show several important behaviors of the discrete KKT with respect to finite frequency spaces. First, the refractive index profile computed from the 1 THz bandwidth (green plot lines) is more horizontal than the 4 THz bandwidth (red plot lines) in Figure 4.33. Therefore, the inclusion of water vapor absorption features from 1–4 THz is observed to increase the variation in the refractive index. Furthermore, extending the operational bandwidth from 1 THz to 4

THz does not appear to affect the range of refractive index values at the frequencies of the dispersion induced inflection caused by the absorption features. However, extending the operational bandwidth from 1 THz to 4 THz does appear to cause an offset in the refractive index, most notably after the frequency of the 751 GHz absorption feature, after each refractive index nonlinearity within the operational bandwidth. Therefore, the research hypothesizes that absorption features located at frequencies outside of the operational bandwidth minimally impact nonlinearities in the refractive index located within the operational bandwidth. A comparison of plot A to plot C in Figure 4.33 shows the impact of the strength of the absorption features on the refractive index. Specifically, uniformly reducing the water vapor absorption coefficients by 99% results in a corresponding decrease in the refractive index profile range and variation. Therefore, the impact of using a finite instead infinite frequency space on the refractive index computed from the Kramers-Kronig relationship is a tendency to decrease the range and variation of the calculated refractive index. The water vapor absorption profile has numerous strong absorption features at frequencies greater than 1 THz. The research hypothesizes that the refractive index profiles calculated using the Kramers-Kronig relationship for materials with only several weak absorption features

outside the operational bandwidth will be minimally impacted by restricting the KKT frequency space to the operational bandwidth.

5. OPTIMIZATION PROCEDURE

The algorithm used to optimize the physical parameters is described in terms of the computational process and optimization processes. First, the parameters used in the algorithm are initialized and bounded. The parameters requiring initialization are frequency-dependent parameters and parameters requiring bounds are frequency-independent parameters. The frequency-dependent parameters are the index of refraction and absorption. The frequency-independent parameters are sample layer thickness, and the Yaw-Pitch-Roll (YPR) orientation of the sample surface relative to the incident radiation propagation vector. A discussion of the role of sample thickness during optimization is provided in Section 5.3, and a discussion of orientation is provided in Section 5.4. Although the incident radiation propagation vector remains constant for all sample measurements, the YPR of the sample will change at each incidence angle due to the manipulation of the mounting apparatus.

The index of refraction is typically initialized using TOF information between the peaks of the single-layer signal data and the single-layer thickness

as measured with the Vernier style Mitutoyo branded micrometer. The case of a multi-layer sample bootstraps the initialization of each layer to the corresponding single-layer initialization result. Once the optimization is started, the frequency-dependent initialization is updated based on the result of the optimization. The index of refraction of air is set to 1.00027 and this value remains constant for all frequencies throughout the optimization. The sample layer thickness is bounded using a buffer applied to the estimated layer thickness. The sample surface orientation is bounded using a buffer applied to the respective YPR angles recorded on the sample mounting stage.

After the parameter initializations and bounds have been defined, the core functionality of the algorithm begins. First, each signal is transformed from the time-domain into the frequency-domain using the Discrete Fourier Transform (DFT). The DFT is used instead of the Fast Fourier Transform (FFT) because the number of data points is not natively $N = 2^p$ where p is positive integer numbers. The use of DFT also avoids zero padding the time-domain data to satisfy the $N = 2^p$ FFT requirement for computation improvement from $2N^2$ to $2N\text{Log}_{10}N$ [60, 61]. The output of the DFT are complex-valued frequency-domain amplitudes and are further used to calculate the measured unwrapped phase and magnitude for each sample signal. The DE and BH only optimize the frequency-independent parameters,

however only the DE optimization parameters are subject to the frequency-independent bounds.

5.1. COMPUTATIONAL PROCESS

The computational process first involves processing the signal data to prepare it for treatment by the physical parameter extraction algorithmic workflow. The computational processes are implemented in the Python programming language. The computer code is compiled using the 64-bit Anaconda-3 distribution of Python 3.6 released by Continuum Analytics [62]. The Nelder-Mead (NM) [63, 64, 65], Basin Hopping (BH) [66, 67, 68], and Differential Evolution (DE) [69] are implemented using the SciPy Optimize software library version 0.19.1 released June 21st, 2017 [70]. The SciPy library has configuration settings for the NM, BH, and DE functions [71, 72, 73]. The SciPy default settings and the settings used in the algorithm are shown in Table 5.1, where N is the number of unknown variables being solved for in the optimization, M is the number of measurements being used in the optimization, $\mathcal{Int}$ is a function that converts decimal precision numbers to rounded whole number integers, and $\mathcal{Log}_{10}$ is a function that computes the base-10 logarithm. Additionally, a restriction is placed on ratios of M and N. In this work, it is defined that $x = \frac{N}{M}$ and $y = \frac{M}{N}$ independently so that there is

no connection between x or y, then $x > 1$ and $y > 1$ without changing the values of M or N. The restriction is illustrated with the example that if $N = 2$ and $M = 1$, then $x = 2$ and $y = 1$. An occurrence of the value 10^{-7} in Table 5.1 implies the order of magnitude of the 32-bit floating point precision limit of the computer system. Specifically, on the computer used in the research, $\mathcal{I}nt(10^{\mathcal{R}ound(\mathcal{L}og_{10}(eps_{32}))-1}) = 10^{-7}$, where $\mathcal{R}ound$ is a function to round decimal precision numbers to the nearest integer, and eps_{32} is the 32-bit machine-dependent precision limit.

Table 5.1a) Configuration settings used for the SciPy Optimize library functions.

Setting Name	**Default Setting**	**Modified Setting**	**SciPy Function**
tol_{min}	10^{-2}	10^{-2}	Minimize
xtol	10^{-4}	10^{-5}	Nelder-Mead
ftol	10^{-4}	10^{-7}	Nelder-Mead
mult_{NM}	200	200	Nelder-Mead
maxiter	$\text{mult}_{\text{NM}} \cdot N$	$\mathcal{I}nt(\text{mult}_{\text{NM}} \cdot (\frac{N}{M}) \cdot (1 + \mathcal{A}bs(\mathcal{L}og_{10}(\frac{\text{tol}_{\text{min}}}{\text{xtol}}))))$	Nelder-Mead
maxfev	$\text{mult}_{\text{NM}} \cdot N$	$\mathcal{I}nt(\text{mult}_{\text{NM}} \cdot (\frac{N}{M}) \cdot (1 + \mathcal{A}bs(\mathcal{L}og_{10}(\frac{\text{tol}_{\text{min}}}{\text{ftol}}))))$	Nelder-Mead
method		Nelder-Mead	Basin-hopping
T	1.0	tol_{min}	Basin-hopping
stepsize	0.5	xtol	Basin-hopping

Table 5.1b) Configuration settings used for the SciPy Optimize library functions.

Setting Name	**Default Setting**	**Modified Setting**	**SciPy Function**
niter	100	$\mathcal{I}nt((\frac{N}{M}) \cdot (1 + \mathcal{A}bs(\mathcal{L}og_{10}(\frac{T}{\text{ftol}}))))$	Basin-hopping
niter_success	None	$\text{niter} - \mathcal{I}nt(\mathcal{A}bs(\mathcal{L}og_{10}(\frac{T}{\text{xtol}})))$	Basin-hopping
mult_{BH}	50	50	Basin-hopping
interval	mult_{BH}	$\mathcal{I}nt(\mathcal{F}loor(\text{mult}_{\text{DE}} \cdot (\frac{\text{niter\_success}}{\text{niter}})))$	Basin-hopping
take_step	None	None	Basin-hopping
accept_test	None	None	Basin-hopping
seed	None	None	Basin-hopping
strategy	best1bin	best1bin	Differential Evolution
popsize	15	$15 \cdot (\frac{N}{M})$	Differential Evolution
tol_{DE}	10^{-2}	$(\frac{M}{N}) \cdot 10^{-7}$	Differential Evolution
mult_{DE}	1000	1000	Differential Evolution
maxfev		$\mathcal{I}nt(\text{mult}_{\text{DE}} \cdot (\frac{N}{M}) \cdot (1 + \mathcal{A}bs(\mathcal{L}og_{10}(\frac{\text{tol}_{\text{min}}}{\text{tol}_{\text{DE}}}))))$	Differential Evolution
maxiter	mult_{DE}	$\mathcal{I}nt(\left(\frac{\text{maxfev}}{\text{popsize}}\right) - 1)$	Differential Evolution
mutation	(0.5, 1)	$(10^{-7}, (2 - 10^{-7}))$	Differential Evolution
recombination	0.7	0.7	Differential Evolution
seed	None	RandomState(7532799)	Differential Evolution
polish	True	False	Differential Evolution

Table 5.1c) Configuration settings used for the SciPy Optimize library functions.

Setting Name	Default Setting	Modified Setting	SciPy Function
init	latinhypercube	latinhypercube	Differential Evolution
atol	0	$(\frac{M}{N}) \cdot 10^{-7}$	Differential Evolution

The NM, BH, and DE optimization algorithms each are functions which test trial values in the objective function to determine the values which minimize the objective function. The optimization algorithms used in the research are be either constrained or non-constrained, depending on if the algorithms enforce boundaries on the trial values or not, respectively. The NM and BH are non-constrained optimization algorithms, and the DE optimization algorithm is constrained. The NM optimization is non-constrained optimization. The BH optimization, which is configured in the research to use the NM method, is also a non-constrained optimization. The DE optimization however, is a constrained optimization. The NM and BH optimizations both take an initial estimate for each unknown parameter value. The initial estimate is used by the NM and BH in the first iteration as the set of parameter values for which a result is generated. The DE optimization is constrained by two values which bound the range of search values permitted for each unknown variable. The two values are the lower and upper bounds of possible values. The integer value 7532799 in the seed configuration of the SciPy DE function in Table 5.1 configures the initial estimate of each unknown parameter value

as the average value of the lower and upper bound of the unknown parameter constraint. This feature of the DE implementation in the research is critical to allow the user and parameter extraction algorithm to control the initial starting trial values of the DE optimization.

5.2. OBJECTIVE FUNCTION

The research implements seven error measures across five different objective function formulations. The relative absolute difference has multiple variations which depend on the behaviors of the Discrete Random Variables (DRV) used in the application. The relative absolute difference $\mathcal{L}$ has multiple variations, some of which are concisely represented by a generalized function $f(x, y)$ in Equation 5.1 [74]. There are six forms of $f(x, y)$ considered in the research and these are defined in Equation 5.2, where the term L() in the last row of Equation 5.2 is the logarithmic mean [74].

$$\mathcal{L} = \frac{\mathcal{A}\mathcal{b}\mathcal{s}(x - y)}{f(x, y)} \tag{5.1}$$

$$f(x, y) = \begin{cases} 1 \\ \mathcal{A}\mathcal{b}\mathcal{s}(x) \\ \mathcal{A}\mathcal{b}\mathcal{s}(x) + 1 \\ \mathcal{A}\mathcal{b}\mathcal{s}(x) + \mathcal{A}\mathcal{b}\mathcal{s}(y) \\ \mathcal{M}ax(\mathcal{A}\mathcal{b}\mathcal{s}(x), \mathcal{A}\mathcal{b}\mathcal{s}(y)) \\ \mathrm{L}(\mathcal{A}\mathcal{b}\mathcal{s}(x), \mathcal{A}\mathcal{b}\mathcal{s}(y)) \end{cases} \tag{5.2}$$

First, if $f(x, y) = 1$ then the error is simply the non-relative absolute difference. As such, it is hypothesized that $f(x, y) = 1$ is not desireable for

the research because there is no degree of scalability to facilitate simultaneous multiple component and multiple measurement optimization. Next, $f(x,y) = \mathcal{Abs}(x)$ produces the standard relative absolute difference. However, $f(x,y) = \mathcal{Abs}(x)$ is not desirable because there are opportunities for a division by zero to occur if $x = 0$, in which case the error measure is not defined. Division by zero can be avoided when $f(x,y) = \mathcal{Abs}(x)$ provided that each value of the DRV represented by x has been shifted such that $\mathcal{M}in(\mathcal{Abs}(x)) > 0$.

The case with $f(x,y) = \mathcal{Abs}(x) + 1$ results in a pseudo-relative absolute difference and is called a mixed error measure. The mixed error measure has desirable properties provided that x is scaled to within orders of magnitude of unity. If $\mathcal{Abs}(x) \ll 1$, the mixed error measure approaches that of the actual absolute difference with $\mathcal{Abs}(x|_{x<<1}) + 1 \cong 1$. If $\mathcal{Abs}(x) \gg 1$, the mixed error approaches the standard relative absolute difference with $\mathcal{Abs}(x|_{x>>1}) + 1 \cong \mathcal{Abs}(x)$. The research hypothesizes that scalability of the mixed error measure is achieved if the directionally unbiased differential form is used as the relative absolute error. Furthermore, the research hypothesizes that undesirable and inadequate scaling is the result of scaling directly by the value of the measured DRV as opposed to the differential of the measured DRV. The desirable property of $f(x,y) = \mathcal{Abs}(x) + 1$ is that

there is no opportunity to divide by zero. The caveat of $f(x,y) = \mathcal{Abs}(x) + 1$ is that the resulting measure is a non-invariant relative absolute error. In contrast, an invariant relative error has the property of Equation 5.3, where λ is any positive non-zero number [74].

$$\mathcal{L}(x,y) = \mathcal{L}(\lambda x, \lambda y) \tag{5.3}$$

The case with $f(x,y) = \mathcal{Abs}(x) + \mathcal{Abs}(y)$ results in an invariant relative absolute difference called the normalized absolute difference. This form has desirable properties because it is only undefined for the situation where $x = y = 0$. The situation of $x = y = 0$ is not fundamentally problematic to implement because it occurs only for which the measured DRV is zero and the simulation DRV is optimal because it is exactly equal to the measured DRV. Incidentally, the case with $f(x,y) = \mathcal{Abs}(x)$ satisfies the invariance property. The case with $f(x,y) = \mathcal{Max}(\mathcal{Abs}(x), \mathcal{Abs}(y))$ is also an invariant relative absolute error measure with the property that it is undefined only at optimality and for which $x = y = 0$.

The case for which $f(x,y) = \mathrm{L}(\mathcal{Abs}(x), \mathcal{Abs}(y))$, where L is the logarithmic mean of $\mathcal{Abs}(x)$ and $\mathcal{Abs}(y)$, is shown as the invariant absolute logarithmic error measure $\mathcal{L}_{\mathrm{ln}}$ defined in Equation 5.4. An undesirable property of Equation 5.4 is that $\mathcal{L}_{\mathrm{ln}}$ is undefined if either $x = 0$ or $y = 0$.

Division by zero can be avoided when $f(x,y) = \mathrm{L}(\mathcal{Abs}(x), \mathcal{Abs}(y))$, provided that each value of the DRV represented by x and y have been shifted such that $\mathcal{Min}(\mathcal{Abs}(x)) > 0$ and $\mathcal{Min}(\mathcal{Abs}(y)) > 0$.

$$\mathcal{L}_{\ln} = \mathcal{Abs}(\mathcal{Ln}\left(\frac{\mathcal{Abs}(x)}{\mathcal{Abs}(y)}\right)) = \mathcal{Abs}(\mathcal{Ln}(\mathcal{Abs}(x)) - \mathcal{Ln}(\mathcal{Abs}(y))) \qquad 5.4$$

An additional representation of relative absolute difference that does not fit into the form of Equation 5.1 is defined by $\mathcal{L}_\theta$ in Equation 5.5, where $\mathcal{T}an_2^{-1}$ is the four-quadrant inverse tangent function used in complex analysis. In the mathematical field of complex analysis, the $\mathcal{T}an_2^{-1}$ function computes the principal value of a complex number in the complex plane. The research identifies two angles at which the minimum $x = y$ occurs in $\mathcal{T}an_2^{-1}$. At the minimum, the equality $x = y$ requires that x and y have the same sign which holds true for positive and negative values of x or y. The two angles occur in the first and third quadrants at 45° and -135°. The research implements a modified principal value as an error measure labelled by $\mathcal{L}_\theta$ in Equation 5.5. The modification rotates the half-planes $y \geq 0$ and $y < 0$ by -45° and 135°, respectively. The modified principal value is therefore constrained by $-45° \leq (\mathcal{T}an_2^{-1}(x,y) + \theta_{\text{patch}}) \leq 135°$, where the conditional θ_{patch} variable defined in Equation 5.6 represents the rotation angle. The modification also takes the absolute value of the quantity

$\mathcal{T}an_2{}^{-1}(x,y) + \theta_{\text{patch}}$ such that negative angles between $-45°$ and $0°$ are folded over the $y = 0$ axis making $\mathcal{L}_\theta$ non-negative. The rotation by θ_{patch} and absolute value $\mathcal{Abs}$ forces the conditionally rotated principal values $\mathcal{L}_\theta$ to lie in the range $0° \leq \mathcal{L}_\theta \leq 135°$. The modified result is that the two minima occur at the same angle, and the smallest angle is $\mathcal{L}_\theta = 0°$. Therefore, the angular relative absolute error $\mathcal{L}_\theta$ is interpreted as the angular separation between two values representing the adjacent and opposing line segments of a triangle. According to Equation 5.3, the error measure $\mathcal{L}_\theta$ is invariant. Because the four-quadrant inverse tangent is used, the error measure $\mathcal{L}_\theta$ is defined for all x and y, excluding if $x = y = 0$ where it is undefined.

$$\mathcal{L}_\theta = \mathcal{Abs}(\mathcal{T}an_2{}^{-1}(x,y) + \theta_{\text{patch}}) \tag{5.5}$$

$$\theta_{\text{patch}} = \begin{cases} -\dfrac{\pi}{4} & y \geq 0 \\ \dfrac{3\pi}{4} & y < 0 \end{cases} \tag{5.6}$$

There are multiple forms that the relative absolute difference of two DRV can have. Seven forms have been presented to compute the absolute difference between two DRV. Undesirable properties of an error measure are: an undefined error in the absence of a shift of the DRV, a non-constant denominator in the relative error for constant measured DRV but variable simulated DRV, and an error measure that violates scale invariance. Of these three properties, an undefined error in the absence of a shift of the DRV will

cause computational warnings and result in an undefined optimization sample. Although shifting the values of a DRV by a constant value is computationally feasible, shifting is avoided in the research because a shifted DRV will have a different relative error than the non-shifted DRV.

The mixed error measure is selected because it consistently yields the lowest simulation error, lowest optical property variation, and guarantees no division by zero. The objective function Δ_j in the minimization Equation 5.7 is made tractable by defining it in terms of the error measure function $\mathcal{L}$ in Equations 5.8–5.9. The arguments of $\mathcal{L}$ in Equation 5.8–5.9 are two scalar values labelled $\mathcal{L}(a, b)$. The $\mathcal{Abs}$ function in Equation 5.8–5.9 performs the 2-norm operation $\mathcal{Abs}(-a) = \|-a\|_2$ such that for scalar arguments $\mathcal{Abs}(-a) = a$. Abbreviated notation is sometimes used to define $\mathcal{Abs}(-a) = |a|$. The directionally unbiased differential error measure in Equation 5.8 is used in the frequency-domain, and centered error measure in Equation 5.9 is used in the time-domain. The candidate Δ_j functions are defined in Equations 5.10–5.14. The formulations in Equations 5.10–5.13 are frequency-domain solutions, and the formulation in Equation 5.14 is a time-domain solution. In Equations 5.10–5.11, $\mathfrak{Re}$ and $\mathfrak{Im}$ isolate the real and imaginary components, respectively, of a complex value such that $\mathfrak{Re}(a + \mathrm{i}b) = a$ and $\mathfrak{Im}(a + \mathrm{i}b) = b$. The formulations in Equation 5.10 and

Equation 5.12 operate on the complex-valued frequency-domain signals, whereas the formulations in Equation 5.11 and Equation 5.13 operate on the complex-valued transfer functions. The formulations in Equations 5.10–5.11 operate directly on the real and imaginary components, whereas the formulations in Equations 5.12–5.13 operate on the phasor components. Lastly, Equations 5.10–5.11 are mathematically equivalent based on Equations 3.67–3.68, and Equations 5.12–5.13 are also mathematically equivalent based on Equations 3.67–3.68. Ideally, in context of Equations 3.67–3.69, the formulations in Equations 5.10–5.14 are all mathematically equivalent.

The formulation of Δ_j in Equation 5.14 is in the time-domain and as such operates on the real-valued measurement and conflation signal amplitudes. Each time-domain measurement contains a sequence of real-valued amplitudes. The sequence is collapsed into a single error value for each usable measurement at the evaluation frequency by average across the non-corrupt amplitudes of the usable measurements. The number of non-corrupt elements in a sequence of amplitudes for the jth usable measurement is N_j. The number of non-corrupt elements in an amplitude sequence can be less than the total number of elements in the sequence, $N_j \leq N$, based on the corrupt indices contained in the time-domain signal. The index i in Equations

5.8–5.9 maps to the non-corrupt times t_i in the amplitude sequence. Whereas Equations 5.10–5.13 are evaluated directly at the single frequency ν_k, use of Equation 5.14 first requires performing the inverse DFT on the entire frequency-domain simulated signal after conflation at the evaluation frequency ν_k. In summary, Equation 5.14 is the average time-domain simulation error across the times for which the amplitudes in the jth usable sequence are not corrupt.

$$\mathcal{M}inimize\left(\frac{1}{L_{\nu_k}} \cdot \sum_{j=1}^{L_{\nu_k}} \Delta_j \left(\nu = \nu_k\right)\right) \tag{5.7}$$

$$\mathcal{L}(a,b) = \frac{\mathcal{A}\mathcal{b}\mathcal{s}(a_{\nu_i} - b_{\nu_i})}{2} \cdot \left(\frac{1}{\mathcal{A}\mathcal{b}\mathcal{s}(a_{\nu_i} - a_{\nu_{i-1}}) + 1} + \frac{1}{\mathcal{A}\mathcal{b}\mathcal{s}(a_{\nu_{i+1}} - a_{\nu_i}) + 1}\right) \tag{5.8}$$

$$\mathcal{L}(a,b) = \frac{\mathcal{A}\mathcal{b}\mathcal{s}(a_{t_i} - b_{t_i})}{1 + \mathcal{A}\mathcal{b}\mathcal{s}(a_{t_i})} \tag{5.9}$$

$$\begin{aligned}\Delta_j(\nu_k) = \mathcal{L}(\Re\mathrm{e}(\tilde{Y}_{\mathrm{measured}_j}), \Re\mathrm{e}(\tilde{Y}_{\mathrm{conflated}_j})) \\ + \mathcal{L}(\Im\mathrm{m}(\tilde{Y}_{\mathrm{measured}_j}), \Im\mathrm{m}(\tilde{Y}_{\mathrm{conflated}_j}))\end{aligned} \tag{5.10}$$

$$\begin{aligned}\Delta_j(\nu_k) = \mathcal{L}(\Re\mathrm{e}(\tilde{H}_{\mathrm{measured}_j}), \Re\mathrm{e}(\tilde{H}_{\mathrm{conflated}_j})) \\ + \mathcal{L}(\Im\mathrm{m}(\tilde{H}_{\mathrm{measured}_j}), \Im\mathrm{m}(\tilde{H}_{\mathrm{conflated}_j}))\end{aligned} \tag{5.11}$$

$$\Delta_j(\nu_k) = \mathcal{L}(\angle\tilde{Y}_{\mathrm{measured}_j}, \tilde{Y}_{\mathrm{conflated}_j}) + \mathcal{L}(|\tilde{Y}_{\mathrm{measured}_j}|, |\tilde{Y}_{\mathrm{conflated}_j}|) \tag{5.12}$$

$$\Delta_j(\nu_k) = \mathcal{L}(\angle\tilde{H}_{\mathrm{measured}_j}, \angle\tilde{H}_{\mathrm{conflated}_j}) + \mathcal{L}(|\tilde{H}_{\mathrm{measured}_j}|, |\tilde{H}_{\mathrm{conflated}_j}|) \tag{5.13}$$

$$\Delta_j(\nu_k) = \frac{1}{N_j} \cdot \sum_{i=1}^{N_j} \mathcal{L}(Y_{\mathrm{measured}_j}(t_i), Y_{\mathrm{conflated}_j}(t_i)) \tag{5.14}$$

The Δ_j defined in Equations 5.10–5.14 in the context of Equation 5.7 are, for all intents and purposes, average fractional percent error objective

functions. This presentation of the objective function contrasts with published approaches which treat the objective function as a summation of actual error [8, 11, 18]. The research hypothesizes that the use of fractional percent error defined in Equations 5.8–5.9 are necessitated because of the multiple measurements that are simultaneously optimized. Comprehensive empirical testing is performed to verify the use of the mixed error measure in Equations 5.8–5.9 instead of the other relative error measures. The summation of actual error cited in [8, 11] is reasonable because single sample measurements are used in the optimization, however the research hypothesizes that these error functions are not applicable to simultaneous multiple measurement optimization. The results of this work leads to the hypothesis that the summation of actual error in [18] could introduce inaccuracy in the extracted parameters caused by the lack of error normalization across the multiple measurements. Lastly, the use of the average computation in Equation 5.7 facilitates comparability of the objective function values for all evaluation frequencies independent of the number of measurements used.

If Equations 5.8–5.9 are replaced with a summation of actual error, then the time-domain function defined by Equation 5.14 is similar to that presented by Palka *et al.* in [5], except that Equation 5.14 is the average across the non-corrupt time indices as opposed to a summation of actual differences. Again,

if Equations 5.8–5.9 are replaced with a summation of actual error, then the functions defined in Equations 5.12–5.13 are similar to the presentation by Dorney *et al.* in [8], with the exception of rescaling the magnitude by the natural logarithm. Similarly, the functions defined in Equations 5.10–5.11 are comparable to the presentation by Hejase in [14] with equal weighting. Although acknowledging the similarities to previously published work, the novelty of Equations 5.10–5.14 is rooted in Equations 5.8–5.9. The relative percent error defined by Equations 5.8–5.9 performs a normalization of the error across all components and measurements.

As an example, the natural logarithm is not needed for rescaling the magnitude to facilitate optimization using phasor components. As another example, measurements recorded at different system SOH's, causing amplitude variation between measurements, are normalized and able to be integrated into a simultaneous optimization. Additionally, unique angle of incidence measurements can be combined because the normalization facilitated by Equations 5.8–5.9 regulates the weighting of measurements as the amplitude decreases with the increasing obliqueness of the incident radiation. Lastly, measurements of different sample thicknesses but comprised of the same material will have varying signal amplitudes based on

thickness, and the research hypothesizes that the measurements are normalized with Equations 5.8–5.9.

5.3. THICKNESS BY REFRACTIVE INDEX VARIATION

The thickness of single layer samples is determined from measurements at normal incidence using the WSU internal transmission system. The determination of sample thickness from the THz-TDS measurement is called data-driven thickness determination. The scope of the research enables the data-driven determination of the thickness of HRSi, HDPE-A, HDPE-B, and HDPE-C using several different data-driven techniques. The first technique uses a minimization of the variation in the optimally determined index of refraction of the sample. The second technique uses a Time-of-Flight (TOF) model to determine both the sample thickness and frequency average index of refraction. Results obtained from the data-driven techniques are compared to the Vernier micrometer thickness measurements recorded for each sample.

The minimization of the variation in the optimally determined index of refraction requires an error function that quantifies variability in the index of refraction. Two different variation calculations are investigated: separation variational, and average absolute variation. The separation variational for the index of refraction $\mathcal{V}_n$ is defined in Equation 5.15 and the average absolute

variation in refractive index D_n is defined using Equation 5.16. Therefore, two different thickness determination results are obtained for each sample using the minimization technique due to the two unique variation error functions. The two alternative minimizations in addition to the TOF technique yield three unique thickness determinations.

$$\mathcal{V}_n = \frac{1}{N}\sum_{i}^{N} \left(\frac{1}{(N-j)}\sum_{j>i}^{N} \mathcal{Abs}(n(\nu_i) - n(\nu_j))\right) \quad 5.15$$

$$D_n = \frac{1}{N-1}\sum_{i}^{N-1} \mathcal{Abs}(n(\nu_{i+1}) - n(\nu_i)) \quad 5.16$$

The TOF model is a data-driven metrology technique which is used to corroborate the result of the minimization of variation technique. The TOF model for simultaneous thickness determination and average refractive index extraction is defined by Equations 5.17–5.27. The TOF model that is presented is only valid for optically thick samples for which an echo pulse is discernable in the sample signal and the first transmission peak is sufficiently separated from the echo pulse. Two peaks are sufficiently separated if the separation satisfies the Rayleigh criterion. All the normal incidence HRSi, and HDPE transmission measurements satisfy the two conditions.

In Equation 5.17, $t_1{}'$ is the time delay location of the reference signal peak amplitude, n_a is the index of refraction for air, c is the speed of light in

vacuum, $(\ell_1 + \ell_2)$ is the combined path length between the transmitter-to-sample and sample-to-receiver, d is the sample thickness, and $t_\delta{}'$ is the reference signal time delay calibration factor. In Equation 5.18, t_1 is the time delay location of the sample signal peak amplitude, n_s is the index of refraction for air, and t_δ is the sample signal time delay calibration factor. Equation 5.19 defines τ_1 as the time delay difference between the reference and sample signal peak amplitudes, and Equation 5.20 shows that the $\frac{n_a}{c}(\ell_1 + \ell_2)$ term cancels out. Equation 5.21 defines t_Δ as the time delay calibration between the reference and sample signal. Equation 5.23 defines τ_2 as the difference between the sample signal time delay location of the peak amplitude of the first echo pulse t_e to the time delay location t_1.

The path length travelled by radiation which internally reflects one cycle inside the sample and then exits the sample on the receiver side is defined in Equation 5.24. Equating the sample thickness d in Equation 5.22 and Equation 5.24 results in Equation 5.25 which enables a determination of the frequency-averaged index of refraction of the sample n_s, as expressed in Equation 5.26. Lastly, substitution of Equation 5.26 into 5.22 for n_s yields an analytic expression for the the sample thickness d in Equation 5.27. There is no TOF-derived absorption calculation implemented in the research. The

research assumes the time delay calibration between reference and sample measurements is zero, as represented in Equation 5.28. No TOF absorption contribution is calculated.

$$t_1{}' = \frac{n_a}{c}(\ell_1 + \ell_2) + \frac{n_a}{c}d + t_\delta{}' \quad 5.17$$

$$t_1 = \frac{n_a}{c}(\ell_1 + \ell_2) + \frac{n_s}{c}d + t_\delta \quad 5.18$$

$$\tau_1 = t_1 - t_1{}' \quad 5.19$$

$$t_1 - t_1{}' = \frac{d}{c}(n_s - n_a) + (t_\delta - t_\delta{}') \quad 5.20$$

$$t_\Delta = t_\delta - t_\delta{}' \quad 5.21$$

$$\tau_1 = \frac{d}{c}(n_s - n_a) + t_\Delta \quad 5.22$$

$$\tau_2 = t_e - t_1 \quad 5.23$$

$$2d = \frac{c}{n_s}\tau_2 \quad 5.24$$

$$d = \frac{c \cdot \tau_2}{2 \cdot n_s} = \frac{c \cdot (\tau_1 - t_\Delta)}{(n_s - n_a)} \quad 5.25$$

$$n_s = \frac{n_a}{1 - (\frac{2(\tau_1 - t_\Delta)}{\tau_2})} \quad 5.26$$

$$d = \frac{\tau_1(\frac{c}{n_a})}{(\frac{1}{1 - (2\frac{(\tau_1 - t_\Delta)}{\tau_2})}) - 1} \quad 5.27$$

$$t_\Delta = 0 \quad 5.28$$

The minimization profile of the variation in refractive index is shown in Figure 5.1 for four different measurements: synthetic (plot A), HRSi (plot B), HDPE-A (plot C), and HDPE-C (plot D). The sampling resolution of the thicknesses in Figure 5.1 is 1 μm. The synthetic measurement in plot A is a synthetically generated data set using a Num Scans value of 1000. The

thickness of the synthetic sample is exactly 500 μm. The Vernier micrometer measured thickness of the HRSi, HDPE-A, HDPE-B, are: 500 ± 25.4 μm, 3070 ± 25.4 μm, 6050 ± 25.4 μm, and 1640 ± 25.4 μm, respectively. The functionality of the minimization of variation varies the thickness to identify the thickness which minimizes the variation of the refractive index. The frequency-dependent index of refraction and extinction coefficient for each optimization trial thickness is determined using the NM Frequency Dependent Optimizer (FDO) outlined in Section 5.5. The vertical plot axis and data markers colored red in Figure 5.1 uses Equation 5.15 as the minimizing error function, and the blue vertical plot axis and data markers in Figure 5.1 uses Equation 5.16.

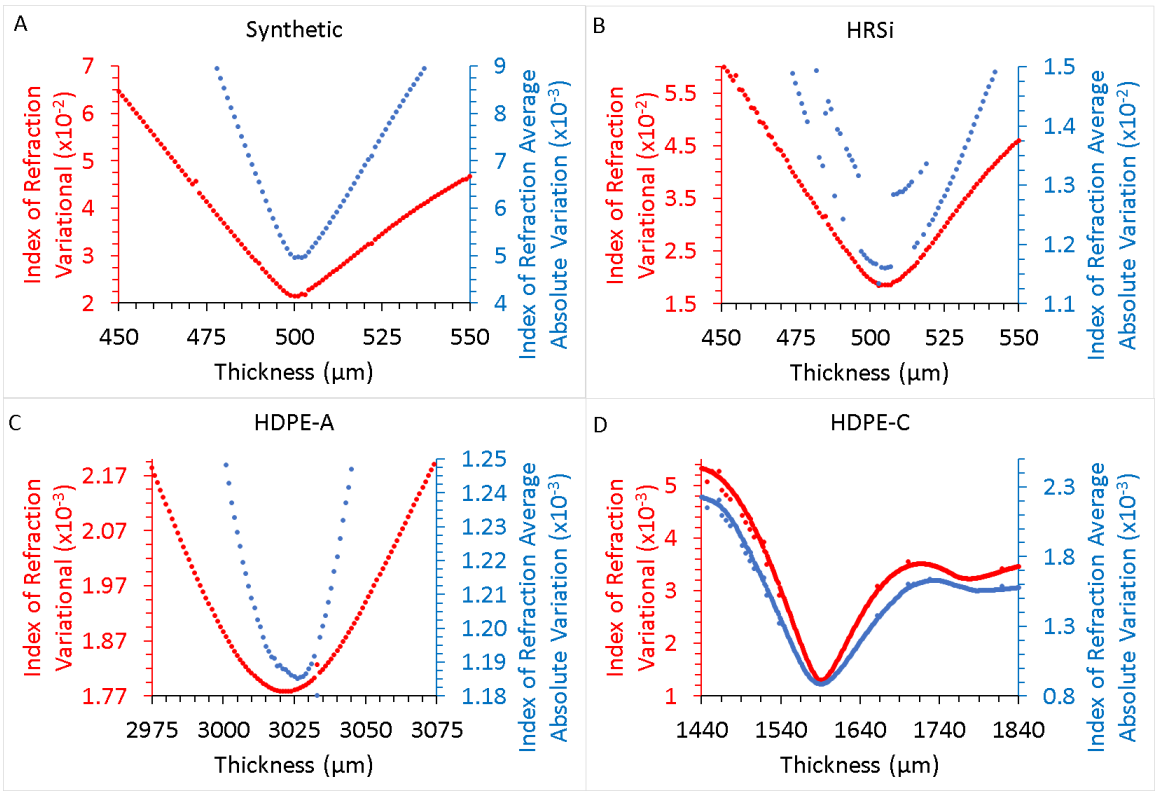

Figure 5.1) Two variation error functions (red and blue) used to solve the minimization of refractive index variation yield slightly different minimal solutions. Results are shown for WSU internal transmission measurements at normal incidence for synthetic (plot A), HRSi (plot B), HDPE-A (plot C), and HDPE-C (plot D) samples.

Analysis of the four plots in Figure 5.1 shows that each sample has a well-defined minimum of refractive index variation. However, the thickness at which the separation variational, proportional to the statistical variance, is minimum is different than the thickness at which the average absolute variation is minimum. The research has found that the thickness at which the variational is minimum is strongly dependent on the frequencies selected to compute the variational, which indicates that the naïve minimization of a refractive index variational using semi-arbitrary frequencies within the measurement bandwidth to determine thickness is not a robust solution. The

research has also found that the thickness at which the total simulation error is minimum also depends on the frequencies used to compute the simulation error. Although the two variation methods qualitatively agree, the separation variational of Equation 5.15 yields a more smooth and consistent minimization profile as a function of thickness compared with the average absolute variation of Equation 5.16. In particular, plot B for HRSi in Figure 5.1 shows that the average absolute variation exhibits unstable behavior, whereas the separation variational is more consistently changing. Furthermore, plot C for HDPE-A in Figure 5.1 indicates that the minimization profile of the separation variational (red markers) is more symmetric and smoothly changing than the average absolute variation (blue markers). Therefore, if a refractive index variational is used to determine the optimal thickness, the research recommends using a statistical variance metric such as Equation 5.15 as the error function in the DE Frequency Independent Optimizer (FIO) outlined in Section 5.5.

The numerical thickness results obtained using the optimization technique for both alternatives, and the TOF model, are presented in Table 5.2. The thickness information in Table 5.2 shows agreement among the data-driven thickness estimates using the two optimizations alternatives and the TOF model. The TOF model yields the largest thickness value of the three

data-driven approaches for all four samples examined. All three of the data-driven thickness determinations yield HDPE thickness values which are significantly less than the Vernier micrometer measured thicknesses. The data-driven techniques yield approximately the same thickness as the micrometer measurement for HRSi. The frequency-averaged HDPE index of refraction presented in the right-most column of Table 5.2 agrees between the HDPE-A, HDPE-B, and HDPE-C samples. In addition, the TOF derived frequency-averaged index of refraction for HRSi and HDPE-A agree to within 99.4% and 99.6%, respectively, of the average values reported using the single-layer non-optimized approach defined in Equations 5.29–5.31. In Equations 5.29–5.31, n, α, and κ are the non-optimized sample material refractive index, absorption coefficient, and extinction coefficient, respectively. The speed of light, frequency, propagation length, refractive index of air, and transfer function phase and magnitude are labelled c, ν, d, n_{air}, $\angle\tilde{H}(\nu)$, and $|\tilde{H}(\nu)|$, respectively.

$$n(\nu) = n_{\text{air}} + \frac{c}{2\pi\nu d} \cdot \angle\tilde{H}(\nu) \tag{5.29}$$

$$\alpha(\nu) = -\frac{2}{d}\mathcal{L}n(|\tilde{H}(\nu)| \cdot \frac{(n(\nu)+1)^2}{4n(\nu)}) \tag{5.30}$$

$$\kappa(\nu) = -\frac{c}{2\pi\nu d}\mathcal{L}n(|\tilde{H}(\nu)| \cdot \frac{(n(\nu)+1)^2}{4n(\nu)}) \tag{5.31}$$

Table 5.2a) Comparison of data-driven determination of sample thickness compared with Vernier micrometer measurements.

Sample Description	Data-Driven Thickness Estimate		
	Avg. Abs. Variation (mm)	Variational (mm)	Time of Flight (mm)
HRSi	0.50147	0.50577	0.50711
HDPE-C	1.59270	1.59288	1.60151
HDPE-A	3.02894	3.02058	3.03159
HDPE-B	5.97934	5.98102	6.00817

Table 5.2b) Comparison of data-driven determination of sample thickness compared with Vernier micrometer measurements.

Sample Description	Data-Driven Avg. Thickness (mm)	Vernier Micrometer (mm)	Vernier Micrometer Error (um)	Time of Flight: Refractive Index
HRSi	0.50479	0.5	-4.78467	3.45958
HDPE-C	1.59570	1.64	44.3033	1.55679
HDPE-A	3.02704	3.07	42.9633	1.55158
HDPE-B	5.98951	6.05	60.49	1.54435

Graphically comparing the thickness values determined using the three data-driven approaches to the Vernier micrometer thickness measurement yields the bar chart on the left in Figure 5.2. In the plot on the left in Figure 5.2, the thickness obtained using the minimization of average absolute variation (Equation 5.16), minimization of separation variational (Equation 5.15), TOF, and Vernier micrometer are colored in blue, red, green, and grey, respectively. The bar chart shows the agreement between the four possible thicknesses for each sample. The bar chart to the right in Figure 5.2 shows the difference, in micrometers, between the Vernier micrometer measured sample

thickness and the average of the three data-driven thickness values for each sample. Assuming the data-driven thicknesses are more accurate than the Vernier micrometer measurements, the error of the micrometer measured thickness appears to increase as the length of the micrometer caliper is extended. The HDPE-B sample is the thickest sample used in the research, and the HRSi sample is the thinnest sample. The micrometer error of the HDPE-B sample is approximately fourteen times greater than that of the HRSi sample. Another statement of the error is that the micrometer error for HRSi is approximately 7% the micrometer error of HDPE-B.

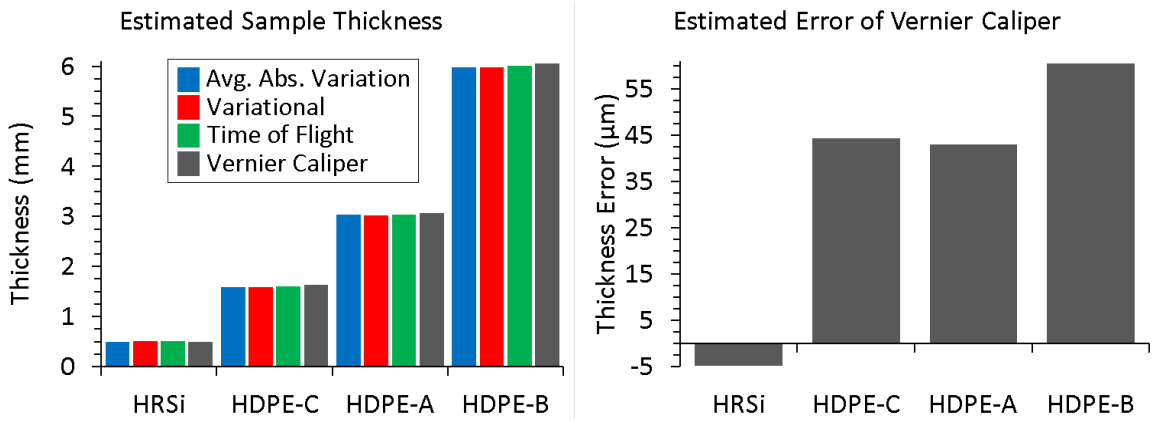

Figure 5.2) The left plot is the data-driven estimates of HRSi and HDPE sample thickness compared with the Vernier micrometer measured thicknesses (grey). The right plot is the difference between the average data-driven thickness and the Vernier micrometer measured thickness for HRSi and the HDPE samples.

The frequency-independent parameter optimization for unknown thickness determination outlined in Section 5.5 relies on the minimal variation of the index of refraction. The technique of minimal variation for thickness determination is effective only for materials for which the refractive index is

nearly constant. The minimal variation technique is not applicable to materials which do not have a constant index of refraction. An attempt is made to develop an algorithm that does not place variation requirements on the material refractive index to enable thickness determination. The development attempts to use the minimization of the error returned by the NM FDO to the DE FIO as the targeted optimization to yield the best thickness estimate without relying on refractive index variation.

The minimization profile of the refractive index separation variational using Equation 5.15 is shown in Figure 5.3 as the red vertical plot axis and data markers. for four different measurements: synthetic (plot A), HRSi (plot B), HDPE-A (plot C), and HDPE-C (plot D). The green colored vertical plot axis and data markers in Figure 5.3 is the total error returned by the NM FDO. The analysis of Figure 5.3 does not reveal any unambiguous global minimum in the optimal NM FDO total error as a function of sample thickness for any of the samples. The lack of discernable minimum in the optimal NM FDO total error is discussed in more detail in Section 5.4, but the brief explanation is that the optimal NM FDO converges on optical parameters which compensate for the changing thickness. Holding the optical parameters constant while optimizing the thickness does generate total error profiles with discernable minimum. Regardless, the lack of discernable minimum in the

optimal NM FDO total error contrasts with the refractive index variational which does unambiguously show a global minimum for each sample. Therefore, the minimization of the optimal NM FDO total error is not able to be used to determine the frequency-independent thicknesses.

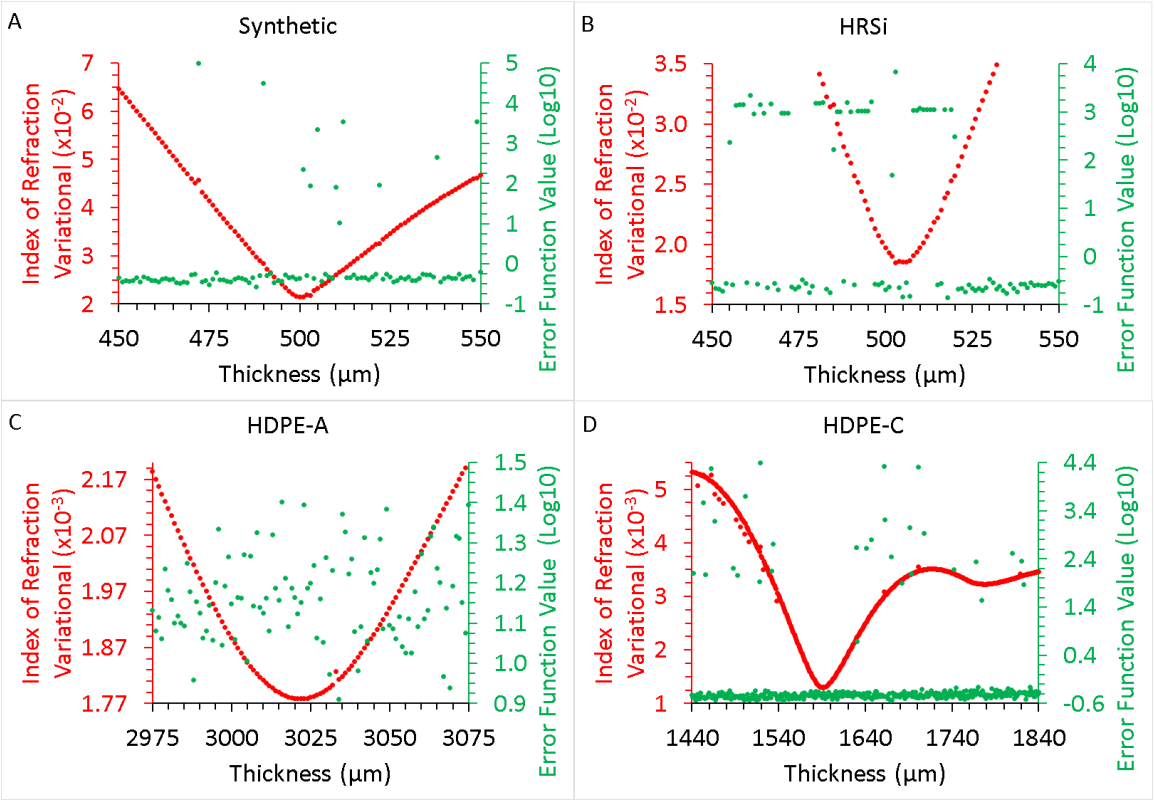

Figure 5.3) The optimal NM FDO total error (green data markers) as a function of sample thickness does not indicate the existence of a global minimum. Results are shown for WSU internal transmission measurements at normal incidence for synthetic (plot A), HRSi (plot B), HDPE-A (plot C), and HDPE-C (plot D) samples. For comparison, the refractive index variational result is shown in red data markers.

The inability to use the optimal NM FDO total error in the bandpass of low air absorption as the minimization value for the DE FIO presents an opportunity for future research. The solution of the problem will avoid the need to make assumptions about the behavior of the refractive index of a

sample prior to optimization, and enable thickness determination for samples with non-constant refractive index. In an effort to guide the future research into the problem, the research presents a modified average absolute variation D' in Equation 5.32 which takes into consideration the extinction coefficient in addition to the index of refraction. Specifically, in Equation 5.32, the variation in extinction coefficient $(\kappa(\nu_{i+1}) - \kappa(\nu_i))$ is used to weight the variation in refractive index $(n(\nu_{i+1}) - n(\nu_i))$. The desired effect is that the contribution by the variation in refractive index is reduced in the vicinity of absorption features because the variation in extinction coefficient is large in the vicinity of the absorption features. Furthermore, it is suggested that residual FP etalon effects that remain in the NM FDO extinction coefficient profile will be correlated with residual FP etalon effects in the refractive index profile so that the weighting is not affected in the FP dominant regions outside of any dominant absorption features.

$$D'(n(\nu), \kappa(\nu)) = \frac{1}{N-1} \sum_{i}^{N-1} \mathcal{Abs}\left(\frac{n(\nu_{i+1}) - n(\nu_i)}{\kappa(\nu_{i+1}) - \kappa(\nu_i)}\right) \qquad 5.32$$

The motivation is that absorption peaks in the extinction coefficient cause absorption induced dispersion in the refractive index, which result in non-uniform variation in the refractive index. The ability to use a variational minimization on the refractive index profile for uniformly varying refractive

index profiles facilitates frequency-independent optimization to determine layer thickness. The use of Equation 5.32 is an attempt to obtain minimization features that resemble unambiguous local minimum patterns. The refractive index of pharmaceutical-grade Oxycodone and Hydrocodone are non-constant and non-uniform in the THz spectral region. Therefore, the pharmaceutical-grade Oxycodone and Hydrocodone WSU external transmission measurements at normal incidence are investigated to determine if Equation 5.32 facilitates identification of local minimum in the minimization profile of the sample thickness. The results for pharmaceutical-grade Oxycodone and Hydrocodone are presented in Figure 5.4, where the sampling resolution of the thicknesses is 1 μm.

The plots in the left column (plots A, C, E) of Figure 5.4 are minimization profile results obtained for pharmaceutical-grade Oxycodone, and the plots in the right column (plots B, D, F) are minimization profiles obtained for Hydrocodone. The red colored vertical plot axis and data markers in the top row (plots A, B) of Figure 5.4 are the minimization profiles using the refractive index separation variational of Equation 5.15. The blue colored vertical plot axis and data markers in the top row (plots A, B) of Figure 5.4 are the minimization profiles using the refractive index average absolute variation of Equation 5.16. The green colored vertical plot axis and data

markers in the middle row (plots C, D) of Figure 5.4 are the minimization profiles using the optimal NM FDO total error. The purple colored vertical plot axis and data markers in the bottom row of Figure 5.4 are the minimization profiles using the refractive index average absolute variation that has been modified with weighting by the extinction coefficient variation defined by D' in Equation 5.32.

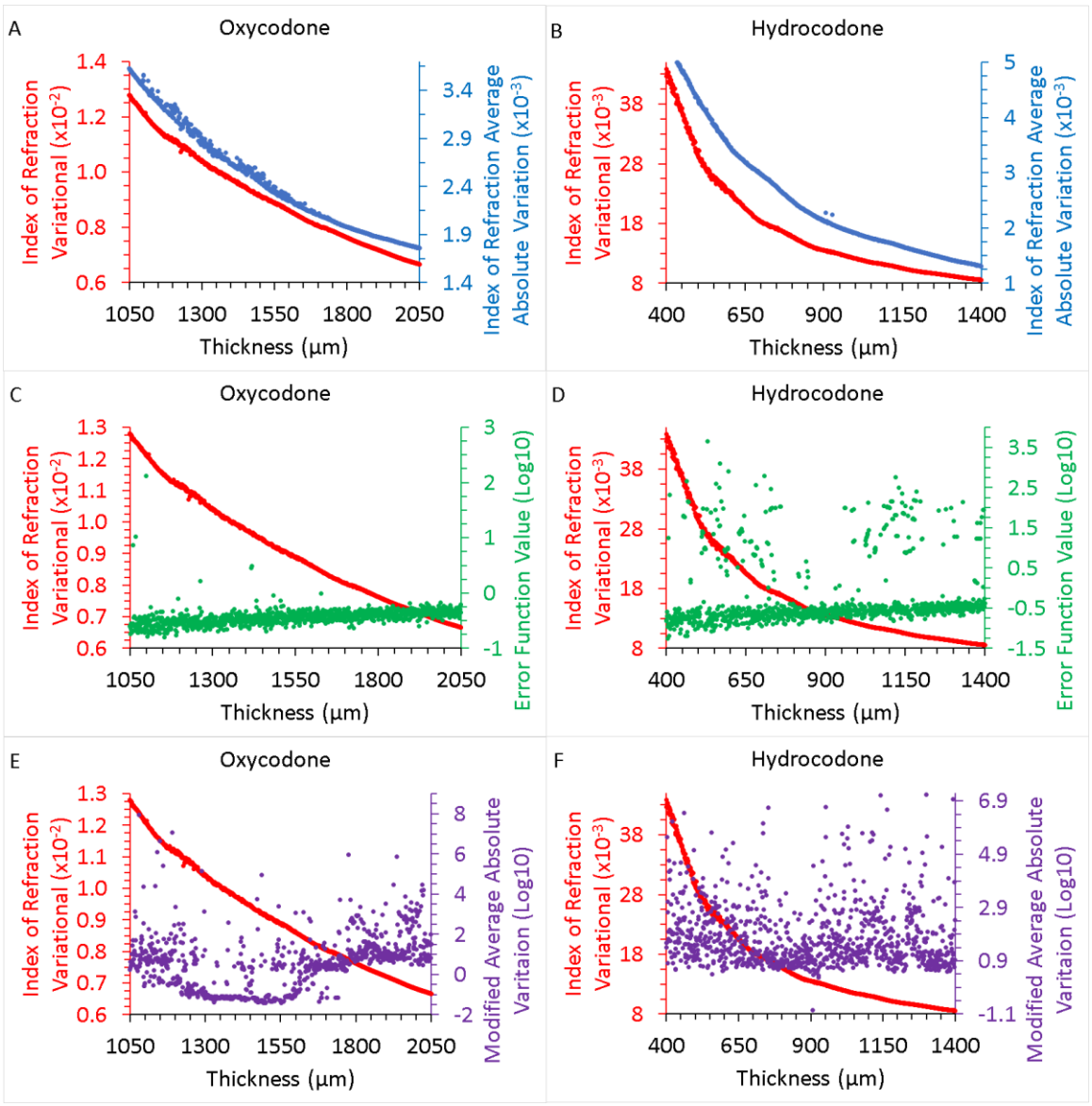

Figure 5.4) The left and right columns are for pharmaceutical-grade oxycodone and hydrocodone, respectively. The top row (plots A–B) are the minimization profiles using refractive index variational metrics (red and blue); no physically realistic minimum is observed. The middle row (plots C–D) are the minimization profile using optimal NM FDO total error (green); no global minimum is observed. The bottom row (plots E–F) shows the minimization profile for the modified variation (purple).

The four plots A–D in the top and middle rows of Figure 5.4 contain the minimization profiles using refractive index variational metrics (red and blue), and optimal NM FDO total error metric. Physically realistic or numerically discernable global minimum are not observed in plots A–D of

Figure 5.4. The two bottom row plots (plots E–F) for pharmaceutical-grade Oxycodone (left) and Hydrocodone (right) suggest the presence of minimum patterns in the vicinity of the Vernier micrometer measured thickness. The Vernier micrometer measured thickness of the washers containing the pharmaceutical-grade Oxycodone and Hydrocodone are 1550 ± 25.4 μm and 900 ± 25.4 μm, respectively. Specifically, plot E in Figure 5.4 shows a region of sustained minima for thickness values ranging 1290–1560 μm, resolved in 1 μm increments. The analysis of plot F in Figure 5.4 shows a small region of minima for thickness values ranging 895–910 μm, resolved at 1μm increments. Most notably, there is an obvious but isolated and possibly coincidental minimum in the minimization profile located at a thickness of 907 μm.

5.4. ORIENTATION BY SIMULATION ERROR

As discussed in Section 5.3, the optimal NM FDO total error cannot be used as the minimizing quantity when optimizing sample layer thicknesses. It is shown in Section 5.3 that optimizing the optical parameters for all frequencies during a single iteration of the thickness optimization will result in a total error which does not show any discernable minimum in the minimization profile. The cause is due to the NM FDO converging on optical parameter values

which minimize the error function and compensate for the non-optimal sample layer thickness. Therefore, the optimal NM FDO, for each trial value of the layer thickness, will obfuscate the validity of the trial thickness by adjusting the optical parameters to maintain the error function minimum. Because the thickness and the sample orientation are correlated in the theoretical model, the same lack of discernable minimum in the minimization profile is observed in the case of optimizing the sample orientation if the optimal NM FDO is used. The connection between thickness and sample orientation is conceptually apparent; rotating the sample surface normal vector away from the radiation propagation vector will cause an effective increase in the propagation length experienced by the radiation inside the sample as determined by Equation 3.57.

Three examples are provided to reinforce the argument that holding the optical properties constant during the sample orientation optimization, or similarly the thickness optimization, if total error is used. The first example, shown in Figure 5.5, uses the HDPE-C sample measured in the WSU external transmission system at normal incidence. The left plot in Figure 5.5 shows the sample orientation minimization profile for the pitch angle of the sample sweeping from normal incidence to ten degrees away from normal incidence, in half degree increments, while the roll angle is held constant at zero degrees.

The right plot in Figure 5.5 shows the sample orientation minimization profile for the roll angle of the sample sweeping from normal incidence to ten degrees away from normal incidence, in half degree increments, while the pitch angle is held constant at zero degrees. Both plots in Figure 5.5 demonstrate that a minimum in the total error minimization profile exists if the optical parameters are held constant during the sample orientation optimization. The thickness of HDPE-C used for the example is 1601.51 μm, and the initial complex index of refraction used is a constant $\tilde{n}_{\mathrm{HDPE}}(\nu) = 1.5 - 0.0006i$. The lines connecting the data points in Figure 5.5 are for illustrative purposes.

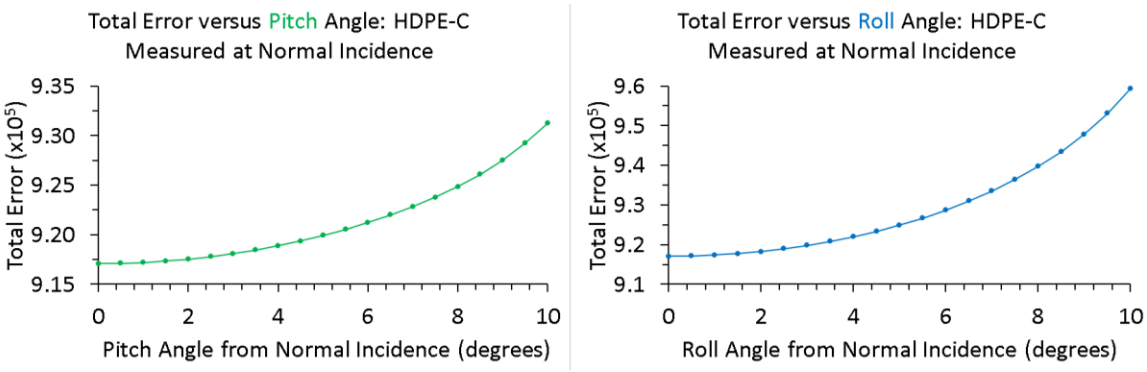

Figure 5. 5) The total error as a function of sample orientation for HDPE-C measured at normal incidence using the WSU external transmission system. The pitch angle (left, green) and roll angle (right, blue) are shown to have minimum at 0°.

The second example, shown in Figure 5.6, uses the HRSi sample measured in the WSU external and internal transmission system at 30° incidence. Parallel polarization is for incident radiation electric field vectors perpendicular to the surface of the sample, and perpendicular polarization is for electric field vectors parallel to the sample surface. The top plot in Figure

5.6 shows the sample orientation minimization profile for HRSi in the WSU internal transmission system at 30° incidence in the perpendicular polarization state while the pitch angle is held constant at 0° and the roll angle of the sample sweeps from 20° to 40° incidence, in 1° increments. The middle plot in Figure 5.6 shows the sample orientation minimization profile for HRSi in the WSU external transmission system at 30° incidence in the perpendicular polarization state while the pitch angle is held constant at 0° and the roll angle of the sample sweeps from 20° to 40° incidence, in 1° increments. The bottom plot in Figure 5.6 shows the sample orientation minimization profile for HRSi in the WSU external transmission system at 30° incidence in the parallel polarization state while the roll angle is held constant at 0° and the pitch angle of the sample sweeps from 20° to 40° incidence, in 1° increments. All three plots in Figure 5.6 demonstrate that a minimum in the total error minimization profile exists if the optical parameters are held constant during the sample orientation optimization. The initial thicknesses of HRSi used for the three examples in Figure 5.6 are 509.955 μm, 491.067 μm, and 500.513 μm for plot A, plot B, and plot C, respectively. The initial complex index of refraction used is a constant $\tilde{n}_{\mathrm{HRSi}}(\nu) = 3.5 - 0.0001i$. The lines connecting the data points in Figure 5.6 are for illustrative purposes.

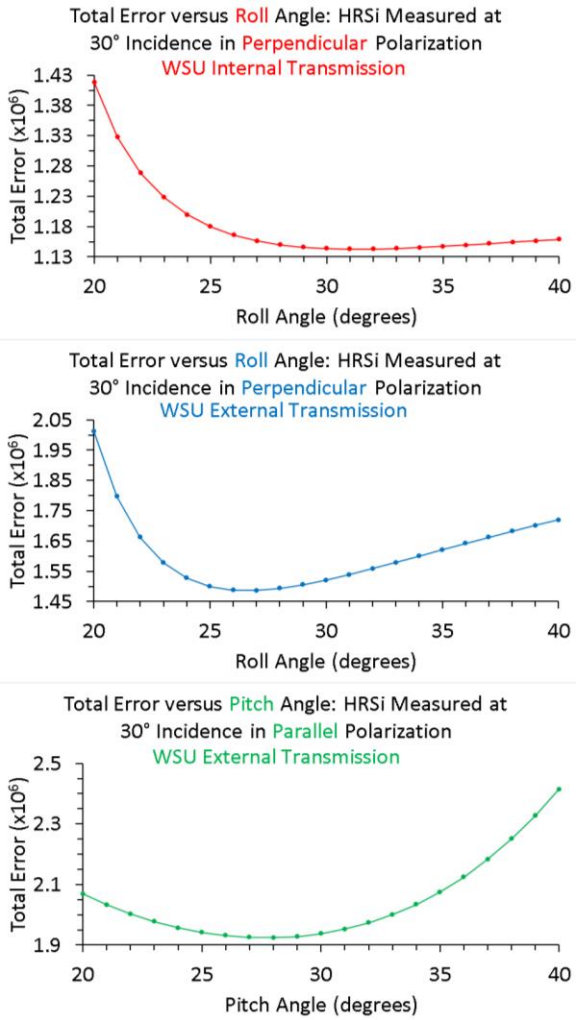

Figure 5.6) The total error as a function of sample orientation for HRSi measured at 30° incidence. The minimum are in the vicinity of 30°. Top plot (red): total error profile for radiation incident on sample surface with electric field parallel to the surface. Middle plot (blue): total error profile for radiation incident on sample surface with electric field parallel to the surface. Bottom plot (green): total error profile for radiation incident on sample surface with electric field parallel to the surface.

The third example demonstrates the ability to achieve a discernable minimum in the minimization profile of Lactose at 30° incidence for parallel and perpendicular polarized radiation relative to the surface orientation of the sample. The measurement system is the WSU external transmission system. The optical properties of Lactose are not constant or uniform as a function of

frequency. Therefore, a frequency-dependent complex index of refraction is utilized. The Lactose complex index of refraction is extracted using the algorithmic workflow outlined in Section 5.5 for a measurement at normal incidence of the Lactose sample without sample orientation optimization. Next the non-uniform frequency-dependent optical properties derived from a normal incidence measurement are held constant s the roll or pitch sweeps from 0°–20°. The initial thickness is set to 2390 μm. The roll is used if the measurement is performed in a perpendicular polarization orientation, and pitch is used if the measurement is performed in a parallel polarization orientation. In the example, the roll and pitch angle are set to 0° is they are not being used to sample the minimization profile. The total error obtained by the computations are shown in Figure 5.7, with the pitch angle sweep in the left plot (green markers), and the roll sweep in the right plot (blue markers). The results show that a discernable minimum is obtainable in the minimization profile for Lactose. The lines connecting the data points in Figure 5.7 are for illustrative purposes.

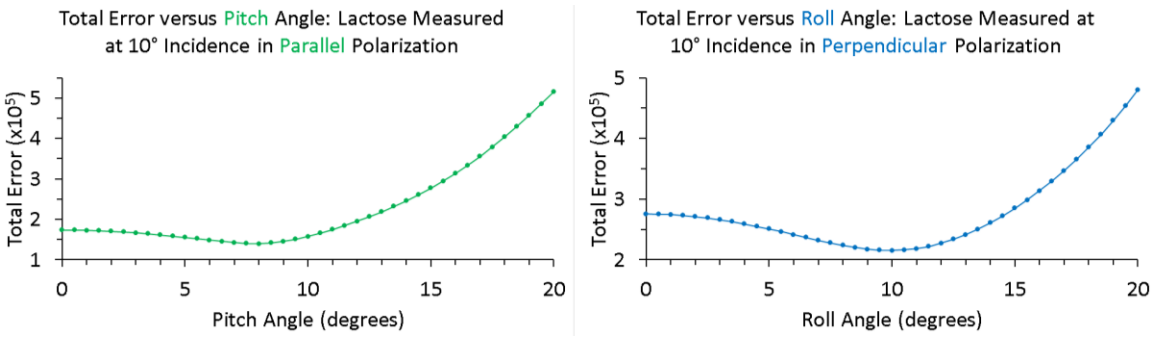

Figure 5.7) The total error as a function of sample orientation for Lactose measured at 10° incidence using the WSU external transmission system. The pitch angle (left, green) and roll angle (right, blue) are shown to have minimum in the vicinity of 10°.

The solution to obtain a total error function minimization profile that contains discernable a minimum is to set the optical parameters of the NM FDO optimization constant during the entire sample orientation optimization. The optical parameter values can be non-uniform and non-constant. In effect, the sample orientation optimization is conducted in such a way that the NM FDO is bypassed for a direct calculation of the transfer function at constant frequency-dependent optical parameter values. Because the optical parameters are held constant during sample orientation optimization, the optimal optical properties are likely to not coincide with the sample orientation determined from the orientation optimization. If the error minimization is used for orientation or thickness determination, then the beginning-to-end sample orientation, thickness, and optical parameter determination process defined by Section 5.5 is repeated with an update of the optical properties at the end of each iteration. The iterative approach facilitates

convergence to obtain a confident and confluent estimate of the sample orientation, layer thickness, and optical property.

The research does not foresee an obstruction that would prohibit the method presented for sample orientation optimization to be extended to thickness determination, in which case the thickness of materials with non-uniform, non-constant, optical properties such as α-lactose monohydrate, pharmaceutical-grade Oxycodone, and Hydrocodone, can be extracted. The approach used for orientation optimization, combined with the approach for thickness determination, facilitates optimization based thickness and orientation determination for uniform optical properties as a function of frequency. Furthermore, the approach used for orientation optimization can be extended to thickness determination to facilitate the optimization based determination of either the layer thickness or the sample orientation of samples which have non-uniform optical properties as function of frequency, such as α-lactose monohydrate, pharmaceutical-grade Oxycodone, and to a lesser extent, Hydrocodone. The Python pseudo-code to demonstrate the functionality of the concept is presented in Figure 5.8. In the case of objective function error used as the minimization quantity for either thickness or orientation determination, the pseudo-code in Figure 5.8 is cycled, with

optical parameter updates at the end of each cycle, until convergence is achieved.

```
if uniform_optical_property is True:
    if unknown_thickness is True and unknown_orientation is True:
        thickness = Error_Minimization()
        orientation = Error_Minimization()
    if unknown_thickness is False and unknown_orientation is True:
        orientation = Error_Minimization()
    if unknown_thickness is True and unknown orientation is False:
        thickness = Variation_Minimization() or Error_Minimization()
if uniform_optical_property is False:
    if unknown_thickness is True and unknown_orientation is True:
        thickness = Error_Minimization()
        orientation = Error_Minimization()
    if unknown_thickness is False and unknown_orientation is True:
        orientation = Error_Minimization
    if unknown_thickness is True and unknown orientation is False:
        thickness = Error_Minimization()
```

Figure 5.8) Python pseudo-code demonstrating the capability of thickness and orientation optimization developed in the research.

The thickness and orientation are bounded optimizations. The centers of the bounds for the target variable, as they relate to the DE FIO, are re-centered at the end of a cycle to the optimal solutions obtained during the cycle and the bounds are correspondingly adjusted. The updated bounds never exceed the original bounds. The updated bounds are modified to always include the center of the original bounds provided at initialization. The re-centering attempts to place the starting trial solution of the next cycle at the optimal solution of the previous cycle. For example, hypothetically let the roll angle be centered at 0° and bounded by -4° and 4° at initialization. If the solution at the end of the first cycle is 1°, then the updated bound is -3° and 3°. If, however, the solution is 3°, then the updated bound is 0° and 4°.

Based on the pseudo-code in Figure 5.8, the alternatives for the case of uniform optical properties such as HDPE and HRSi are as follows. If the thickness and the orientation are simultaneously unknown quantities and the optical properties are uniform, then the thickness and orientation are sequentially solved. The thickness is first solved using minimization of either the refractive index variation or the total simulation error. The orientation is subsequently solved, using the thickness solution, by minimization of the total simulation error across all the simulation frequencies. If the thickness is known but the orientation is unknown and the optical properties are uniform, then the orientation is determined by the minimization of total simulation error, depending on user preference. If the thickness is unknown and the orientation is known and the optical properties are uniform, then the thickness is determined by either the variational minimization or total simulation error.

Based on the pseudo-code in Figure 5.8, the alternatives for the case of non-uniform optical properties such as α-lactose monohydrate and pharmaceutical-grade Oxycodone are as follows. If the thickness and the orientation are simultaneously unknown quantities and the optical properties are not uniform, then neither quantity can be determined using the algorithm. If the thickness is known but the orientation is unknown and the optical properties are not uniform, then the orientation must be determined by the

error minimization. If the thickness is unknown and the orientation is known and the optical properties are not uniform, then the thickness must also be determined using the error minimization.

5.5. PHYSICAL PARAMETER OPTIMIZERS

The scheme presented in previous section is used as the basis for estimating the air absorption corresponding to a measurement. The air absorption compensation is incorporated into a frequency-independent optimization of the fractional percent of water vapor and is optimized separately from the frequency-independent thickness and orientation. The DE is used to solve for the thickness and sample orientation frequency-independent parameters, and BH is used to solve for the H_2O fractional percent volume. The DE is called in two sequential processes to first determine the layer thicknesses and then sample orientations. First, the low absorption bands of air are identified from an absorption profile generated using HITRAN [75, 76, 77, 78]. The frequencies within the low absorption bands are solved in the DE optimization for the optimal layer thicknesses and YPR angles of the sample. The unknown YPR angles are solved separate from the unknown sample layer thicknesses. Next, the high absorption bands of air are identified using HITRAN. The frequencies in the high absorption bands are solved in the BH optimization using the YPR and thicknesses from the

solution of the DE optimization. The parameter which is optimized in the BH is a scalar value for each time-domain signal measurement. The results of the BH optimization are scalar values which scale the HITRAN absorption profile such that the objective function is minimized. The calling sequence used to solve the frequency-independent parameter optimization is shown in Figure 5.9. The strategy outlined in Figure 5.9 is called the frequency-independent optimization algorithm, and the DE and BH are each a Frequency Independent Optimizer (FIO).

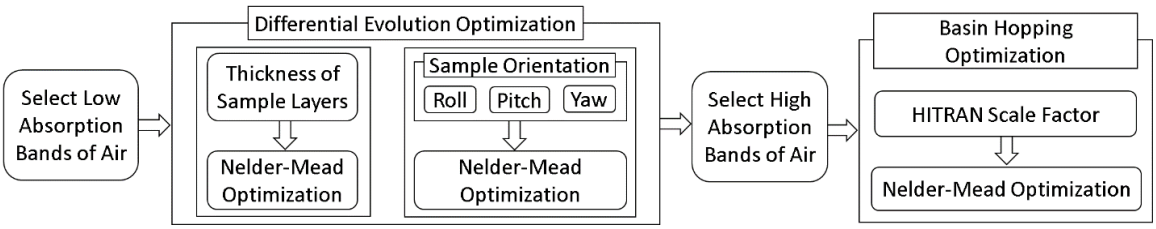

Figure 5.9) The organization of the optimization process showing the Nelder-Mead optimization nested within the differential evolution and basin hopping frequency-independent optimizers.

The NM optimization returns a list of error function values, one for each evaluation frequency bin, to the FIO for each frequency-independent trial solution. The NM optimization also returns the frequency-dependent optical parameter values which yield the error function values. The NM optimization is called a Frequency Dependent Optimizer (FDO). The error function values returned by the NM FDO are the optimal NM FDO errors and the optical parameter values are the optimal values used to calculate the optimal NM FDO errors.

The DE FIO first solves the sample layer thicknesses using either the variation of the refractive index or the total objective function error value as the minimization quantity. If measurements within the configuration are defined to have unknown sample orientation, then unknown YPR angles for DE FIO sample layer thickness determination are generated by averaging the extrema bound of the frequency-independent parameter constraint for each unknown orientation angle. For example, if the roll angle x in the DE optimization is constrained by $a \leq x \leq b$, where a and b are lower and upper bounding values, then the temporary value placed on the roll angle is $x = \frac{a+b}{2}$. After the sample layer thicknesses are determined, the DE FIO solves the sample orientation using the total error function value as the minimization quantity.

If the sample orientation is unknown, then the DE FIO optimizes the YPR sample orientation angles using the total error function value as the minimization quantity while the optical properties are held constant. This research has found that orientation determination using a refractive index variation minimization is not a correct solution because there is no orientation which can decrease the physical, non-projected, thickness of a layer. The workflow in Figure 5.9 is repeated until convergence of the orientation angles is achieved as outlined by in Section 5.4. If the thickness is unknown and the

refractive indices are uniformly varying, such as HDPE, then the DE FIO can solve the sample layer thicknesses using either the summation of absolute variation of the refractive index of the variable sample layers, or the total optimal simulation error, as the minimization quantity. If the thickness is unknown and the refractive indices are not uniformly varying, such as Lactose, then the DE FIO must solve the sample layer thicknesses using the total optimal simulation error function value as the minimization quantity while the optical properties are held constant. The algorithm can simultaneously solve for thickness and orientation regardless of the optical property uniformity. The topic of thickness and orientation determination is discussed further in Section 5.3 and Section 5.4. Lastly, the BH FIO error is a summation of the list of NM error function values at each evaluation frequency, but with each error normalized relative to a reference value.

The DE FIO for thickness determination minimizes the absolute variation of the index of refraction of an optimization configuration. The refractive index of a material in the sample is included in the variation calculation if the thickness of the layer is unknown and the refractive index of the material which composes the layer is unknown, and the user has selected the variational method in the algorithm configuration. The refractive index of a material, regardless of the number of layers that contain the material and the

number of measured samples included in the optimization that contain the material, is included no more than once in the variation calculation. The absolute variation used to compute the error is defined in Section 5.3 using Equation 5.15. The BH FIO error is a summation of the list of error returned by the NM optimization. The sample layer thicknesses and sample orientation are entered into the BH FIO as known parameters because they have been optimally determined in the DE FIO. The BH FIO is designed so that the initial guess for the unknown fractional percent water volume of air is always at zero percent water content.

There are two benefits to using frequency-independent optimization as shown in Figure 5.9. The first is that the YPR and thicknesses are determined using a smaller number of frequency indices than for the entire usable bandwidth of the instrument, and therefore the runtime is decreased. Second, an estimate for the absorption of air for a given sample measurement can be obtained, and the estimate is obtained using a subset of frequencies within the instrument bandwidth where the absorption of air is high, thus improving runtime performance over the use of the entire instrument bandwidth. In contrast, the previously published research literature avoids estimating the absorption of air assuming that the absorption is zero at all frequencies for all measurements. A requirement to enable the use of high absorption spectral

bands of air, exclusively, in the DE optimization for air absorption is the presence of a sufficiently wide and usable bandwidth. The bandwidth must contain enough negligible air absorption features of varying absorption levels to adequately represent the absorption contrast and obtain an accurate and stable optimization from HITRAN.

The Nelder-Mead (NM) simplex optimization is called within the FIO and uses the values that the FIO has assigned to the frequency-independent parameters as input. The frequencies solved for by the NM FDO when being tasked by the DE and BH FIO are only those frequencies for which the absorption of air is negligible and appreciable, respectively. The NM FDO is used to optimize the frequency-dependent parameters. The optimization parameters of the NM method are frequency-dependent and the NM solves for the parameters at one frequency within a loop of frequencies. The parameter initialization is updated after each successive frequency solution is obtained. The workflow within the NM FDO is shown in Figure 5.10.

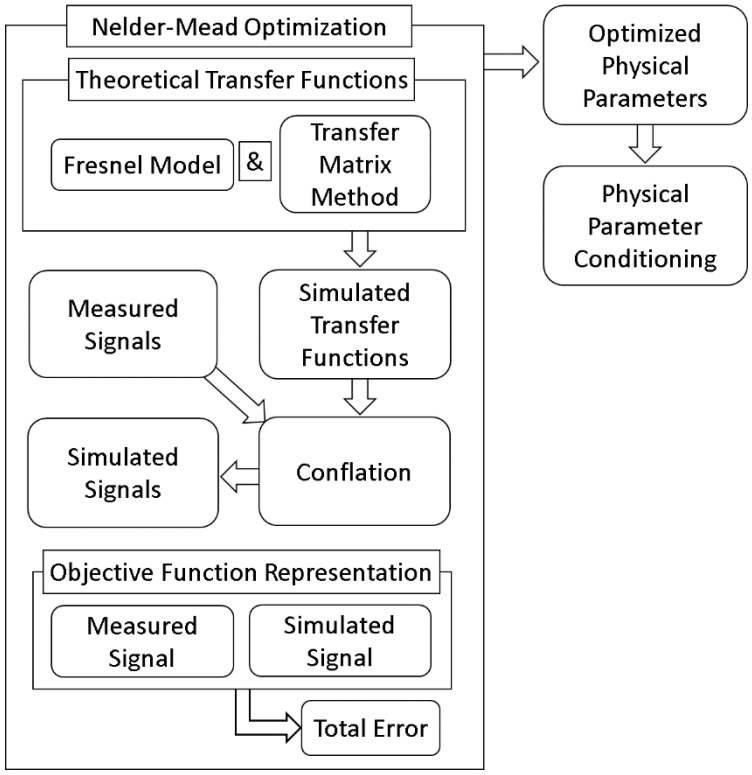

Figure 5.10) The Nelder-Mead optimization for determining the optimal solution of frequency-dependent physical parameters.

There are occurrences when updates to the physical parameters at the evaluation frequency are not desirable. If the optimization returns a flag that the solution did not converge within the allowed number of iterations, then the frequency is removed from the frequency-dependent physical parameters for all parameters after the parameters at each evaluation frequency have been optimized. If the solution fails to converge at an evaluation frequency, then the parameter values of the previous evaluation frequency are used as the update, but then the flagged frequencies are removed after all frequencies have been evaluated. Ultimately, only parameter solutions at frequencies for which the NM FDO is convergent are returned by the algorithm.

The result of the NM optimization at all the evaluation frequencies is an estimate of the frequency-dependent physical parameters at the usable frequencies of the measurement data. However, it is observed that the non-constrained NM optimization tends to converge at undesired objective function minima at evaluation frequencies for which the measurement data signal clutter value is challenging. The NM optimization converges at undesired minima because the objective function has multiple possible solutions that are within the uncertainty of the measurements. The issue is explained most clearly by examining the objective function sampled to a grid of parameter values. As an example, the objective function for single-layer HRSi at normal incidence is evaluated at a thickness of 500 μm and variable index of refraction ranging from 1–10 in steps of 0.0075. The extinction coefficient used to generate the image is the optimally determined value that pairs with the optimal index of refraction at each evaluation frequency. The image, along with the re-optimization result, is shown in Figure 5.11. Information regarding representative, frequency-dependent, signal-to-noise ratio (SNR) and signal clutter of the measurements used in Figure 5.11 are contained in Section 4.3, Section 4.4, and Section 4.6.2. The SNR information indicates that the SNR at frequencies of 1 THz, 2 THz, and 3 THz is approximately 60 decibels (dB), 40 dB and 20 dB, respectively.

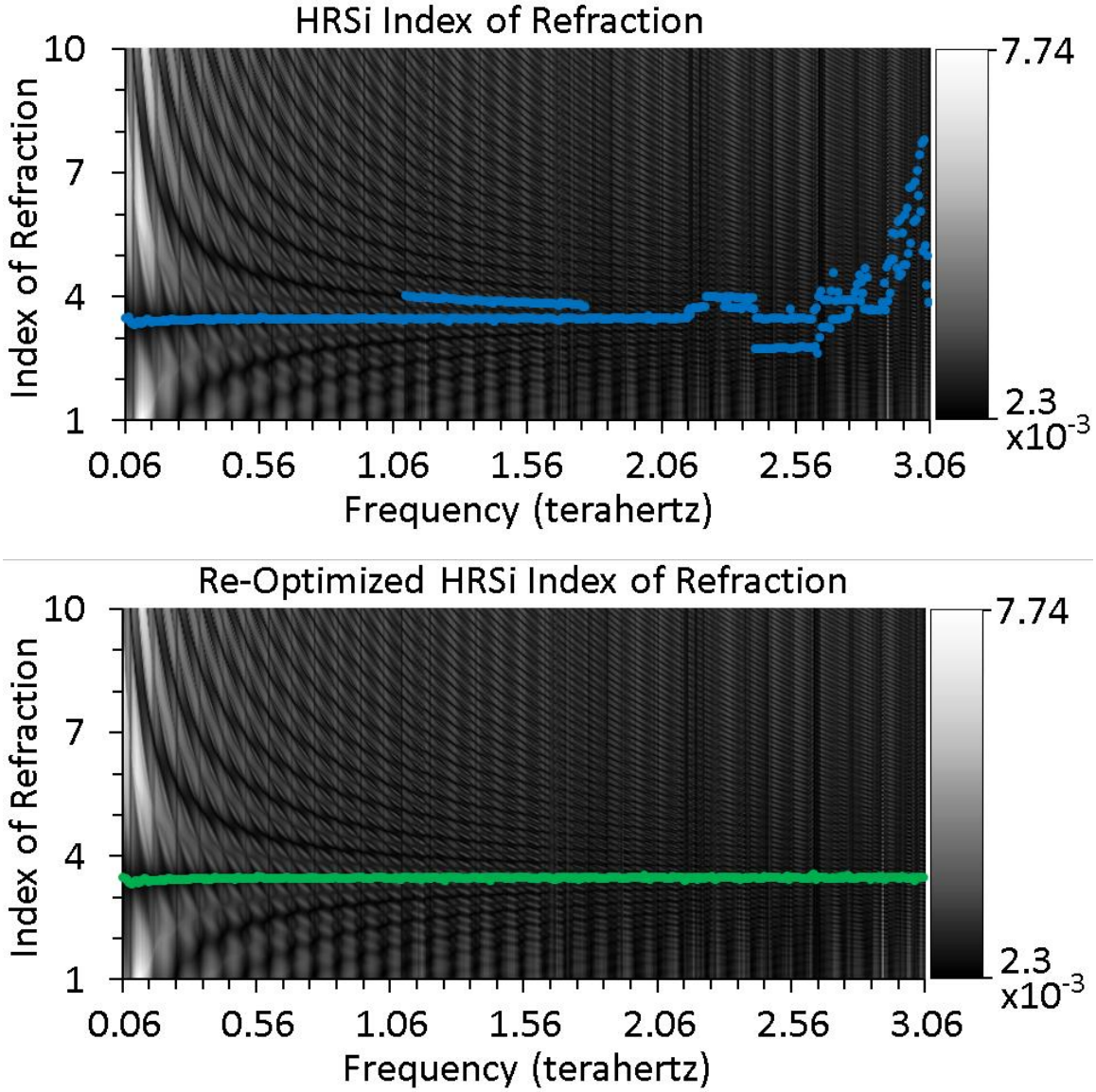

Figure 5.11) The background image in the two plots is the same. The image is the error function surface. The minimum is 2.30 and the maximum is 7.74, using a transfer function magnitude and phase formulation. The top plot (blue markers) is the index of refraction prior to re-optimization. The bottom plot (green markers) is the re-optimized result. The extinction coefficient did not meet the criteria needed to qualify for re-optimization.

The implication of the undesired minima are frequency-dependent physical parameter values that have the appearance of toggling between adjacent valleys of local minima values. The toggling of parameter values represents non-physically realistic solution behavior caused by an inability of

the algorithm to remain focused on the desired solution. Therefore, the research has found it necessary to re-optimize the parameter values at frequencies larger than the frequency at which the global minimum occurs and for which the parameters undergo excessively large variation. The extracted index of refraction of single-layer HRSi shown in the top plot of Figure 5.11 demonstrates the effect of the toggling between local minima. The frequency-domain transfer function magnitude and phase objective function formulation is used to generate the results presented in Figure 5.11.

The following explanation describes the approach that is implemented to enable the algorithm to maintain focus in the vicinity of the desired solution set. The research asserts that a portion of the desired objective function valley is contained in the final NM optimization solution. The NM optimization returns, in addition to the optimized physical parameter values, the optimal objective function value at each evaluation frequency. The research asserts that the smallest object function value returned by the NM optimization is contained in the desired portion of the NM optimization solution set.

First, the evaluation frequency that coincides with the minimum objective function value is identified. Next, the algorithm sequentially analyzes the extracted physical parameter values with increasing frequency, starting with the frequency at which the measured reference signal frequency-

domain magnitude is maximum. The frequency at which the magnitude is largest is interpreted as the frequency for which the most energy arrives at the receiver. With respect to the reference signal, the frequency of maximum signal magnitude should ideally correlate with the frequency which has the highest signal-to-clutter ratio (SCR). If multiple measurements are being simultaneously optimized, then algorithm records the frequency at which the maximum magnitude occurs for each measurement. Then, the starting frequency is the frequency at which the minimum objective function value occurs within the set of frequencies of maximum magnitude.

At each frequency, the algorithm determines if the optimal parameter value is an outlier by comparing the absolute change between the parameter value at the evaluation frequency and the preceding frequency with a threshold. If the parameter value has changed by more than the threshold, then a re-optimization at the evaluation frequency occurs and the parameter values are updated with the new result. If the parameter value has changed less than the threshold, then the parameter values at the next frequency are analyzed. The re-optimization is iterated up to a limit of ten times to achieve the desired solution. Lastly, the algorithm sequentially analyzes the extracted physical parameter values with decreasing frequency, starting with the frequency of minimum objective function value, using the same process as in the forward

frequency scanning direction. The critical assumption of the approach requires that the extracted frequency-dependent parameter values at the frequencies for which the measured reference signals frequency-domain magnitude are maximum must belong to the set of desired optimization solutions. If the extracted frequency-dependent parameter values at the frequencies for which the measured magnitudes are maximum are in the set of desired optimization solutions, then the frequency among the frequencies of maximum magnitude at which the objective function is minimum also has parameter values in the set of desired optimization solutions.

The threshold is a user defined percentage of the difference between the extrema values acceptable for a parameter. For example, the algorithm requires that all refractive indices will be constrained between 1–10. Therefore, if the user defined percentage is one, then the threshold for percent change between adjacent frequencies for the index of refraction is 0.09. As another example, if the user defined percentage is one, the algorithm requires that all extinction coefficients be constrained between 0–5. Therefore, the threshold for percent change between adjacent frequencies for the extinction coefficient is 0.05. The value of the user defined percentage depends on the material under evaluation and the whether the target variable is the index of refraction or the extinction coefficient. The research determines the

percentage by experimentation on a case-by-case basis. The methodology works well for materials with uniform optical parameter profiles such as HRSi and HDPE, but is not sufficiently robust to materials with non-uniform optical parameter profiles. Additionally, the human labor involved in manually determining the user defined percentages is incentive for the methodology to be automated in future research. The research does not investigate the applicability of the re-optimization method to adjustment of the extinction coefficient, however the research hypothesizes that the methodology is extensible to the extinction coefficient.

In the case that the physical parameter value at the evaluation frequency represents a change greater than the threshold, then the parameters at the evaluation frequency that violate the threshold are re-optimized using the constrained DE optimization. The NM optimization is an unconstrained optimization and therefore no bounds are provided for the parameter to the NM. If NM is performed in the re-optimization then it is highly likely that the same parameter value that causes the threshold violation will be obtained. Therefore, DE is used to constrain the search region of the re-optimization. To achieve a constrained DE minimization, the algorithm first identifies two of the largest objective function values. The two largest objective functions values are determined by a constrained DE maximization. The first and second

maximum are from below and above, respectively, the parameter value at the frequency preceding the evaluation frequency. The first maximization is bounded by Equations 5.33–5.34, where the lower bound is $\delta_{\mathrm{lower\_}}$, the upper bound is $\delta_{\mathrm{upper\_}}$, δ_i is the parameter value at the evaluation frequency, and δ_{i-1} is the parameter value at the frequency preceding the evaluation frequency. The second maximization is bounded by Equations 5.35–5.36, where the lower bound is $\delta_{\mathrm{lower}_+}$, the upper bound is $\delta_{\mathrm{upper}_+}$. The lower and upper global parameter value limits are $\delta_{\min}$ and $\delta_{\max}$, respectively.

$$\delta_{\mathrm{lower\_}} = (\delta_{i-1} - \mathcal{Abs}(\delta_{i-1} - \delta_i)) \geq \delta_{\min} \quad 5.33$$

$$\delta_{\mathrm{upper\_}} = \delta_{i-1} \quad 5.34$$

$$\delta_{\mathrm{lower}_+} = \delta_{i-1} \quad 5.35$$

$$\delta_{\mathrm{upper}_+} = (\delta_{i-1} + \mathcal{Abs}(\delta_{i-1} - \delta_i)) \leq \delta_{\max} \quad 5.36$$

The result of the two maximizations are two parameter values which bound the DE minimization at the evaluation frequency for the parameter that has adjacent point-to-point change which exceeds the change threshold of the algorithm. The DE re-optimization is then the minimization of the objective function constrained by the two objective function peaks on either side of the valley representing the desired solution. The re-optimization of frequency-dependent parameters which violate the change threshold results in qualitatively plausible physical parameter extractions. The result of the re-optimizing on the HRSi physical parameter extraction corresponding to the

top plot of Figure 5.11 is the bottom plot (green markers) in the bottom plot of Figure 5.11.

The final computational step is a post-processing that takes the extracted physical parameter values determined by the optimization to generate a simulated signal from a conflation of the theoretical model and measured data for each time-domain measurement. The simulated time-domain signals can be used to compare the accuracy of the physical parameter extraction results with by a direct comparison with the corresponding measured time-domain signal. The output of the computational process are three data structures. The first data structure contains the frequency-independent parameter values such as sample layer thicknesses and three-dimensional sample rotations. The second data structure contains the frequency-dependent parameter values such as complex index of refraction and complex magnetic permeability of each sample layer and for the reference measurement background. The third data structure contains the synchronized simulated sample, measured reference, and measured sample signal.

The signals are provided in the data structure as time and frequency-domain representations corresponding to each time-domain measurement. The time-domain representations include the time delay in units of seconds, the equivalent delay rail positions in units of meters, and the real-valued signal

amplitude. The frequency-domain representations include: frequencies in units of hertz, complex-valued signal amplitude, signal magnitude, and signal phase in units of radians. In addition, the frequency-domain representations include the magnitude and phase of the transfer function for simulated and measured signals. The time-domain and frequency representations are provided for each simulated sample, measured reference, and measured sample signal triad.

6. PHYSICAL PARAMETER EXTRACTIONS

The physical parameters extractions provide estimates of the optical properties of a material using the mixed error measure in the time-domain objective function formulation. The optical properties examined in the research are the frequency-dependent index of refraction and absorption coefficient. Where possible, comparisons are made between the results obtained with the approach presented in this research and results found in literature for similar materials. Because the samples and algorithms used in this research have not been evaluated by other research groups, the results presented using our algorithm and our samples are unique to this research. An ideal comparison of our results with other research approaches would consist of either the other research groups operating their algorithms on our measurement data, or us operating our algorithms on their research data algorithms. Such an ideal has not been feasible to-date.

The thousands of THz-TDS transmission measurements collected for the research are used to obtain estimates of the index of refraction and

absorption coefficient for five materials: HRSi, HDPE, α-lactose monohydrate, pharmaceutical-grade Oxycodone, and Hydrocodone. The optimal results obtained by NDE of single layer samples at normal incidence are first presented. In the case of HDPE, the optical properties of three HDPE sample thicknesses are obtained. The three HDPE samples are listed in order of increasing thickness: HDPE-C, HDPE-A, and HDPE-B. The estimated optical properties of the three HDPE samples are compared for consistency.

Furthermore, the single layer samples are also stacked using a cage plate. The resulting stacks facilitate simultaneous NDE of two samples separated by an air gap. The multi-layer samples are composed of HRSi and HDPE layers. The α-lactose monohydrate, pharmaceutical-grade Oxycodone, and Hydrocodone have not been stacked together interchangeably or with the HRSi or HDPE layers in this research. The estimated optical properties of the individual layers of a multi-layer sample are compared with the estimated optical properties extracted from the corresponding single layer measurements for consistency. Several of the multi-layer samples have a significant reduction in transmitted energy due to the additional reflections and absorption of the stacked materials. The reduction in transmitted energy also decreases the SCR sufficiently that the algorithm cannot guarantee the confidence of the optical property estimates at frequencies greater than the

frequencies presented in this section. The estimates of the optical properties are obtained for all the single and multi-layer samples at non-normal angles of incidence. Comparisons are made between the estimates at normal and non-normal incidence and normal-incidence for consistency. At increasingly oblique angles of incidence, the proportion of reflected energy typically increases which reduces the amount of transmitted energy into the material. The propagation length of the radiation transmitted into the material also increases with increasingly non-normal angles of incidence, causing an increase in the proportion of energy absorbed by the material. The highly configurable capability of the proposed algorithm facilitates simultaneous optimization of single layer and multi-layer samples.

There are two primary sources of uncertainty in the THz-TDS measurement data which directly impact the minimum thickness that extractable by the algorithm. The first source of uncertainty is the delay rail resolution. The delay rail resolution is the sampling interval between adjacent positions on the delay rail axis. The delay rail resolution is interchangeably expressed as spatial resolution and temporal resolution. The second source of uncertainty is the numerical precision of the measurement data. The measurement data is found to have a constant numerical precision of 10^{-6} for

all the data generated during the research. Statistics regarding the measurement data resolution and precision are provided in Table 6.1.

Table 6.1) Measurement statistics for the WSU external, WSU internal, and OSU internal transmission systems.

Transmission System	**WSU External**	**WSU Internal**	**OSU Internal**
Number of Measurements	554	1189	2680
Time-Domain Signal Length	16868	16769	16531
Average Spatial Resolution (μm)	3.05176	3.07302	3.11562
Average Temporal Resolution (fs)	20.3592	20.5010	20.7852
Average Frequency Resolution (GHz)	2.91190	2.90883	2.91036
Numerical Precision	10^{-6}	10^{-6}	10^{-6}

The signal length, resolution, and precision statistics presented in Table 6.1 are generated using the number of measurements for each of the three transmission systems used during the research. The research observes that for constant Teraview software settings, the WSU external transmission system yields the longest signal in terms of the number of elements in the signal, whereas the OSU internal system yields the fewest. The research observes that the average spatial resolution, and therefore temporal resolution, of the digitized delay positions is finest for the WSU external transmission system and coarsest for the OSU internal transmission system. The research observes

that the average frequency resolution, using the maximum time-domain signal lengths provided in Table 6.1, is finest for the WSU internal transmission system and coarsest for the WSU external transmission system. of the digitized delay positions is the smallest for the WSU external transmission system and largest for the OSU internal transmission system. The numerical precision of the THz-TDS measurement data is a constant 10^{-6} for all three systems and Teraview reports that the precision is not able to be affected by changing the software settings.

The non-optimized, closed-form equations used to calculate the refractive index and absorption coefficient defined in Equation 5.29 and Equation 5.30 are used to estimate a representative value for the refractive index uncertainty and absorption coefficient uncertainty. The equations used to calculate the optical property uncertainty estimates are provided in Equation 6.1 and Equations 6.2. The refractive index uncertainty is n_σ and the absorption coefficient uncertainty is α_σ. The numerical precision of certainty is defined $\Delta_\sigma = 10^{-5}$. The numerical precision of certainty is ten times the 10^{-6} numerical precision because the trailing digit in the numerical precision is uncertain. The speed of light is labelled c. The spatial and frequency resolution is labelled d_σ and ν_σ, respectively.

$$n_\sigma = \frac{c \cdot (\Delta_\sigma - (-\Delta_\sigma))}{2\pi \cdot (2 \cdot d_\sigma)} \cdot (\frac{1}{\nu_\sigma} - \frac{1}{2\nu_\sigma}) \quad 6.1$$

$$\alpha_\sigma = -\frac{2}{(2 \cdot d_\sigma)} \cdot \mathcal{L}n(\frac{((1 + n_\sigma) + 1)^2}{4 \cdot (1 + n_\sigma)}) \cdot (\mathcal{L}n(\frac{1 + \Delta_\sigma}{1}) - \mathcal{L}n(\frac{1 - \Delta_\sigma}{1})) \quad 6.2$$

The refractive index and absorption coefficient uncertainty defined by Equation 6.1 and 6.2 are used because they provide a closed-form frequency-domain calculation using the frequency resolution, spatial resolution, and measurement precision. In contrast, propagation of uncertainty directly using the optimization algorithm is a high-dimensionality, non-closed-form, logic-based, multi-measurement, multi-system fusion solution requiring more information than has been gathered during the research. The result of using Equations 6.1 and 6.2, combined with the information in Table 6.1, results in the thickness, refractive index, and absorption coefficient minimum uncertainty estimates as a function of transmission system provided in Table 6.2. The research does not provide numerical orientation uncertainty estimates, but the research hypothesizes that the orientation uncertainty is correlated to the measurement resolution and numerical precision.

Table 6.2) Physical parameter minimum uncertainty for the WSU external, WSU internal, and OSU internal transmission systems.

Transmission System	**WSU External**	**WSU Internal**	**OSU Internal**	**Average**
Thickness Uncertainty (μm)	6.10353	6.14603	6.23124	6.16027
Refractive Index Uncertainty ($x10^{-2}$)	2.68463	0.889623	0.438498	1.33758
Absorption Coefficient Uncertainty ($x10^{-2}$ cm^{-1})	5.311540	6.05883	6.17099	5.84712

The results of Table 6.2 show that the OSU internal transmission system has the highest thickness minimum uncertainty, and the WSU external transmission system has the lowest thickness minimum uncertainty. The reason is because the thickness uncertainty is directly proportional to the system spatial resolution. The refractive index minimum uncertainty is largest for the WSU external transmission system, and smallest for the OSU internal transmission system. Similarly, the absorption coefficient minimum uncertainty is largest for the WSU external transmission system, and smallest for the OSU internal transmission system. The optimized and non-optimized thickness, refractive index, and absorption coefficients have the average minimum uncertainty provided in the right-most column of Table 6.2. The TOF frequency-averaged thickness and refractive index have uncertainties unique from the minimum uncertainty provided in Table 6.2. The TOF uncertainties do not include measurement numerical precision and use time-

domain governing equations which are different than Equation 6.1 and Equation 6.2.

6.1. SINGLE LAYER SAMPLES

The goal is to demonstrate the ability of the proposed algorithm to accurately provide estimates of the optical properties of single layer and multi-layer samples at normal incidence. Typically, the normal incidence measurements have lower signal attenuation compared with non-normal incidence measurements, which yields normal incidence bandwidth that extends beyond the reliable bandwidth of non-normal incidence measurements. The useable frequency methodology attempts to provide a mechanism by which measurement data with a low confidence at the evaluation frequency are excluded from the optimization. The useable frequency methodology therefore reinforces the optical property estimates in the spectral region where the useable frequencies of the measurements mutually overlap and maintains the confidence of the estimated optical properties across the largest possible bandwidth by discarding measurement data for which the algorithm indicates the measurement signal strength is sufficiently low relative to the signal clutter.

6.1.1. OPTIMIZATIONS AT NORMAL INCIDENCE

The estimated optical properties of the single layer samples at normal incidence are presented in this section. The simplest measurement configuration investigated are the single layer samples at normal incidence. The optical property estimates obtained in this section provide a high-confidence baseline for which estimates obtained using multi-layer and non-normal incidence measurements are compared. The optical property is estimated by extracting the index of refraction and absorption coefficient of the material that composes the sample. The optical properties of five materials are estimated: HRSi, HDPE, α-lactose monohydrate, pharmaceutical-grade Oxycodone, and Hydrocodone. The optical properties of HDPE are estimated using index of refraction and absorption coefficient extractions obtained separately from the HDPE-A, HDPE-B, and HDPE-C transmission measurements. The optical property estimate of HDPE is also obtained by a simultaneous optimization of synchronized HDPE-A, HDPE-B, and HDPE-C measurements. The individual optical property estimates obtained from HDPE-A, HDPE-B, and HDPE-C are compared with the synchronized estimate.

The outline of the subsections describe the results obtained for each of the single layer samples. The frequency-domain transmission transfer

function magnitude and phase of each measurement is computed. Next, a TOF model is used to compute the thickness of the samples for each measurement. The thickness, magnitude, and phase are used in the non-optimized optical parameter equations, Equations 5.29–5.31, to calculate an initial estimate of the optical properties. Uncertainty is calculated for each evaluation frequency based on the variability in the multiple measurements. The same measurements used in the non-optimized optical parameter estimation are used in a simultaneous optimization to extract the optical properties using the optimization algorithm developed in the research. Unless specifically discussed for a particular sample, the re-optimization component of the algorithm is operated with an index of refraction threshold of 0.045, or equivalently 0.5%. No re-optimization is performed on the absorption coefficients. The thickness is determined by the optimization for the HRSi and HDPE samples using minimization of the refractive index variation. Thicknesses and orientation determination using minimization of the total optimal simulation error for the HRSi, HDPE, and α-lactose monohydrate samples are provided in Section 6.1.2. The extinction coefficient that is determined by optimization is then used in the Kramers-Kronig relationship to determine the analytic index of refraction. The analysis for each single-

layer sample investigated concludes with comparisons that are made between the non-optimized, optimized, and Kramers-Kronig results.

6.1.1.1. HIGH-RESISTIVITY SILICON

The repeated measurement of the single layer HRSi sample in varying environments using different measurement systems facilitates a simultaneous optimization of multiple measurements to estimate the sample thickness and optical parameters of HRSi. First, the thickness of the sample for each measurement is determined using a TOF model. A total of six measurements are included in the single-layer HRSi analysis. The Num Scans value of these measurements is either 100 or 1,000. The measurements are collected at OSU using the internal transmission system, and at WSU using the internal and external transmission systems. The TOF measurement specific thicknesses are presented in Table 6.3. The average and standard deviation of the six thicknesses are calculated in Table 6.4. The TOF model used in the research facilitates a calculation of the frequency-averaged index of refraction, but not absorption coefficient. The TOF center thickness and center refractive index are the values at the center of the temporal bins. The TOF lower and upper thickness are the minimum and maximum thickness bounds, respectively, calculated from the TOF uncertainty. The TOF lower and upper refractive index are the minimum and maximum thickness bounds, respectively, based

strictly on the sampling resolution of the measurement data and the TOF equations. It is important observe that the physical absorption coefficient of HRSi cannot be a negative quantity, but the non-optimized and optimized data-driven estimates yield small negative-valued absorption coefficients. The numbers in Table 6.3 and Table 6.4 are accurate to the numerical precision of the data.

Table 6.3) Time-of-Flight single layer sample thickness and frequency-averaged index of refraction and and frequency-averaged absorption coefficient for HRSi.

Time-of-Flight	**Measurement Number (1–6)**					
	1	**2**	**3**	**4**	**5**	**6**
Lower Thickness (μm)	491.361	481.915	506.355	503.497	500.802	497.211
Center Thickness (μm)	500.513	491.068	515.508	512.650	509.955	506.363
Upper Thickness (μm)	509.666	500.220	524.660	521.803	519.108	515.516
Lower Refractive Index	3.43115	3.48965	3.35024	3.35106	3.38636	3.39193
Center Refractive Index	3.48780	3.548474	3.40381	3.40493	3.44112	3.44721
Upper Refractive Index	3.54656	3.60954	3.45931	3.46077	3.49795	3.50453

Table 6.4) Time-of-Flight single layer sample thickness, frequency-averaged index of refraction, and frequency-averaged absorption coefficient for HRSi.

Time-of-Flight	**Average**	**Standard Deviation**
Center Thickness (μm)	506.010	8.20039
Center Refractive Index	3.45556	0.050317

The synchronized time-domain measurements of the HRSi sample and air reference are converted into the frequency-domain. The sample and reference measurements are divided in the frequency-domain to obtain fractional percent transmission magnitude and phase information. The magnitude and phase of the HRSi measurements, with frequency-dependent uncertainty bars, are shown in Figure 6.1. Observable in the magnitude and phase profiles are the Fabry-Perot (FP) etalon effect. The variability of the data is noticeable at frequencies greater than 1.6 THz. The bandwidth shown in Figure 6.1 is approximately 2 THz, which is the bandwidth determined by the heuristic algorithm developed in the research. All six measurements are used at each frequency in the bandwidth. The spectral magnitude profile is shown in the left plot (blue circle markers), and the spectral phase profile is shown in the right plot (green circle markers) of Figure 6.1. The solid lines connecting the data points in the plots of Figure 6.1 are for illustrative purposes.

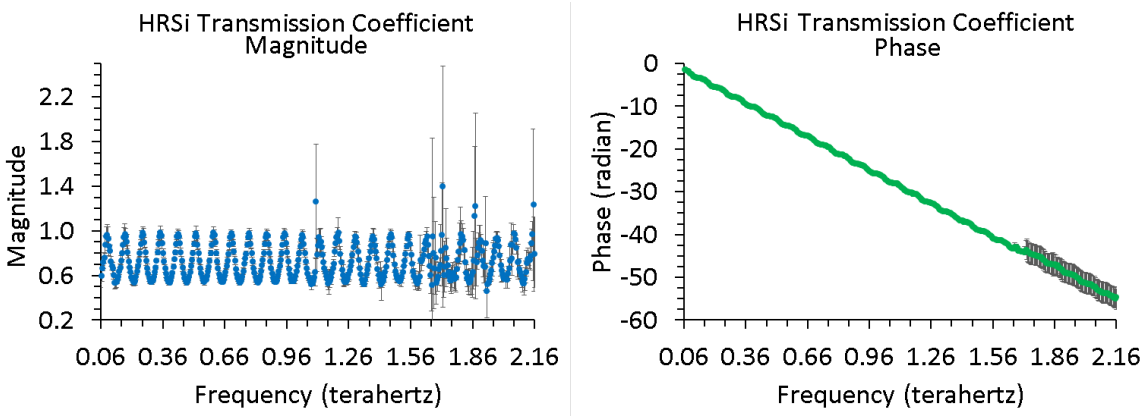

Figure 6. 1) The average of six normal incidence transmission magnitude (left) and phase (right) profiles for the HRSi sample. The uncertainty bars are the standard deviation of all the measurement values at individual frequencies.

The thickness information in Table 6.3, combined with the magnitude and phase in Figure 6.1, is used to determine non-optimized estimates for the index of refraction and absorption coefficient of HRSi across the six measurements. The non-optimized optical properties of HRSi are shown in Figure 6.2. The oscillatory features that are present in the magnitude and phase propagate to the extracted index of refraction, and the uncertainty at frequencies greater than 1.6 THz is also represented. The average non-optimized index of refraction and absorption coefficient at frequencies between 0.06–1.60 THz is approximately 3.47 and -0.45 cm^{-1}, respectively. The non-optimized average index of refraction agrees with the TOF frequency average index of refraction, however the absorption coefficient is a negative value. The index of refraction is shown in the left plot (blue triangle markers), and the absorption coefficient is shown in the right plot (green triangle

markers) of Figure 6.2. The solid lines connecting the data points in the plots of Figure 6.2 are for illustrative purposes.

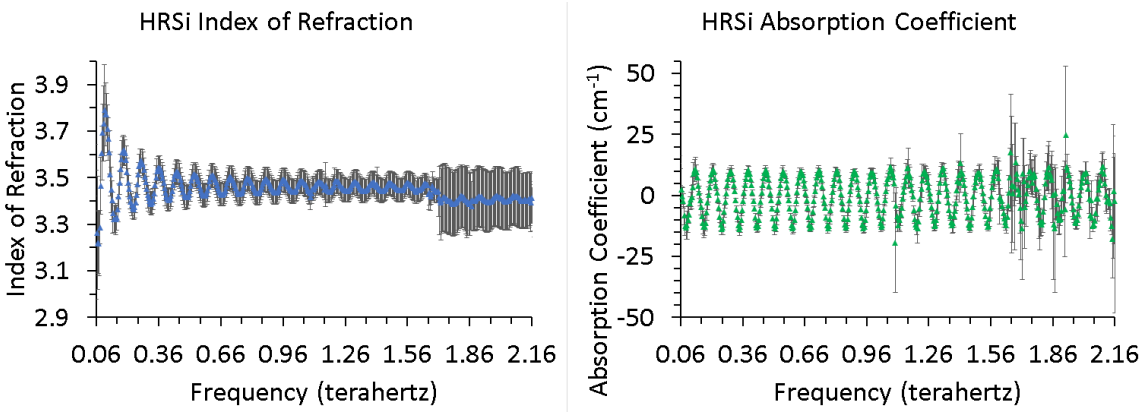

Figure 6.2) The average of six non-optimized refractive index (left) and absorption coefficient (right) profiles for the HRSi sample. The uncertainty bars are the standard deviation of all the measurement values at the frequency.

The optimization algorithm developed during the research is used to extract the thickness, index of refraction, and absorption coefficient of HRSi for the six measurements. The optimization results are shown in Figure 6.3. In Figure 6.3, the index of refraction is shown in the left plot (blue triangle markers), and the absorption coefficient is shown in the right plot (green triangle markers) of Figure 6.3. The solid lines connecting the data points in the plots of Figure 6.3 are for illustrative purposes. The average optimized index of refraction and absorption coefficient at frequencies between 0.06–2.16 THz is approximately 3.43 and 0.78 cm^{-1}, respectively. In comparison, an estimate from literature for the absorption coefficient of HRSi at 1 THz is 0.05 cm^{-1} [41, 79, 80]. The research observes the frequency region 1.56–1.86

THz in Figure 6.3 has elevated absorption. In comparison to the 0.06–2.16 THz frequency range, the average optimized absorption coefficient at frequencies between 0.06–1.56 THz is 0.053 cm^{-1} which is in better agreement with the estimate from literature. It is important to observe in Figure 6.3 that the optimized absorption coefficient does drop into negative values. The optimized average index of refraction agrees with the TOF frequency average index of refraction, with an improvement over the non-optimized result because the optimized absorption coefficient is a positive value. Furthermore, the FP etalon effect is significantly reduced in the optimized optical parameters of Figure 6.3 compared with then non-optimized optical parameters in Figure 6.2. The increased levels of variation in the absorption coefficient at frequencies greater than 1.6 THz in Figure 6.3 is correlated with the increased measurement uncertainty in the same frequency region in Figure 6.1.

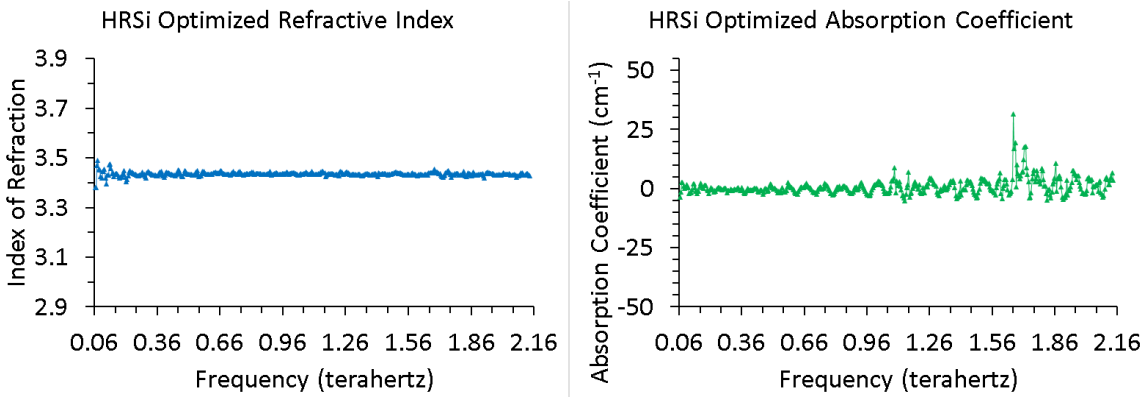

Figure 6.3) The six-measurement optimization extracted refractive index (left) and absorption coefficient (right) profile of the HRSi sample.

In addition to the index of refraction and absorption coefficient of HRSi, the sample thickness and effective fractional percent water vapor by air volume are determined by the optimization algorithm. The thickness is determined to be 509.627 μm, and the effective percent water vapor is 0.0049%. Referring to Table 6.3, the thickness parameter bounds are defined 491.068–515.508 μm. The final component of the analysis for HRSi is a comparison with the Kramers-Kronig result. The HRSi optimization extracted absorption coefficient is used to compute the discrete form of the analytical Kramers-Kronig relationship for refractive index, shown in the left plot (blue triangle markers) of Figure 6.4. Shown in the right plot of Figure 6.4 is the percent difference of the optimized and Kramers-Kronig refractive index (red triangle markers).

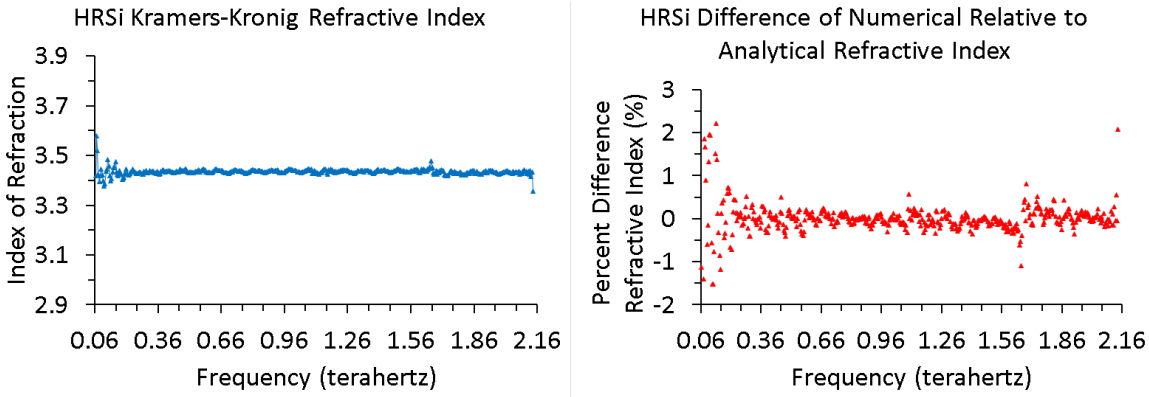

Figure 6.4) The left plot is the Kramers-Kronig index of refraction determined using the six-measurement optimization extracted HRSi absorption coefficient. The right plot is the percent difference of the numerically optimized refractive index relative to the discrete form of the analytical Kramers-Kronig relationship.

The average absolute difference between the Kramers-Kronig and optimization extracted index of refraction is $3.8x10^{-2}$. Based on the evidence provided in the right plot of Figure 6.4, the largest negative and largest positive percent difference between the Kramers-Kronig and optimization extracted index of refraction is -1.5% and 2.2%, respectively. Therefore, the research assesses that the HRSi refractive index extracted by numerical optimization agrees with the analytic form, and satisfies the causality principle for stable physical systems.

6.1.1.2. HIGH-DENSITY POLYETHYLENE

The repeated measurement of three single layer HDPE samples, each of different thickness, in varying environments using different measurement systems facilitates a simultaneous optimization of multiple measurements to estimate the sample thickness and optical parameters of the HDPE samples. The three samples are labelled HDPE-A, HDPE-B, and HDPE-C. The Num Scans value of these measurements is either 100 or 1,000. The measurements are collected at OSU using the internal transmission system, and at WSU using the internal and external transmission systems. The section first analyzes the single layer HDPE-A, HDPE-B, and HDPE-C optimization results. Next, the research performs a simultaneous optimization of all the single layer HDPE-A, HDPE-B, and HDPE-C collected together in one

simulation. Then the simultaneous optimization of single-layer HDPE-A and HDPE-C is analyzed.

First, the thickness of the HDPE-A sample for each measurement is determined using a TOF model. A total of eight measurements are included in the single layer HDPE-A analysis. The TOF measurement specific thicknesses are presented in Table 6.5a and Table 6.5b. The average and standard deviation of the eight thicknesses from Table 6.5a and Table 6.5b are presented in Table 6.6. The TOF model used in the research facilitates a calculation of the frequency-averaged index of refraction, but not absorption coefficient. The TOF center thickness and center refractive index are the values at the center of the temporal bins. The TOF lower and upper thickness are the minimum and maximum thickness bounds, respectively, calculated from the TOF uncertainty. The TOF lower and upper refractive index are the minimum and maximum thickness bounds, respectively, based strictly on the sampling resolution of the measurement data and the TOF equations. It is important observe that the physical absorption coefficient of HRSi cannot be a negative quantity, but the non-optimized and optimized data-driven estimates yield small negative-valued absorption coefficients. The numbers in Table 6.2 are accurate to the numerical precision of the data.

Table 6.5a) Time-of-Flight single layer sample thickness and frequency-averaged index of refraction for HDPE-A.

Time-of-Flight	**Measurement Number (1–4)**			
	1	**2**	**3**	**4**
Lower Thickness (μm)	3005.20	3017.33	3014.64	3032.91
Center Thickness (μm)	3014.36	3026.48	3023.79	3042.06
Upper Thickness (μm)	3023.51	3035.63	3032.95	3051.22
Lower Refractive Index	1.55539	1.54518	1.55159	1.5423
Center Refractive Index	1.55911	1.54885	1.55528	1.54594
Upper Refractive Index	1.56284	1.55253	1.55899	1.5496

Table 6.5b) Time-of-Flight single layer sample thickness and frequency-averaged index of refraction for HDPE-A.

Time-of-Flight	Measurement Number (5–8)			
	5	6	7	8
Lower Thickness (μm)	3026.93	3038.77	3017.49	3014.03
Center Thickness (μm)	3036.08	3047.92	3026.64	3023.19
Upper Thickness (μm)	3045.23	3057.07	3035.80	3032.34
Lower Refractive Index	1.54533	1.54332	1.54910	1.54983
Center Refractive Index	1.54899	1.54695	1.55278	1.55351
Upper Refractive Index	1.55266	1.55061	1.55647	1.55721

Table 6.6) Time-of-Flight single layer sample thickness and frequency-averaged index of refraction for HDPE-A.

Time-of-Flight	Average	Standard Deviation
Center Thickness (μm)	3030.07	10.34995
Center Refractive Index	1.55143	4.22227×10^{-3}

The synchronized time-domain measurements of the HDPE-A sample and air reference are converted into the frequency-domain. The sample and reference measurements are divided in the frequency-domain to obtain fractional percent transmission magnitude and phase information. The magnitude and phase of the HDPE-A measurements, with frequency-

dependent uncertainty bars, are shown in Figure 6.5. Observable in the spectral magnitude and phase profiles are the Fabry-Perot (FP) etalon effect. The FP etalon effect in the plots of Figure 6.5 is less pronounced than the FP etalon effect observed in Figure 6.1 for HRSi. The possible source of the FP etalon effect greater in HRSi than HDPE, for same sample thickness, is because the refractive index of HRSi is 2.3 time greater than HDPE which increases internal sample reflections. The variability of the fractional percent transmission data is noticeable at frequencies greater than 1.0 THz. The bandwidth shown in Figure 6.5 is approximately 1.6 THz, which is the bandwidth determined by the heuristic algorithm developed in the research. All eight measurements are used at each frequency in the bandwidth. The magnitude is shown in the left plot (blue circle markers), and the phase is shown in the right plot (green circle markers) of Figure 6.5. The solid lines connecting the data points in the plots of Figure 6.5 are for illustrative purposes.

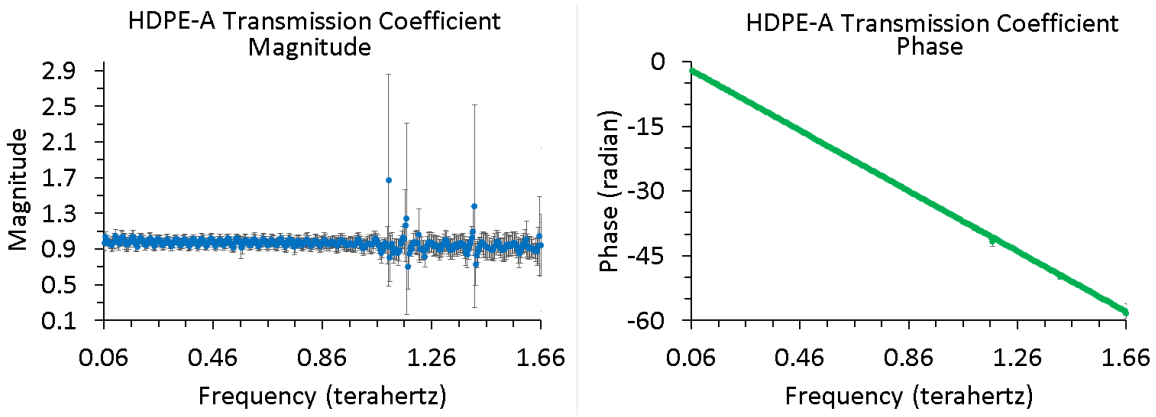

Figure 6.5) The average of eight normal incidence transmission magnitude (left) and phase (right) profiles for the HDPE-A sample. The uncertainty bars are the standard deviation of all the measurement values at individual frequencies.

The thickness information in Table 6.5, combined with the magnitude and phase in Figure 6.5, is used to determine non-optimized estimates for the index of refraction and absorption coefficient of HDPE-A across the eight measurements. The non-optimized optical properties of HDPE-A are shown in Figure 6.6. The oscillatory features that are present in the magnitude and phase propagate to the extracted index of refraction, and the uncertainty at frequencies greater than 1.0 THz is also represented. The average non-optimized index of refraction and absorption coefficient at frequencies between 0.06–1.06 THz is approximately 1.55 and -0.10 cm^{-1}, respectively. The non-optimized average index of refraction agrees with the TOF frequency average index of refraction, however the absorption coefficient is a negative value. The index of refraction is shown in the left plot (blue triangle markers), and the absorption coefficient is shown in the right plot (green triangle

markers) of Figure 6.6. The solid lines connecting the data points in the plots of Figure 6.6 are for illustrative purposes.

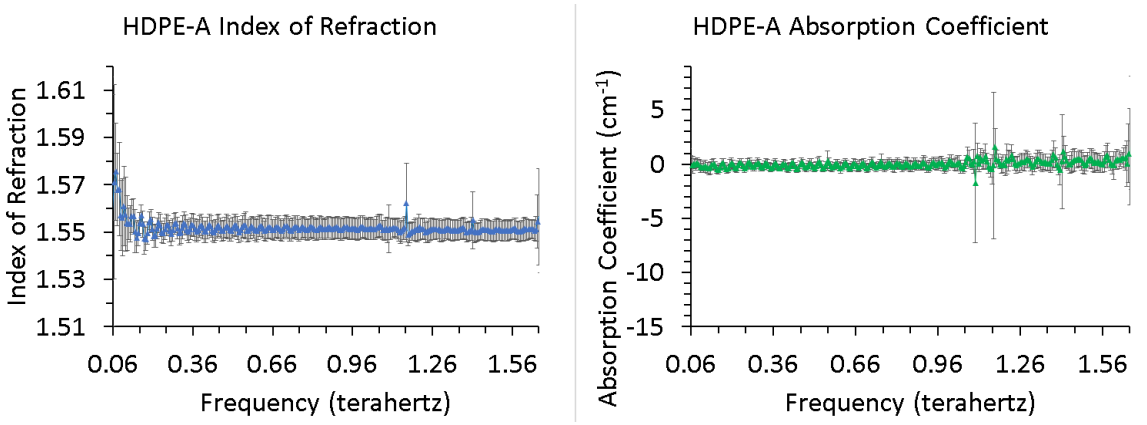

Figure 6.6) The average of eight non-optimized refractive index (left) and absorption coefficient (right) profiles for the HDPE-A sample. The uncertainty bars are the standard deviation of all the measurement values at the frequency.

The optimization algorithm developed during the research is used to extract the thickness, index of refraction, and absorption coefficient of HDPE-A for the eight measurements. The optimization results are shown in Figure 6.7. The index of refraction is shown in the left plot (blue triangle markers), and the absorption coefficient is shown in the right plot (green triangle markers) of Figure 6.7. The solid lines connecting the data points in the plots of Figure 6.7 are for illustrative purposes. The average optimized index of refraction and absorption coefficient at frequencies between 0.06–1.06 THz is approximately 1.55 and 0.014 cm^{-1}, respectively. In comparison, an estimate from literature for the absorption coefficient of HDPE at 1 THz is 0.27 cm^{-1} [81, 82, 83, 84, 85, 86, 87]. In comparison to the 0.06–1.06 THz frequency

range, the average optimized absorption coefficient at frequencies between 0.06–1.66 THz, ignoring the five largest positive-valued outliers at frequencies greater than 1.09 THz, is 0.15 cm^{-1} which is in better agreement with the estimate from literature. It is important to observe in Figure 6.7 that the optimized absorption coefficient does drop into negative values. The optimized average index of refraction agrees with the TOF frequency average index of refraction, with an improvement over the non-optimized result because the optimized absorption coefficient is a positive value. Furthermore, the FP etalon effect is significantly reduced in the optimized optical parameters of Figure 6.7 compared with then non-optimized optical parameters in Figure 6.6. The increased levels of variation in the absorption coefficient at frequencies greater than 1.0 THz in Figure 6.7 is correlated with the increased measurement uncertainty in the same frequency region in Figure 6.5.

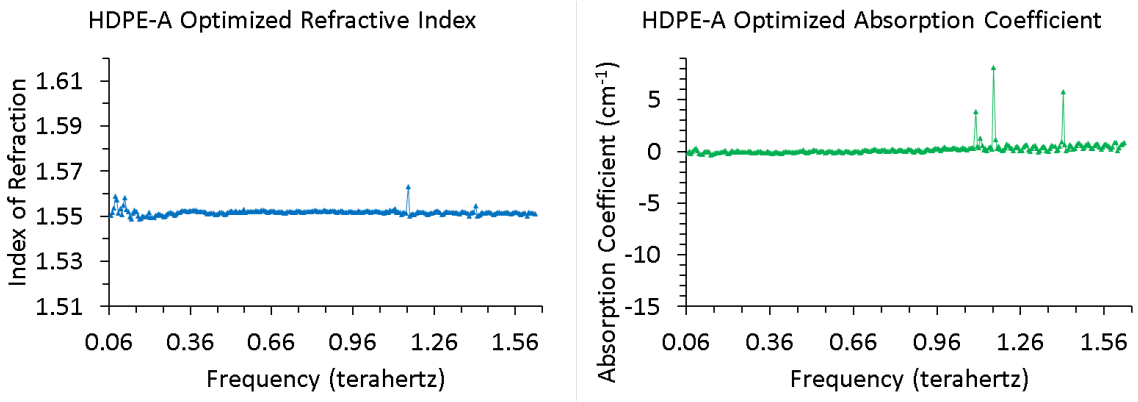

Figure 6.7) The eight-measurement optimization extracted refractive index (left) and absorption coefficient (right) profile of the HDPE-A sample.

In addition to the index of refraction and absorption coefficient of HDPE-A, the sample thickness and effective fractional percent water vapor by air volume are determined by the optimization algorithm. The thickness is determined to be 3025.41 μm, and the effective percent water vapor is 0.03%. Referring to Table 6.5, the thickness parameter bounds are defined 3014.36–3047.92 μm. The final component of the analysis for HDPE-A is a comparison with the Kramers-Kronig result. The HDPE-A optimization extracted absorption coefficient is used to compute the discrete form of the analytical Kramers-Kronig relationship for refractive index, shown in the left plot (blue triangle markers) of Figure 6.8. Shown in the right plot of Figure 6.8 is the percent difference of the optimized and Kramers-Kronig refractive index (red triangle markers).

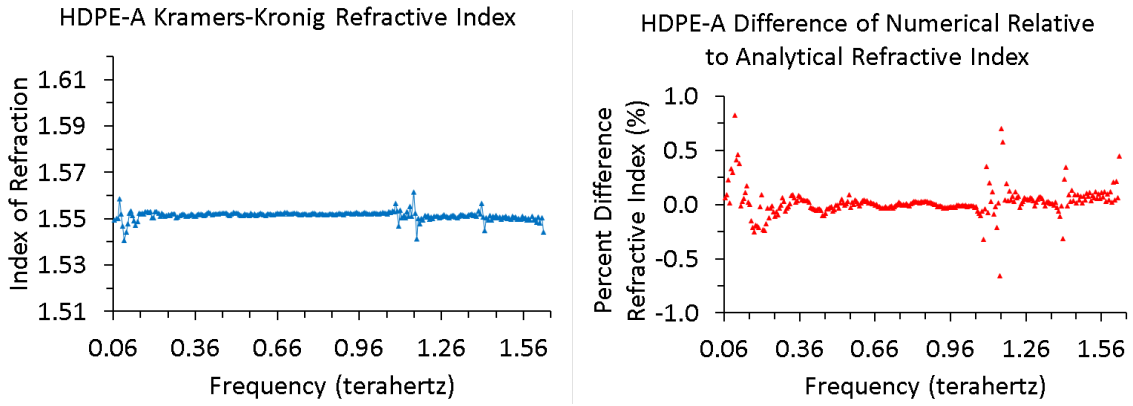

Figure 6.8) The left plot is the Kramers-Kronig index of refraction determined using the eight-measurement optimization extracted HDPE-A absorption coefficient. The right plot is the percent difference of the numerically optimized refractive index relative to the discrete form of the analytical Kramers-Kronig relationship.

The average absolute difference between the Kramers-Kronig and optimization extracted index of refraction is 9.545×10^{-4}. Based on the evidence provided in the right plot of Figure 6.8, the largest negative and largest positive percent difference between the Kramers-Kronig and optimization extracted index of refraction is -0.66% and 0.82%, respectively. Therefore, the research assesses that the HDPE-A refractive index extracted by numerical optimization agrees with the analytic form, and satisfies the causality principle for stable physical systems.

The thickness of the HDPE-B sample for each measurement is determined using a TOF model. A total of five measurements are included in the single layer HDPE-B analysis. The TOF measurement specific thicknesses are presented in Table 6.7. The average and standard deviation of the five thicknesses are calculated in Table 6.8. The TOF model used in the research facilitates a calculation of the frequency-averaged index of refraction, but not absorption coefficient. The TOF center thickness and center refractive index are the values at the center of the temporal bins. The TOF lower and upper thickness are the minimum and maximum thickness bounds, respectively, calculated from the TOF uncertainty. The TOF lower and upper refractive index are the minimum and maximum thickness bounds, respectively, based strictly on the sampling resolution of the measurement data and the TOF

equations. It is important observe that the physical absorption coefficient of HRSi cannot be a negative quantity, but the non-optimized and optimized data-driven estimates yield small negative-valued absorption coefficients. The numbers in Table 6.7 and Table 6.8 are accurate to the numerical precision of the data.

Table 6.7) Time-of-Flight single layer sample thickness and frequency-averaged index of refraction for HDPE-B.

Time-of-Flight	**Measurement Number (1–5)**				
	1	**2**	**3**	**4**	**5**
Lower Thickness (μm)	5982.83	5940.42	5973.69	5994.82	6003.96
Center Thickness (μm)	5991.98	5949.58	5982.84	6003.97	6013.11
Upper Thickness (μm)	6001.13	5958.73	5991.99	6013.12	6022.27
Lower Refractive Index	1.54542	1.54824	1.54115	1.54334	1.53948
Center Refractive Index	1.55911	1.54885	1.55528	1.54594	1.54899
Upper Refractive Index	1.54913	1.55199	1.54485	1.54703	1.54315

Table 6.8) Time-of-Flight single layer sample thickness and frequency-averaged index of refraction for HDPE-B.

Time-of-Flight	Average	Standard Deviation
Center Thickness (μm)	5988.30	21.9281
Center Refractive Index	1.54538	0.003106

The transmission transfer function magnitude and phase of the HDPE-B measurements, with frequency-dependent uncertainty bars, are shown in Figure 6.9. Observable in the magnitude and phase profiles are the FP etalon effect. The amplitude of the FP etalon effect is less than that in the HRSi and HDPE-A sample measurements. The FP etalon effect is less pronounced in the HDPE-B measurements compared with HDPE-A. The cause is because the HDPE-B is twice as thick, which reduces the radiation power by half compared to HDPE-A each time the radiation propagates across the sample. HDPE-B internally reflected radiation that eventually is transmitted to the receiver will have diminished power compared to HDPE-A, and the detected power decreases for radiation contributions that experience more internal reflections. Additionally, the variability of the data is noticeable at a majority of the frequencies throughout the spectral magnitude profile. The bandwidth shown in Figure 6.9 is approximately 1.6 THz, which is the bandwidth determined by the heuristic algorithm developed in the research. All five

measurements are used at each frequency in the bandwidth. The magnitude is shown in the left plot (blue circle markers), and the phase is shown in the right plot (green circle markers) of Figure 6.9. The solid lines connecting the data points in the plots of Figure 6.9 are for illustrative purposes.

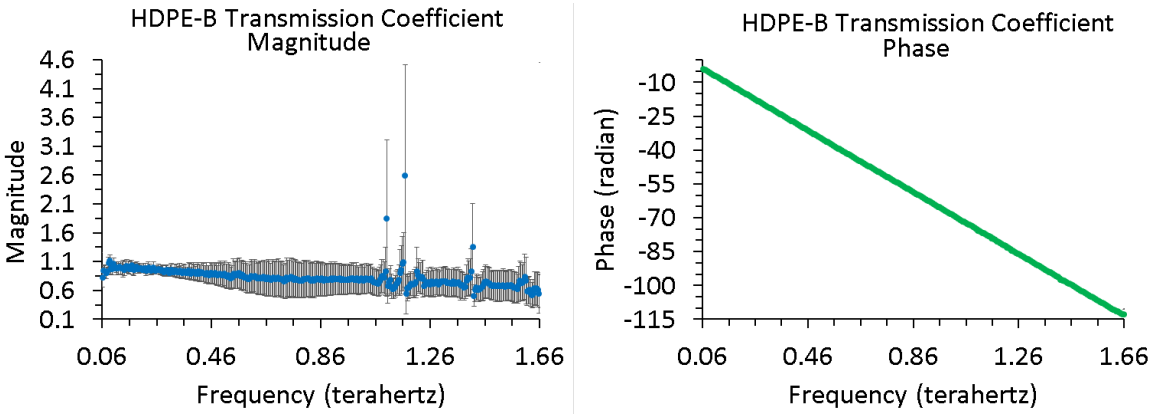

Figure 6.9) The average of five normal incidence transmission magnitude (left) and phase (right) profiles for the HDPE-B sample. The uncertainty bars are the standard deviation of all the measurement values at individual frequencies.

The thickness information in Table 6.7, combined with the magnitude and phase in Figure 6.9, is used to determine non-optimized estimates for the index of refraction and absorption coefficient of HDPE-B across the five measurements. The non-optimized optical properties of HDPE-B are shown in Figure 6.10. The oscillatory features that are present in the magnitude and phase propagate to the extracted index of refraction, and the uncertainty at frequencies greater than 1.6 THz is also represented. The average non-optimized index of refraction and absorption coefficient at frequencies between 0.06–1.60 THz is approximately 1.55 and 0.189 cm^{-1}, respectively.

The non-optimized average index of refraction agrees with the TOF frequency average index of refraction and the absorption coefficient is a positive value. The index of refraction is shown in the left plot (blue triangle markers), and the absorption coefficient is shown in the right plot (green triangle markers) of Figure 6.10. The solid lines connecting the data points in the plots of Figure 6.10 are for illustrative purposes.

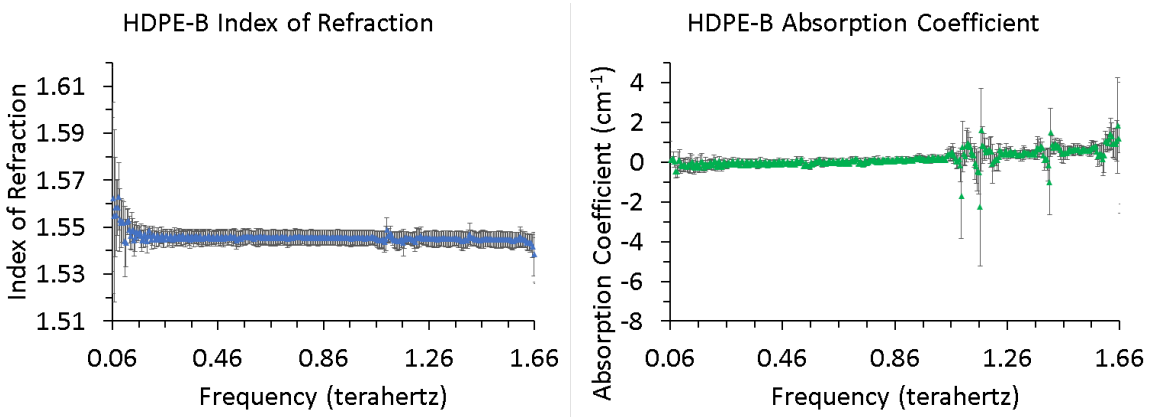

Figure 6.10) The average of five non-optimized refractive index (left) and absorption coefficient (right) profiles for the HDPE-B sample. The uncertainty bars are the standard deviation of all the measurement values at the frequency.

The optimization algorithm developed during the research is used to extract the thickness, index of refraction, and absorption coefficient of HDPE-B for the five measurements. The optimization results are shown in Figure 6.11. The optimization results are shown in Figure 6.11. The index of refraction is shown in the left plot of Figure 6.11 using blue triangle markers, and the absorption coefficient in the right plot using green triangle markers. The solid lines connecting the data points in the plots of Figure 6.11 are for

illustrative purposes. The average optimized index of refraction and absorption coefficient at frequencies between 0.06–1.06 THz is approximately 1.54 and 0.0083 cm^{-1}, respectively. In comparison to the 0.06–1.06 THz frequency range, the average optimized absorption coefficient at frequencies between 0.06–1.66 THz is 0.32 cm^{-1} which is close to the estimate of 0.27 cm^{-1} from literature, but twice as large as the optimized result of 0.15cm^{-1} in the same frequency range for HDPE-A. The optimized average index of refraction agrees with the TOF frequency average index of refraction, with an improvement over the non-optimized result because the optimized absorption coefficient is a positive value. Furthermore, the FP etalon effect is significantly reduced in the optimized optical parameters of Figure 6.11 compared with then non-optimized optical parameters in Figure 6.10. The increased levels of variation in the absorption coefficient at frequencies greater than 1.0 THz in Figure 6.11 is correlated with the increased measurement uncertainty in the same frequency region in Figure 6.9 and Figure 6.10.

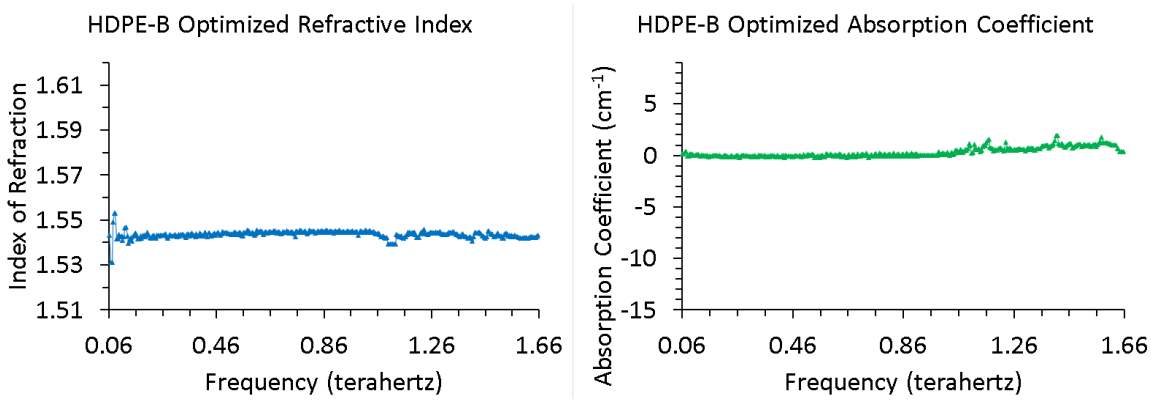

Figure 6.11) The five-measurement optimization extracted refractive index (left) and absorption coefficient (right) profile of the HDPE-B sample.

The difficulty presented by the HDPE-B data is associated with the combined effect of the absorption over the large thickness of the sample. As a result, a more aggressive re-optimization is performed on the HDPE-B refractive index. Ultimately, the result is degraded confidence in the results at frequencies greater than 1.0 THz. The HDPE-B optimization determined thickness is 5997.82 μm, and the effective percent water vapor is (7.71×10^{-3})%. Referring to Table 6.7, the thickness parameter bounds are defined 5949.58–6013.11 μm. The final component of the analysis for HDPE-B is a comparison with the Kramers-Kronig result. The HDPE-B extracted absorption coefficient is used to compute the discrete form of the analytical Kramers-Kronig relationship for refractive index, shown in Figure 6.12.

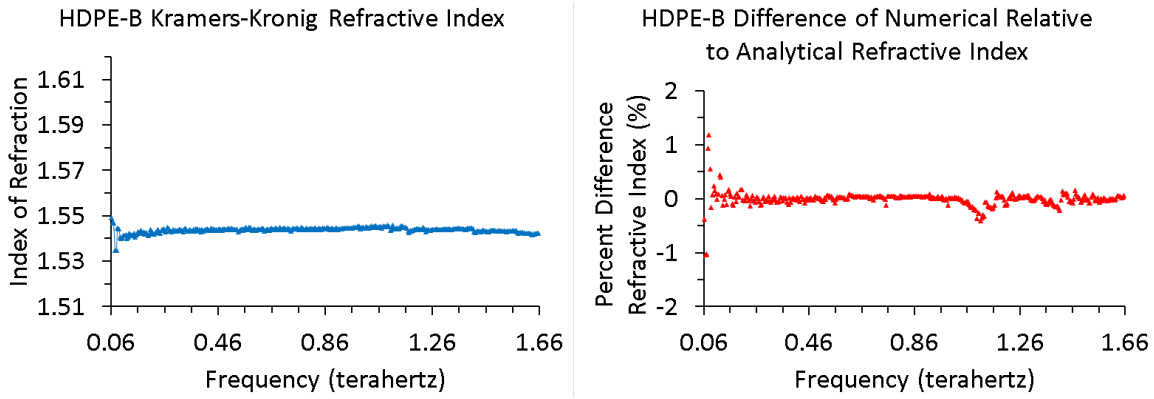

Figure 6.12) The left plot is the Kramers-Kronig index of refraction determined using the five-measurement optimization extracted HDPE-B absorption coefficient. The right plot is the percent difference of the numerically optimized refractive index relative to the discrete form of the analytical Kramers-Kronig relationship.

The average absolute difference between the Kramers-Kronig and optimization extracted index of refraction is 5.8×10^{-3}. Based on the evidence provided in the right plot of Figure 6.12, the largest negative and largest positive percent difference between the Kramers-Kronig and optimization extracted index of refraction is -1.04% and 1.18%, respectively. Therefore, the research assesses that the HDPE-B refractive index extracted by numerical optimization agrees with the analytic form, and satisfies the causality principle for stable physical systems.

The thickness of the HDPE-C sample is obtained using the only normal incidence measurement available at the time of the writing of this manuscript. The thickness is determined using the TOF model. The single TOF thicknesses is presented in Table 6.9. The TOF model used in the research facilitates a calculation of the frequency-averaged index of refraction, but not

absorption coefficient. The TOF center thickness and center refractive index are the values at the center of the temporal bins. The TOF lower and upper thickness are the minimum and maximum thickness bounds, respectively, calculated from the TOF uncertainty. The TOF lower and upper refractive index are the minimum and maximum thickness bounds, respectively, based strictly on the sampling resolution of the measurement data and the TOF equations. It is important observe that the physical absorption coefficient of HRSi cannot be a negative quantity, but the non-optimized and optimized data-driven estimates yield small negative-valued absorption coefficients. The numbers in Table 6.9 are accurate to the numerical precision of the data.

Table 6.9) Time-of-Flight single layer sample thickness and frequency-averaged index of refraction for HDPE-C.

Time-of-Flight	**Measurement Number (1)**
	1
Lower Thickness (μm)	1592.36
Center Thickness (μm)	1601.51
Upper Thickness (μm)	1610.67
Lower Refractive Index	1.54984
Center Refractive Index	1.55679
Upper Refractive Index	1.56382

The transmission transfer function magnitude and phase of the HDPE-C measurement is shown in Figure 6.13. Observable in the magnitude and

phase profiles are the FP etalon effect. The FP etalon effect is most pronounced for HDPE-C compared with HDPE-A and HDPE-B. The HDPE-C sample is the thinnest of the three HDPE samples. The amplitude of the FP oscillations is greatest for HDPE-C and least for HDPE-B, and the thickness of HDPE-C is the smallest and HDPE-B the largest. The variability of the magnitude data is noticeable at frequencies greater than 1.2 THz, with variability increasing at frequencies greater than 1.6 THz. The bandwidth shown in Figure 6.13 is 2.3 THz, but 3.0 THz is the bandwidth determined by the heuristic algorithm developed in the research. The spectral magnitude is shown in the left plot (blue circle markers), and the spectral phase is shown in the right plot (green circle markers) of Figure 6.13. The solid lines connecting the data points in the plots of Figure 6.13 are for illustrative purposes.

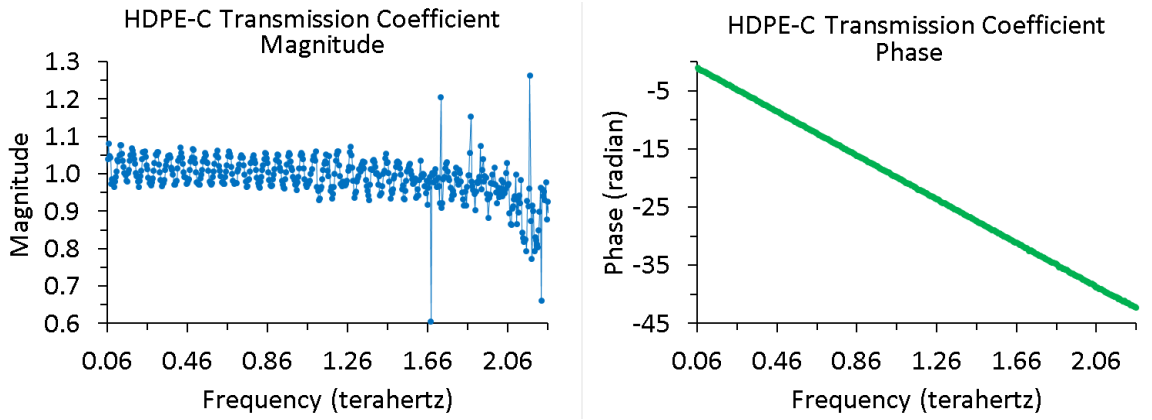

Figure 6.13) The normal incidence transmission magnitude (left) and phase (right) profile of the HDPE-C sample. The uncertainty bars are the standard deviation of the measurement at individual frequencies.

The thickness information in Table 6.9, combined with the magnitude and phase in Figure 6.13, is used to determine a non-optimized estimate for the index of refraction and absorption coefficient of HDPE-C. The non-optimized optical properties of HDPE-C are shown in Figure 6.14. The oscillatory features that are present in the magnitude and phase propagate to the extracted index of refraction. The average non-optimized index of refraction and absorption coefficient at frequencies between 0.06–2.06 THz is approximately 1.56 and -0.58 cm^{-1}, respectively. The non-optimized average index of refraction agrees with the TOF frequency average index of refraction, however the absorption coefficient is a negative value. The non-optimized result shows the presence of a weak absorption feature with a peak absorption coefficient of 2.6 cm^{-1} centered around a frequency of 2.17 THz. The index of refraction is shown in the left plot (blue triangle markers), and the absorption coefficient is shown in the right plot (green triangle markers) of Figure 6.14. The solid lines connecting the data points in the plots of Figure 6.14 are for illustrative purposes.

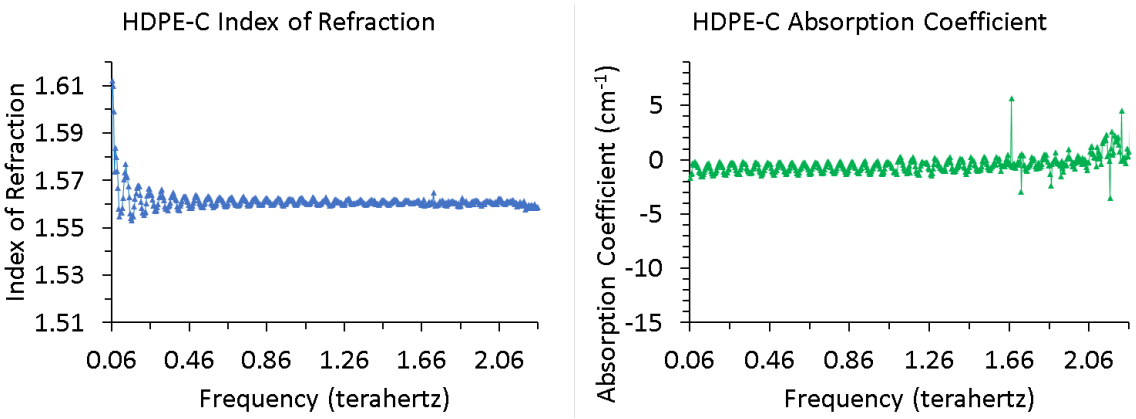

Figure 6.14) The non-optimized refractive index (left) and absorption coefficient (right) profile of the HDPE-C sample.

The optimization algorithm developed during the research is used to extract the thickness, index of refraction, and absorption coefficient of HDPE for the single HDPE-C normal incidence measurement. The optimization results are shown in Figure 6.15. In Figure 6.15, the index of refraction is shown in the left plot (blue triangle markers), and the absorption coefficient is shown in the right plot (green triangle markers) of Figure 6.15. The solid lines connecting the data points in the plots of Figure 6.15 are for illustrative purposes. The average optimized index of refraction and absorption coefficient at frequencies between 0.06–2.06 THz is approximately 1.56 and -0.53 cm^{-1}, respectively. The optimized average index of refraction agrees with the TOF frequency average index of refraction and the non-optimized result, however the absorption coefficient is a negative value but agrees with the non-optimized result. Similar to the non-optimized result, the optimized result shows the presence of a weak absorption feature centered around a

frequency of 2.17 THz. Additionally, the FP etalon effect is significantly reduced in the optimized optical parameters of Figure 6.15 compared with then non-optimized optical parameters in Figure 6.14. The increased levels of variation in the absorption coefficient at frequencies greater than 2.0 THz in Figure 6.15 is correlated with the variability in the corresponding non-optimized optical properties in Figure 6.14

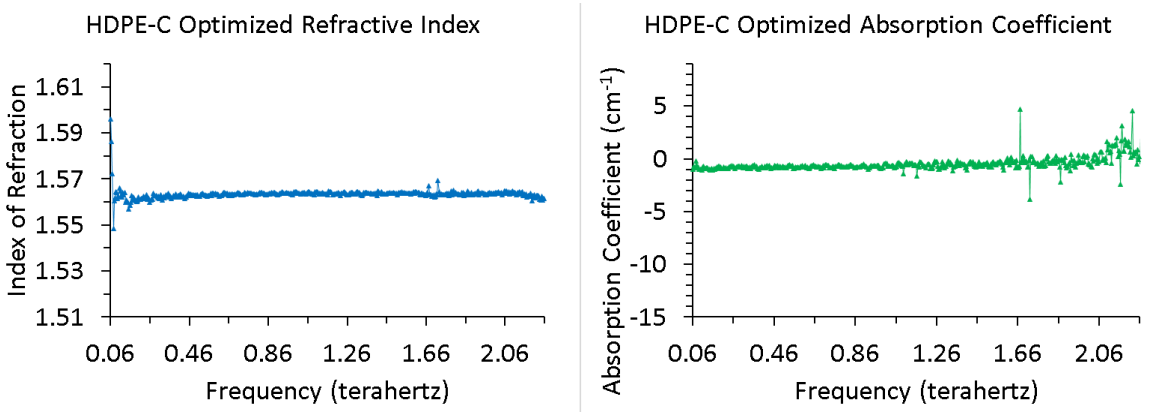

Figure 6.15) The single-measurement optimization extracted refractive index (left) and absorption coefficient (right) profile of the HDPE-C sample.

In addition to the index of refraction and absorption coefficient of HDPE-C, the sample thickness and effective fractional percent water vapor by air volume are determined by the optimization algorithm. The thickness is determined to be 1592.46 μm, and the effective percent water vapor is 0.0%. The thickness parameter bounds are defined 1550.0–1650.0 μm. The expanded range is used even though one micrometer is approximately the smallest thickness interval that can be calculated using the TOF model for the HDPE-C measurement, based on the delay rail sampling interval of the time-

domain data. The final component of the analysis for HDPE-C is a comparison with the Kramers-Kronig result. The HDPE-C optimization extracted absorption coefficient is used to compute the discrete form of the analytical Kramers-Kronig relationship for refractive index, shown in the left plot (blue triangle markers) of Figure 6.16. Shown in the right plot of Figure 6.16 is the percent difference of the optimized and Kramers-Kronig refractive index (red triangle markers).

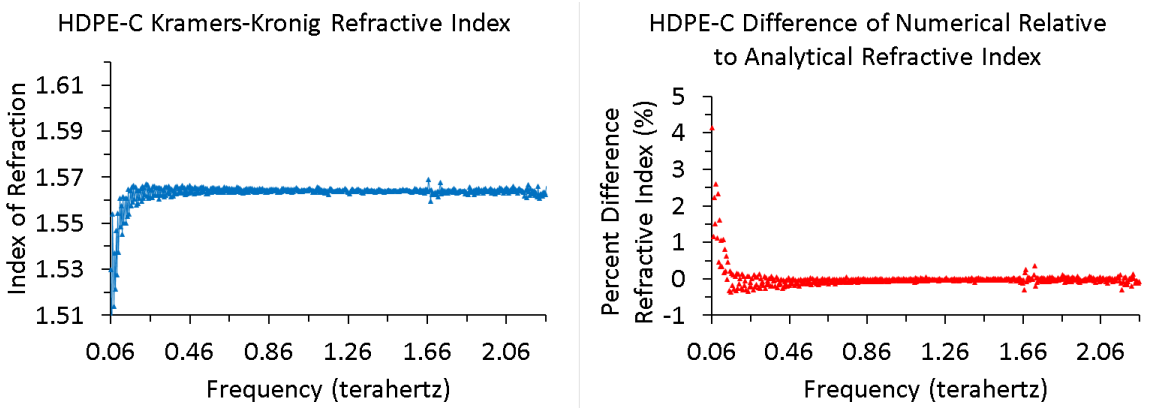

Figure 6.16) The left plot is the Kramers-Kronig index of refraction determined using the single-measurement optimization extracted HDPE-C absorption coefficient. The right plot is the percent difference of the numerically optimized refractive index relative to the discrete form of the analytical Kramers-Kronig relationship.

The average absolute difference between the Kramers-Kronig and optimization extracted index of refraction is 1.7×10^{-2}. Based on the evidence in the right plot of Figure 6.16, the largest negative and largest positive percent difference between the Kramers-Kronig and optimization extracted index of refraction is -0.3% and 4.1%, respectively. Therefore, the research assesses that the HDPE-C refractive index extracted by numerical optimization agrees

with the analytic form, and satisfies the causality principle for stable physical systems. The research observes that the thickness of HDPE-B is twice as thick as HDPE-A, and HDPE-A is twice as thick as HDPE-C. The research further observes that the average absorption coefficient of HDPE-B, HDPE-A, and HDPE-C in the frequency range 0.06–1.66 THz is 0.32cm^{-1}, 0.15cm^{-1}, and -0.67 cm^{-1}. Therefore, the optimized average absorption coefficient of HDPE appears to be dependent on the thickness of the HDPE layer, specifically that the optimized average absorption decreases with decreasing thickness.

The Kramers-Kronig analysis demonstrates that the frequency-dependent behavior of the optimization extracted absorption coefficients matches analytically with the optimization extracted refracted index. Therefore, the research hypothesizes that the measured transmission of samples with low total attenuation and low reflection is matched to the measured transmission of the air reference within the uncertainty introduced by measurement clutter. The close matching of transmission combined with the uncertainty due to measurement clutter causes sufficient uncertainty in the optimization extracted absorption coefficient that the frequency-averaged absorption coefficient can become negative. Furthermore, the research hypothesizes that the time delayed transmission of FP echo pulses in samples

with low attenuation cause oscillations in the transmission profile which periodically yield transmission greater than unity.

The individual, single-layer, HDPE-A, HDPE-B, and HDPE-C sample measurements are collected together into a single simultaneous optimization. The set of measurements is abbreviated HDPE-A,B,C. The index of refraction and absorption coefficient are computed using fourteen sample measurement reference measurement pairs for the HDPE-A,B,C optimization and the non-optimized index of refraction and absorption coefficient are shown in Figure 6.17. Next, the individual, single-layer, HDPE-A and HDPE-C sample measurements are collected together into a single simultaneous optimization. The set of measurements is abbreviated HDPE-A,C. The index of refraction and absorption coefficient are computed using nine sample measurement reference measurement pairs for the HPDPE-A,C optimization and the non-optimized index of refraction and absorption coefficient are shown in Figure 6.18.

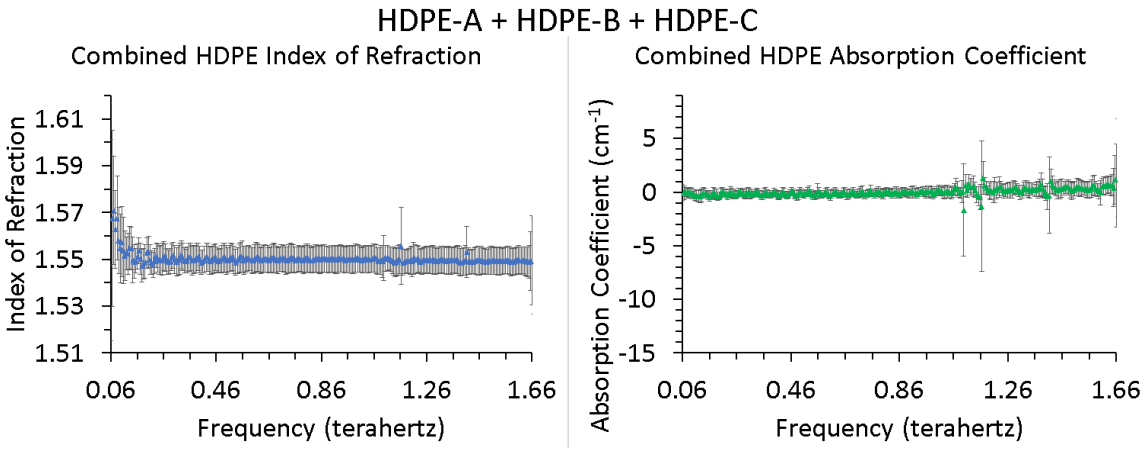

Figure 6.17) The average of fourteen non-optimized refractive index (left) and absorption coefficient (right) profiles for all the single layer HDPE samples. The HDPE-A, HDPE-B, and HDPE-C sample measurements are represented. The uncertainty bars are the standard deviation of all the measurement values at the frequency.

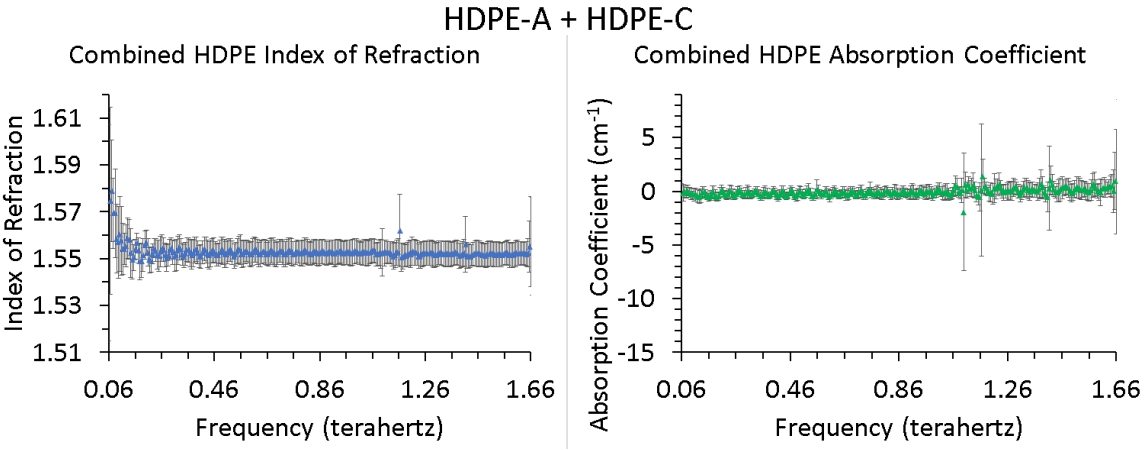

Figure 6.18) The average of nine non-optimized refractive index (left) and absorption coefficient (right) profiles for two single layer HDPE samples. The HDPE-A and HDPE-C sample measurements are represented. The uncertainty bars are the standard deviation of all the measurement values at the frequency.

The optimization extracted index of refraction and absorption coefficient for the simultaneous optimization using the HDPE-A,B,C sample measurements are shown in Figure 6.19. The optimization extracted index of refraction and absorption coefficient for the simultaneous optimization using the HDPE-A,C sample measurements are shown in Figure 6.20. The HDPE-A,B,C optimized refractive index in the frequency region 0.5–1.0 THz has

lower variation compared with the same frequency region for HDPE-A,C. The HDPE-A,B,C optimized absorption coefficient in the frequency region 1.2–1.7 THz has higher variation compared with the same frequency region for HDPE-A,C. This indicates that the contribution of the HDPE-B measurements to the optimization is beneficial to the optimization up to a frequency of approximately 1.0 THz, and detrimental to the optimization at frequencies greater than 1.0 THz. The Kramers-Kronig index of refraction for the HDPE-A,B,C and HDPE-A,C optimizations are shown in Figure 6.21.

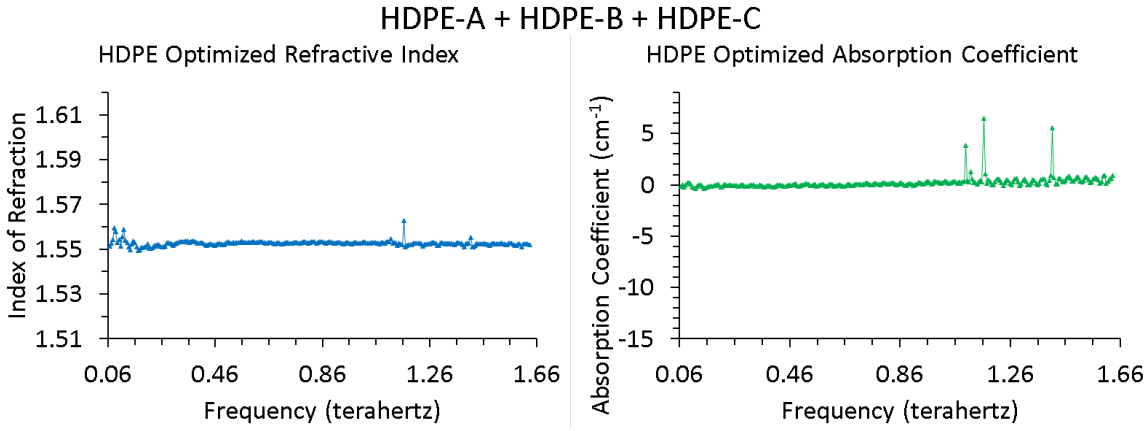

Figure 6.19) The fourteen-measurement optimization extracted refractive index (left) and absorption coefficient (right) profile for the combined simultaneous optimization of the single layer HDPE-A, HDPE-B, and HDPE-C samples.

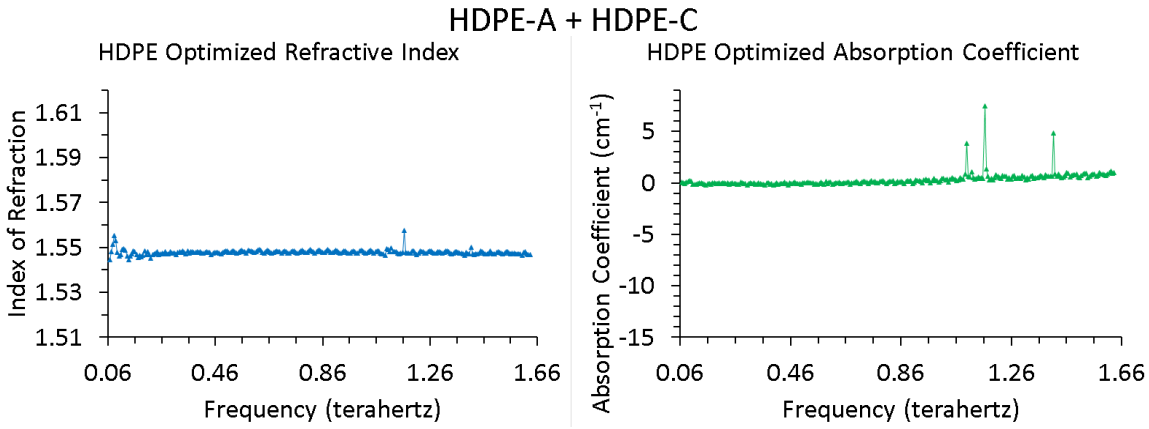

Figure 6.20) The nine-measurement optimization extracted refractive index (left) and absorption coefficient (right) profile for the combined simultaneous optimization of the single layer HDPE-A and HDPE-C samples.

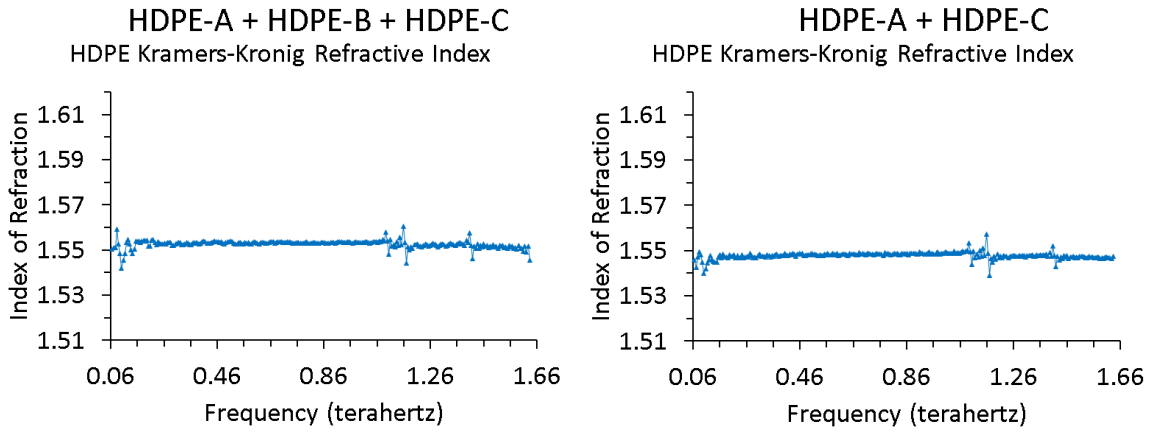

Figure 6.21) The Kramers-Kronig index of refraction determined using the fourteen-measurement (left) and nine-measurement (right) optimization extracted HDPE absorption coefficient.

The research hypothesizes the cause of the improvement in the 0.5–1.0 THz region for the HDPE-A,B,C optimization is due to the reinforcement of the error function minimum by including the HDPE-B measurements compared with the HDPE-A,C optimization. The reason is attributable to the good performance of the HDPE-B measurements at frequencies less than 1.0 THz. The statistics for the non-optimized, optimized, and Kramers-Kronig index of refraction and absorption coefficient for the frequency region 0.5–

1.0 THz is shown in Table 6.10. The research hypothesizes the cause of the degradation in the 1.0–1.7 THz region for the HDPE-A,B,C optimization is due to the detractive impact of the HDPE-B measurement, in contrast to excluding it in the HDPE-A,C optimization, on the error function minimum. The reason is attributable to the poor performance of the HDPE-B measurements at frequencies greater than 1.0 THz as observed in Figure 6.11.

Table 6.10) Statistics for the average and variation of the optical properties of HDPE in the frequency range 0.5–1.0 THz.

HDPE Combo	**Method**	**Index of Refraction**		**Absorption Coefficient (cm^{-1})**	
		Average	**Average Absolute Variation**	**Average**	**Average Absolute Variation**
A,B,C	**Non-optimized**	1.550	2.991×10^{-4}	-5.538×10^{-2}	9.354×10^{-2}
	Optimized	1.553	2.033×10^{-4}	9.977×10^{-2}	7.101×10^{-2}
	Kramers-Kronig	1.553	2.305×10^{-4}	NA	NA
A,C	**Non-optimized**	1.553	4.382×10^{-4}	-0.138	0.143
	Optimized	1.548	4.355×10^{-4}	0.118	0.115
	Kramers-Kronig	1.549	3.673×10^{-4}	NA	NA

The research has successfully demonstrated that numerous measurements, collected using different instrument systems, of HDPE with varying thicknesses are able to be combined into a single simultaneous optimization to facilitate optical parameter extraction and thickness

determination. The reduction in the average variation of the index of refraction and absorption coefficient for the HDPE-A,B,C optimization compared with the HDPE-A,C optimization in the frequency range of 0.5–1.0 THz demonstrates the improvement. Lastly, the thicknesses extracted using the HDPE-A,B,C optimization are 3047.38 μm, 5949.91 μm, and 1601.12 μm for HDPE-A, HDPE-B, and HDPE-C, respectively. The thicknesses extracted using the HDPE-A,C optimization are 3020.71 μm and 1601.46 μm for HDPE-A and HDPE-C, respectively. The percent volume water vapor determined by the HDPE-A,B,C and HDPE-A,B optimizations are 0.0% and 0.0124%, respectively.

6.1.1.3. ALPHA-LACTOSE MONOHYDRATE

The α-Lactose Monohydrate sample is evaluated exclusively using the WSU external transmission system. Two measurements of the Lactose sample are made at normal incidence, but with the sample rotated 90° about the surface normal between the two measurements. The presentation of the normal incidence results for Lactose do not include thickness optimization. The re-optimization is not applied to the Lactose optical parameters because of the natural non-uniformity of the optical parameters as a function of frequency. The optimization of the Lactose measurements is performed using both measurements simultaneously and separately. The spectral magnitude

and phase of the Lactose measurements, with frequency-dependent uncertainty bars, are shown in Figure 6.22. Because only two measurements are used, a single side of the uncertainty is equivalent to the absolute difference between the two measured points at the frequency. Observable in the magnitude profile, especially at frequencies less than 0.4 THz, is a spectral ringing that the research hypothesizes is due to the Fabry-Perot (FP) etalon effect. The variability of the magnitude is noticeable at frequencies between 0.6–0.9 THz. The bandwidth shown in Figure 6.22 is approximately 1.2 THz, which is the bandwidth determined by the heuristic algorithm developed in the research. Both measurements are used at each frequency in the bandwidth. The magnitude is shown in the left plot (blue circle markers), and the phase is shown in the right plot (green circle markers) of Figure 6.22. Solid lines are not used to connect the data points in the plots of Figure 6.22 to enable the uncertainty to be clearly identified at the absorption features.

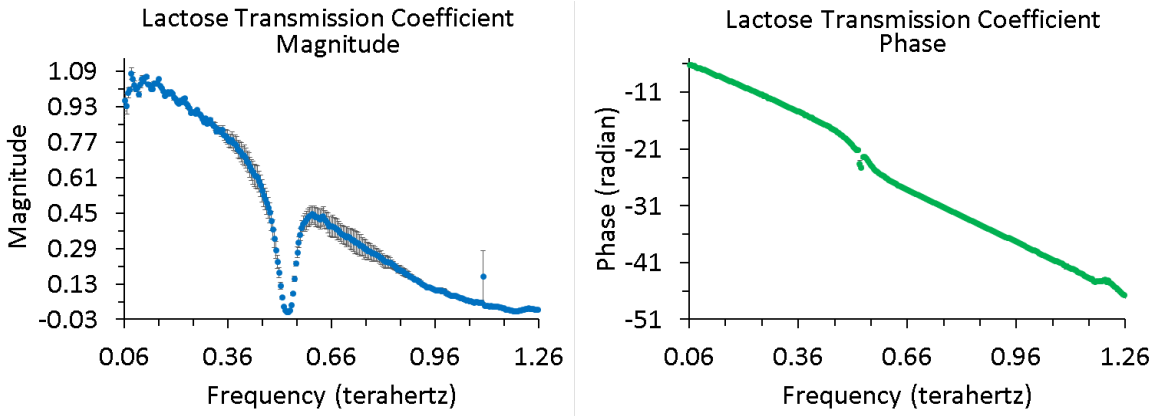

Figure 6.22) The average of two normal incidence transmission magnitude (left) and phase (right) profiles for the Lactose sample.

The measured percent transmission, equivalently the fractional amount of incident power that is detected by the receiver, for the Lactose sample at normal incidence in the transmission configuration recorded with the WSU external system is shown in Figure 6.23. The lines connecting the data points in the plot of Figure 6.23 are for illustrative purposes. The purple horizontal line in Figure 6.23 represents 100% transmission. The physical interpretation of a transfer function magnitude greater than a value of one is a sample composed of a material which is its own source of energy separate from the energy emitted by the transmitter; the material is called a positive gain material. The cause of a transfer function magnitude exceeding a value of one is hypothesized to be a clutter effect due to time-dependent phenomenon affecting the reference and sample measurement pairs. Therefore, the usable frequency selection allows a buffer region to exist if the transfer function magnitude exceeds unity. Consequently, measured transfer function magnitudes greater than a value of one are still classified as usable with the understanding that none of the materials investigated in the research physically exhibit positive gain phenomenology even though the extracted absorption coefficients may be negative.

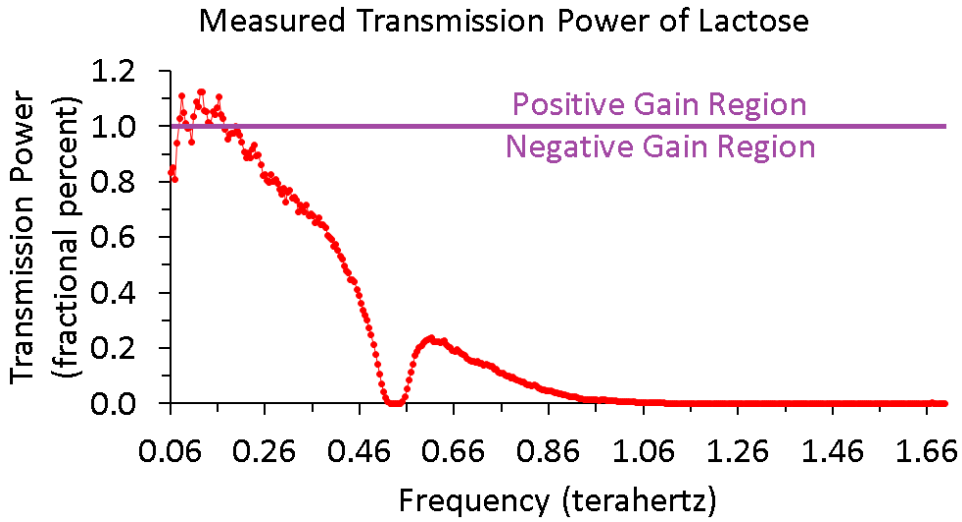

Figure 6.23) The frequency-domain fractional percent transmission of a normal incidence Lactose time-domain measurement. The transmission is colored red, and the line of 100% transmission is colored purple.

The non-optimized Lactose index of refraction and absorption coefficients are determined from the magnitude and phase information using the Vernier micrometer measured thickness of 2390 $\pm$ 25.4 μm. The index of refraction is shown in the left plot of Figure 6.24 using blue triangle markers, and the absorption coefficient is shown in the right plot using green triangle markers. Solid lines are not used to connect the data points in the plots of Figure 6.24 to enable the statistical uncertainty to be clearly identified at the absorption features. The index of refraction of Lactose using the non-optimized result shows a steeply declining index of refraction up until a frequency of approximately 0.3 THz. The research hypothesizes that the monotonic increase in baseline absorption with increasing frequency is caused by scattering of the THz pulses by the Lactose particulates. In addition, there

is spectral ringing apparent in the non-optimized Lactose absorption coefficient up to a frequency of approximately 0.3 THz. There are two prominent absorption features in the absorption profile, one centered at 529.399 ± 2.2 GHz, and another centered at 1195.56 ± 2.2 GHz [88, 89, 90, 91]. The sampling interval between frequency bins is approximately 4.4 GHz. The baseline slope adjusted base-to-peak absorption coefficient height corresponding to the first and second absorption features are 45.6288 cm^{-1} and 10.2890 cm^{-1}, respectively. The baseline slope adjustment compensates for the difference in absorption coefficient at the start and end of the absorption feature, which is intended to locally remove scattering effects from the absorption coefficient in the vicinity of the absorption feature. The baseline slope adjusted frequency width at half the absorption coefficient maximum for the first and second absorption features is 20.9327 ± 4.4 GHz and 35.8801 ± 4.4 GHz. Reports from literature vary on the width of the absorption features, between 23–80 GHz for the 530 GHz absorption feature, depending on the measurement system used and whether the absorption feature is fit using a Gaussian or Lorentzian model [88, 89, 90, 91, 92]. The frequencies at which the two absorption features occur are correlated with dispersion induced fluctuation in the refractive index.

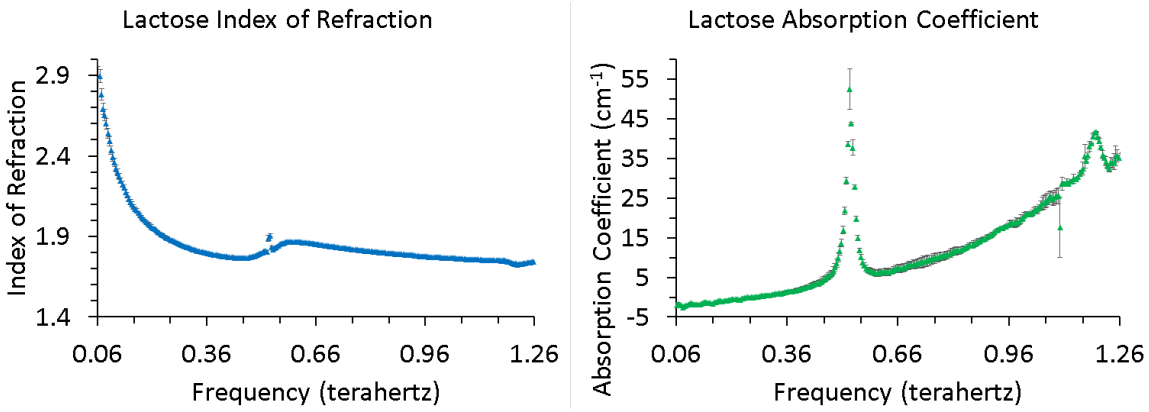

Figure 6.24) The average of two refractive index (left) and absorption coefficient (right) profiles for the Lactose sample.

The simultaneous two-measurement optimized Lactose index of refraction is shown in the left plot of Figure 6.25 using blue triangle markers, and the absorption coefficient is shown in the right plot using green triangle markers. The solid lines connecting the data points in the plots of Figure 6.25 are for illustrative purposes. In contrast to the non-optimized index of refraction, the optimized index of refraction does not show the steep decline in refractive index. The optimized absorption coefficient profile has the two absorption features identified in the non-optimized result. The center frequencies of the two absorption features in the optimized result are 529.399 $\pm$ 2.2 GHz and 1195.56 $\pm$ 2.2 GHz. The sampling interval between frequency bins is approximately 4.4 GHz. The effective percent water vapor calculated during the optimization is 0.15%, which has an impact of 4.35×10^{-3} cm^{-1} at the location of the peak of the 559 GHz water vapor absorption feature. Apparent in the optimized absorption coefficient profile that is not present in

the non-optimized result is spectral ringing throughout the bandwidth of the optimized absorption profile. Lastly, a region of high variation exists in the optimized refractive index shown in the left plot of Figure 6.25 for frequencies greater than 1.2 THz where to optimization is challenged to converge on the desirable solution. The research hypothesizes that the region of high variation causes a degradation in the confidence of the coefficients of the 1195.56 ± 2.2 GHz absorption feature.

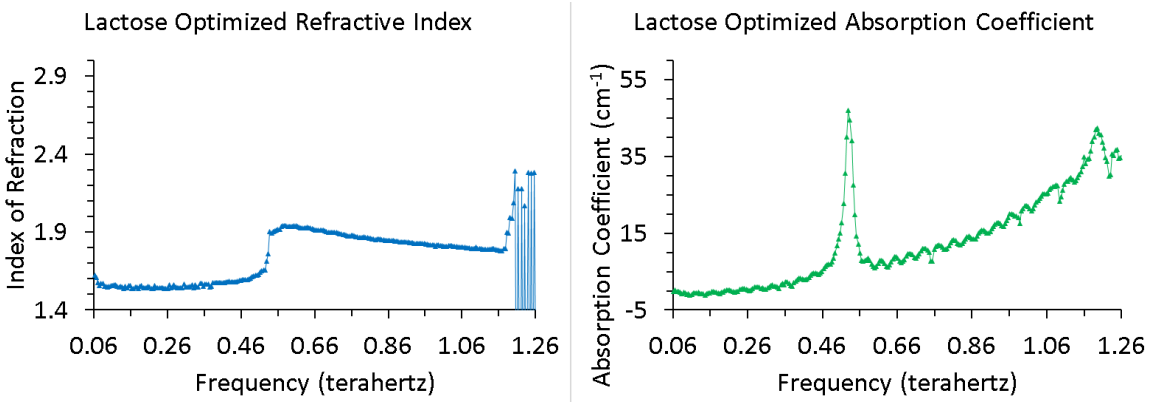

Figure 6.25) The two-measurement optimization extracted refractive index (left) and absorption coefficient (right) profile of the Lactose sample.

The undesired refractive index solutions at frequencies greater than 1.2 THz is remedied by computing the average of two separate single-measurement optimizations so that there is a well-defined, desired, solution path in the optimization error function. The average of the two separate optimizations for Lactose results in the spectral refractive index profile shown in the left plot of Figure 6.26 using blue triangle markers, and the absorption coefficient shown in the right plot using green triangle markers. Solid lines

are not used to connect the data points in the plots of Figure 6.26 to enable the uncertainty to be clearly identified at the absorption features. Because only two optical parameter profiles are used to compute the average, a single side of the uncertainty is equivalent to the absolute difference between the two optical parameter values at the frequency. In contrast to the simultaneous two-measurement optimized index of refraction, the average single-measurement optimized index of refraction does not show the high variation at frequencies greater than 1.2 THz. The averaged optimized absorption coefficient profile has the same two absorption features identified in the non-optimized and simultaneous two-measurement optimized result. The center frequencies of the two absorption features in the averaged optimized result remain 529.399 $\pm$ 2.2 GHz and 1195.56 $\pm$ 2.2 GHz. The sampling interval between frequency bins remains approximately 4.4 GHz. The center frequencies obtained by the optimization are compared to results obtained using a physics-based approach for continuous-wave frequency-domain measurement data [92]. The continuous-wave approach yields absorption feature center frequencies of 530.4 $\pm$ 0.5 GHz and 1195 $\pm$ 1 GHz, which are in good agreement with the optimization-based absorption feature center frequencies of 529.399 $\pm$ 2.2 GHz and 1195.56 $\pm$ 2.2 GHz. The baseline slope adjusted base-to-peak absorption coefficient height of the first and second absorption features are

45.6538 cm^{-1} and 10.4349 cm^{-1}, respectively. The baseline slope adjustment compensates for the difference in absorption coefficient at the start and end of the absorption feature, which is intended to locally remove scattering effects from the absorption coefficient in the vicinity of the absorption feature. The baseline slope adjusted frequency width at half the absorption coefficient maximum for the first and second absorption features is 20.8668 ± 4.4 GHz and 36.7552 ± 4.4 GHz. Reports from literature vary on the width of the absorption features, between 23–80 GHz for the 530 GHz absorption feature, depending on the measurement system used and whether the absorption feature is fit using a Gaussian or Lorentzian model [88, 89, 90, 91, 92]. The effective percent water vapor calculated during each of the separate single-measurement optimizations are 0.0%.

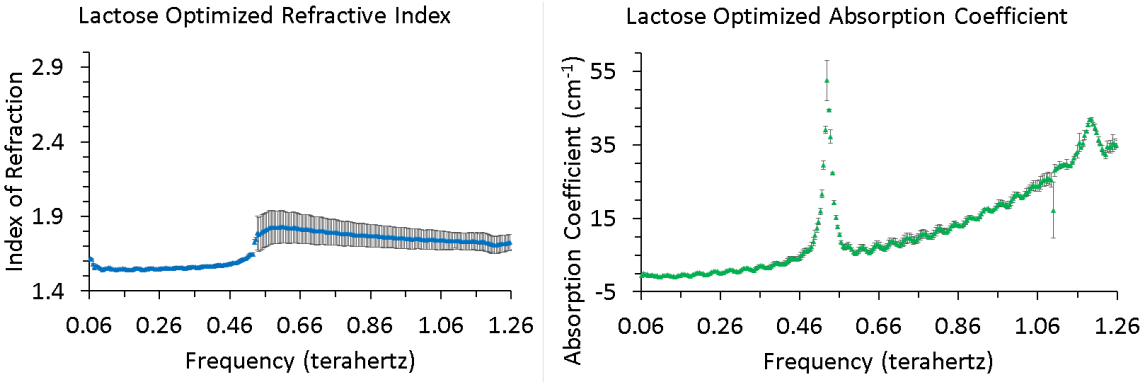

Figure 6.26) The average refractive index(left) and absorption coefficient (right) from two single-measurement optimizations for Lactose.

The Kramers-Kronig index of refraction computed from the optimized extinction coefficient profile and Equation 4.18 is shown in the plot of Figure

6.27 using blue triangle markers and solid lines connecting the points for illustrative purposes. The Kramers-Kronig result shows agreement with the optimized index of refraction. The Kramers-Kronig and optimized index of refraction profile contain the same dispersion induced fluctuation at the first absorption feature of Lactose.

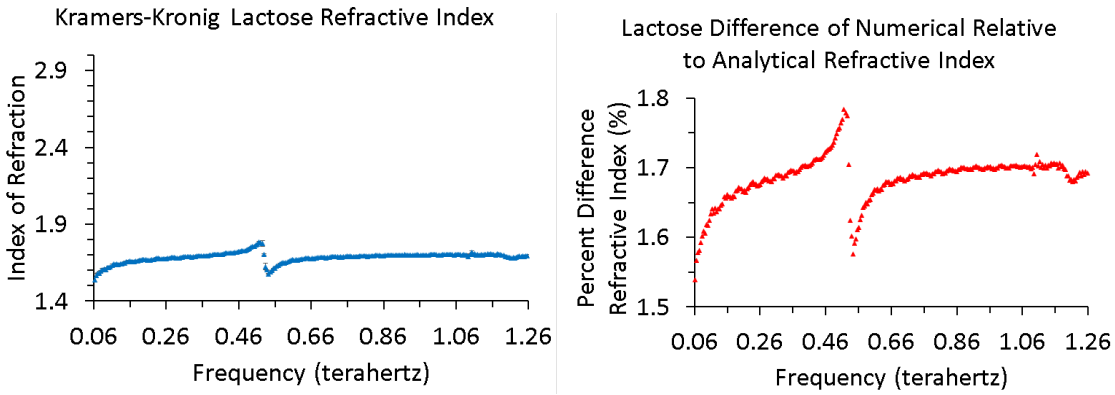

Figure 6.27) The left plot is the average Kramers-Kronig index of refraction determined by taking the average of two unique Kramers-Kronig refractive index profiles. The separate profiles are obtained from the absorption coefficients of two separate single-measurement optimizations of the Lactose sample. The right plot is the percent difference of the numerically optimized refractive index relative to the discrete form of the analytical Kramers-Kronig relationship.

Based on the evidence in the right plot of Figure 6.27, the largest negative and largest positive percent difference between the Kramers-Kronig and optimization extracted index of refraction is -1.56% and 4.79%, respectively. Therefore, the research assesses that the Lactose refractive index extracted by numerical optimization agrees with the analytic form, and satisfies the causality principle for stable physical systems.

6.1.1.4. PHARMACEUTICAL-GRADE OXYCODONE

The pharmaceutical-grade Oxycodone sample is evaluated exclusively using the WSU external transmission system. Pharmaceutical-grade Oxycodone uses α-lactose monohydrate as an inert filler material. Therefore, the research anticipates that there is correlation between the optical properties of pharmaceutical-grade Oxycodone and Lactose. The mass fraction of Lactose in the pharmaceutical-grade Oxycodone sample used in the research is unknown, but the optical property of the Lactose filler ingredient typically dominates the optical property of the pure Oxycodone active ingredient in pharmaceutical-grade Oxycodone [93]. Two measurements of the pharmaceutical-grade Oxycodone sample are made at normal incidence, but with the sample rotated 90° about the surface normal between the two measurements. The presentation of the normal incidence results for pharmaceutical-grade Oxycodone do not include thickness optimization. The re-optimization is not applied to the pharmaceutical-grade Oxycodone optical parameters because of the natural non-uniformity of the parameters as a function of frequency. The optimization of the pharmaceutical-grade Oxycodone measurements is done using both measurements simultaneously and separately. The magnitude and phase of the pharmaceutical-grade Oxycodone measurements, with frequency-dependent uncertainty bars, are

shown in Figure 6.28. Because only two measurements are used, a single side of the uncertainty is equivalent to the absolute difference between the two measured points at the frequency. It is not possible to discern, using the qualitative analysis employed in the research, the presence of FP etalon effect oscillations in the spectral profiles of pharmaceutical-grade Oxycodone in the 1.7 THz bandwidth that is analyzed. Both measurements are used at each frequency in the bandwidth. The magnitude is shown in the left plot (blue circle markers), and the phase is shown in the right plot (green circle markers) of Figure 6.28. Solid lines are not used to connect the data points in the plots of Figure 6.28 to enable the uncertainty to be clearly identified at the absorption features.

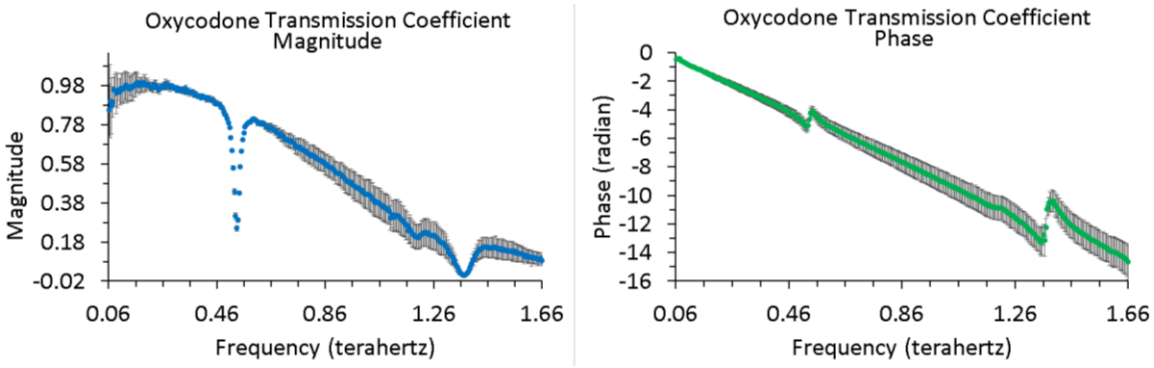

Figure 6.28) The average of two normal incidence transmission magnitude (left) and phase (right) profiles for the Oxycodone sample. The uncertainty bars are the standard deviation of the two measurement values at individual frequencies.

The two pharmaceutical-grade Oxycodone normal incidence measurements create two transmission profiles that envelope the average transmission. The measurement associated with the upper bound of the

magnitude transmission envelope, represented by the positive uncertainty bars in the left plot of Figure 6.28, indicates that less net absorption has occurred compared to the average. The measurement associated with the lower bound of the magnitude transmission envelope, represented by the negative statistical uncertainty bars, indicates that more net absorption has occurred compared to the average. The net absorption at a single frequency depends on the distance through the sample that the radiation has propagated, the density of the sample along the propagation path, and the absorption coefficient of the sample at the frequency. The increasing statistical uncertainty with increasing frequency in the phase plot of Figure 6.28 indicates that the thickness of the pharmaceutical-grade Oxycodone sample at the sample surface evaluation location for each measurement is not the same. A steeper phase slope is associated with more revolutions of the electromagnetic radiation wave vector with respect to the phasor representation. The inference is made that the measurement with the steeper phase slope has a larger sample thickness at the sample surface evaluation location compared with the measurement with less steep phase slope.

The non-optimized pharmaceutical-grade Oxycodone index of refraction and absorption coefficients are determined from the magnitude and phase information using the Vernier micrometer measured thickness of 1550

$\pm$ 25.4 μm. The index of refraction is shown in the left plot of Figure 6.29 using blue triangle markers, and the absorption coefficient is shown in the right plot using green triangle markers. Solid lines are not used to connect the data points in the plots of Figure 6.29 to enable the statistical uncertainty to be clearly identified at the absorption features. The research hypothesizes that the monotonic increase in baseline absorption with increasing frequency is caused by scattering of the THz pulses by the pharmaceutical-grade Oxycodone particulates. There is no spectral ringing apparent in the non-optimized pharmaceutical-grade Oxycodone absorption coefficient. There are two prominent absorption features in the absorption profile, one centered at 532.784 $\pm$ 2.2 GHz, and another centered at 1369.39 $\pm$ 2.2 GHz. There is a third, minor, absorption feature centered at 1202.07 $\pm$ 2.2 GHz. The baseline slope adjusted base-to-peak absorption coefficient height corresponding to the dominant first and second absorption features are 15.3601 cm^{-1} and 39.8045 cm^{-1}, respectively. The baseline slope adjusted base-to-peak absorption coefficient height corresponding to the minor absorption feature is 2.81866 cm^{-1}. The baseline slope adjustment compensates for the difference in absorption coefficient at the start and end of the absorption feature, which is intended to locally remove scattering effects from the absorption coefficient in the vicinity of the absorption feature. The baseline slope adjusted frequency

width at half the absorption coefficient maximum for the first and second dominant absorption features are 28.5023 $\pm$ 4.4 GHz and 75.2029 $\pm$ 4.4 GHz. The baseline slope adjusted frequency width at half the absorption coefficient maximum for the minor absorption feature is 49.2533 $\pm$ 4.4 GHz. The sampling interval between frequency bins is approximately 4.4 GHz. The frequencies at which the two dominant absorption features occur are correlated with dispersion induced fluctuation in the refractive index. Furthermore, the center frequency of the first dominant absorption feature and the minor absorption feature in the pharmaceutical-grade Oxycodone are strongly correlated with the absorption features reported for Lactose in Section 6.1.1.3 and all three absorption feature center frequencies agree with the center frequencies reported in literature for α-lactose monohydrate [90, 91, 92]. The ambiguity between the two measurements with respect to the sample orientation and sample thickness at the location which the sample is evaluated is manifest by the uncertainty bars in the plots of Figure 6.29.

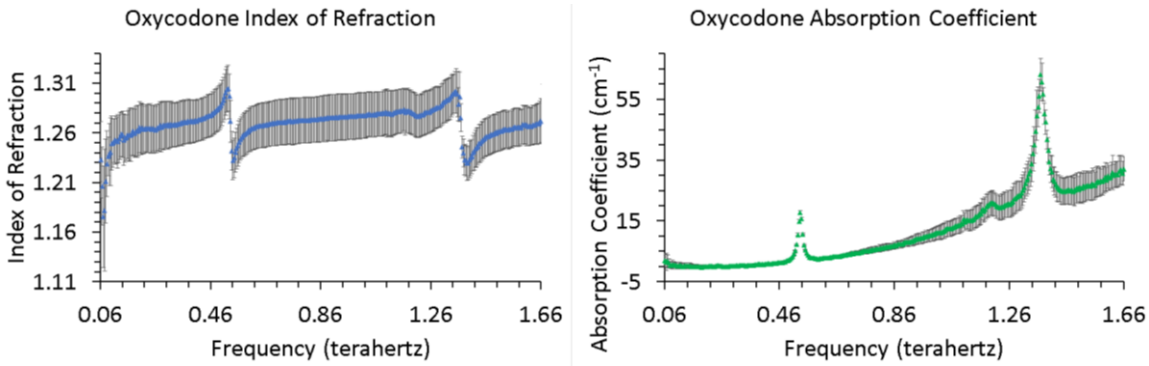

Figure 6.29) The average of two refractive index (left) and absorption coefficient (right) profiles for the pharmaceutical-grade Oxycodone sample. The uncertainty bars are the standard deviation of the two measurement values at the frequency.

The two-measurement optimized pharmaceutical-grade Oxycodone index of refraction is shown in the left plot of Figure 6.30 using blue triangle markers, and the absorption coefficient is shown in the right plot using green triangle markers. The solid lines connecting the data points in the plots of Figure 6.30 are for illustrative purposes. Immediately observable in both plots of Figure 6.30 is the toggling between solutions in the frequency range 0.9–1.1 THz. At frequencies greater than 1.1 THz, the solution is observed to shift to a lower solution path. The toggling and shifting behavior, especially because it is nearly in the middle of the optical parameter profiles, is undesirable. Specifically, the toggling and subsequent shifting behavior causes a lack of confidence in the refractive index and absorption coefficient values at frequencies greater than 1.1 THz.

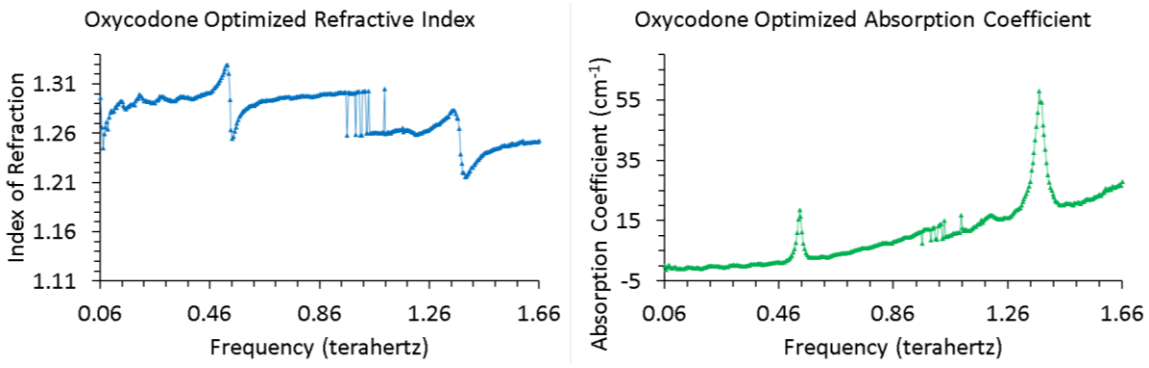

Figure 6.30) The two-measurement optimization extracted refractive index (left) and absorption coefficient (right) profile of the pharmaceutical-grade Oxycodone sample.

The solution toggling and subsequent shifting is remedied by computing the average of two separate single-measurement optimizations so that there is a well-defined solution path in the optimization error function. The average of the two separate optimizations for pharmaceutical-grade Oxycodone results in the index of refraction shown in the left plot of Figure 6.31 using blue triangle markers, and the absorption coefficient shown in the right plot using green triangle markers. Solid lines are not used to connect the data points in the plots of Figure 6.31 to enable the uncertainty to be clearly identified at the absorption features. Because only two optical parameter profiles are used, a single side of the uncertainty is equivalent to the absolute difference between the two optical parameter values at the frequency.

In contrast to the non-optimized index of refraction, the average optimized index of refraction and absorption coefficient profiles both show indications of spectral ringing. The average optimized absorption coefficient

profile has the two dominant and one minor absorption features identified in the non-optimized result. Identical to the non-optimized result, the two prominent absorption features in the absorption profile are centered at 532.784 $\pm$ 2.2 GHz and 1369.39 $\pm$ 2.2 GHz. The minor absorption feature is centered at 1202.07 $\pm$ 2.2 GHz. The baseline slope adjusted base-to-peak absorption coefficient height corresponding to the dominant first and second absorption features are 15.6269 cm^{-1} and 40.2022 cm^{-1}, respectively. The baseline slope adjusted base-to-peak absorption coefficient height corresponding to the minor absorption feature is 2.85088 cm^{-1}. The baseline slope adjustment compensates for the difference in absorption coefficient at the start and end of the absorption feature, which is intended to locally remove scattering effects from the absorption coefficient in the vicinity of the absorption feature. The baseline slope adjusted frequency width at half the absorption coefficient maximum for the first and second dominant absorption features are 28.9764 $\pm$ 4.4 GHz and 75.6245 $\pm$ 4.4 GHz. The baseline slope adjusted frequency width at half the absorption coefficient maximum for the minor absorption feature is 49.4828 $\pm$ 4.4 GHz. The sampling interval between frequency bins is approximately 4.4 GHz. The frequencies at which the two dominant absorption features occur are correlated with dispersion induced fluctuation in the refractive index. Furthermore, the center frequency of the first dominant

absorption feature and the minor absorption feature in the pharmaceutical-grade Oxycodone are strongly correlated with the absorption features reported for Lactose in Section 6.1.1.3 and all three absorption feature center frequencies agree with the center frequencies reported in literature for α-lactose monohydrate [90, 91, 92]. The effective percent water vapor calculated during the optimization is 0.025%, which has an impact of 7.25×10^{-3} cm^{-1} at the location of the peak of the 559 GHz water vapor absorption feature. The frequencies at which the two dominant absorption features occur are correlated with dispersion induced fluctuation in the refractive index. The ambiguity between the two measurements with respect to the sample orientation and sample thickness at the location which the sample is evaluated is manifest by the uncertainty bars in the plots of Figure 6.31.

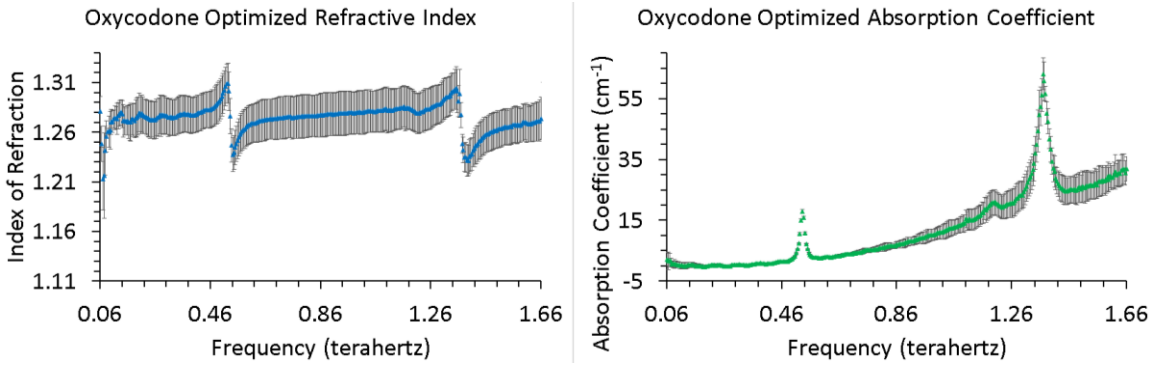

Figure 6.31) The average refractive index(left) and absorption coefficient (right) from two single-measurement optimizations for pharmaceutical-grade Oxycodone.

The Kramers-Kronig index of refraction computed from the optimized extinction coefficient profile and Equation 4.18 is shown in the plot of Figure

6.32 using blue triangle markers and solid lines connecting the points for illustrative purposes. The Kramers-Kronig result shows agreement with the optimized index of refraction. The Kramers-Kronig and optimized index of refraction profile contain the same dispersion induced fluctuation at the first and second dominant absorption features of pharmaceutical-grade Oxycodone.

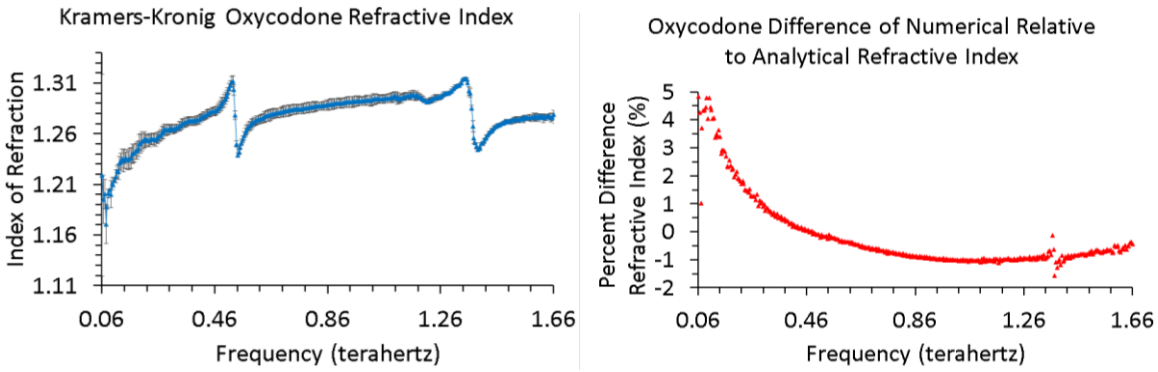

Figure 6.32) The left plot is the average Kramers-Kronig index of refraction determined by taking the average of two unique Kramers-Kronig refractive index profiles. The separate profiles are obtained from the absorption coefficients of two separate single-measurement optimizations of the pharmaceutical-grade Oxycodone sample. The right plot is the percent difference of the numerically optimized refractive index relative to the discrete form of the analytical Kramers-Kronig relationship.

Based on the evidence in the right plot of Figure 6.32, the largest negative and largest positive percent difference between the Kramers-Kronig and optimization extracted index of refraction is -1.56% and 4.79%, respectively. Therefore, the research assesses that the pharmaceutical-grade Oxycodone refractive index extracted by numerical optimization agrees with the analytic form, and satisfies the causality principle for stable physical systems.

The final analysis of the optimization results for the pharmaceutical-grade Oxycodone sample is provided in Figure 6.33. The plots in Figure 6.33 show the baseline slope adjusted absorption coefficient heights of the three α-lactose monohydrate absorption features at frequencies less than 1.5 THz. The baseline slope adjustment is applied locally at each of the three absorption features. The baseline slope adjustment is a compensation technique used to approximately remove, post-processing, the scattering component of the absorption. The compensation effectively adjusts the absorption coefficients to only reflect the energy absorbed, not scattered, by the particulate samples. In Figure 6.33, the red square markers are the absorption coefficient heights for α-lactose monohydrate, and the blue square markers are the absorption coefficient heights for the pharmaceutical-grade Oxycodone. The pharmaceutical-grade Oxycodone uses α-lactose monohydrate as a filler ingredient. The straight lines in the plots of Figure 6.33 are used for illustrative purposes.

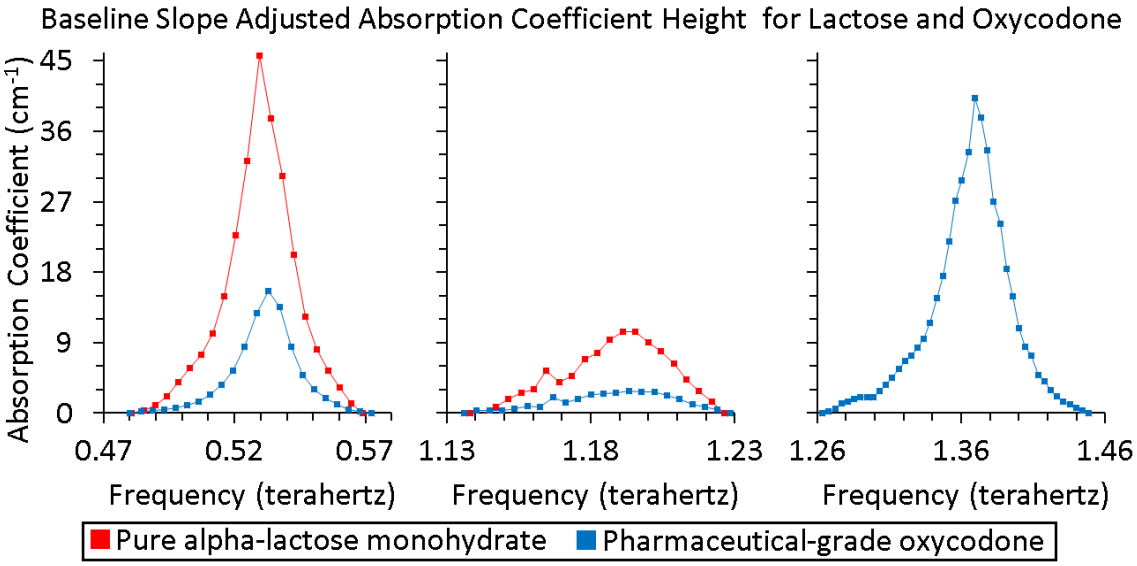

Figure 6.33) The local baseline slope adjusted absorption coefficient heights of the three Lactose absorption features for 100% pure Lactose and pharmaceutical-grade Oxycodone.

The analysis of the plots in Figure 6.33 show strong correlation between the absorption features of Lactose and pharmaceutical-grade Oxycodone. The Lactose absorption feature centered at 1.37 THz is not provided for pure α-lactose monohydrate because of bandwidth limitations for those measurements. A computation of the area under the curve for the absorption coefficient heights at each of the absorption features provides insight into the mass fraction of α-lactose monohydrate in the pharmaceutical-grade Oxycodone sample. The area under the baseline slope adjusted absorption coefficient height curve for the 530 GHz and 1202 GHz absorption features is computed for the pure α-lactose monohydrate and pharmaceutical-grade Oxycodone samples. The ratio divides the absorption coefficient height area corresponding to pharmaceutical-grade Oxycodone by the absorption

coefficient height area of pure α-lactose monohydrate. With respect to pharmaceutical-grade Oxycodone, the research hypothesizes that the area under the absorption coefficient curve is proportional to the density of α-lactose monohydrate in the sample. The research further hypothesizes that the mass fraction of α-lactose monohydrate present in the pharmaceutical-grade Oxycodone sample is proportional to the density of α-lactose monohydrate present in the pharmaceutical-grade Oxycodone sample. The individual percent area ratios for the 530 GHz and 1202 GHz absorption features are 32.3% and 30.4%, respectively. The area is calculated using the trapezoidal quadrature rule for discrete integration. The area calculation for the 1202 GHz absorption feature excludes the singular data spike at 1165 GHz. The percent area ratio for the combined 530 GHz and 1202 GHz absorption features is 31.8%. This indicates that an initial estimate of the mass fraction of α-lactose monohydrate in the pharmaceutical-grade Oxycodone is possibly 32%.

6.1.1.5. HYDROCODONE

The Hydrocodone sample is evaluated exclusively using the WSU external transmission system. Two measurements of the Hydrocodone sample are made at normal incidence, but with the sample rotated 90° about the surface normal between the two measurements. The presentation of the normal incidence results for Hydrocodone do not include thickness

optimization. The re-optimization is not applied to the Hydrocodone optical parameters. The optimization of the Hydrocodone measurements is done using both measurements simultaneously and separately. The magnitude and phase of the Hydrocodone measurements, with frequency-dependent uncertainty bars, are shown in Figure 6.34. Because only two measurements are used, a single side of the uncertainty is equivalent to the absolute difference between the two measured points at the frequency. The research discerns, using qualitative analysis, the slight presence of spectral ringing in the magnitude transmission and transmission phase profiles of Hydrocodone in the 1.7 THz bandwidth that is analyzed. Both measurements are used at each frequency in the bandwidth. The magnitude is shown in the left plot (blue circle markers), and the phase is shown in the right plot (green circle markers) of Figure 6.34. Solid lines are not used to connect the data points in the plots of Figure 6.34 to enable the uncertainty to be clearly identified at the absorption features.

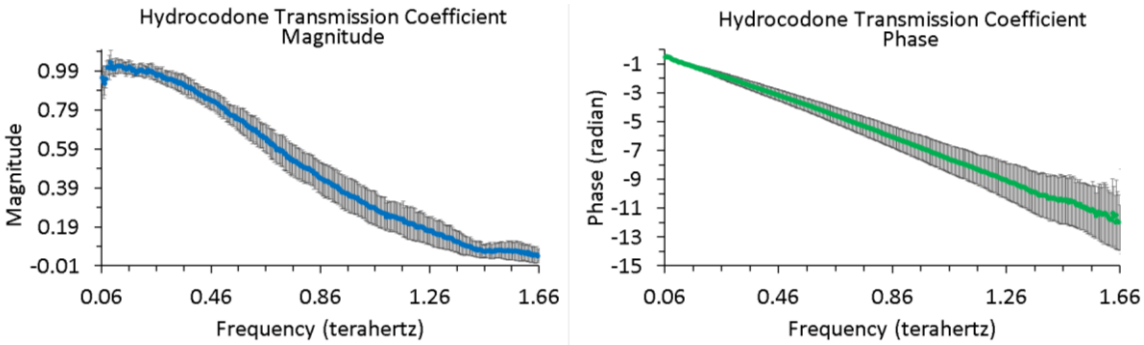

Figure 6.34) The average of two normal incidence transmission magnitude (left) and phase (right) profiles for the Hydrocodone sample. The uncertainty bars are the standard deviation of the two measurement values at individual frequencies.

The two Hydrocodone normal incidence measurements create two transmission profiles that envelope the average transmission. The measurement associated with the upper bound of the magnitude transmission envelope, represented by the positive uncertainty bars in the left plot of Figure 6.34, indicates that less net absorption has occurred compared to the average. The measurement associated with the lower bound of the magnitude transmission envelope, represented by the negative uncertainty bars, indicates that more net absorption has occurred compared to the average. The net absorption at a single frequency depends on the distance through the sample that the radiation has propagated, the density of the sample along the propagation path, and the absorption coefficient of the sample at the frequency. The increasing uncertainty with increasing frequency in the phase plot of Figure 6.34 indicates that the thickness of the Hydrocodone sample at the sample surface evaluation location for each measurement is not the same. A steeper phase slope is associated with more revolutions of the

electromagnetic radiation wave vector with respect to the phasor representation. The inference is made that the measurement with the steeper phase slope has a larger sample thickness at the sample surface evaluation location compared with the measurement with less steep phase slope.

The non-optimized Hydrocodone index of refraction and absorption coefficients are determined from the magnitude and phase information using the Vernier micrometer measured thickness of 900 ± 25.4 μm. The index of refraction is shown in the left plot of Figure 6.35 using blue triangle markers, and the absorption coefficient is shown in the right plot using green triangle markers. Solid lines are not used to connect the data points in the plots of Figure 6.35 to enable the statistical uncertainty to be clearly identified at the absorption features. There is a single prominent absorption feature in the monotonically increasing absorption profile. The research hypothesizes that the monotonic increase in baseline absorption with increasing frequency is caused by scattering of the THz pulses by the Hydrocodone particulates. The center of the absorption feature is difficult to identify because the single absorption feature appears to have multiple regions of elevated absorption, but the same baseline slope adjustment is applied to the entire absorption feature. It is possible that some of the variation across the single absorption feature is caused by a combination of low SNR and residual water vapor

absorption effects. For example, three distinct baseline slope adjusted base-to-peak absorption coefficient heights are 4.566 cm^{-1}, 6.832 cm^{-1}, and 6.968 cm^{-1}, located at frequencies of 1387.25 $\pm$ 2.2 GHz, 1435.69 $\pm$ 2.2 GHz, and 1453.31 $\pm$ 2.2 GHz, respectively. The initial and final frequency of the absorption feature is subjectively defined by the research to be 1.33 THz, and 1.51 THz, respectively. The sampling interval between frequency bins is approximately 4.4 GHz. A convex hull, bounded from below by zero absorption, might be more appropriate than a sloped line hull for a baseline given the large total width, approximately 180 GHz, of the Hydrocodone absorption feature. If a concave hull is used as the baseline instead of the slope of a line, then the absorption height at 1435.69 $\pm$ 2.2 GHz is more greatly increased compared with the 1387.25 $\pm$ 2.2 GHz and 1453.31 $\pm$ 2.2 GHz absorption heights. Lastly, there appears to be slight spectral ringing at frequencies less than 200 GHz in the index of refraction profile. The ambiguity between the two measurements with respect to the sample orientation and sample thickness at the location which the sample is evaluated is manifest by the uncertainty bars in the plots of Figure 6.35.

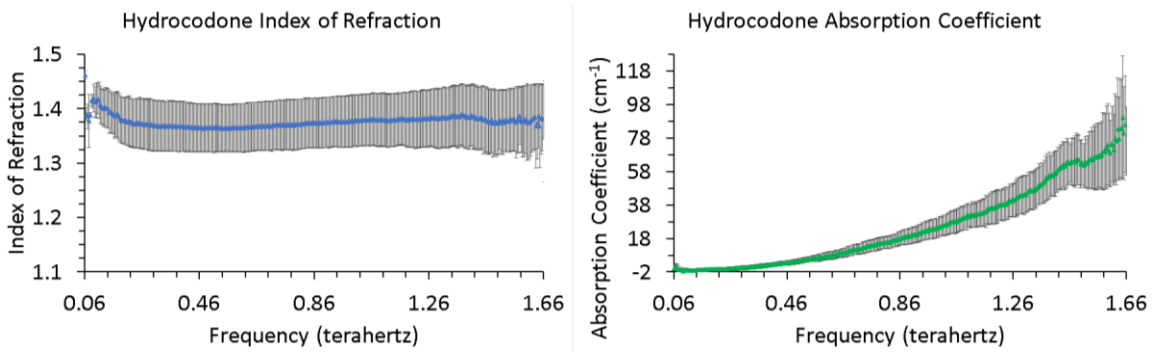

Figure 6.35) The average of two refractive index (left) and absorption coefficient (right) profiles for the Hydrocodone sample. The uncertainty bars are the standard deviation of the two measurement values at the frequency.

The simultaneous two-measurement optimized Hydrocodone index of refraction is shown in the left plot of Figure 6.36 using blue triangle markers, and the absorption coefficient is shown in the right plot using green triangle markers. The solid lines connecting the data points in the plots of Figure 6.36 are for illustrative purposes. The optimized absorption coefficient profile has the single absorption feature identified in the non-optimized result. The absorption coefficient peak of the absorption feature in the simultaneous two-measurement optimization is more difficult to discern compared with the non-optimized result. The effective percent water vapor calculated during the simultaneous optimization is 0.22%, which has an impact of 6.32×10^{-3} cm^{-1} at the location of the peak of the 559 GHz water vapor absorption feature. Apparent in the simultaneous two-measurement optimized refractive index and absorption coefficient profiles, is a low periodicity spectral ringing at frequencies less than 1.0 THz. The periodicity is approximately 120 GHz.

Lastly, a region of high variation exists in the optimized refractive index and absorption coefficient shown in the plots of Figure 6.36 for frequencies greater than 1.4 THz, which includes the Hydrocodone absorption feature.

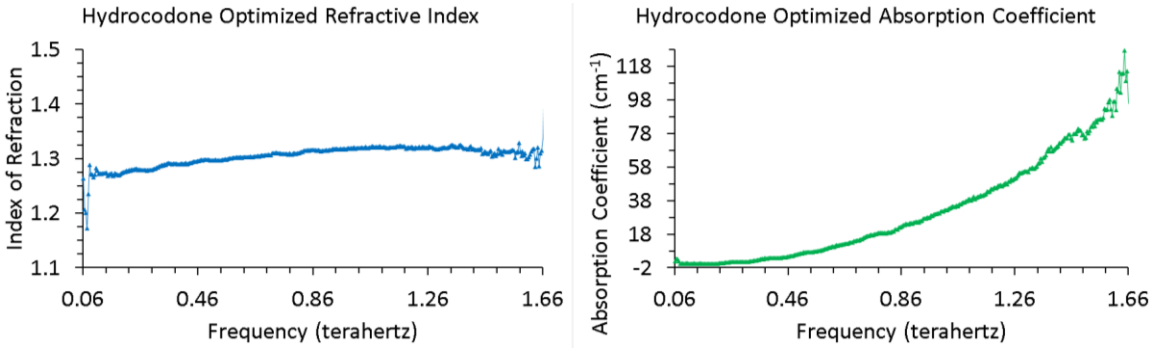

Figure 6.36) The single-measurement optimization extracted refractive index (left) and absorption coefficient (right) profile of the Hydrocodone sample using the first of the two normal incidence measurements.

The average of two separate optimizations for Hydrocodone results in the index of refraction shown in the left plot of Figure 6.37 using blue triangle markers, and the absorption coefficient shown in the right plot using green triangle markers. Solid lines are not used to connect the data points in the plots of Figure 6.37. Because only two optical parameter profiles are used, a single side of the uncertainty is equivalent to the absolute difference between the two optical parameter values at the frequency. The average optimized absorption coefficient profile contains the dominant absorption feature identified in the non-optimized result. Identical to the non-optimized result, the research hypothesizes that the optimized absorption coefficient is monotonically increasing with increasing frequency due to the scattering of THz pulses from

the Hydrocodone particulates. The research hypothesizes that the monotonic increase in baseline absorption with increasing frequency is caused by scattering of the THz pulses by the Hydrocodone particulates. Similar to the non-optimized result, the center of the optimized absorption feature is difficult to identify because the single absorption feature appears to have multiple regions of elevated absorption. The effective percent water vapor calculated for each of the two separate optimizations are both 0.0%. The ambiguity between the two measurements with respect to the sample orientation and sample thickness at the location which the sample is evaluated is manifest by the uncertainty bars in the plots of Figure 6.37.

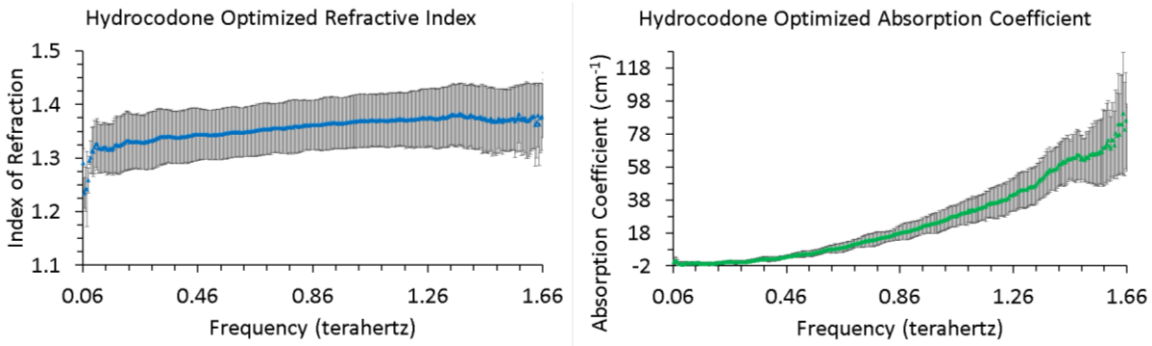

Figure 6.37) The single-measurement optimization extracted refractive index (left) and absorption coefficient (right) profile of the Hydrocodone sample using the second of the two normal incidence measurements.

The baseline slope adjusted absorption feature is shown in Figure 6.38. The green square markers and purple square markers in the plot of Figure 6.38 is the optimized and non-optimized absorption coefficient height, respectively. The straight lines connecting the data points in the plot of Figure

6.38 is for illustrative purposes. It is possible that some of the variation across the single absorption feature is caused by a combination of low SNR and residual water vapor absorption effects.

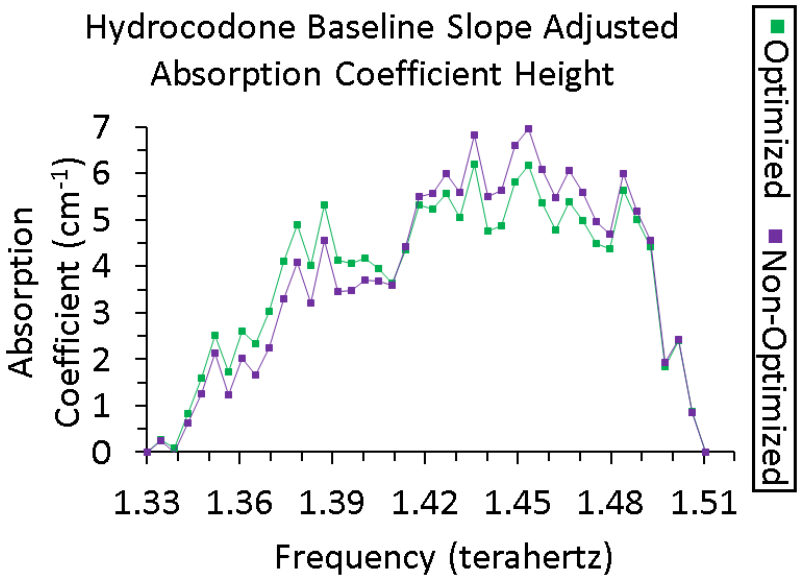

Figure 6.38) The baseline slope adjusted absorption coefficient height of the Hydrocodone absorption feature for the non-optimized (purple) and optimized (green) results.

Three distinct baseline slope adjusted base-to-peak absorption coefficient heights are 5.313 cm^{-1}, 6.184 cm^{-1}, and 6.180 cm^{-1}, located at frequencies of 1387.25 $\pm$ 2.2 GHz, 1435.69 $\pm$ 2.2 GHz, and 1453.31 $\pm$ 2.2 GHz, respectively. The initial and final frequency of the absorption feature is subjectively defined by the research to be 1.33 THz, and 1.51 THz, respectively. The sampling interval between frequency bins remains approximately 4.4 GHz. A convex hull, bounded from below by zero absorption, might be more appropriate than a sloped line hull for a baseline

given the large total width, approximately 180 GHz, of the Hydrocodone absorption feature. If a concave hull is used as the baseline instead of the slope of a line, then the absorption height at 1435.69 $\pm$ 2.2 GHz is more greatly increased compared with the 1387.25 $\pm$ 2.2 GHz and 1453.31 $\pm$ 2.2 GHz absorption heights.

The Kramers-Kronig index of refraction computed from the optimized extinction coefficient profile and Equation 4.18 is shown in the plot of Figure 6.39 using blue triangle markers and solid lines connecting the points for illustrative purposes. The Kramers-Kronig result shows agreement with the optimized index of refraction.

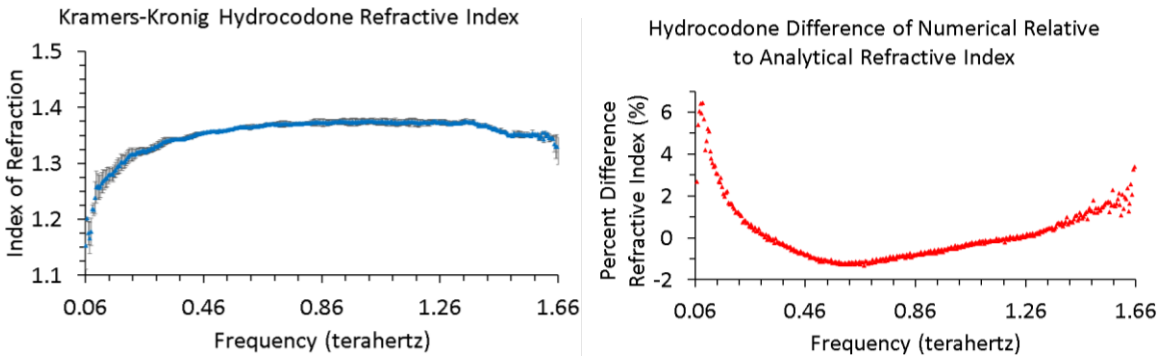

Figure 6.39) The left plot is the average Kramers-Kronig index of refraction determined by taking the average of two unique Kramers-Kronig refractive index profiles. The separate profiles are obtained from the absorption coefficients of two separate single-measurement optimizations of the Hydrocodone sample. The right plot is the percent difference of the numerically optimized refractive index relative to the discrete form of the analytical Kramers-Kronig relationship.

Based on the evidence in the right plot of Figure 6.39, the largest negative and largest positive percent difference between the Kramers-Kronig and optimization extracted index of refraction is -1.32% and 6.45%,

respectively. Therefore, the research assesses that the Hydrocodone refractive index extracted by numerical optimization agrees with the analytic form, and satisfies the causality principle for stable physical systems.

6.1.2. SIMULTANEOUS ORIENTATION AND THICKNESS

The computational tools developed by the research enable either the thickness or the orientation, with respect to incident radiation, to be extracted from THz-TDS measurement data. If the thickness is unknown and the material under evaluation has uniform optical properties, then either the refractive index variational or the total optimal simulation error function value can be used as the minimization quantity. As presented in Section 5.3 and Section 5.4, the extracted thickness resulting from minimizing the variational and minimizing the simulation error will commonly not be identical. If the orientation is unknown and the material under evaluation has uniform optical properties, then the total optimal simulation error function value is used as the minimization quantity.

The use of a refractive index variational as the minimization quantity has the benefit that the optimization path is guided by a known physical property of the material. The minimization of the refractive index variational specifically targets the Fabry-Perot (FP) etalon effect to reduce the FP etalon

oscillation in the spectral profile of the optical properties. In contrast, the use of simulation error does not enforce *a priori* knowledge about the behavior of the optical properties of the material being evaluated. As a result, the research observes that the extracted optical properties using minimization of simulation error for thickness determination have higher refractive index variation due to higher levels of FP etalon effect remaining in the solution. However, the research observes that the extracted optical properties using minimization of simulation error for thickness determination results in lower actual simulated signal error relative to the measured signals, compared with higher actual simulated signal error when minimization of refractive index variation is used for thickness determination. Furthermore, the optimal thickness determined using minimization of the refractive index variation, minimization of the refractive index variance, and minimization of the optimal simulation error are all typically different. All three optimal thicknesses are typically different because the locations of the minimum of each minimization quantity, as a function of thickness, do not coincide.

The observations regarding the refractive index variation and simulation error are concisely presented quantitatively in Table 6.11 using single-measurement optimization of the single-layer HRSi normal incidence measurements. The HRSi sample is selected because it has the largest

refractive index of the five samples used in the research and will have pronounced FP etalon effects. The optimizations of the six HRSi measurements are performed separately and the frequency-independent component of the optimization only includes thickness determination. Lastly, a single iteration of the thickness optimization by relative simulation error is used to generate the corresponding results in Table 6.11 and data in the frequency range 0.160–0.979 THz are used to optimize the thickness.

Table 6.11) The dependence of average actual absolute simulation error (abbreviated: Avg. Act. Abs. Sim. Err.) and average refractive index variation (abbreviated: Avg. Ref. Ind. Var.) on the minimization metric for thickness optimization.

Metric		**HRSi (1)**	**HRSi (2)**	**HRSi (3)**	**HRSi (4)**	**HRSi (5)**	**HRSi (6)**
Optimize Thickness by Relative Simulation Error Minimization	**Avg. Act. Abs. Sim. Err. (10^{-4})**	13.1	13.5	61.1	33.7	5.4	19.2
	Avg. Ref. Ind. Var. (10^{-4})	89.0	126.1	119.1	59.5	129.9	164.3
Optimize Thickness by Refractive Index Variation Minimization	**Avg. Act. Abs. Sim. Err. (10^{-4})**	13.2	3117.3	31305.6	5873.0	7685.7	6770.7
	Avg. Ref. Ind. Var. (10^{-4})	65.1	56.9	40.5	52.4	115.0	156.2

The computational tools developed during the research also enable simultaneous determination of thickness and orientation. The optimizations are performed using the approach outlined in Section 5.5, strictly using the minimization of the total optimal simulation error function value. The ability to extract the sample orientation requires accurate and precise information regarding the layer thicknesses if orientation is unknown but the thickness is

configured as a known quantity. The ability to extract the layer thicknesses requires accurate and precise information regarding the sample orientation if layer thicknesses are unknown but the orientation is configured as a known quantity. Performing orientation extraction and layer thickness extraction separately, using inaccurate or imprecise information, will result in an optimized orientation solution that is inconsistent with the orientation used in the thickness extraction and conversely will result in optimized thickness solutions that are inconsistent with the thicknesses used in the orientation extraction. Even if the thicknesses or orientations are known to high accuracy and precision, the known thicknesses and orientation are unlikely to be the values that define the minimum of a data-driven minimization processes. Therefore, the research recommends performing simultaneous thickness and orientation determination.

The thickness and orientation are simultaneously extracted using an iterative procedure with updates to the frequency-dependent optical parameters at the conclusion of each iteration cycle. The thickness and orientation extraction is performed on materials with uniform and non-uniform optical properties. Materials that are grouped into the class of uniform optical properties include HDPE and HRSi. The HDPE-C and HRSi samples measured at normal incidence are used to demonstrate the thickness and

orientation determination capability within the uniform optical property class of materials. Materials that are grouped into the class of non-uniform optical properties include Lactose, Oxycodone, and Hydrocodone. The Lactose sample measured at 10° incidence in the parallel polarization state is used to demonstrate the thickness and orientation determination capability within the non-uniform optical property class of materials. The optical properties resulting from an optimization of a Lactose measurement at 10° incidence in the perpendicular polarization state are in agreement with the optical properties of Lactose at 10° incidence in the parallel polarization state. The demonstrations using HDPE-C, HRSi, and Lactose each use single-measurement optimizations. Lastly, because of runtime restrictions and to simplify analysis, no re-optimization or air absorption optimization is performed in the demonstration.

The research uses a standard operating procedure when a suite of sample measurements is performed. First, the sample is balanced using a two-dimensional bubble level placed on the mounted sample to level the sample surface parallel to the ground. Next, the sample is brought to perpendicular incidence by adaptively rotating the sample about the angular orientation degree of freedom until the real-time Teraview display of the time-domain signal indicates the peak amplitude signal is at the minimum in time delay.

The angular degree of freedom is either the roll or pitch separately. The roll and pitch cannot be adjusted simultaneously due to the limitation of the apparatus constructed for the research. Next the sample is measured from normal incidence through the final terminating angle of the suite of measurements. Therefore, the research hypothesizes that the physical angle that defines the angular degree of freedom relative to the incident radiation is close to zero, or equivalently nearly exactly normally incident within the dimension of the angle.

6.1.2.1. HIGH-RESISTIVITY SILICON

The single-layer HRSi sample is evaluated using the WSU internal transmission system at normal incidence. A single measurement at normal incidence is used in the optimization. The optimization configuration is configured to optimize the sample thickness and sample orientation. The pitch and roll angles each have the same lower and upper bound of -2.5° and 2.5° in the optimization configuration. The yaw angle is set to 0°. The optimization uses a thickness bound of 50 μm applied to a center thickness of 509.955 μm, which equates to a lower bound of 459.955 μm and an upper bound of 559.955 μm. The center thickness estimate of 509.955 μm is the TOF model thickness estimate for the measurement. The optimization uses a constant initial

complex refractive index of $\tilde{n}_{\mathrm{HRSi}}(\nu) = 3.44 - 0.00012i$. The optimization for sample orientation is limited to ten iterations based on computational runtime requirements. The ten iterations require approximately 19 hours. The final optimized thickness value is 509.843 μm. The final optimized pitch and roll angles are $(3.83\text{x}10^{-3})°$ and $(6.10\text{x}10^{-2})°$, respectively. The convergence behavior of the frequency-independent parameters are shown in the plots of Figure 6.40. The left plot in Figure 6.40 shows the thickness (blue square markers) and angle of incidence (red square markers) evolution through the ten iterations. The right plot in Figure 6.40 shows the pitch angle (purple square markers) and roll angle (green square markers) evolution through the ten iterations. The solid lines in the convergence plots of Figure 6.40 are for illustrative purposes.

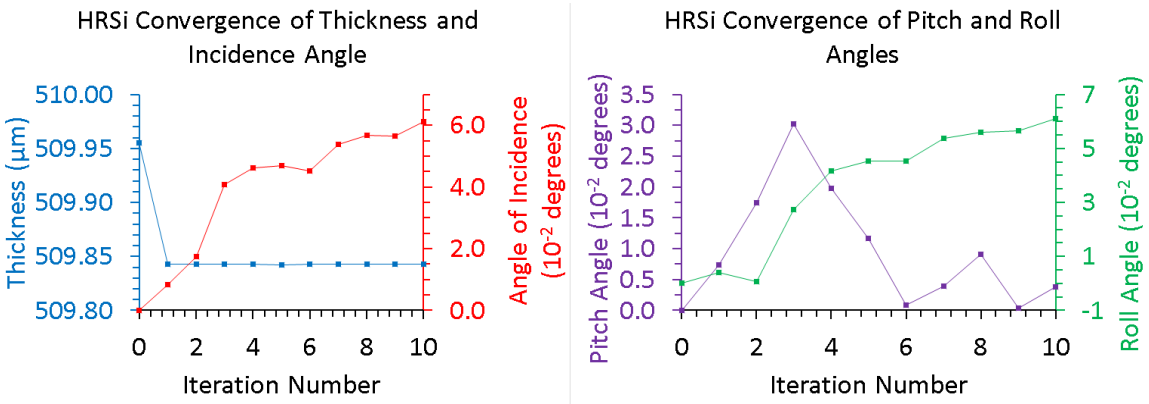

Figure 6. 40) The plot at left shows the convergent behavior of the thickness (blue squares) and orientation (red squares). The plot at right shows convergence of the pitch (purple squares) and roll (green squares) components of the sample orientation.

The index of refraction and absorption coefficient extracted by the optimization is shown in Figure 6.41 with refractive index in the left plot (blue circle markers), and absorption coefficient in the right plot (green circle markers). The solid lines connecting the points in the plots of Figure 6.41 are for illustrative purposes. A re-optimization of 2% on the refractive index is required at the conclusion of the ten iterations in the HRSi example presented here because of an undesired optimization solution path that begins at a frequency of 1.6 THz. The re-optimization extends the usable bandwidth of the optical properties. The refractive index shown in Figure 6.41 is the re-optimization result. The absorption coefficient has not been re-optimized.

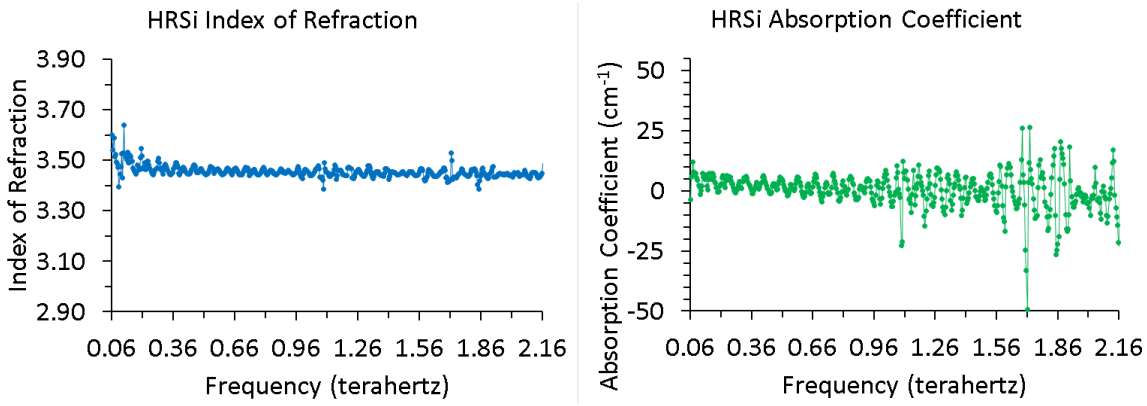

Figure 6.41) The refractive index (left, blue circles) and absorption coefficient (right, green circles) of the HRSi sample using optimization to simultaneously extract thickness and orientation.

A direct comparison of the optical properties provided in this example are not given with respect to the results of Section 6.1.1.1 for two reasons. The first reason is because the center frequencies of the frequency bins in this example are different than those of Section 6.1.1.1. The frequencies are not

identical because Section 6.1.1.1 use a synchronization across six measurements and this example uses a single measurement. The second reason is because the results presented in Section 6.1.1.1 are from a six-measurement optimization using thickness optimized by refractive index variation minimization without orientation minimization. The result of this section uses single-measurement optimization with error function minimization for both thickness and orientation determination. A direct comparison of the optical properties in this section to those of Section 6.1.1.1 will necessitate a single-measurement optimization using refractive index variation minimization. An indirect comparison is made however. The comparison assesses the presence of the FP etalon effect in the optimized refractive index. The statistical variance in refractive index in the frequency range of 0.16–1.06 THz for the single-measurement optimization of this section is 2.3×10^{-4}. The refractive index variance for the same frequency range for Section 6.1.1.1 is 4.0×10^{-5}. The conclusion is that the refractive index variation in Section 6.1.1.1 is nearly an order of magnitude less than the variation in this section because of a combination of the five additional measurements and the targeting of the FP etalon effect by refractive index variation minimization. The influence of measurement clutter present in the measured signal is incorporated into the thickness and orientation

optimization based on simulation error minimization without *a priori* knowledge of the expected behavior of the optical property.

6.1.2.2. HIGH DENSITY POLYETHYLENE

The single-layer HDPE-C sample is evaluated using the WSU internal transmission system at normal incidence. A single measurement at normal incidence is used in the optimization. The optimization configuration is configured to optimize the sample thickness and sample orientation. The pitch and roll angles each have the same lower and upper bound of -2.5° and 2.5° in the optimization configuration. The yaw angle is set to 0°. The optimization uses a thickness bound of 50 μm applied to a center thickness of 1601.51 μm, which equates to a lower bound of 1551.51 μm and an upper bound of 1651.51 μm. The center thickness estimate of 1601.51 μm is the TOF model thickness estimate for the measurement. The optimization uses a constant initial complex refractive index of $\tilde{n}_{\mathrm{HDPE}}(\nu) = 1.56 - 0.00061i$. The optimization for sample orientation is limited to ten iterations based on computational runtime requirements. The ten iterations require approximately 18 hours. The final optimized thickness value is 1611.65 μm. The final optimized pitch and roll angles are $(1.64\text{x}10^{-2})°$ and $(4.16\text{x}10^{-1})°$, respectively. The convergence behavior of the frequency-independent parameters are shown in the plots of

Figure 6.42. The left plot in Figure 6.42 shows the thickness (blue square markers) and angle of incidence (red square markers) evolution through the ten iterations. The right plot in Figure 6.42 shows the pitch angle (purple square markers) and roll angle (green square markers) evolution through the ten iterations. The solid lines in the convergence plots of Figure 6.42 are for illustrative purposes.

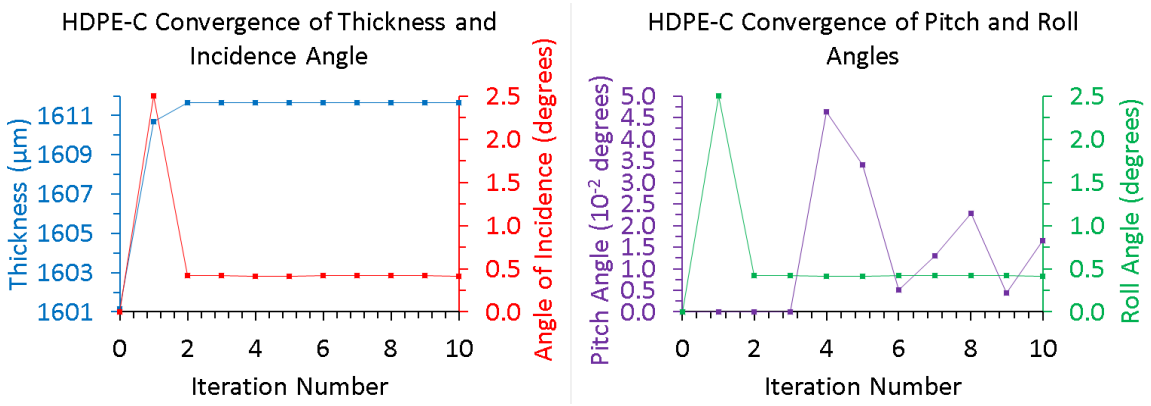

Figure 6.42) The plot at left shows the convergent behavior of the thickness (blue squares) and orientation (red squares). The plot at right shows convergence of the pitch (purple squares) and roll (green squares) components of the sample orientation.

The index of refraction and absorption coefficient extracted by the optimization is shown in Figure 6.43 with refractive index in the left plot (blue circle markers), and absorption coefficient in the right plot (green circle markers). The solid lines connecting the points in the plots of Figure 6.43 are for illustrative purposes. Generally, more oscillation in the optical property spectral profiles are present in the result of this section compared with the results of Section 6.1.1.2 due to the presence of residual FP etalon effect not accounted for in the optimized physical model parameters.

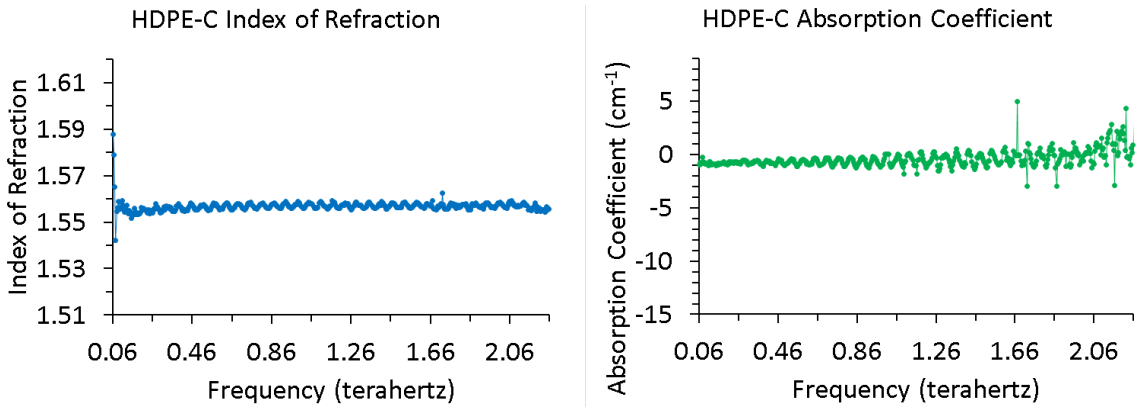

Figure 6.43) The refractive index (left, blue circles) and absorption coefficient (right, green circles) of the HDPE-C sample using optimization to simultaneously extract thickness and orientation.

A partially direct comparison of the optical properties provided in this example is given with respect to the results of Section 6.1.1.2. The center frequencies of the frequency bins in this example are identical to those of Section 6.1.1.2. Both this section and Section 6.1.1.2 use the same single measurement for optimization. The comparison is partial because the results of Section 6.1.1.2 are for thickness optimization without orientation optimization, but this section is for thickness and orientation optimization. A direct comparison of the refractive index variation between the two sections is possible if the results of this section are generated using thickness optimization by simulation error minimization without orientation optimization. The statistical variance in refractive index in the frequency range of 0.16–1.06 THz for the single-measurement optimization of this section is 1.5×10^{-6}. The refractive index variance for the same frequency range for Section 6.1.1.2 is 8.5×10^{-7}. The conclusion is that the refractive index

variation in Section 6.1.1.2 is more than an order of magnitude less than the variation in this section because of the targeting of the FP etalon effect by refractive index variation minimization. The influence of measurement clutter present in the measured signal is incorporated into the thickness and orientation optimization based on simulation error minimization without *a priori* knowledge of the expected behavior of the optical property.

6.1.2.3. ALPHA LACTOSE MONOHYDRATE

The Lactose sample is evaluated using the WSU internal transmission system at 10° incidence with parallel electric field polarization relative to the incident radiation and the surface of the sample. A measurement at 10° incidence is used, in contrast to the simultaneous thickness and orientation optimizations using HRSi and HDPE-C at normal incidence, to demonstrate the ability of the algorithm to function at non-normal angles of incidence. A single measurement is used in the optimization. The optimization configuration is configured to optimize the sample thickness and sample orientation. The pitch angle in the optimization configuration has a lower and upper bound of 7.5° and 12.5°, respectively. The pitch angle in the optimization configuration has a lower and upper bound of -2.5° and 2.5°, respectively. The yaw angle is set to 0°. The optimization uses a thickness bound of 50 μm applied to a center thickness of 2390 μm, which equates to a

lower bound of 2340 μm and an upper bound of 2440 μm. The center thickness estimate of 2390 $\pm$ 25.4 μm is the Vernier micrometer measured thickness of the metal washer used to encase the Lactose particles. The optimization uses a constant initial complex refractive index of $\tilde{n}_{\text{Lactose}}(\nu) = 1.7 - 0.01i$. The optimization for sample orientation is limited to ten iterations based on computational runtime requirements. The ten iterations require approximately 16 hours. The final optimized thickness value is 2389.88 μm. The final optimized pitch and roll angles are 9.96° and (9.30×10^{-4})°, respectively. The convergence behavior of the frequency-independent parameters are shown in the plots of Figure 6.44. The left plot in Figure 6.44 shows the thickness (blue square markers) and angle of incidence (red square markers) evolution through the ten iterations. The right plot in Figure 6.44 shows the pitch angle (purple square markers) and roll angle (green square markers) evolution through the ten iterations. The solid lines in the convergence plots of Figure 6.44 are for illustrative purposes.

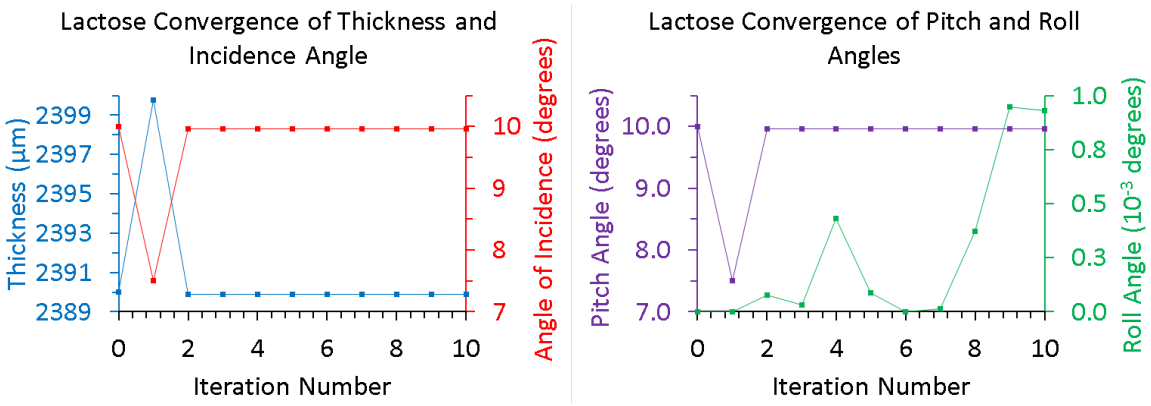

Figure 6.44) The plot at left shows the convergent behavior of the thickness (blue squares) and orientation (red squares). The plot at right shows convergence of the pitch (purple squares) and roll (green squares) components of the sample orientation.

The index of refraction and absorption coefficient extracted by the optimization is shown in Figure 6.45 with refractive index in the left plot (blue circle markers), and absorption coefficient in the right plot (green circle markers). The solid lines connecting the points in the plots of Figure 6.45 are for illustrative purposes. The grey box in the left plot of Figure 6.45 highlights a region of the refractive index solution that is an undesirable solution path. The frequency that marks the onset of the undesired solution path is correlated with the second absorption feature at 1.19467 THz. The optimization is also performed for Lactose at 10° incidence with perpendicular electric field polarization relative to the incident radiation and the sample surface. Although not shown, the parallel and perpendicular optical properties are in agreement. The agreement indicates that the optical properties of the Lactose sample are isotropic.

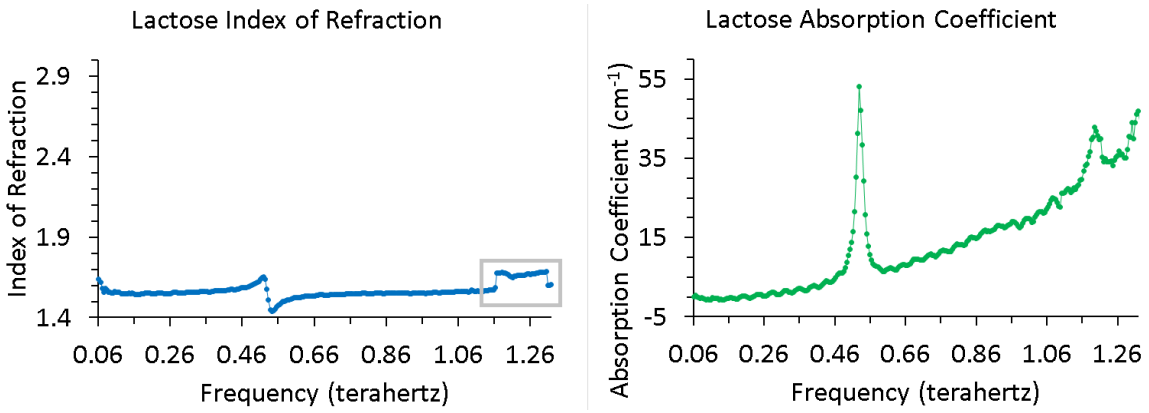

Figure 6.45) The refractive index (left, blue circles) and absorption coefficient (right, green circles) of the Lactose sample using optimization to simultaneously extract thickness and orientation. The elevated values in the grey box in the lower right corner of the left plot indicates an undesired refractive index solution path.

A direct comparison of the optical properties provided in this example are not given with respect to the results of Section 6.1.1.3 for two reasons. The first reason is because the center frequencies of the frequency bins in this example are different than those of Section 6.1.1.3. The frequencies are not identical because Section 6.1.1.3 use a synchronization of two measurements and this example uses a single measurement. The second reason is because the results presented in Section 6.1.1.3 do not optimize for thickness or orientation. The result of this section uses single-measurement optimization with error function minimization for both thickness and orientation determination. A direct comparison of the optical properties in this section to those of Section 6.1.1.3 will necessitate a single-measurement optimization using refractive index variation minimization. An indirect comparison is made however. The comparison assesses the presence of the FP etalon effect in the

optimized refractive index. The average absolute variation in refractive index in the frequency range of 0.10–0.45 THz for the single-measurement optimization of this section is 1.728×10^{-3}. The refractive index variation for the same frequency range for Section 6.1.1.3 is 1.838×10^{-3}. The variation is used instead of the variance to mitigate effects of the curvature of the refractive index in the variational assessment. The 350 GHz bandwidth used to compute the variation contains 80 data points. The conclusion is that the refractive index variation in Section 6.1.1.3 is slightly greater than the variation in this section. Although a small difference, the reduced average absolute variation indicates the thickness and orientation optimization better incorporates the FP etalon effect into the physical model parameter values compared with the non-optimized values used in Section 6.1.1.3.

6.2. MULTI-LAYER SAMPLES

Two demonstrations are provided which represent the capability of optical parameter extraction using multi-layer sample measurement optimization. The demonstrations use normal incidence measurements in the transmission configuration. The first demonstration shows the ability of the algorithm to detect the presence of air gaps in HDPE. The second demonstration shows the ability of the algorithm to perform identification of unknown materials in HRSi-HDPE multi-layer stacks.

6.2.1. AIR GAP DETECTION IN HDPE

The air gap detection capability is demonstrated using HDPE. The air gap detection is a capability of potential interest to manufacturing for quality control of products. Although detecting an air gap using a single layer-model should be possible, this presentation extends the capability using a multi-layer model. First, an optical parameter extraction is performed on single layer HDPE-B. The Vernier micrometer measured thickness of HDPE-B is 6050 $\pm$ 25.4 μm. The HDPE-B sample is used in the demonstration as the nominal product generated during a hypothetical manufacturing process. Next, two separate optical parameter extractions are performed on measurements of a single multi-layer sample consisting of two layers of HDPE-A separated by a half-inch air gap. The multi-layer sample is abbreviated HDPE-A|Air|HDPE-A. The Vernier micrometer measured thickness of HDPE-A is 3070 $\pm$ 25.4 μm. The presence of the air gap in the HDPE sample is a hypothetical defect that represents a failure of the manufacturing process. The goal is to demonstrate the ability to detect the air gap defect.

The first parameter extraction of HDPE-A|Air|HDPE-A is performed using an air gap included the theoretical model. The second parameter extraction of HDPE-A|Air|HDPE-A is performed without an air gap included

in the theoretical model. The extracted index of refraction and absorption coefficient of HDPE-B are shown in the left plot of Figure 6.46. The extracted index of refraction and absorption coefficient of the HDPE-A|Air|HDPE-A multilayer structure theoretically modeled to include the air gap are shown in the right plot of Figure 6.46.

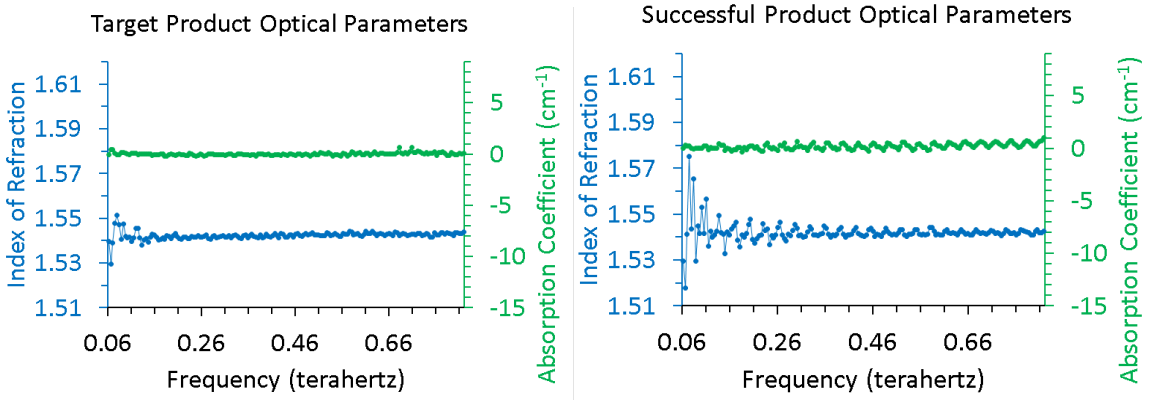

Figure 6.46) The refractive index (left, blue circles) and absorption coefficient (left, green circles) of single layer HDPE-B. The refractive index (right, blue triangles) and absorption coefficient (right, green triangles) of the multi-layer HDPE-A|Air|HDPE-A sample including the air gap in the theoretical model.

Qualitatively, the optical parameters of the HDPE-B extraction agree with the optical properties the HDPE-A|Air|HDPE-A extraction using the theoretical air gap in the model, which indicates that the manufacturing process has failed. The accuracy of the statement is proven by showing the index of refraction and absorption coefficient extracted for HDPE-A|Air|HDPE-A without the air gap included theoretically in the model in Figure 6.47. The limited bandwidth presented in Figure 6.47 is indicative of the low signal strength of the 6050 μm thick HDPE-B measurements due to

the combination of thickness and absorption coefficient of the HDPE-B sample. The signal strength for the measurement of two layers of 3070 μm thick HDPE-A is comparably low to the HDPE-B measurements because the total thickness of HDPE in the HDPE-A|Air|HDPE-A multi-layer is nearly equal to that of single-layer HDPE-B. The strong spectral ringing in the optical properties of HDPE extracted from the HDPE-A|Air|HDPE-A measurements are hypothesized to be Fabry-Perot (FP) etalon effects that are enhanced, relative to the single-layer HDPE-B, due to the two additional interfaces in the HDPE-A|Air|HDPE-A multi-layer.

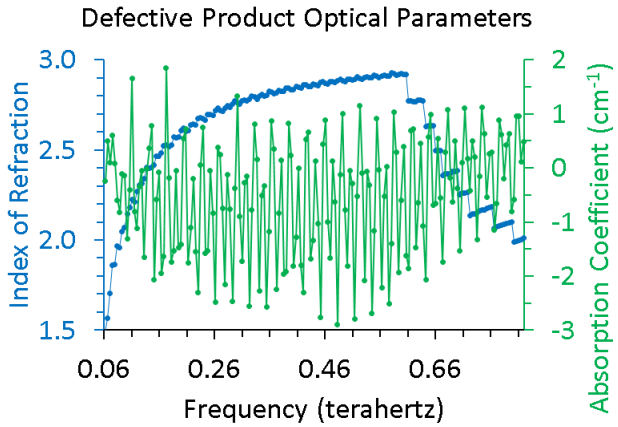

Figure 6.47) The refractive index (left, blue circles) and absorption coefficient (right, green circles) of the multi-layer HDPE-A|Air|HDPE-A sample excluding the air gap from the theoretical model.

6.2.2. MATERIAL IDENTIFICATION IN MULTI-LAYERS

The second demonstration using a multi-layer sample is the identification of a hypothetically unknown material in in a stack of HRSi and HDPE-A with a half-inch air gap between the HRSi and HDPE-A. The three-

layer stack is labelled HRSi|Air|HDPE-A. First, an optimization is performed using three transmission measurements of the HRSi|Air|HDPE-A sample and five single-layer HRSi measurements. The measurements are recorded using the WSU internal, WSU external, and OSU internal transmission systems. All the measurements are normal incidence measurements. The first scenario tests to determine if an optical property profile is able to be extracted for HDPE that correlates with the single-layer HDPE optical property profile. A known thickness of 506.010 μm and 3031.13 μm is used for the thickness of HRSi and HDPE-A, respectively. The thicknesses are the average of the thicknesses derived using the TOF model on the single layer HRSi and HDPE-A samples. No air absorption optimization or optical parameter re-optimization is applied to obtain the results. The extracted refractive index and absorption coefficient of HRSi is shown in the top row of Figure 6.48 The extracted refractive index and absorption coefficient of the hypothetically unidentified layer, HDPE-A in the first example, is shown in the bottom row of Figure 6.48.

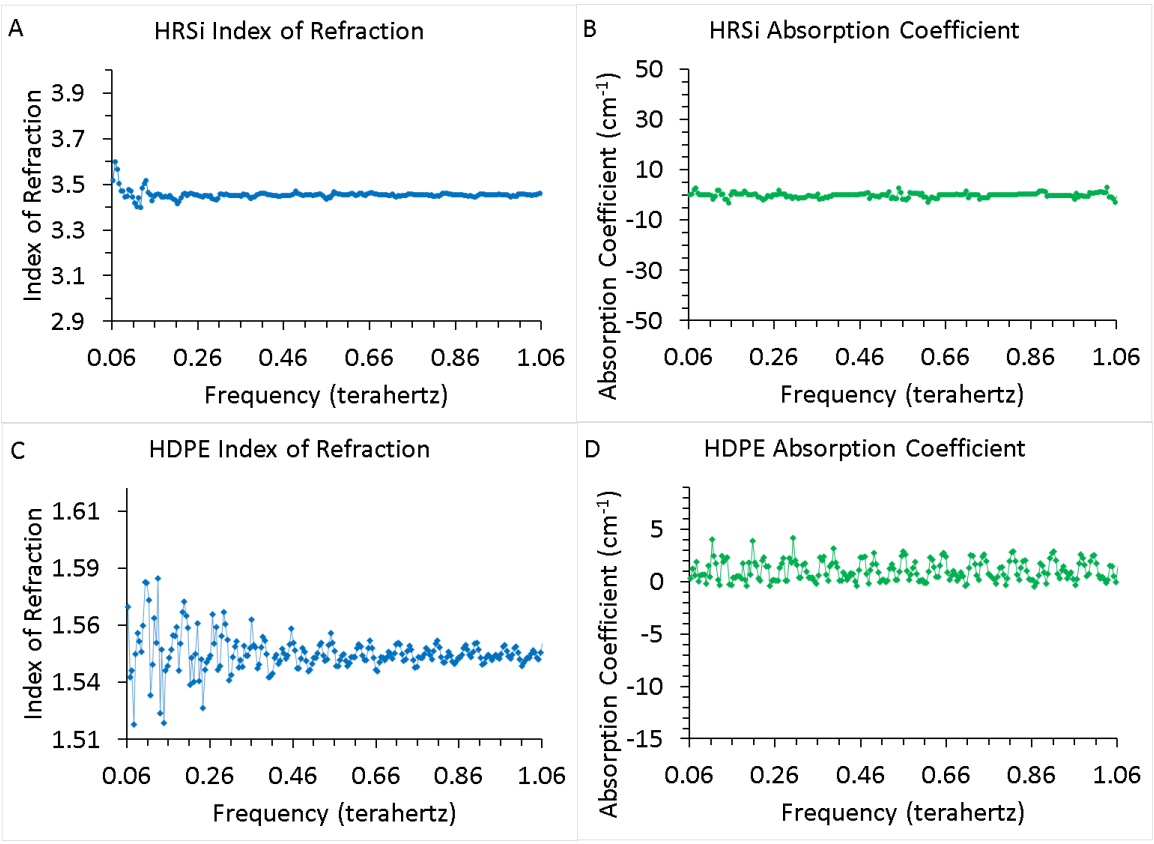

Figure 6.48) The HRSi refractive index (plot A, top left) and absorption coefficient (plot B, top right). The unidentified material refractive index (plot C, bottom left) and absorption coefficient (plot D, bottom right). The unidentified material is HDPE.

The second example of unidentified material identification is an optimization performed using three transmission measurements of the HRSi|Air|HDPE-A sample, six single-layer HDPE-A measurements, and an HDPE-C measurement. The measurements are recorded using the WSU internal, WSU external, and OSU internal transmission systems. All the measurements are normal incidence measurements. The second scenario tests to determine if an optical property profile is able to be extracted for HRSi that correlates with the single-layer HRSi optical property profile. A known thickness of 506.010 μm and 3031.13 μm is used for the thickness of HRSi

and HDPE-A, respectively. The thicknesses are the average of the thicknesses derived using the TOF model on the single layer HRSi and HDPE-A samples. No air absorption optimization or optical parameter re-optimization is applied to obtain the results. The extracted refractive index and absorption coefficient of HDPE-A is shown in the bottom row of Figure 6.49 The extracted refractive index and absorption coefficient of the hypothetically unidentified layer, HRSi in the second example, is shown in the top row of Figure 6.49.

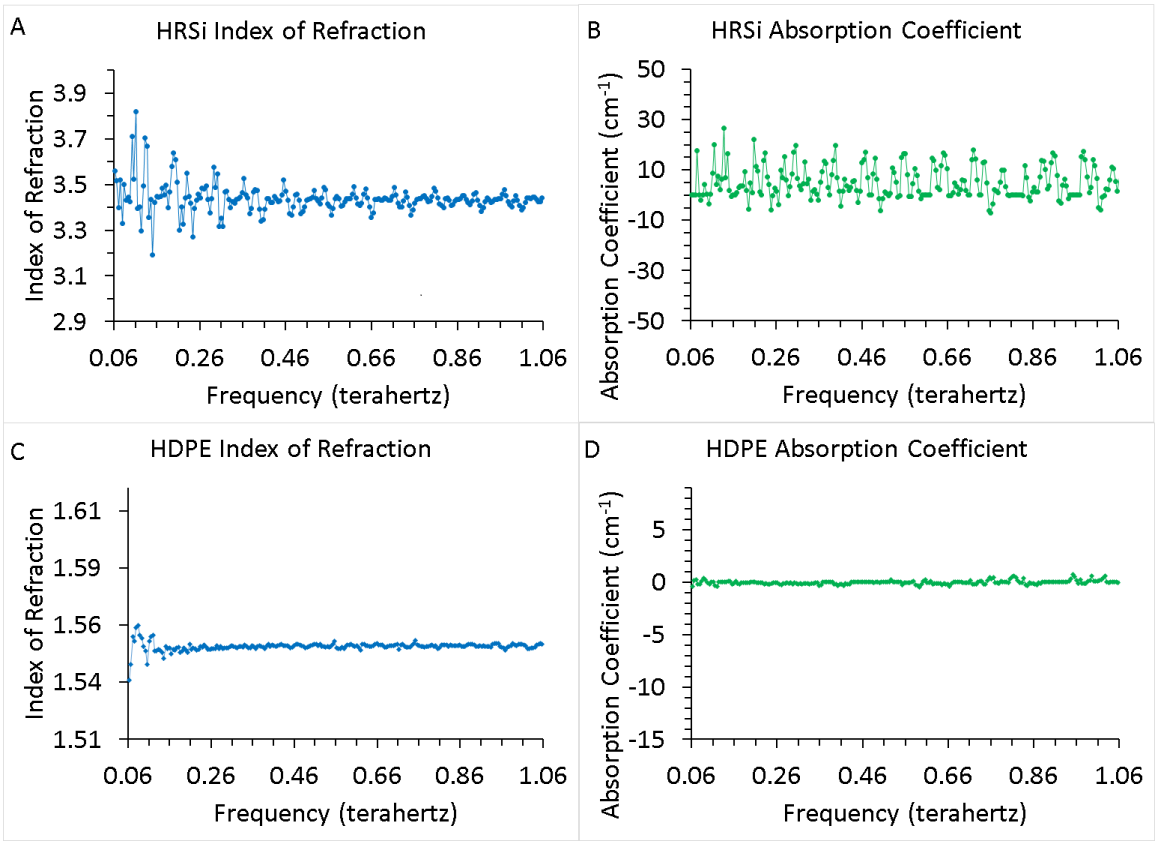

Figure 6.49) The unidentified material refractive index (plot A, top left) and absorption coefficient (plot B, top right). The HDPE refractive index (plot C, bottom left) and absorption coefficient (plot D, bottom right). The unidentified material is HRSi.

Analysis of Figure 6.48 shows that if the HRSi is known to exist in the multi-layer sample, the approximate optical properties of the HDPE layer can be successfully extracted. A comparison of the optical property of the hypothetically unknown HDPE layer with the single-layer HDPE optical property profiles show positive correlation. Analysis of Figure 6.49 shows that if the HDPE is known to exist in the multi-layer sample, the approximate optical properties of the HRSi layer can be successfully extracted. A comparison of the optical property of the hypothetically unknown HRSi layer with the single-layer HRSi optical property profiles also show positive correlation. The multi-layer optical property extractions for the hypothetically unknown materials do show higher variation compared with extractions of the single-layer counterpart. No re-optimization is performed to generate the optical property profiles shown in Figure 6.48 and Figure 6.49. An attempt is made to reduce the variation by including three additional measurements of the multi-layer sample in the HDPE-A|Air|HRSi arrangement. The HDPE-A|Air|HRSi sample arrangement places the THz radiation incident first on the HDPE-A layer, whereas the HRSi|Air|HDPE-A arrangement places the radiation incident first on the HRSi layer. The additional three measurements do not significantly reduce the overall variation in the optical properties extracted by optimization.

7. COMPUTATIONAL RUNTIME ANALYSIS

The computational runtime of many of the optimizations are recorded for runtime profiling purposes. The runtime profiles are provided for the FDO and FIO components of the algorithm. A runtime profiling of the objective functions and error measures facilitates identification of runtime bottlenecks in the computer code. The identification of bottlenecks enables runtime improvements specifically targeting the bottlenecks to be implemented which improve functioning of the algorithm. Because of the runtime profiling, the optimization algorithm developed during the research has evolved significantly throughout the project. Measurable runtime reduction is achieved in the phase error calculation of the magnitude and phase objective function. However, the most dramatic improvement in runtime is obtained regarding the computational runtime required for optimization using the time-domain objective function. Meaningful reduction in runtimes are also achieved by creating a computational branch which uses simplified equations for purely normal incidence transfer functions. Implementation of the computational linker strategy has also significantly reduced the computational runtime of the FDO. The runtime profiling at each major step of the

optimizations for various configurations aides in future improvements utilizing parallelization, multi-threading, and cluster computing.

7.1. COMPUTATIONAL RUNTIME IMPROVEMENT

The goal of this section is to improve the programmatic implementation of all five objective function formulations to achieve physical parameter efficacy in the least amount of computational runtime. The physical parameters extracted from the improved implementations are verified with the original implementations with the benefit that the extractions require less computer time. The computer time for each extraction is reduced in two ways. First, reformulations of the objective functions are identified which decrease the number of mathematical operations. Second, pure Python interpretive computer code is exchanged for Numpy and Numba compiled libraries within the Python programming language.

The objective function analysis indicates that the time-domain signal amplitude objective function formulation provides physical parameter extractions with the least amount of solution error and physical parameters that agree with published results. Therefore, the time-domain objective function formulation is the suggested formulation, based of accuracy of the results. However, the time-domain objective function formulation, as

implemented in Equation 5.14, is the most computationally intensive objective function of the five possible objective function formulations because the time-domain formulation requires the inverse DFT at each trial solution to transform the frequency-domain conflated signal into the time-domain. Additionally, the time-domain objective function must compute the difference between the measured signal and the conflated signal at each time delay position; the list of time delay values has twice as many elements as the list of frequencies due to the definition of the DFT. Lastly, once the conflated complex-valued frequency-domain amplitudes are transformed into real-valued time-domain amplitudes, the non-corrupt indices of the time-domain conflated signal must be isolated. The frequency-domain magnitude and phase objective formulations, both the signal and transfer function versions, are the second most computationally intensive objective functions to compute because of the cumulative phase and phase unwrapping calculations that must occur. The least computationally intensive objective functions are the complex frequency-domain signal amplitude and transfer function formulations because only the value at the frequency index under evaluation needs to be operated.

The evolution of the computational runtime improvement of the five objective function formulations is provided in Table 7.1. The white

highlighted cells in Table 7.1 represent pure interpretive Python implementations. The green highlighted cells represent a hybridized implementation of pure interpretive Python and compiled Numpy plus Numba implementations. In Table 7.1, cells with numbers as black text are the original mathematical implementations, and cells with numbers as red text are implementations which use a mathematical re-formulation to reduce the number of operations. The execution times in Table 7.1 are the average execution times for a single pass through the objective function calculation. One pass through the objective function includes: theoretical transfer function calculation, signal conflation, signal transformation, error function calculation, and precision limit enforcements throughout the objective function computations. The average execution time is across 1,000 timing events for six-measurement optimization, using the simplified normal incidence Fresnel equations. The functions calls are performed serially. The computer configuration used to test the execution times is a 64-bit Windows 8 operating system with an Intel Core i7 4790K clocked at 4.0 GHz and 32 GB of 12800 MB/s DDR3 clocked at 1600 MHz.

Table 7.1) Evolution of the average execution time of a single call to the objective function.

Objective Function	Implementation-1 Average Execution Time (ms)	Implementation-2 Average Execution Time (ms)	Implementation-3 Average Execution Time (ms)	Execution Time Improve-ment Factor
Complex FD Transfer Function	1.1	1.1	1.1	1.0 X
Complex FD Amplitude	1.1	1.1	1.1	1.0 X
Magnitude & Phase	2.0	1.5	1.5	1.3 X
Transfer Function Magnitude & Phase	2.0	1.5	1.5	1.3 X
Real TD Amplitude	248.78	10.80	6.0	41.5 X

The runtime performance of the complex frequency-domain transfer function and complex frequency-domain signal amplitude formulations are shown in the first and second row of Table 7.1, respectively. The error computed in the objective function using the complex frequency-domain transfer function and complex frequency-domain signal amplitude formulations only require the complex values at the evaluation frequency. There is no change in these two objective functions between implementation-1 and implementation-3 in Table 7.1 and therefore the runtime is unchanged.

These two objective functions are recast into vectorized computations using the Numpy and Numba libraries in implementation-3. The changes made in implementation-3 effectively yields no change in runtime performance for these two objective functions, as shown in the first two rows of the right-most column in Table 7.1.

The runtime performance of the two magnitude and phase objective functions using the frequency-domain signal and transfer function formulations are shown in the third and fourth rows of Table 7.1, respectively. Because the magnitude at a frequency is not dependent on the magnitude at previous frequencies, the magnitude error computed in the objective function only requires the magnitude at the evaluation frequency and therefore the magnitude error calculation is unchanged in the three implementations. However, the phase is a cumulative variable as a function of frequency.

The phase error of implementation-1 computes the measured and conflated unwrapped cumulative phase using the frequency-domain signal or transfer function from the zero-frequency bin up to and including the bin of the evaluation frequency as defined in Equations 7.1–7.2. The total difference Δ in phase between measurement and theory, defined in Equation 7.3, only requires the cumulative unwrapped phase of the measurement and conflation

at the bin of the evaluation frequency. In implementation-2, the calculation of the conflated phase at the evaluation frequency is modified. First, the unwrapped cumulative measured phase at the frequency preceding the evaluation frequency, labelled $\mathscr{p}_{\text{measured}_{k-1}}$, is computed as the phase offset. Next, the conflated complex frequency-domain signal or transfer function values at the evaluation frequency and the preceding frequency, labelled χ and $f_{\text{measured}_{k-1}}$ respectively, are used to compute the phase change using the phase unwrap function. Lastly, the conflated phase change $\delta_{\mathscr{p}}$ defined in Equation 7.4 is added to the phase offset to obtain the modified implementation of the conflated unwrapped cumulative phase $\mathscr{p}_{\text{conflated}_k}$ at the evaluation frequency defined in Equation 7.5.

$$\mathscr{p}_{\text{measured}_k} = (\mathcal{U}nwrap(\mathcal{T}an_2{}^{-1}(\frac{\Im\mathfrak{m}(\tilde{f}_{\text{measured}_{0:k}})}{\Re\mathfrak{e}(\tilde{f}_{\text{measured}_{0:k}})})))_k \tag{7.1}$$

$$\mathscr{p}_{\text{conflated}_k} = (\mathcal{U}nwrap(\mathcal{T}an_2{}^{-1}(\frac{\Im\mathfrak{m}(\tilde{f}_{\text{measured}_{0:k-1}}, \tilde{\chi})}{\Re\mathfrak{e}(\tilde{f}_{\text{measured}_{0:k-1}}, \tilde{\chi})})))_k \tag{7.2}$$

$$\Delta = \mathscr{p}_{\text{measured}_k} - \mathscr{p}_{\text{conflated}_k} \tag{7.3}$$

$$\delta_{\mathscr{p}} = (\mathcal{U}nwrap(\mathcal{T}an_2{}^{-1}(\frac{\Im\mathfrak{m}(\tilde{f}_{\text{measured}_{k-1}}, \tilde{\chi})}{\Re\mathfrak{e}(\tilde{f}_{\text{measured}_{k-1}}, \tilde{\chi})})))_{k-1} \tag{7.4}$$

$$\mathscr{p}_{\text{conflated}_k} = \mathscr{p}_{\text{measured}_{k-1}} + \delta_{\mathscr{p}} \tag{7.5}$$

The implementation change introduced by replacing Equation 7.2 with Equation 7.5 yields the same optimization solution as the original

implementation. The same phase error calculation in implementation-2 is leveraged in implementation-3. The two magnitude and phase objective functions are recast into vectorized computations using the Numpy and Numba libraries in implementation-3. The changes made in implementation-3 yields a factor of 1.3 improvement over implementation-1 for these two objective functions, shown in the third and fourth rows of the last column in Table 7.1. The objective function computation includes calculating the: theoretical transfer functions, signal conflations and transformations, error function values, and precision limit enforcements.

The runtime performance of the real-valued time-domain signal amplitude is shown in the last row of Table 7.1. In implementation-1, the Inverse-DFT (IDFT) is used to convert the conflated frequency-domain signal amplitudes into conflated time-domain signal amplitudes for error calculation. In implementation-2, the time-domain amplitude objective function is recast into vectorized computations using the Numpy and Numba libraries. In implementation-3, it is observed that in the case of frequency-domain based optimizations which only affect the parameters at a single frequency, information from no more than a single column of the IDFT matrix is needed to determine the change in time-domain signal amplitude. The change yields the same optimization solution as the original implementation. The changes

made in implementation-3 yields a factor of 41.5 improvement over implementation-1, shown in the last row of the last column in Table 7.1.

The general concept that leads to the time-domain objective function formulation in implementation-3 is outlined by Equations 7.6–7.14. Equation 7.6 defines the elements of the DFT matrix [94]. Equation 7.7 defines the inverse of the DFT matrix as the complex conjugate of the DFT matrix, and $\vec{a}_k$ represent the columns of the matrix where k is the column of the IDFT matrix. The row and column of the matrix is n and k, respectively. The number of rows and columns are equal to N, which is the number of elements in the time-domain signal. Each column of the IDFT matrix corresponds to a frequency bin in the measured $\vec{f}_{\text{measured}}$ and conflated $\vec{f}_{\text{conflated}}$ frequency-domain signals which are defined in terms of the time-domain signals $\vec{t}_{\text{measured}}$ and $\vec{t}_{\text{conflated}}$ in Equations 7.8–7.9. The error vector $\vec{\Delta}$ of the element-wise difference between the measured and conflated frequency-domain signals is defined in Equations 7.10–7.11. The error vector is explicitly shown for several elements in Equation 7.12. In Equation 7.12, the complex value of the conflated signal at the frequency bin corresponding to the evaluation frequency is represented by the optimization variable $\tilde{\chi}$. Carrying out the Matrix multiplication and vector subtraction in Equation 7.12

shows a reduction to the simplified error calculation in Equation 7.13. Rearranging terms to obtain Equation 7.14 demonstrates mathematical equivalence to Equation 7.10. The term $(\tilde{f}_k \cdot \vec{a}_k + \tilde{f}_k^{\,*} \cdot \vec{a}_{-k})$ in Equation 7.14 is pre-computed and input to the objective function, whereas the $(\tilde{\chi} \cdot \vec{a}_k + \tilde{\chi}^* \cdot \vec{a}_{-k})$ term is computed dynamically on each iteration of the objective function optimization. The notation $\vec{a}_{-k}$ selects the *k*th column starting from the last column of the IDFT matrix.

$$A_{n,k} = (e^{-i\frac{2\pi}{N}})^{(n \cdot k)} \tag{7.6}$$

$$A^{-1} = A^* = \left[\vec{a}_1 \vec{a}_2 \vec{a}_3 \cdots \vec{a}_{N-1} \vec{a}_N\right] \tag{7.7}$$

$$A \cdot \vec{t}_{\text{measured}} = \vec{f}_{\text{measured}} \tag{7.8}$$

$$A \cdot \vec{t}_{\text{conflated}} = \vec{f}_{\text{conflated}} \tag{7.9}$$

$$\vec{\Delta} = A^{-1} \cdot \vec{f}_{\text{measured}} - A^{-1} \cdot \vec{f}_{\text{conflated}} \tag{7.10}$$

$$\vec{\Delta} = A^{-1}(\vec{f}_{\text{measured}} - \vec{f}_{\text{conflated}}) \tag{7.11}$$

$$\vec{\Delta} = \left[\vec{a}_1 \vec{a}_2 \vec{a}_3 \cdots \vec{a}_{N-1} \vec{a}_N\right] \left(\begin{bmatrix} \tilde{f}_1 \\ \tilde{f}_2 \\ \tilde{f}_3 \\ \vdots \\ \tilde{f}_3^{\,*} \\ \tilde{f}_2^{\,*} \end{bmatrix} - \begin{bmatrix} \tilde{f}_1 \\ \tilde{\chi} \\ \tilde{f}_3 \\ \vdots \\ \tilde{f}_3^{\,*} \\ \tilde{f}_2^{\,*} \end{bmatrix} \right) \tag{7.12}$$

$$\vec{\Delta} = (\tilde{f}_k - \tilde{\chi})\vec{a}_k - (\tilde{f}_k^{\,*} - \tilde{\chi}^*)\vec{a}_{-k} \tag{7.13}$$

$$\vec{\Delta} = (\tilde{f}_k \cdot \vec{a}_k + \tilde{f}_k^{\,*} \cdot \vec{a}_{-k}) - (\tilde{\chi} \cdot \vec{a}_k + \tilde{\chi}^* \cdot \vec{a}_{-k}) \tag{7.14}$$

The calculation of the right-most term $A^{-1} \cdot \vec{f}$ in Equation 7.10 requires *N(8N - 2)* mathematical operations, where *N* is the number of time-domain amplitude elements. The number of operations are for complex values, six operations for each pair of complex value multiplication, and two operations for each pair of complex value addition. The operations do not count the imaginary number arithmetic. In the case of multiplication, the mathematical operations counted are in red: $(x_1 + \mathrm{i}y_1) \cdot (x_2 + \mathrm{i}y_2) = ((x_1 \cdot x_2) + (\mathrm{i}y_1 \cdot \mathrm{i}y_2)) + ((x_1 \cdot \mathrm{i}y_2) + (x_2 \cdot \mathrm{i}y_2))$. In the case of addition, the mathematical operations counted are also in red: $(x_1 + \mathrm{i}y_1) + (x_2 + \mathrm{i}y_2) = (x_1 + x_2) + (\mathrm{i}y_1 + \mathrm{i}y_2)$. In comparison, the calculation of the right-most term $(\tilde{\chi} \cdot \vec{a}_k + \tilde{\chi}^* \cdot \vec{a}_{-k})$ in Equation 7.14 requires *14N* operations. Mathematically, Equation 7.14 provides a theoretical factor of *(8N - 2)/14* reduction in the number of operations. A single measurement time-domain signal of length *N = 10,000* is representative of the data used in the research, and the number of operations are reduced by a factor of 5,714.

Further computational simplification is achieved beyond Equation 7.14. The general result for the addition of the product of two complex numbers with the product of their complex conjugates is defined in Equation 7.15. In the case that the frequency bin, represented by the integer index k, is

not the first bin or the last bin then Equation 7.16 is valid. In the first line of Equation 7.16, *N* is the number of elements in the time-domain signal which can be an even or odd number. Calculation of the $(\Re\mathrm{e}(\tilde{\chi}) \cdot \Re\mathrm{e}(\vec{a}_k) - \Im\mathrm{m}(\tilde{\chi}) \cdot \Im\mathrm{m}(\vec{a}_k))$ term in the second line of Equation 7.16 requires three operations, with each operation in red; The total number of operations across each frequency bin is approximately *3N*. Mathematically, Equation 7.16 provides a theoretical factor of *(8N - 2)/3* reduction in the number of operations. A single measurement time-domain signal of length *N = 10,000* is representative of the data used in the research, and the number of operations are reduced by a factor of 26,666.

$$\begin{aligned}\tilde{x} \cdot \tilde{y} + \tilde{x}^* \cdot \tilde{y}^* &= (x_{\mathrm{re}} + \mathrm{i}x_{\mathrm{im}}) \cdot (y_{\mathrm{re}} + \mathrm{i}y_{\mathrm{im}}) + (x_{\mathrm{re}} - \mathrm{i}x_{\mathrm{im}}) \cdot (y_{\mathrm{re}} - \mathrm{i}y_{\mathrm{im}}) \\ &= 2(x_{\mathrm{re}} \cdot y_{\mathrm{re}} - x_{\mathrm{re}} \cdot y_{\mathrm{re}})\end{aligned} \tag{7.15}$$

$$if \quad 0 < k < \left(\frac{N}{2} - 1\right) \quad then \quad \vec{a}_{-k} = \left(\vec{a}_k\right)^* \quad \therefore$$

$$\begin{aligned}\vec{\Delta} = 2((&\Re\mathrm{e}(\tilde{f}_k) \cdot \Re\mathrm{e}(\vec{a}_k) - \Im\mathrm{m}(\tilde{f}_k) \cdot \Im\mathrm{m}(\vec{a}_k)) - (\Re\mathrm{e}(\tilde{\chi}) \cdot \Re\mathrm{e}(\vec{a}_k) - \Im\mathrm{m}(\tilde{\chi}) \\ &\cdot \Im\mathrm{m}(\vec{a}_k)))\end{aligned} \tag{7.16}$$

The runtime improvement of the time-domain amplitude objective function formulation in implementation-3 results in calculations which are a factor of 5.5 slower than the complex signal and transfer function objective function calculations. Additionally, the time-domain amplitude objective function formulation of implementation-3 results in calculations which are a factor of 4.0 slower than the magnitude and phase objective function

calculations. The computational runtime improvement in the time-domain objective function is not much less than the corresponding decrease in mathematical operations of Equation 7.16. The research hypothesizes the discrepancy between computational runtime and mathematical operations is partially because the IDFT implemented in Python which is used to solve Equation 7.10 is a compiled function, whereas Equation 7.16 is implemented interpretively in Python. Specifically, Numpy implements the DFT and IDFT as a C porting of the Fortran FFTPACK library, whereas SciPy directly calls the Fortran FFTPACK library. An additional source in the discrepancy is that the multiplicative factors provided in Table 7.1 are for the entire objective function computation, not just the IDFT signal transformation. The entire objective function computation includes calculating the: theoretical transfer functions, signal conflations and transformations, error function values, and precision limit enforcements. However, the comparable runtime performance of all five objective functions, combined with the superior accuracy of the time-domain objective function formulation make the time-domain objective function the selected formulation for determining the error which drives the optimizations.

7.2. RUNTIME OF MEASUREMENT CONFIGURATIONS

The optimizations performed to generate the results for Section 6.1 are characterized by the measurements, configurations, degrees of freedom, and computational runtime of the optimizations. The three tables provided in this section list the optimization performance of most of the optimizations in Section 6 in descending order according to the placement within Section 6 which the result appears. The performance of the optimization algorithm is assessed using comparisons of the optimization configuration with the time required to complete the optimization. Additional analysis is provided using runtime profiling of the four primary components of the objective function computations as a function of the number of layers in the sample and number of measurements in the optimization. Three general observations are the optimization runtime increases with increasing number of measurements, increasing number of degrees of freedom, and increasing number of unique measurement configurations.

The number of initial measurements, number of optimization measurement pairs, and bandwidth of the extracted optical properties are provided in Table 7.2. The number of initial measurements includes measurements that are eventually combined into a single signal, and the reference measurement bookends on either side of a sample measurement

collection. The number of optimization measurement pairs are the number of sample measurement and reference measurement pairs used to perform the optimizations. The number of unique configurations are the number of unique combinations of thickness, sample material, sample orientation, and polarization state. For example, if two measurement configurations yield two different theoretical transfer functions for a single frequency, then the two measurement configurations are unique. In contrast, if two measurement configurations yield the same theoretical transfer function for a single frequency, then the two measurement configurations are the same.

Table 7.2) The number of measurements, configurations, and parameter unknowns used in the optimization for the samples used in the research.

Config. ID	Sample	Initial Measure-ments	Optimization Measurement Pairs	Unique Configurations	Band-width (THz)
1	HRSi	72	6	1	2.1
2	HRSi	3	1	1	2.9
3	HDPE-A	78	8	1	1.6
4 (5)	HDPE-B (*)	42	5	1	2.1
6	HDPE-C	3	1	1	3.0
7	HDPE-C	3	1	1	3.0
8	HDPE-ABC	123	14	3	1.6
9	HDPE-AC	81	9	2	1.6
10	Lactose	6	2	1	1.6
11	Lactose	3	1	1	1.7
12	Oxycodone	6	2	1	2.0
13	Hydrocodone	6	2	1	2.0
14	HRSi|Air|HDPE-A	57	10	3	2.9
15	HRSi|Air|HDPE-A	66	13	4	2.9
16	HRSi|Air|HDPE-A	60	11	3	2.1

The computer runtime required to calculate the theoretical transfer function from one to fourteen unique measurement configurations is shown in

Figure 7.1. The left and right plots of Figure 7.1 are the times required to calculate the transfer function using the normal and non-normal incidence equations, respectively. A single measurement is used to generate the results shown in Figure 7.1. The red and blue circle markers in Figure 7.1 are the times required to calculate the theoretical transfer function using vectorized and iterative computations, respectively. Each runtime data point in Figure 7.1 is the average of 10,000 theoretical transfer function calculations. Each runtime data point in Figure 7.1 corresponds to the transfer function at a single frequency. The lines connecting the data points in the plots of Figure 7.1 are for illustrative purposes.

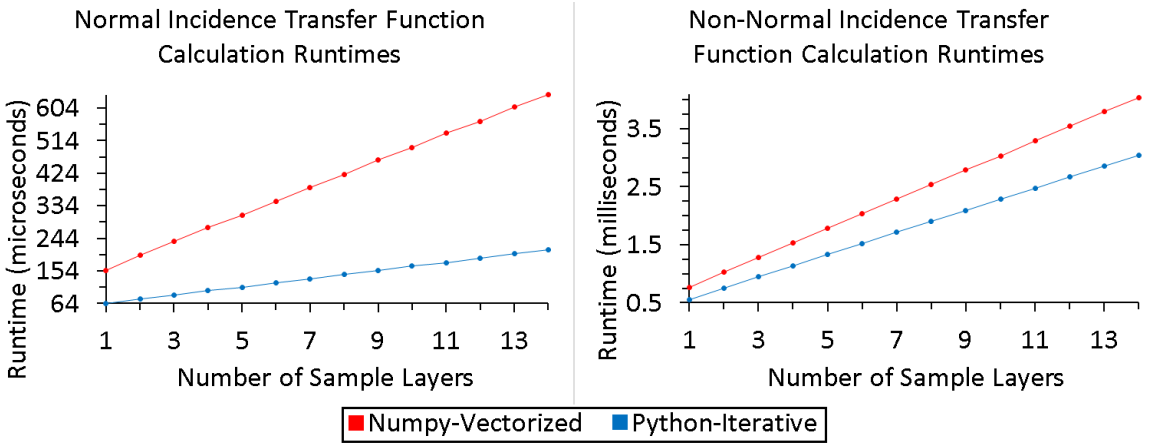

Figure 7.1) The left and right plots are the computer runtime required to compute the theoretical transfer function at normal and non-normal incidence, respectively. Each data point is the average of 10,000 computations. The number of sample layers are the number of layers in the sample being evaluated, for a single measurement.

The vectorized computations leverage Numpy 32-bit floating-point arithmetic and Numpy vector functions. The iterative computations leverage native Python 64-bit floating-point arithmetic and iterative list operations.

Interestingly, the computational overhead time required to create, operate, and maintain Numpy arrays is greater than the runtime benefit of the vectorized operations because of the small number of vector elements. Generally, Numpy vector operations outperform Python iterative operations once the vector lengths exceed hundreds of elements. In the theoretical transfer function calculation, the vector length is equal to the number of layers in the sample, but the number of samples in the multi-layer stacks investigated in the research are at most three layers. Referring to Figure 7.1, the average multiplicative gain factor using the fourteen runtime results of Python operations over Numpy operations for normal and non-normal incidence is 2.9 and 1.3, respectively. The fourteen runtime results indicate that for every additional layer added to the multi-layer sample, the multiplicative gain factor increases by 0.032 and decreases by 0.0025 for normal and non-normal incidence, respectively.

Insight into the ability of non-vectorized operations in Python to outperform Numpy vectorized operations is provided by examining the number of object attributes associated with newly created variables. The number of built-in and total attributes for the Numpy 32-bit floating-point object is 66 and 133, respectively. The number of built-in and total attributes for the Numpy 64-bit floating-point object is 70 and 141, respectively. In

comparison, the number of built-in and total attributes for the Python 64-bit floating-point object is 50 and 57, respectively. The number of built-in and total attributes for both the Numpy 64-bit and 128-bit complex-valued floating-point objects is 67 and 134, respectively. In comparison, the number of built-in and total attributes for the Python 128-bit complex-valued floating-point object is 46 and 49, respectively. The attribute inheritance property of Numpy array objects is the mechanism that facilitates fast array manipulation for large numbers of vector elements. There does not exist native Python 32-bit floating-point or 64-bit complex-valued floating-point objects in the Python programming language. Because of the results demonstrated in Figure 7.1, the native Python floating-point arithmetic is implemented in the production version of the code for theoretical transfer function calculations.

The number of unknown thicknesses, pitch angles, roll angles, yaws angles, air absorption profiles, and unknown complex refractive indices are provided in Table 7.3. The number of unknown thicknesses is the total number of thickness variables being optimized. The optimization algorithm is constructed so that multiple measurements can be linked to the same thickness variable. The number of unknown orientations are the number of unknown pitch, roll, and yaw variables being optimized. Similar to thickness, the optimization is constructed to facilitate a linking of measurements to specific

pitch, roll, and yaw variables. The number of unknown air absorptions is the total number of air absorption profiles which need to be determined. The optimization algorithm facilitates a linking of measurements to specific air absorption profiles. Due to computational resource constraints, the research computes a single effective air absorption profile for all of the measurements in an optimization. Lastly, the number of unknown complex refractive indices is the number of refractive index and extinction coefficient pairs that are unknown, for a single frequency, in the optimization. The number of unknown complex refractive indices is representative of the number of materials in the sample that for which the optical properties are being extracted.

Table 7.3) The number of measurements, configurations, and parameter unknowns used in the optimization for the samples used in the research.

Config. ID	**Sample**	**Number of Unknowns**					
		Thick-ness	**Pitch**	**Roll**	**Yaw**	**Air Absorp-tion**	**Complex Refractive Index**
1	HRSi	1	0	0	0	1	1
2	HRSi	1	1	1	0	0	1
3	HDPE-A	1	0	0	0	1	1
4 (5)	HDPE-B (*)	1	0	0	0	1	1
6	HDPE-C	1	0	0	0	1	1
7	HDPE-C	1	1	1	0	0	1
8	HDPE-ABC	3	0	0	0	1	1
9	HDPE-AC	2	0	0	0	1	1
10	Lactose	0	0	0	0	1	1
11	Lactose	1	1	1	0	0	1
12	Oxycodone	0	0	0	0	1	1
13	Hydrocodone	0	0	0	0	1	1
14	HRSi|Air|HDPE-A	1	0	0	0	1	2
15	HRSi|Air|HDPE-A	1	0	0	0	1	2
16	HRSi|Air|HDPE-A	1	0	0	0	1	2

Lastly, computation runtime information is provided in Table 7.4 to characterize the computational demands of the optimization algorithm. The computer configuration used to test the execution times is a 64-bit Windows 8 operating system with an Intel Core i7 4790K clocked at 4.0 GHz and 32 GB of 12800 MB/s DDR3 clocked at 1600 MHz. The optimizations performed in this section are ran in parallel, with no more than seven optimizations running concurrently. Seven concurrent processes brought the CPU usage up to approximately 88% and does not saturate the processor. The memory usage never exceeded 20–30% of the available memory. The information is presented as a disclaimer that the runtimes are not based on a single optimization process in a computational environment dedicated to that one optimization. The computer runtime, in minutes, for each of the primary components of the optimization algorithm is provided in in computational runtime tables. The runtime is recorded at intersections of the primary components of the optimization algorithm in Unix time, so that the sum of the individual components represents the total beginning-to-end computer time used.

Table 7.4) The computer runtime for the primary components of the optimization algorithm for the samples used in the research.

Con-fig. ID	Samples	Optimization Runtime (minutes)					
		Thick-ness	Orient-ation	Air Absorp.	Comp. Refract. Index	Re-Optimize	Total
1	HRSi	377	0	21	6	2	439
2	HRSi	8	101	0	2	0	113
3	HDPE-A	46	0	35	5	20	156
4	HDPE-B	215	0	28	5	245	549
5	HDPE-B*	278	0	42	6	46	421
6	HDPE-C	27	0	5	2	19	53
7	HDPE-C	6	93	0	8	0	110
8	HDPE-ABC	1274	0	18	6	< 1	1364
9	HDPE-AC	193	0	31	4	6	280
10	Lactose	0	0	25	2	0	29
11	Lactose	7	87	0	1	0	97
12	Oxycodone	0	0	17	3	0	22
13	Hydrocodone	0	0	22	3	0	27
14	HRSi |Air| HDPE-A	1179	0	83	43	0	1313
15	HRSi |Air| HDPE-A	4673	0	139	30	0	4859
16	HRSi |Air| HDPE-A	5024	0	124	29	0	5191

The total runtimes listed in Table 7.4 are large relative to the time in a day. For example, the six-measurement simultaneous optimization of HRSi with thickness optimization requires over seven hours to complete. In contrast, the single-measurement optimization of HDPE-C with thickness optimization requires fifty-three hours to complete. Even faster, the two-measurement simultaneous optimization of Hydrocodone without thickness optimization required twenty-seven minutes to complete. The longest

runtimes are the HRSi|Air|HDPE-A three-layer sample optimizations with thickness optimization. The HRSi|Air|HDPE-A optimizations with thickness determination required as much as eighty-seven hours to complete. The configuration ID numbers 2, 7, and 11 in Table 7.4 correspond to the simultaneous thickness and orientation determination using single-measurement optimization of HRSi, HDPE-C, and Lactose, respectively. As indicated in Table 7.4, each of these three optimizations required nearly two hours to complete a single iteration, but ten iterations are performed for each optimization. The maximum possible number of iterations for the DE optimization encountered by the research, based on the configurations identified in Table 7.2 and Table 7.3 and the SciPy configurations defined in Table 5.1, is 399 iterations. Similarly, the maximum possible number of iterations for the BH optimization is 800 iterations and 1200 function evaluations. Lastly, the maximum possible number of iterations for the NM optimization for each evaluation frequency is 1600 iterations and 2400 function evaluations.

Although the total runtimes are large in many of the optimizations, the runtimes are much longer without the innovative computational improvements to the algorithm implementation explained in Section 7.1. As a demonstration, Figure 7.2 shows the runtime improvement gained by

strategically calculating the IDFT instead of a full matrix multiplication. The left plot in Figure 7.2 shows the runtime required to compute the time-domain signal using the IDFT for up to fourteen measurements. The blue circle markers in the left plot of Figure 7.2 correspond to the native Python strategic-interpretive solution developed in the research for reducing the runtime of the IDFT transformation. The red circle markers in the left plot of Figure 7.2 correspond to the full matrix calculation using the Numpy vectorized and C-compiled implementation of the FORTRAN FFTPACK library IRFFT function. The right plot of Figure 7.2 using black circle markers is the runtime of the Numba vectorized error function calculation. The runtime improvement of the Numba vectorized error function implementation over the iterative implementation is sufficiently dramatic the comparison is considered trivial. The lines connecting the data points in the plots of Figure 7.2 are for illustrative purposes.

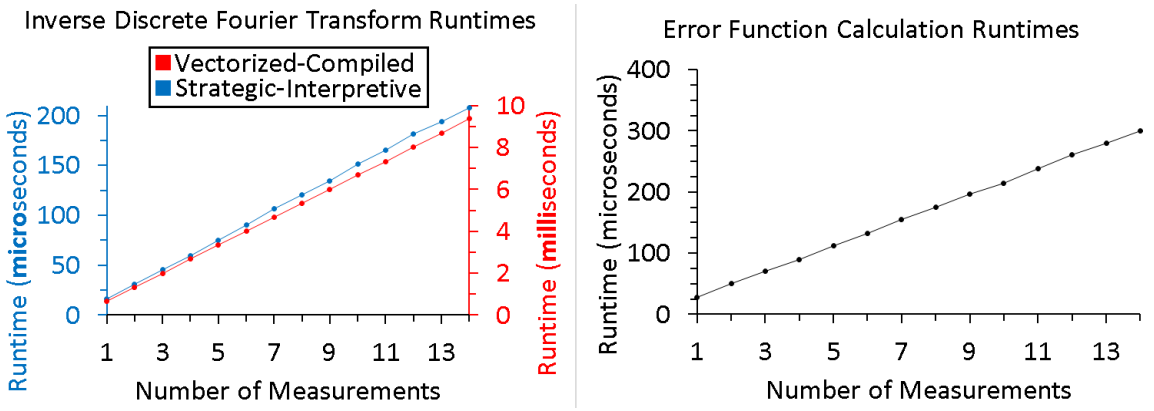

Figure 7.2) The left plot is the runtime to compute the IDFT using a strategic-interpretive implementation (blue) versus the Numpy vectorized C-compiled Fortran porting of the FFTPACK library. The right plot is the runtime for the error function calculation.

Referring to IDFT runtimes in the left plot of Figure 7.2, the average multiplicative gain factor using the fourteen runtime results of strategic-interpretive Python over vectorized-compiled Numpy operations is 44.1 multiplicative units. The fourteen runtime results indicate that for every additional measurement, the multiplicative gain factor increases by 0.23 multiplicative units. The strong runtime improvement reinforces the utility of the approaches in Section 7.1.

8. CONCLUSIONS

There are many accomplishments of the research. The accomplishments of the research span the disciplines of signal processing, optimization objective function research, and physical parameter extraction. All three of these topics have been integrated by the research to facilitate the multi-measurement optimization-based determination of physical parameters.

The research examined seven error measures across five objective function formulations and found that the directionally unbiased differential form of the mixed error measure in the frequency-domain representations of the objective function yields the smallest variation of refractive index for material optical properties with nearly constant refractive index. The research also found that the centered form of the mixed error measure in the time-domain representation of the objective function yields the smallest variation of refractive index for material optical properties with nearly constant refractive index. The findings of the research show that the relative error measures perform no worse than the legacy error measures for single-measurement optimizations in the presence of AWGN. In addition, the

research has found that the directionally unbiased differential form of the mixed error measure for the transfer function magnitude and phase objective function formulation has a 40% reduction in average variation of HRSi complex refractive index for a six-measurement optimization compared with the legacy approach. Furthermore, the centered form of the mixed error measure for the time-domain amplitude objective function formulation has a 28% reduction in average variation of HRSi complex refractive index compared with the legacy approach for six-measurement optimizations.

The research has shown that the centered form in the time-domain amplitude objective function formulation yields lower simulation error and optical property variation compared with the directionally unbiased differential form of the mixed error measure in the four frequency-domain objective function formulations. The results of testing the mixed error measure among the five objective function formulations show that the time-domain objective function formulation yields simulation error between 27% and 83% less than the four other objective function formulations using analysis of single-layer HDPE and HRSi six-measurement optimization. The research has shown the mixed error measure, in the case of six-measurement HRSi optimization, reduces the FP oscillations in refractive index by as much

as 92% and in extinction coefficient by as much as 43% compared with best pedigree single-measurement HRSi optimization.

The research has demonstrated the capability to perform simultaneous sample orientation, layer thickness, and optical property extraction of samples which are composed of materials with uniform and non-uniform optical property variation. The research has shown that simultaneous multi-measurement optimizations yield smaller variation in optical property as a function of frequency compared with separate extractions of single-layer optimizations. The research has shown that, for a 3 THz bandwidth starting at 60 GHz, the percent difference between the numerical and analytic refractive index is no more than 4% and 6% for uniform and non-uniform optical property materials, respectively. Lastly, the research has demonstrated the ability to perform material identification of unknown materials in multi-layer stacks of HRSi and HDPE.

The research investigated particulate samples in the form of α-lactose monohydrate, pharmaceutical-grade oxycodone, and hydrocodone. The particulate samples are granular powders. A large opportunity currently exists in the THz community to develop new technology for the detection and identification of powders [95, 96]. Examples include explosives, illicit drugs such as opioids, and bio-toxins such as anthrax [96]. One challenge of

measuring powder-based samples in the laboratory is that particulate samples typically experience shifting during the handling process. The shifting can result in significant thickness variation across the THz beam. The results of the research indicate that the algorithm is robust against non-constant sample thickness across the THz beam and therefore is highly applicable to granular powder optical property characterization. The algorithm is robust against non-constant sample thickness because the multi-measurement optimization can connect the optical property of the sample across the measurements while requiring unique thickness and orientation solutions or each measurement. The results obtained for α-lactose monohydrate, pharmaceutical-grade Oxycodone, and Hydrocodone demonstrate the ability to extract the optical properties of the respective samples. Furthermore, the research has demonstrated the ability to extract the optical properties of powder samples for uncertain sample thickness and orientation. Although the algorithm developed during the research is sufficiently robust to extract the optical properties of powder samples, the algorithm is not sufficiently developed to distinguish the absorption contribution from the scattering contribution. The scattering contribution is a scattering component that is currently present in the extracted absorption coefficients of the powder samples. An important future development of this research is the ability to robustly account for the

scattering component to obtain pure absorption coefficients that do not contain scattering loss contributions.

There are multiple items contained within the scope of the research requiring further investigation. First, an alternative method for seeding the first trial solution of the Differential Evolution optimization is necessary. The current implementation controls the first trial solution by adjusting the bounds for each active variable so that the average of the lower and upper bound is the first trial solution. The most robust solution is not to adjust the bounds, but rather to adjust the RandomState() seed in the DE to identify any location within the bounds as the first trial solution. Another item that requires more investigation is reducing the computational runtime of the algorithms. One path to address the runtime issue is adjusting the implementation of the code, and finding more efficient functions and approaches to calculations in the computer code. The DE and BH algorithms are computationally intensive, and the research anticipates runtime reductions can be achieved by altering the optimization configuration for the SciPy function. Additional runtime reductions are achievable by leveraging computational parallelism using multi-core Central Processing Unit (CPU), Graphics Processing Unit (GPU), and computer clustering technology. The research suggests the runtime improvements to facilitate discovery.

The research identifies the need to more robustly demonstrate the ability to perform simultaneous thickness and orientation determination for multi-measurement optimizations and to more rigorously prove that effective thickness and orientation determination for multi-measurement optimization is valid. The research identifies the need for a method to identify a statistically significant set of frequencies for which the thickness and orientation extraction are sufficiently stable. The research suggests investigating separate and simultaneous thickness and orientation determination for an expanded range of incidence angles, polarization states, materials, and multi-layer compositions. Another future research opportunity is to determine the feasibility of reducing the number of air absorption features to include only the three water vapor absorption features in the frequency range 0.0–1.0 THz. The motivation for reducing the number of features is do avoid air absorption optimization in frequency regions with low signal strength. Additionally, the research suggests re-evaluating the frequency range and number of excluded frequency regions when optimizing the frequency-independent parameters such as thickness and orientation, because the thickness and orientation solutions are strongly coupled to the frequencies used to calculate the simulation error and refractive index variance. The benefit is more stable and reliable frequency-independent parameter optimization solution. Validating

the optimization extracted layer thicknesses and sample orientations is necessary to empirically establish the confidence in the optimization results. The research suggests the first step to frequency-independent parameter validation is the physical measurement of the sample thicknesses to single micrometer accuracy and precision. Lastly, the research advices a more complete and comprehensive demonstration of the validity of simultaneous thickness and orientation determination for materials with non-uniform optical properties, as demonstrated in Section 6.1.1.3.

REFERENCES

[1] W. Withayachumnankul, M. Naftaly, "Fundamentals of Measurement in Terahertz Time-Domain Spectroscopy." *Journal of Infrared Millimeter and Terahertz Waves* 35 (2014): 610–637.

[2] T. Chang, et al., "Measurement of Complex Terahertz Dielectric Properties of Polymers using an Improved Free-Space Technique." *IOP Publishing, Measurement Science and Technology Meas. Sci. Technol.* 28 (2017): 1–A.

[3] M. Scheller, "Data Extraction from Terahertz time-domain Spectroscopy Measurements." *Springer Science+Business Media New York, J Infrared Milli Terahz Waves* 35 (2014): 638–648.

[4] M. Naftaly, R. Miles, "Terahertz Beam Interactions with Amorphous Materials." *Terahertz Frequency Detection and Identification of Materials and Objects, NATO Science for Peace and Security Series B: Physics and Biophysics, Springer*, (2007): 107–122.

[5] *TPS Spectra 3000 – THz Pulse Imaging and Spectroscopy* (August 3, 2017). Retrieved from http://www.teraview.com/products/terahertz-pulsed-spectra-3000/index.html (Accessed on April 7, 2018).

[6] L. Duvillaret, F. Garet, J.-F. Roux, J.-L. Coutaz, "Analytical Modeling and Optimization of Terahertz Time-Domain Spectroscopy Experiments, using Photoswitches as Antennas." *IEEE Journal of Selected Topics in Quantum Electronics* (2001) Vol. 7 Iss. 4: 615–623.

[7] L. Duvillaret, et al., "A Reliable Method for Extraction of Material Parameters in Terahertz Time-Domain Spectroscopy." *IEEE Journal of Selected Topics in Quantum Electronics* 2.3 (1996): 739–746.

[8] N. Palka, et al., “Precise Determination of Thicknesses of Multilayer Polyethylene Composite Materials by Terahertz Time-Domain Spectroscopy.” *Journal of Infrared Millimeter and Terahertz Waves* 36.6 (2015): 578–596.

[9] M. Scheller, et al., “Fast and Accurate Thickness Determination of Unknown Materials using Terahertz time-domain Spectroscopy.” *Journal of Infrared Millimeter and Terahertz Waves* 30.7 (2009): 762–769.

[10] L. Duvillaret, et al., “Highly Precise Determination of Optical Constants and Sample Thickness in Terahertz Time-Domain Spectroscopy.” *Applied Optics* 38.2 (1999): 409–415.

[11] T.D. Dorney, et al., “Material Parameter Estimation with Terahertz Time-Domain Spectroscopy.” *Journal of the Optical Society of America A-Optics Image Science and Vision* 18.7 (2001): 1562–1571.

[12] I. Pupeza, et al., “Highly Accurate Optical Material Parameter Determination with THz Time-Domain Spectroscopy.” *Optics Express* 15.7 (2007): 4335–4350.

[13] M. Scheller, “Real-Time Terahertz Material Characterization by Numerical Three-Dimensional Optimization.” *Optics Express* 19.11 (2011): 10647–10655.

[14] W. Withayachumnankul, et l., “Material Thickness Optimization for Transmission-Mode Terahertz Time-Domain Spectroscopy.” *Optics Express* 16.10 (2008): 7382–7396.

[15] W. Withayachumnankul, M. Naftaly, “Fundamentals of Measurement in Terahertz Time-Domain Spectroscopy.” *J Infrared Milli Terahz Waves* 35 (2014): 610–637.

[16] S. Krimi, et al., “Inline Multilayer Thickness Sensing by using Terahertz Time-Domain Spectroscopy in Reflection Geometry.” *2013 38th International Conference on Infrared, Millimeter, and Terahertz Waves* (2013).

[17] R. Fastampa, et al., "Cancellation of Fabry-Perot Interference Effects in Terahertz Time-Domain Spectroscopy of Optically Thin Samples." *Physical Review A* 95, 063831 (2017).

[18] J.A. Hejase, "Terahertz time-domain Methods for Material Characterization of Layered Dielectric Media." *Ph.D. Thesis Dissertation, Electrical Engineering, Michigan State University* (2012).

[19] J.A. Hejase, et al., "A Multiple Angle Material Parameter Extraction Method for Stacked Layers of Dielectrics using THz time-domain Spectroscopy." *Review of Progress in Quantitative Nondestructive Evaluation, AIP Conf. Proc.* 1430 (2012): 581–588.

[20] M. Exter, C. Fattinger, D. Grischowski, "Terahertz Time-Domain Spectroscopy of Water Vapor." *Optics Letters* Vol. 14, Iss. 20 (1989): 1128–1130.

[21] D.M. Slocum, et al., "Atmospheric Absorption of Terahertz Radiation and Water Vapor Continuum Effects." *Journal of Quantitative Spectroscopy and Radiative Transfer* Vol. 127 (September 2013): 49–63.

[22] D.J. Griffiths, "Introduction to Electrodynamics." *Prentice-Hall Inc., 3rd Ed.* (1999).

[23] P. Yeh, "Optical Waves in Layered Media." *John Wiley & Sons Inc.* (2005).

[24] J.D. Jackson, "Classical Electrodynamics." *John Wiley & Sons Inc., 3rd Ed.* (1999).

[25] P. Markos, C.M. Soukoulis, "Wave Propagation: From Electrons to Photonic Crystals and Left-Handed Materials." *Princeton University Press* (2008).

[26] M. Born, E. Wolf, "Principles of Optics." *Cambridge University Press 7th Ed.* (1999).

[27] H. Goldstein, C. Poole, J. Safko, "Classical Mechanics." *Pearson Education Inc., 3rd Ed.* (2002).

[28] L.D. Landau, E.M. Lifshitz, L.P. Pitaevskii, "Course of Theoretical Physics Volume 8: Electrodynamics of Continuous Media." *2nd Ed., Published by Elsevier* (2007).

[29] S. Sanders, "OSE5312 Slides Class 04 - Kramers-Kronig Relations." *Computer-Aided Engineering, College of Engineering, University Wisconsin at Madison*. Retrieved from https://homepages.cae.wisc.edu/~ssanders/me_770/supplemental_material/kramers-kronig/kramers_kronig_lecture_notes_UCF.pdf (Accessed on April 6, 2018).

[30] C. Bedard, A. Destexhe, "Kramers-Kronig Relations and the Properties of Conductivity and Permittivity in Heterogeneous Media." *Journal of Electromagnetic Analysis and Applications* Vol. 10, Iss. 2 (Jan. 2018): 34–51.

[31] M. Herrmann, et al., "Combination of Kramers–Kronig Transform and Time-Domain Methods for the Determination of Optical Constants in THz Spectroscopy." *Elsevier Ltd., Vibrational Spectroscopy* 60 (2012): 107–112.

[32] K.W. Holman, R.J. Jones, A. Marian, S.T. Cundiff, J. Ye, "Detailed Studies and Control of Intensity-related Dynamics of Femtosecond Frequency Combs from Mode-locked Ti:Sapphire Lasers." *IEEE J. Sel. Topics Quantum Electr.*, (2003) 9: 1018-1024.

[33] S.T. Cundiff, "Optical Frequency Metrology with Mode Locked Lasers." *Publication of JILA NIST and University of Colorado*: 1–35.

[34] H.L. Hall, "Defining and Measuring Optical Frequencies: The Optical Clock, Opportunity, and More." *Nobel Lecture* (2005): 103–135.

[35] H.Z. Ahmed, "Femtochemistry: Atomic-Scale Dynamics of the Bond using Ultrafast Lasers." *Nobel Lecture* (1999): 274–367.

[36] J.L. Hall, J. Ye, S.A. Diddams, L.S. Ma, S.T. Cundiff, D.J. Jones, "Ultrasensitive Spectroscopy, Ultrastable Lasers, Ultrafast Lasers, and

Seriously Nonlinear Fiber: A New Alliance for Physics and Metrology.*" IEEE J. of Quantum Electr.* (2001) 37 12: 1482–1492.

[37] N. Katzenellenbogen, D. Grischkowsky, J.M. Woodall, M.R. Melloch, "Subpicosecond, Freely Propagating Electromagnetic Pulse Generation and Detection Using GAAS-AS Epilayers." *Appl. Phys. Lett.* (1991) 58 14: 1512–1514.

[38] H. Zhang, J.K. Wahlstrand, S.B. Choi, S.T. Cundiff, "Contactless Photoconductive Terahertz Generation." *Opt. Lett.* (2011) 36: 223–225.

[39] K.A. McIntosh, et al., "Investigation of Ultrashort Photocarrier Relaxation Times in Low-Temperature-Grown GaAs." Appl. Phys. Lett. 70, 354 (1997): 354–356.

[40] J. Wheatcroft, "Terahertz Time-Domain Spectroscopy and Fresnel Coefficient Based Predictive Model." *Wright State University Physics MS Thesis* (2012).

[41] J. Dai, et al., "Terahertz Time-Domain Spectroscopy Characterization of the Far-Infrared Absorption and Index of Refraction of High-Resistivity, Float-Zone Silicon." *J. Opt. Soc. Am. B,* 21.7 (2004): 1379–1386.

[42] *Personal Communications*, Mr. Andrew Niklas and Dr. Weidong Zhang, Ph.D. (2017).

[43] L. Duvillaret, et al., "Analytical Modeling and Optimization of Terahertz Time-Domain Spectroscopy Experiments Using Photoswitches as Antennas." *IEEE Journal on Selected Topics in Quantum Electronics* Vol. 7 No. 4 (Jul./Aug. 2001): 615–623.

[44] M. Naftaly, R. Dudley, "Methodologies for Determining the Dynamic Ranges and Signal-to-Noise Ratios of Terahertz Time-Domain Spectrometers." *Optics Letters* Vol. 34, No. 8 (Apr. 2009): 1213–1215.

[45] S. Mickan, et al., "The limit of spectral resolution in THz time-domain spectroscopy." *Proc. of SPIE, Photonics: Design, Technology, and Packaging* Vol. 5277 (2004): 54–64.

[46] P.F. Goldsmith, “Quasioptical Systems: Gaussian Beam Quasioptical Propagation and Applications.” *1st Ed., John Wiley & Sons, Inc., IEEE Press Series on RF and Microwave Technology Series #4* (1998).

[47] C. Tim Lei (tim.lei@colorado.edu), “Chapter 5, Gaussian Beam.” *University of Colorado, Boulder Department of Physics*. Retrieved from https://www.colorado.edu/physics/phys4510/phys4510_fa05/Chapter5.pdf (Accessed on April 24, 2018).

[48] R.D. Guenther, "Modern Optics" *2nd Ed., John Wiley & Sons, Inc.* (2015).

[49] K.M. Nam, “Modeling Terahertz Diffuse Scattering from Granular Media using Radiative Transfer Theory.” *M.S. Thesis Dissertation, Electrical and Computer Engineering, Portland State University* (2011).

[50] E.R. Brown, et al., “Attenuation Contrast between Biomolecular and Inorganic Materials at Terahertz Frequencies.” Appl. Phys. Lett. Vol. 85, No. 13, (Sep. 2004): 2523–2525.

[51] M. Kaushik, et. al., “Reduction of Scattering Effects in THz-TDS Signals.” *IEEE Photonics Technology Letters* Vol. 24, No. 2 (Jan. 2012): 155–157.

[52] A.J. Cox, A.J. DeWeerd, J. Linden, “An Experiment to Measure Mie and Rayleigh Total Scattering Cross Sections." *American Journal of Physics* 70 6 (Jun. 2002): 620–625.

[53] M. Kaushik, “Characterizing and Mitigating Scattering Effects in Terahertz Time Domain Spectroscopy Measurements.” *Ph.D. Thesis Dissertation, Electrical and Electronic Engineering, University of Adelaide* (2013).

[54] Meggle Excipients & Technology, “Technical Brochure: Milled and Sieved Lactose.” (Mar. 2014). Retrieved from https://www.meggle-pharma.com/cn/documents/upload/141/meggle-brochure-milled-sieved-20140327-en-office.pdf (Accessed on May 2, 2018).

[55] Sympatec GmbH (2017), "Application: Lactose." Retrieved from https://www.sympatec.com/en/applications/lactose/ (Accessed on May 2, 2018).

[56] F. Podczeck, "The Influence of Particle Size Distribution and Surface Roughness of Carrier Particles on the in vitro Properties of Dry Powder Inhalations." *Aerosol Science & Technology, American Association for Aerosol Research* 31 (1999): 301–321.

[57] P. Du, J. Du, H.D.C. Smyth, "Evaluation of Granulated Lactose as a Carrier for DPI Formulations 1: Effect of Granule Size." *American Association of Pharmaceutical Scientists (AAPS) PharmSciTech* Vol. 15, No. 6 (Dec. 2014): 1417–1428.

[58] M. Kaushik, et al., "Mitigating Scattering Effects in THz-TDS Measurements." *Proc. 35th Int. Conf. Infr., Millimeter Terahertz Waves, Rome, Italy* (Sep. 2010): 1–2.

[59] "ScipPy.org: scipy.signal.hilbert." Retrieved from https://docs.scipy.org/doc/scipy/reference/generated/scipy.signal.hilbert.html (Accessed on April 7, 2018).

[60] "SciPy.org: Discrete Fourier Transform." Retrieved from https://docs.scipy.org/doc/numpy-1.13.0/reference/routines.fft.html (Accessed on April 6, 2018).

[61] "SciPy.org: Discrete Fourier transforms (scipy.fftpack)." Retrieved from https://docs.scipy.org/doc/scipy/reference/fftpack.html (Accessed on April 6, 2018).

[62] *Download Anaconda Distribution Version: 5.0.1 | Release Date October 25, 2017* (January 8, 2018). Retrieved from https://www.continuum.io/downloads (Accessed on April 7, 2018).

[63] J.A. Nelder, R. Mead, "A Simplex Method for Function Minimization." *The Computer Journal* Vol. 7, Iss. 4 (Jan. 1965): 308–313.

[64] M.H. Wright, "Nelder, Mead, and the Other Simplex Method." *Documenta Mathematica - Extra Volume ISMP* (2012): 271–276.

[65] Y. Huang, W.F. McColl, " An Improved Simplex Method for Function Minimization." *IEEE International Conference on Systems, Man, and Cybernetics* (Oct. 1996): 1702–1705.

[66] D.J. Wales, J.P.K. Doye, "Global Optimization by Basin-Hopping and the Lowest Energy Structures of Lennard-Jones Clusters Containing up to 110 Atoms." *Journal of Physical Chemistry A* 101 28 (1997): 5111–5116.

[67] D.J. Wales, H.A. Scheraga "Global Optimization of Clusters, Crystals, and Biomolecules." *American Association for the Advancement of Science, Science, New Series* Vol. 285, No. 5432 (Aug. 1999): 1368–1372.

[68] Z. Li, H.A. Scheraga, "Monte Carlo-Minimization Approach to the Multiple-Minima Problem in Protein Folding." *Proc. Natl. Acad. Sci. USA, Chemistry Vol. 84* (Oct. 1987): 6611–6615.

[69] R. Storn, K. Price, "Differential Evolution - a Simple and Efficient Heuristic for Global Optimization over Continuous Spaces, Journal of Global Optimization." 11 (1997): 341–359.

[70] "SciPy.org: Optimization (scipy.optimize)." Retrieved from https://docs.scipy.org/doc/scipy/reference/tutorial/optimize.html (Accessed on April 6, 2018).

[71] "SciPy.org: minimize(method='Nelder-Mead')." Retrieved from https://docs.scipy.org/doc/scipy/reference/optimize.minimize-neldermead.html (Accessed on April 6, 2018).

[72] "SciPy.org: scipy.optimize.basinhopping." Retrieved from https://docs.scipy.org/doc/scipy/reference/generated/scipy.optimize.basinhopping.html (Accessed on April 6, 2018).

[73] "SciPy.org: scipy.optimize.differential_evolution." Retrieved from https://docs.scipy.org/doc/scipy/reference/generated/scipy.optimize.differential_evolution.html (Accessed on April 6, 2018).

[74] L. Tornqvist, P. Vartia, Y.O. Vartia "How Should Relative Changes be Measured?" The American Statistician Vol. 39, No. 1 (Feb. 1985): 43-46.

[75] *The HITRAN Database* (August 5, 2017). Retrieved from https://www.cfa.harvard.edu/hitran/

[76] C. Hill, et al., "HITRANonline: An Online Interface and the Flexible Representation of Spectroscopic Data in the HITRAN Database." *J. Quantitative Spectroscopy and Radiative Transfer* Vol. 177 (July 2016): 4–14.

[77] R.V. Kochanov, et al., "HITRAN Application Programming Interface (HAPI): A Comprehensive Approach to Working with Spectroscopic Data." *J. Quantitative Spectroscopy and Radiative Transfer* Vol. 177 (July 2016): 15–30.

[78] "HAPI: The HITRAN Application Programming Interface." Retrieved from http://hitran.org/hapi/ (Accessed on April 6, 2018).

[79] A. Sengupta et al., "Far Infrared Studies of Silicon using Terahertz Spectroscopy" *Materials Science and Tech.* (2005): 39–48.

[80] D. Grischowsky, et al., "Far-Infrared Time-Domain Spectroscopy with Terahertz Beams of Dielectrics and Semiconductors." *J. Opt. Soc. Am. B* 7.10 (1990).

[81] T. Chang, et al., "Accurate Determination of Dielectric Permittivity of Polymers from 75 GHz to 1.6 THz using both S-Parameters and Transmission Spectroscopy." *Applied Optics* 56.12 (2017): 3287–3292.

[82] P.D. Cunningham, et al., "Broadband Terahertz Characterization of the Refractive Index and Absorption of some important Polymeric and Organic Electro-Optic Materials." *J. Applied Physics* 109 (2011).

[83] A.L. Chung, "Material Parameter Extraction in Terahertz time-domain Spectroscopy." *Ph.D. Thesis Dissertation, Faculty of Physical and Applied Sciences School of Physics and Astronomy, University of Southampton* (2012).

[84] S. Sommer et al., "THz-Spectroscopy on High Density Polyethylene with Different Crystallinity." *J. Infrared Milli Terahz Waves* 37 (2016): 189–197.

[85] M. Naftaly, R.E. Miles, "Terahertz Time-Domain Spectroscopy for Material Characterization.", *Proc. IEEE* 95.8 (2007):1658–1665.

[86] M. Naftaly, R.E. Miles, "THz Transmission in Polymer Materials – a Data Library." *Proc. Joint 32nd Intl. Conf. IRMMW-THz* (2007).

[87] R. Piesiewicz et al., "Properties of Building and Plastic Materials in the THz Range." *Int. J. Infrared Milli. Waves* 28.363 (2007).

[88] E.R. Brown, J.E. Bjarnason, "On the Strong and Narrow Absorption Signature in Lactose at 0.53 THz." *American Institute of Physics Applied Physics Letters* 90 061908 (2007): 1–3.

[89] J.E. Bjarnason, E.R. Brown, T.M. Korter, "Comparison of the THz Absorption Feature in Lactose to Related Saccharides." *Terahertz for Military and Security Applications V, Proc. of SPIE* Vol. 6549 65490L (2007): 1–9.

[90] B. Fischer, et al., "Chemical Recognition in Terahertz Time-Domain Spectroscopy and Imaging." Semiconductor Science and Technology, Institute of Physics Publishing 20 (2005): S246–S253.

[91] B.M. Fischer, "Broadband THz Time-Domain Spectroscopy of Biomolecules: A Comprehensive Study of the Dielectric Properties of Biomaterials in the Far-Infrared." *Ph.D. Thesis Dissertation, Albert-Ludwigs University* (Oct. 2005).

[92] A. Roggenbuck, et al., "Coherent Broadband Continuous-Wave Terahertz Spectroscopy on Solid-State Samples." *New Journal of Physics* 12 (2010) 043017: 1–13.

[93] *Personal Communications*, Mr. Andrew Niklas and Dr. Elliott Brown, Ph.D. (2018).

[94] E. Kreyszig, "Advanced Engineering Mathematics*." John Wiley & Sons Pte. Ltd. 10th Ed.* (2011).

[95] K. Kawase, et al., "Non-Destructive Terahertz Imaging of Illicit Drugs using Spectral Fingerprints." *Optics Express, Optical Society of America* Vol. 11, No. 20 (Oct. 2003): 2549–2554.

[96] A.G. Davies, et al., "Terahertz Spectroscopy of Explosives and Drugs." Materials Today Vol. 11, No. 3 (Mar. 2008): 18–26.